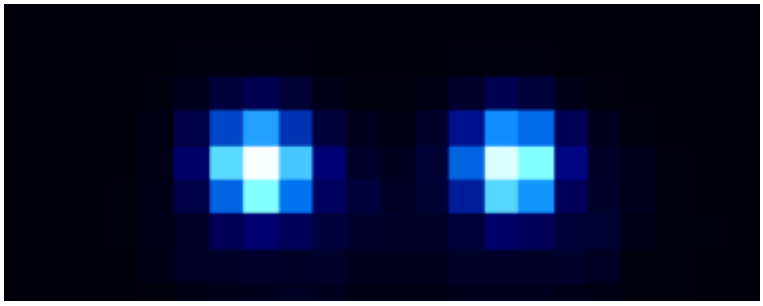
Towards study of Ion-Atom Interactions in Cold and Ultracold Regime

Anand Prakash

Raman Research Institute
Bengaluru



A thesis submitted to
Jawaharlal Nehru University, New Delhi
for the degree of
Doctor of Philosophy





Declaration

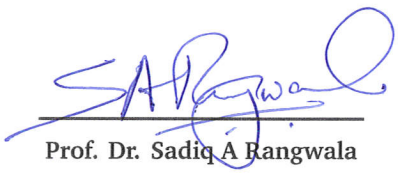
I, ***Anand Prakash***, hereby declare that the content presented in this thesis entitled ***'Towards Study of Ion-Atom interactions in cold and Ultracold Regime'*** is entirely original. This thesis has been composed independently by me at the ***Raman Research Institute (RRI)*** under the supervision of ***Prof. Dr Sadiq A Rangwala***. The subject matter presented in this thesis has not previously formed the basis for awarding any degree, diploma, membership, associateship, fellowship, or any other similar title of any other university or institution. I also declare that this thesis has been checked using the DrillBit plagiarism software.

Prof. Dr Sadiq A Rangwala
(Thesis supervisor)
Light and Matter Physics Group
Raman Research Institute,
Bengaluru-560080, India.

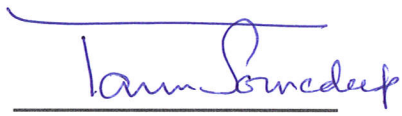
Anand Prakash

Certificate

This is to certify that the thesis entitled ***'Towards Study of Ion-Atom Interactions in cold and Ultracold Regime'*** submitted by ***Anand Prakash*** for the award of the degree of ***Doctor of Philosophy*** of the Jawaharlal Nehru University, New Delhi, India is his original work. The work presented in the thesis has not been published or submitted elsewhere for any degree or diploma award.



Prof. Dr. Sadiq A Rangwala
(Thesis supervisor)
Light and Matter Physics Group
Raman Research Institute,
Bengaluru-560080, India.



Prof. Tarun Souradeep
Director
Raman Research Institute,
Bengaluru-560080, India.

Synopsis

Thesis Title: Towards Study of Ion-Atom Interactions in Cold and Ultracold Regime

A trapped ion system is a versatile tool for studying a wide class of exciting physics, such as the interaction of a fully compensated ion with an environment [1], precision spectroscopy [2–4], metrology [5–14], optical clocks [15–18], quantum computing [19–22], Rydberg ions [23–26], thermodynamics of small systems [27–29], Coulomb crystal [30–32] and other phenomena related to crystals like melting, phase transition, spectroscopy and defects. A recent development is the invention of hybrid traps [33–59], which combine trapped ions with cold and ultracold neutral atoms and molecules. Ion-atom interaction has been studied in great detail by our group in the past and has presented some very insightful results, like resonant charge exchange(RCE) cooling of co-trapped dark ions by homonuclear co-trapped cold atoms [38, 48, 55], buffer gas cooling of lighter co-trapped ions using laser coolable ultracold co-trapped atoms [46]. In these experiments, the ions in the experiments at RRI were not amenable to laser cooling since the ions were singly ionized alkali atoms. This is because singly ionized alkali ions have a rare gas electronic configuration and a very large energy gap to the first excited states, precluding these ions' laser cooling. To go into the regime of ultracold ion-atom interactions, we need laser coolable ions which can interact with the laser cooled atoms. This allows precise control over the trapped ions' number and state. The ions produced from Group II, alkaline earth elements, are ideal candidates for such studies since, after ionization, they possess a single valance electron in the ground S state, and therefore, the singly ionized Group II ion is configurationally similar to a neutral alkali atom. This makes the Group II ion laser coolable, and with some care, the ion can be cooled to the ground state of the effective trapping potential of the ion trap. Such a single trapped ion or few ions is then the ideal system to study the nature of interactions between ion-neutral atoms and ion-field.

The practical implementation of such an experimental system is challenging and requires careful design and attention to every parameter. To achieve the ultimate goals, we need to build the scientific apparatus. While several efforts are ongoing in the country, no one has yet managed to see a single trapped fluorescing ion in the ground state of the trap. The present thesis, therefore, deals with the challenges of designing and constructing the ion trap system with a Ca^+ ion.

This brings us to the objectives of the thesis, which are

- To design, develop, and characterize an end-cap type Paul trap [1, 60].
- Design, fabrication and characterization of low divergence cold wall oven for loading ion traps.
- Characterize and optimize the driving and filter circuits of the trap.
- Design and building of the whole experimental setup from scratch.
- Experimental characterization and the study of the limits of laser cooling of the ions with the available resources, with a goal of studying Coulomb crystals.
- Theoretical/Numerical study of idealised ion-atom interaction for multipolar traps and for this trap.
- Conclusions and future work.

Ion Trap Design, Development and Fabrication

Keeping in mind the long-term objective of the study of trapped ion-atom interactions in the quantum limit, we have limited possibilities to design our trap. The requirements for our trap are (a) tight confinement, where the ion can be cooled into the ground motional state of the trap, and (b) large optical access so that laser-cooled and trapped atoms are easily introduced in the volume of the ion trap. The commonly used geometry for ion-atom interactions is the linear Paul trap and its variants, like the blade trap. However, considering our parallel experimental objectives of precision spectroscopy and optical clocks, we have decided to go with the end-cap Paul trap design. Deviating from the Paul trap's ideal geometry leads to anharmonic and higher-order harmonic terms. It leads to instability and a shift in the energy of the trapped ions, which is crucial in precision measurement. Another challenge was machining all trap parts within 10 microns tolerance and the average surface roughness of the crucial parts up

to 400 nanometers, as well as achieving axial alignment of the inner electrodes within 10 microns in India. The machining constraints have limited the electrodes' dimensions, and for feasible machining dimensions, we have optimized the quadruple coefficient and minimised the higher-order multiples contribution. This trap assembly has been assembled at RRI. We will describe all the details of the production and construction of the trap in detail so that future experiments can use our experience to improve on the various aspects of its production.

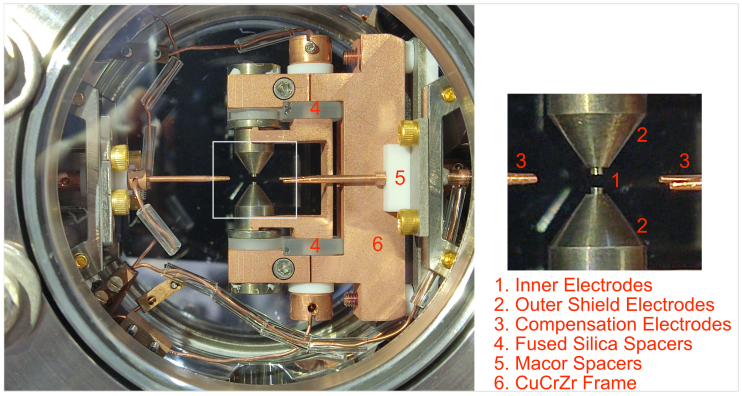


Fig. 1.: Ion trap assembly mounted inside the vacuum chamber

Low Divergence Cold Wall Oven

In the miniaturized traps, the distance between the electrodes is of the order of 1mm. Due to the coating of inhomogeneous material on the trap surface, patch potential develops, and it leads to excess micromotion due to distortion in trapping potential. To minimize the problem of patch potential, we have developed and characterized a low divergence, short response time oven. It is made from 316- stainless steel. The inner diameter, outer diameter and length of the tube are 0.9mm, 1.25mm, and 160mm, respectively. Calcium is filled up to 117mm from one end, and this part is electrically heated. Rest 43mm from the electrically heated part acts as a cold wall and helps to narrow down the atomic beam's divergence. This whole oven is mounted on a Con-Flat(CF) 16 feedthrough and aligned with the help of Macor blocks at two points with respect to the chamber. Doppler spectroscopy is used to determine the temperature of the atoms coming out of the oven. Fluorescence image and signal due to an orthogonal laser beam with respect to the direction of the atomic beam is used to determine the divergence and flow rate of the beam. Experimental $1/e^2$ diameter and the flow rate of the beam are 1.6 ± 0.17mm and 1.5 ± 0.2 atoms s^{-1} at oven current 4.5A. The temperature of the oven corresponding to this current is 702 ± 7K.

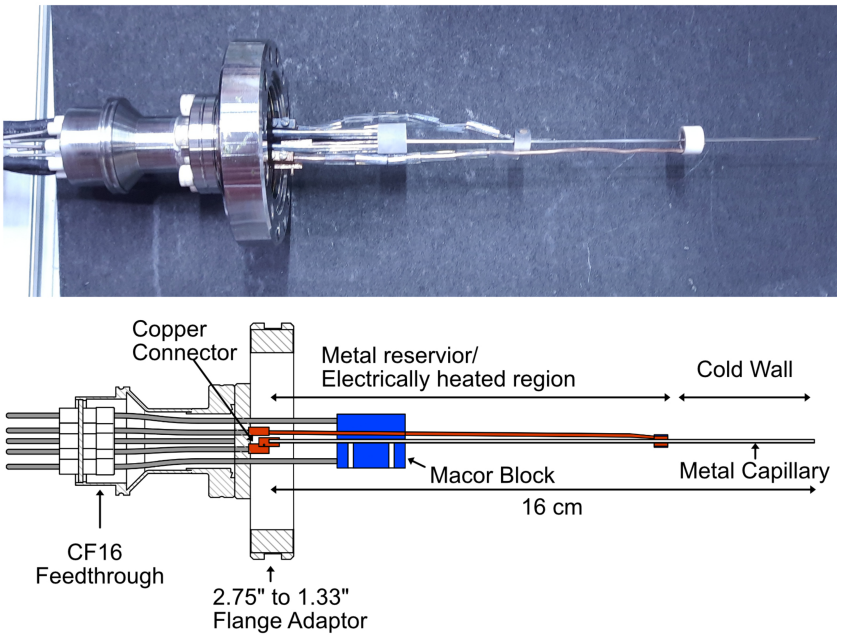


Fig. 2.: Top Panel: Image of the mounted oven on CF16 feedthrough used for the characterisation. Bottom Panel: A 2D sketch of the oven with details of the components.

Driving Circuit and Filter Circuits for the Traps

To trap the ions, a combination of controllable DC voltages and a very high voltage (HV) high fidelity radio frequency (RF) source is required to produce the time-varying confining potential, which will trap the ion loaded into it from the oven described above. As such, HV rf sources are not easily available; they would need to be made. To this end, we are using a helical resonator to drive this trap. It consists of two coils: an antenna coil and a main coil. Input voltage is provided through the antenna coil, and the same is picked up and amplified by the main coil. The main coil acts as an amplifier and a filter for the noise injected by the power supply and primary amplifier into the antenna coil. The theoretical capacitance of the trap is 14pF, and the resonator has been designed such that when a trap of 14pF is loaded across it, the resonant frequency should be around 30MHz. The initial parameters of the resonator are chosen using the reference. The theoretical unloaded resonant frequency and the resonator's quality factor are 50MHz and 1000, respectively. A bidirectional coupler is used to measure the reflected voltage from the resonator to find out the resonant frequency and quality factor. The experimentally determined unloaded frequency is 48.3MHz, and the quality factor is 853. The discrepancy between the theoretical and experimental values is due to changes in impedance at solder joints and insulators in the path. The system's impedance is matched by changing the distance between the main and antenna coil.

Compensation and other electrodes at ground potential act as an antenna, pick up the RF field and reradiate it. The Re-radiated field distorts the trapping potential and

results in the heating of the trapped ions. We need to discharge the picked-up voltage; for this, we are using shunt capacitors in the path, but effectiveness depends on the position of the capacitors. In our case, capacitors are outside the vacuum chamber.

Characterization of the Trap and Initial Experiments

Characterizing the assembled trap is a crucial step in this direction. It includes the determination of the quadruple coefficient of the assembled trap and the determination of the deviation of the assembly from the ideal one and compensation for it. A low-noise single-photon PMT and signal correlator are used to determine the excess micromotion, and it will give us the deviation in the assembled geometry. A high-resolution imaging system is also required to image the trapped ions and determine the spacing between the trapped ions in case of a string of ions. We already have the set of lasers required for cooling the ions up to the Doppler limit and the imaging system. I will present the results of the characterization and the initial experiments.

Theoretical/Numerical study of idealised ion-atom interaction for multipolar traps and for this trap

Due to our interest in ion-atom interaction in low energy regimes, we have simulated the ion-atom collision for multipole configuration to understand the effect of trapping potential on collision partners in terms of change in energy of the ion-atom system. The simulation is classical in nature, and we have closely followed the framework mentioned in Cetina *et al.* [61]. Our results [62] show that energy gained in the higher-order poles is much lower for the similar Mathieu parameter than in the quadruple configuration. Hence, higher-order pole configuration is more favourable for this kind of experiment, but it suffers from other problems like shallow trap depth and formation of local saddle points due to imperfection in the trap alignment, etc. Simulation for higher-order poles is also important due to cross terms, $x^m y^m$, in the trapping potential. I have also simulated the collision in 3 dimensions for Ca-Ca^+ for our trap. It is an extension of 1 dimension because there are no cross terms in the trapping potential of the quadruple configuration.

Summary

In this thesis, I will present the design, assembly, and characterization of an end-cap type Paul trap. This trap has been designed to study a wide class of physics and will serve as a building block for them. We will start with the characterization of the trap and initial experiments like ion loading rate, multi-ion trapping etc. Our next aim is to

pursue ion crystal dynamics with the ultimate goal of incorporating this trap for studying ion atom collision in low energy and different density regimes. Along this theme, I have built and characterized other necessary components for the experiment, like low divergence cold wall oven, helical resonator, compensation electrodes, and filter circuit. This low-divergence oven design can be used for other species, too. Simulation of ion atom collision in a perfectly compensated trap gives us helpful insight into collision dynamics. This trap will be used for our parallel interest in precision spectroscopy, optical clocks, condensed matter systems, and thermodynamics of small systems after characterizing the black body radiation effect on the trapped ion.

List of Publications

1. M. Niranjan, A. Prakash, and S. A. Rangwala, "Analysis of Multipolar Linear Paul Traps for Ion–Atom Ultracold Collision Experiments", Atoms 9, 38 (2021)

2. A. Prakash, A. Ayyadevara, E. Krishnakumar, and S. A. Rangwala, "Low divergence cold-wall oven for loading ion traps", Review of Scientific Instruments 95, 033202 (2024)

Prof. Dr Sadiq A Rangwala
(Thesis supervisor)
Light and Matter Physics Group
Raman Research Institute,
Bengaluru-560080, India.

Anand Prakash

Acknowledgement

PhD is a long journey; it took me eight years to complete. In this journey, I have received support, encouragement, help, and feedback from several people. I want to convey my sincere appreciation to each one of them. I thank my supervisor, Prof. Sadiq A Rangwala, for providing the opportunity to work in his lab. Prof. Andal Narayanan and Prof. Sanjib Sabhapandit for annual evaluation of the progress of my thesis work, discussion and feedback. Prof. E Krishnakumar, thank you for sharing experimental expertise, going through the details of the proposed work, and providing critical input at the required stages. Prof. Joseph Samuel and Prof. Yashodhan Hatwalne, thank you for your valuable time discussing the mathematical part of the work. Dr. Vaibhav Prabhudesai from TIFR for lending Molybdenum rods to start trial machining of the electrodes. Administration, Purchase, Accounts Library, E&B, EEG and MES for facilitating the research work at RRI.

The experimental set up required for carrying out the research was not possible without support and feedback of experts from different fields. Md. Ibrahim played a crucial role in the design of the oven, trap, and complete set up. Precision work for development of the prototype trap, oven, and setup is done by Ananda B K, Sivasakthi, Abdul Majeed, and others from the RRI workshop. My collaborators Subhadeep De and Sayan Patra have actively provided their input to develop the trap design. Design files are made by Harikrishna Sahu. Josh Hacko from Sydney Watches, Niranjan Reddy from CMTI and Devanand B N from GTTC provided important feedback during the machining process's inception to make the design simple and feasible. K M Yatheendran has done SEM and AFM to inspect the trap parts. Prof. Piet Schmidt, Dr Christian Tamm, and Dr Nils Huntemann from PTB Germany have shared their experience regarding the achievable surface roughness of the metal parts, the heating rate of the trapped due to rough trap electrode surfaces during operation and solutions to reduce it. Somashekhar R, Keerthipriya, Sujatha, and Meena M S from RRI helped to characterize the helical resonator and designed the PCB circuit for connection and other purposes. Prof. Tanja Mehlstaubler from PTB Germany and Martina Knoop from CNRS have shared valuable information on the trap cleaning process, helical resonator and filter circuits. Vasduha K N, Vishnu Deo Mishra, Md. Arsalan Ashraf, Chandeshwar, Sukh Veer, Cell Bio-Physics lab, Bio-Physics lab and Rheo DLS lab have shared equipment and expertise occasionally. My

junior Akhil has worked with me and independently developed crucial parts of the set up. Thanks to I-STEM for sharing the Comsol 6 license. Thanks to Md. Arsalan Ashraf for scientific discussions, sharing the license of Affinity designer, helping in making schematic diagram, and image of the experimental setup.

My journey as a researcher at RRI has been joyful due to support and continuous scientific discussions with my labmates Amarendra, Rahul Sawant, Niranjan, Sreyas, Subodh, Nishant, Vardhan, Arun, Gokul, Akhil, Vaibhav, Srijit, Arup and Raghuveer. Apart from the labmates, Surya Narayan Sahu has played important role in shaping my understanding of physics. Stay at RRI and RMV hostel was very pleasant due to the cordial and cooperative environment created by Sushil Dubey, Nomaan, Subodh, Gaurav Tiwari, Meera, Sreeja, Irla, Varun, Simanraj, Raj Prince, Mari, Anindya, Swami, Saurabh, Nancy, Sukh Veer, Arsalan, Ashish, Vishnu, Chandeshwar, Akhil, Abhishek Ghadai, Saumya Ranjan Behra, Sacchidanand, Kinjal, Manish, Mukesh, Rupak, Vaibhav, Aman, Shashank, Nishant, Sebanti, Niharika and others. Trekking, cooking, tea time, and gossip experience with friends at RRI are immemorable experiences, especially tea by Sukhveer and Chandeshwar and food prepared by Nancy, Nishu, Abhishek Ghadai and Arsalan.

On a personal note, I would like to thank my long-time friends Prakhar, Deepnarayan, Harikrishna Sahu, Deekshant, Sumit, Nancy, Raj Prince, Sushil Dubey, Arsalan, Vishnu, Chandeshwar, Sukh Veer, Ashish, Nadia and Ankit for their continuous support and feedback. Prof. Bipul Kr Sinha from A N College, Patna, for inspiring me to pursue physics. Sports facilities, yoga and other extracurricular activities at RRI have helped to keep the motivation alive. The assistance of Savitha, Shiva and Manju in the purchase process and other official work, doctors at the RRI clinic, the MES workshop family, Cooks at the RMV hostel, and Security personnel at the RRI and hostel have made my PhD life simple in an unimaginable way. Last but not the least, my family members for supporting my decision and encouraging me to pursue the PhD.

Contents

1 Introduction **1**

1.1 Overview 1

1.2 Motivation and Objectives 2

1.3 Organization of the thesis 3

2 Theory of Ion Trap and Numerical Study of Effect of Trap Geometries on Ion-Atom Interaction **5**

2.1 Introduction 5

2.2 Earnshaw's Theorem 6

2.3 Paul Trap 6

2.3.1 Equation of Motion of Charged Particles in the Ideal Paul Trap and Stability Region 9

2.4 Linear Paul Trap 14

2.5 Ion-Atom collision in Linear Paul Trap 21

2.6 Discussion 30

3 Why A New Experiment **33**

3.1 Why a New Experiment 33

3.2 Experimental Setup Requirements 33

4 Low Divergence Atomic Source **35**

4.1 Introduction 35

4.2 Design Details and Alignment 35

4.3 Experimental Details 38

4.4 Results 39

4.4.1 Divergence 39

4.4.2 Temperature and Flow Rate 40

4.4.3 Characterizing the Alignment of Atomic Beam 44

4.4.4 Observation of Ca Isotopes 46

4.4.5 Response Time of the Oven 46

4.5 Conclusion 47

5 Ion Trap Design and Fabrication **49**

5.1 Introduction 49

5.2 The End Cap Trap . . . 49
5.2.1 Design Details and Potential Analysis . . . 53
5.2.2 Material Selection . . . 56
5.2.3 Machining and Alignment . . . 57
5.2.4 Characterization of Final Assembly Parts and The Aligned Assembly 61
5.3 Conclusion . . . 67

6 Experimental Setup 69
6.1 Introduction . . . 69
6.2 System Design and Components Details . . . 69
6.2.1 System Design . . . 69
6.2.2 Components Detail . . . 70
6.3 Cleaning, Assembly and Bake out . . . 72
6.3.1 Cleaning and Assembly . . . 72
6.3.2 Baking . . . 74
6.4 Trap Drive Electronics . . . 78
6.4.1 Helical Resonator and Voltage Probe . . . 78
6.4.2 Filter circuits . . . 85
6.5 Laser and Detection System . . . 87
6.5.1 Laser System . . . 87
6.5.2 Detection System . . . 88
6.6 Initial Test . . . 88
6.7 Conclusion . . . 90

7 Trap Characterization and Initial Experiments 93
7.1 Introduction . . . 93
7.2 Trap Characterization . . . 93
7.2.1 Trap Loading . . . 93
7.2.2 Quantum Jumps . . . 95
7.2.3 Determination of Quadrupole coefficient ($a_{2,0}$) . . . 97
7.3 Excess Micromotion Compensation . . . 99
7.4 Temperature of a Single Ion and Trapping Life Time . . . 104
7.5 Lifetime of Metastable State . . . 106
7.6 RF Heating and Cloud to Coulomb Crystal Transition . . . 108
7.7 Observation of Ion Crystals . . . 110
7.8 Conclusion . . . 115

8 Summary and Future Prospects 117
8.1 Summary . . . 117
8.2 Future Prospect . . . 118

A Trap Design 121

B Trap Mounting Accessories 129

Bibliography 133

1 Introduction

1.1 Overview

The advent of laser cooling and trapping of ions [63–65] and atoms [66–68] opened the pathway for a new class of experiments. These systems could now be prepared both in the motional state of the trapping potential and internal state. As a result, there is control over the total number of trapped ions, the initial state of the particles, better isolation of interaction with the environment, and very long hold times. These properties of the trapped ion systems makes it an excellent platform for studying controlled interaction of trapped ions with co-trapped atoms [33–59], quantum information processing and quantum computation [19–22, 69–75], quantum logic spectroscopy [76], precision spectroscopy [2–4], optical frequency standards [15–18, 77–83], test of quantum mechanics [84–86], measurement of gravitational potential [87, 88], condensed matter systems [89–91], Coulomb crystals [30–32, 92], measurement of fundamental constants [78, 93–95], Rydberg-ions [23–26] and thermodynamics of small systems [27–29].

Confinement of charged particles can be achieved by combination of static electric and magnetic fields or a time-varying electric field. Traps working on the first principle are known as Penning traps [96], and the traps working on the second principle are known as Paul traps [97]. In the thesis, only Paul trap will be discussed. Since the proposal of the trapping principle in 1958 and the first demonstration of spectroscopy of free ions in 1962 [98], the trap design has undergone geometrical modification to make it suitable for different experiments. Details of the trapping principle and geometrical variations will be discussed in the later chapters of the thesis.

The idea of optical cooling [99] of vapours by resonant light was first proposed by Alfred Kastler in 1950. In 1974, Zel'dovich generalized Kastler's idea of optical cooling for a two-level system [100]. In 1975, Hansch and Schawlow [101] and Wineland and Dehmelt [102] independently proposed the optical cooling of free atoms using radiation pressure. Laser cooling of the trapped ions was observed by Neuhauser *et al.* [63] in 1978 for Ba^+ and by Wineland *et al.* [64] for Mg^+.

Since the demonstration of cooling of trapped ions, ideas and experimental realization for a new class of experiments using trapped ions started growing rapidly. This led to a quest for trap design modification depending on the experimental requirements and exploration of cooling mechanisms in detail. In the last 35 years, experiments related to optical clocks and quantum information and computation have received more attention due to their technological application. The use of a trapped ion system for optical frequency standard was proposed by H. G. Dehmelt [103]. Optical clocks are based on spectroscopy of narrow transitions between two metastable states. Electron shelving state detection by observing quantum jumps [104–107] is used to observe a high signal to noise ratio spectroscopy. Optical clocks are benchmarked by accuracy and stability. They are given in terms of fractional uncertainty in frequency, $\delta\nu/\nu$. In the ideal case, when an atom is at rest, a given transition of all copies of a free atom will be the same. In reality, a time-varying electric field is used to confine a charged particle in three dimensions. Energy levels of the trapped ion shift in the presence of external electric and magnetic fields. This is called systematic frequency shift. Stability error (statistical error) arises from measurement fluctuations and can be reduced by increasing integration time and number of atoms. Systematic errors depend on the trap and ion species. There is no informed way to point out the most preferred ion species for optical frequency standards because the accurate determination of atomic parameters of different states of an ionic species is hard. Systematic shift can only be estimated not measured. So for the most accurate frequency standard the systematic shifts should be known with sufficient precision. That is why, since the proposal of trapped ion based frequency standard, clocks/spectroscopy with different ion species are being tried. Some of them are Hg^+ [108], Yb^+ [16, 109, 110], Sr^+ [111, 112], Al^+ [7, 8], Ca^+ [80, 113, 114]. There is an ongoing effort to reduce systematic frequency shift, $\delta\nu/\nu$, below 10^{-19} by optimizing the trap geometry to reduce the heating rates and selecting the appropriate atomic species depending on their properties [15–18, 77–83]. Endeavour to make portable trapped ion clocks is also going on [115, 116].

1.2 Motivation and Objectives

Our group at RRI is involved in studying ion-atom collision [37, 38, 44, 46, 48, 50, 55, 117, 118] in different energy regimes. It has given a deep insight into ion-atom interaction mechanisms like cooling by charge exchange collision [38, 48, 118], cooling of co-trapped lighter ion [46] below a critical mass ratio ($m_a/m_i = 1$) [119] and photodissociation of molecular ions [44]. We wanted to extend our experience with alkali ions to trapping and cooling of alkaline ion (Ca^+) with the aim of developing an indigenous optical frequency standard as well as using it for study of interaction mechanism trapped and cooled ion system with co-trapped atoms. In the Old experiments, the ion trap was not designed for ground state cooling of the trapped

ion. It led us to design a new experimental setup where loading of laser coolable ions is possible, trap geometry is suitable for frequency standards, and it can be integrated with a co-trapped atom system. Designing, machining, assembly and testing a complete experimental setup is a very long project. It has been divided into the following parts for ease of organization:

- Design of atomic source to load ions.
- Ion trap design.
- Vacuum system and assembly and alignment of trap and atomic source in the assembly.
- Trap drive and filter circuit.
- Testing and characterization.
- Initial experiments.

1.3 Organization of the thesis

- In Chapter 1, we start with an overview of the ion trap system and its applications.
- In Chapter 2, basics of ion trapping are discussed and numerical study of the effect of trap geometry on the ion-atom interaction process is presented. It guides us in choosing trap geometry based on experiments.
- In Chapter 3, the motivation for the new experimental setup is discussed in detail.
- In Chapter 4, the design, development and characterization of low divergence atomic source is presented.
- In Chapter 5, trap design, material selection, machining, assembly and alignment process are discussed in detail.
- In Chapter 6, the integration of trap and oven in vacuum assembly, baking process, drive, and filter circuit for the trap is presented.
- In Chapter 7, the characterization of the trap and initial experiments for Coulomb crystal is presented.
- In Chapter 8, the summary and future prospects of the experimental setup are discussed.

2 Theory of Ion Trap and Numerical Study of Effect of Trap Geometries on Ion-Atom Interaction

2.1 Introduction

Ion traps are at the heart of the experiments and the work discussed in this thesis. It is, therefore, important to discuss the basics of ion trapping and the geometries used to produce such confining potential. Here we will discuss the equation of motion of a trapped ion and the condition for the stable trapping in the ideal trap [120] geometry. There are several geometrical variations of the ideal trap suitable for different classes of experiments. The linear Paul trap [121] is one such geometrical variations and is widely used trap geometry for studying co-trapped ion-atom interaction.

Co-trapped ions and atoms open a new area of interesting physics in different energy regimes ranging from eV to neV. The collision between co-trapped hetero-nuclear and homo-nuclear ion atom species have been studied experimentally [33, 35, 37, 45, 46, 48, 53, 55, 59, 122–132] and numerically [40–42, 47, 57, 61, 62, 133–138]. The interesting outcomes of these experiments include sympathetic cooling of trapped ions, cooling of ions by charge exchange, and cooling of co-trapped ions beyond the critical mass ratio ($m_a/m_i = 1$) [119]. It has motivated the community to investigate the details of the cooling limit of trapped ions and their equilibrium energy distribution [41, 42, 47, 61, 134, 135, 137, 139]. This is a complex problem because the ion, as we shall see, is dynamically trapped. The trapping field can pump energy into the ion-atom system if the ion's driven motion is disturbed by collision with an atom [119]. In such a scenario, the ion-atom collision constantly repartitions energy, making the steady state and equilibrium complicated. There are two mechanisms for energy pumping into the trapped ion during ion-atom collision. First, interruption of micromotion [119] and second, nonadiabatic motion of ion relative to the ion trapping potential due to ion-atom interaction potential [61]. We shall later see that the second mechanism dominates the first mechanism in a realistic trap. This chapter discusses the energy change of the ion-atom system due to different trap geometries. Results presented in the last section of the chapter have already been published in the reference [62] for 4 and 8-pole traps.

This model is further extended for the end-cap type trap presented in the thesis and 6-pole trap. Our analysis of the problem is from first principles.

2.2 Earnshaw's Theorem

Starting with the first principle, a charged particle cannot be held in stable equilibrium by electrostatic force alone [140]. In other words, the Laplace equation, equation 2.1, has no solution with local maxima or minima in free space. It means that the force on a charged particle against displacement cannot be restoring in all directions. Therefore, a charged particle cannot be stably confined using a time-independent electric potential alone.

$$\nabla^2\phi = 0 \tag{2.1}$$

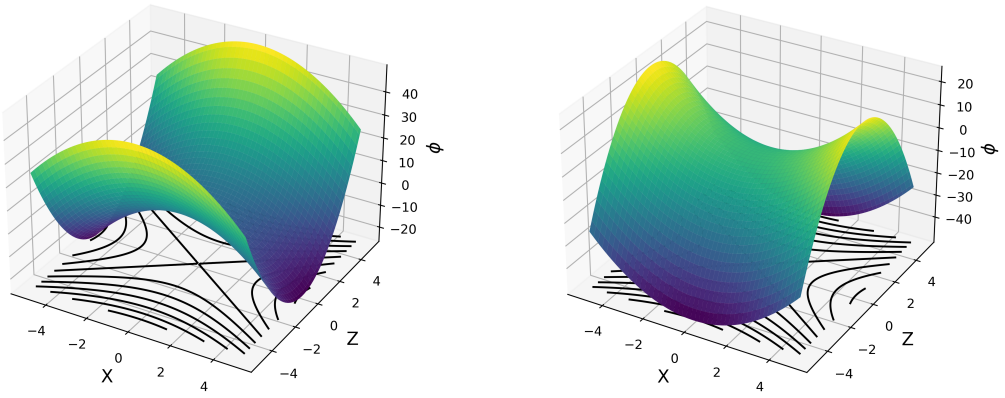
2.3 Paul Trap

Trapping of charged particles with electric fields becomes possible with time-varying electric fields. The class of ion traps which combines static and time-varying electric fields to trap ions is called Paul trap [97]. A time-varying electric potential of quadrupolar form satisfies equation 2.1 and provides restoring force in all three directions. The form of the trapping potential is given by equation 2.2

$$\Phi(r,t) = \Phi_0(2z^2 - x^2 - y^2)\cos\Omega t, \tag{2.2}$$

where Ω is the frequency of the trapping field, typically in the radiofrequency (RF) band. The shape of the potential at different times in the x-z plane is shown in the figure 2.1. The average force on a particle in an inhomogeneous field, equation 2.2, where the spatial variation in the electric field is very small over the amplitude of the rapid oscillation, can be derived using the formalism built on adiabatic approximation [139, 141–143]. To understand this, let's consider the motion of a particle having charge, Q, and mass, m, in 1-dimension in a combination of static and time-varying potential $U(x)$ and $\phi(x,t)$, respectively. Here, the frequency of the time-varying potential is assumed to be much higher than the frequency of motion of the particle in static potential. The magnitude of the field due to time-varying potential is not necessarily smaller than that of the static field. The equation of motion will be

$$m\frac{d^2x(t)}{dt^2} = Q(-\frac{dU}{dx} - \frac{d\phi}{dx}). \tag{2.3}$$



(a) (b)

Fig. 2.1.: (a) Shape of the potential in x-z plane at time $t = 0$.(b) The shape of the potential in the x-z plane at time $t = \frac{\pi}{\Omega}$.

Let's assume that the field due to the static potential is $E_0(x)$ and the field due to the time-varying potential is $E_\Omega(x,t)\cos(\Omega t)$ i.e.

$$\begin{aligned} -\frac{dU}{dx} &= E_0(x) \\ -\frac{d\phi}{dx} &= E_\Omega(x,t)\cos(\Omega t). \end{aligned} \tag{2.4}$$

Substituting equation 2.4 into equation 2.3, we get the following form of the equation of motion

$$m\frac{d^2x(t)}{dt^2} = Q(E_0(x) + E_\Omega(x,t)\cos(\Omega t)). \tag{2.5}$$

With the assumption that the oscillation amplitude due to the time-varying field, $E_\Omega(x,t)\cos\Omega t$, is small compared to the static field, $E_0(x)$, the solution can be assumed of the following form

$$x(t) = X(t) + \xi(t), \tag{2.6}$$

where $\xi(t)$ corresponds to the small oscillation and $X(t)$ to the static part. Substituting the above form of solution in the equation of motion, equation 2.5, expanding the field, $E(x,t)$, in powers of ξ and retaining only the first-order terms, we get the following equation

$$m\frac{d^2X(t)}{dt^2} + m\frac{d^2\xi(t)}{dt^2} = Q[E_0(x) + \xi\frac{dE_0(X)}{dX} + E_\Omega(X)\cos\Omega t + \xi\frac{dE_\Omega(X)}{dX}\cos\Omega t]. \tag{2.7}$$

The first term on the right-hand side of equation 2.7 is static; the second term is small due to the presence of ξ; the third term is rapidly oscillating due to $\cos(\Omega t)$, and the fourth term is rapidly oscillating but small due to the presence of ξ. Both sides of equation 2.7 contain slowly and rapidly varying terms, and they must satisfy the equation separately.

Equating the rapidly oscillating term, we get the equation 2.8

$$m\frac{d^2\xi}{dt^2} = QE_\Omega(X)\cos(\Omega t). \tag{2.8}$$

Equation 2.8 has the solution of the following form

$$\xi(t) = -\frac{Q}{m}\frac{E_\Omega(X)}{\Omega^2}\cos\Omega t. \tag{2.9}$$

Substituting equation 2.9 in equation 2.7, we get the following

$$\begin{aligned}\frac{d^2X(t)}{dt^2} + \frac{Q}{m}E_\Omega(X)\cos(\Omega t) = \frac{Q}{m}[E_0(x) + (-\frac{Q}{m}\frac{E_\Omega(X)}{\Omega^2}\cos\Omega t)\frac{dE_0(X)}{dX} + \\ E_\Omega(X)\cos\Omega t + (-\frac{Q}{m}\frac{E_\Omega(X)}{\Omega^2}\cos\Omega t)\frac{dE_\Omega(X)}{dX}\cos\Omega t].\end{aligned} \tag{2.10}$$

Integration of equation 2.10 over the period of the rapidly oscillating field gives

$$m\frac{d^2X(t)}{dt^2} = QE_0 - \frac{Q^2}{m\Omega^2}\langle E_\Omega\frac{dE_\Omega}{dX}\cos^2(\Omega t)\rangle. \tag{2.11}$$

Since force is negative of the gradient of potential energy. The right-hand side of the equation 2.11 can be re-written as

$$-\frac{dU_{eff}}{dX} = QE_0 - \frac{Q^2}{m\Omega^2}\langle E_\Omega\frac{dE_\Omega}{dX}\cos^2(\Omega t)\rangle. \tag{2.12}$$

Integration of equation 2.12 with respect to X gives us the form of the effective potential. Hence, the equation for secular motion can be determined from an effective potential, equation 2.13, known as pseudopotential.

$$U_{eff} = U_0 + \frac{Q^2E_\Omega^2(X)}{4m\Omega^2}, \tag{2.13}$$

where U_0 is related to static field part E_0. The strength and direction of the effective potential are determined by the gradient of E_Ω^2, and particles are always pushed towards the region of weaker fields, i.e., the center of the trap. We have considered only the first-order terms in ξ and neglected the higher order terms. It is clear from the assumptions made to write the solution of equation 2.5 that the separation of motion into smooth and rapid oscillatory parts is not always possible. To quantify the regime, where it is possible to decompose the motion in slow and fast oscillating parts, a dimensionless parameter, η, is defined. It is also known as the adiabaticity parameter. It is defined as the ratio of change in the electric field over complete micromotion amplitude to the value of the electric field itself

$$\eta = \frac{|2\xi dE_\Omega(X)/dX|}{|E_\Omega(X)\cos(\Omega t)|}. \tag{2.14}$$

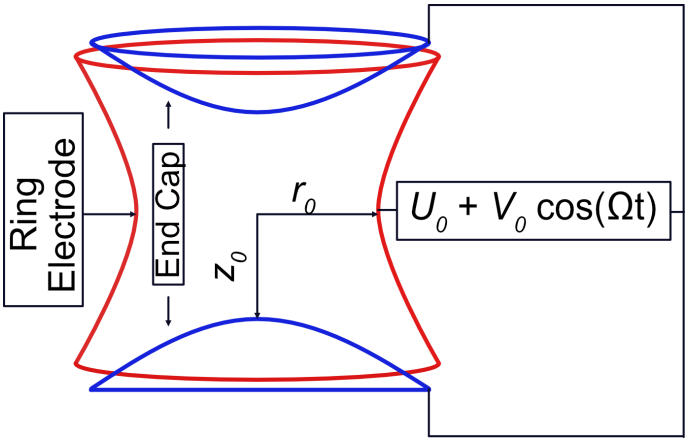


Fig. 2.2.: Electrode configuration to generate potential of quadrupolar form

There is no general way to derive the maximum value of η so that the adiabatic approximation holds for all values of η below η_{max}. According to empirical results, $\eta \leq 0.3$ guarantees adiabatic approximation for quadrupolar fields [144].

2.3.1 Equation of Motion of Charged Particles in the Ideal Paul Trap and Stability Region

In an ideal Paul trap [97], an RF potential combined with a DC potential is applied between the ring and the two end cap electrodes, as shown in figure 2.2. The form of the potential generated by the above configuration in the trapping region is given by equation 2.15

$$\phi = \frac{U_0 + V_0 \cos \Omega t}{2d^2}(2z^2 - x^2 - y^2), \quad 2d^2 = r_0^2 + 2z_0^2. \tag{2.15}$$

The equation of motion of a charged particle in the above potential will be

$$m\frac{d^2\vec{r}}{dt^2} = -Q\nabla\phi. \tag{2.16}$$

The resulting equation of motion of the x, y and z components are

$$\begin{aligned} \frac{d^2x}{dt^2} - \frac{Q}{m}\frac{(U_0 + V_0\cos\Omega t)}{d^2}x &= 0 \\ \frac{d^2y}{dt^2} - \frac{Q}{m}\frac{(U_0 + V_0\cos\Omega t)}{d^2}y &= 0 \\ \frac{d^2z}{dt^2} + \frac{2Q}{m}\frac{(U_0 + V_0\cos\Omega t)}{d^2}z &= 0 \end{aligned} \tag{2.17}$$

A change of variable to

$$\begin{aligned} &u_1 = x, \quad u_2 = y, \quad u_3 = z \\ &\tau = \Omega t/2, \quad a_x = a_y = -\frac{4QU_0}{md^2\Omega^2}, \quad a_z = \frac{8QU_0}{md^2\Omega^2} \\ &q_x = q_y = \frac{2QV_0}{md^2\Omega^2}, \quad \text{and} \quad q_z = -\frac{4QV_0}{md^2\Omega^2} \end{aligned} \tag{2.18}$$

gives the differential equations, equation 2.19, of homogeneous Mathieu type [145]

$$\ddot{u}_j + (a_j - 2q_j \cos 2\tau)u_j = 0, \quad j = 1, 2, 3. \tag{2.19}$$

According to Floquet's theorem, the solution of the equation 2.19 has the following form

$$y_1(\tau) = \exp(\rho\tau)\phi_1(\tau), y_2 = \exp(-\rho\tau)\phi_2(\tau), \tag{2.20}$$

where $\phi_1(\tau)$ and $\phi_2(\tau)$ are periodic functions having period π and $\rho = \alpha \pm i\beta$, α and β are real functions of a and q, and i is $\sqrt{-1}$. For $\alpha \neq 0$ or $\alpha = 0$ and $\beta \neq n$, where n is an integer, y_1 and y_2 will be linearly independent and the general solution of the equation 2.19 can be written as a linear combination of y_1 and y_2. For $\alpha \neq 0$, then the general solution contains a term that grows with time, and the solution is unbounded; hence, it is classified as an unstable solution.

For $\alpha = 0$ and β not an integer, the solution is bounded as $\tau \to \infty$. However, when $\rho = in$, where n is an integer, one of the general solutions is periodic with period π, and the other linearly independent solution becomes unbounded. Thus, ρ, which depends on a and q, demarcates the boundary between stable and unstable solutions. For $\alpha = 0$, we can expand the general solution of the equation 2.19 in terms of the Fourier series

$$u_j(\tau) = \sum_0^\infty A_{2n\pm\beta_j} \cos(2n \pm \beta_j)\tau + \sum_0^\infty B_{2n\pm\beta_j} \sin(2n \pm \beta_j)\tau. \tag{2.21}$$

The above series represents the solution with period 2π when β_j is odd, and the period is π for even β_j. To find out the transition curve between stable solution and unstable solution, we equate the coefficients of $\cos(2n \pm \beta_j)$ and $\sin(2n \pm \beta_j)$ for integer values of β_j. Inserting the equation 2.21 into the equation 2.19, simplifying and equating coefficients of $\cos(2n \pm \beta_j)\tau$ and $\sin(2n \pm \beta_j)\tau$ to 0 for $\beta_j = 0, 1$ gives the following recursion relations:

For cosine coefficients

$$\begin{aligned} aA_0 - qA_2 &= 0 \\ (a-1)A_1 - q(A_3 + A_1) &= 0 \\ (a-4)A_2 - q(A_4 + 2A_0) &= 0 \\ (a-n^2)A_n - q(A_{n+2} + A_{n-2}) &= 0 \end{aligned} \tag{2.22}$$

For sine coefficients

$$\begin{aligned} (a-1+q)B_1 - qB_3 &= 0 \\ (a-4)B_2 - qB_4 &= 0 \\ (a-n^2)B_n - q(B_{n-2} + B_{n+2}) &= 0 \end{aligned} \tag{2.23}$$

To solve these equations, let's put them in the matrix form
For the cosine coefficient with even indexes, we get

$$\begin{bmatrix} a & -q & 0 & 0 & 0 & 0 & \\ -2q & (a-4) & -q & 0 & 0 & 0 & \\ 0 & -q & a-4^2 & -q & 0 & 0 & \\ 0 & 0 & -q & a-6^2 & -q & 0 & \\ 0 & 0 & 0 & . & . & . & \\ 0 & 0 & 0 & 0 & . & . & . \\ 0 & 0 & 0 & 0 & 0 & . & . \end{bmatrix} \begin{bmatrix} A_0 \\ A_2 \\ A_4 \\ A_6 \\ . \\ . \\ . \end{bmatrix} = \begin{bmatrix} 0 \\ 0 \\ 0 \\ 0 \\ . \\ . \\ . \end{bmatrix} \tag{2.24}$$

For the sine coefficient with even indexes, we get

$$\begin{bmatrix} a-2^2 & -q & 0 & 0 & 0 & 0 \\ -q & (a-4^2) & -q & 0 & 0 & 0 \\ 0 & -q & a-6^2 & -q & 0 & 0 \\ 0 & 0 & . & . & . & . \\ 0 & 0 & 0 & . & . & . \\ 0 & 0 & 0 & 0 & . & . \end{bmatrix} \begin{bmatrix} B_2 \\ B_4 \\ B_6 \\ . \\ . \\ . \end{bmatrix} = \begin{bmatrix} 0 \\ 0 \\ 0 \\ . \\ . \\ . \end{bmatrix} \tag{2.25}$$

For the cosine coefficient with odd indexes, we get

$$\begin{bmatrix} a-1-q & -q & 0 & 0 & 0 & 0 & \\ -2q & (a-3^2) & -q & 0 & 0 & 0 & \\ 0 & -q & a-5^2 & -q & 0 & 0 & \\ 0 & 0 & -q & a-7^2 & -q & 0 & \\ 0 & 0 & 0 & . & . & . & \\ 0 & 0 & 0 & 0 & . & . & . \\ 0 & 0 & 0 & 0 & 0 & . & . \end{bmatrix} \begin{bmatrix} A_1 \\ A_3 \\ A_5 \\ A_7 \\ . \\ . \\ . \end{bmatrix} = \begin{bmatrix} 0 \\ 0 \\ 0 \\ 0 \\ . \\ . \\ . \end{bmatrix} \tag{2.26}$$

For the sine coefficients with odd indexes, we get

$$\begin{bmatrix} a-1+q & -q & 0 & 0 & 0 & 0 & \\ -2q & (a-3^2) & -q & 0 & 0 & 0 & \\ 0 & -q & a-5^2 & -q & 0 & 0 & \\ 0 & 0 & -q & a-7^2 & -q & 0 & \\ 0 & 0 & 0 & . & . & . & \\ 0 & 0 & 0 & 0 & . & . & . \\ 0 & 0 & 0 & 0 & 0 & . & . \end{bmatrix} \begin{bmatrix} B_1 \\ B_3 \\ B_5 \\ B_7 \\ . \\ . \\ . \end{bmatrix} = \begin{bmatrix} 0 \\ 0 \\ 0 \\ 0 \\ . \\ . \\ . \end{bmatrix} \tag{2.27}$$

To have a non-trivial solution, one of the coefficient determinants mentioned in the equation 2.24, equation 2.25, equation 2.26, and equation 2.27 must be zero. These determinants also give us a relation between a and q, which helps us to find the region of stable solutions. Setting $q = 0$ makes it easy to see where these transition curves cross at a-axis. For A_{even} and B_{even}, it crosses at $a_n = n^2$ and for A_{odd} and B_{odd}, $b_{n+1} = (n+1)^2$ where $n \geq 0$.

The above determinants are of infinite dimension; we can expand a in terms of q around the crossing point on the a-axis for smaller q [146, 147] and plot the stability curve. Another way to plot the stability region is by using the following functions in Mathematica [148], MathieuCharacteristicA and MathieuCharacteristicB. The stability diagram of the solution in $a_z - q_z$ and $a_r - q_r$ planes is plotted in figures 2.3 and 2.4, respectively. The intersection of stability regions in $a_r - q_r$ and $a_z - q_z$ planes gives us

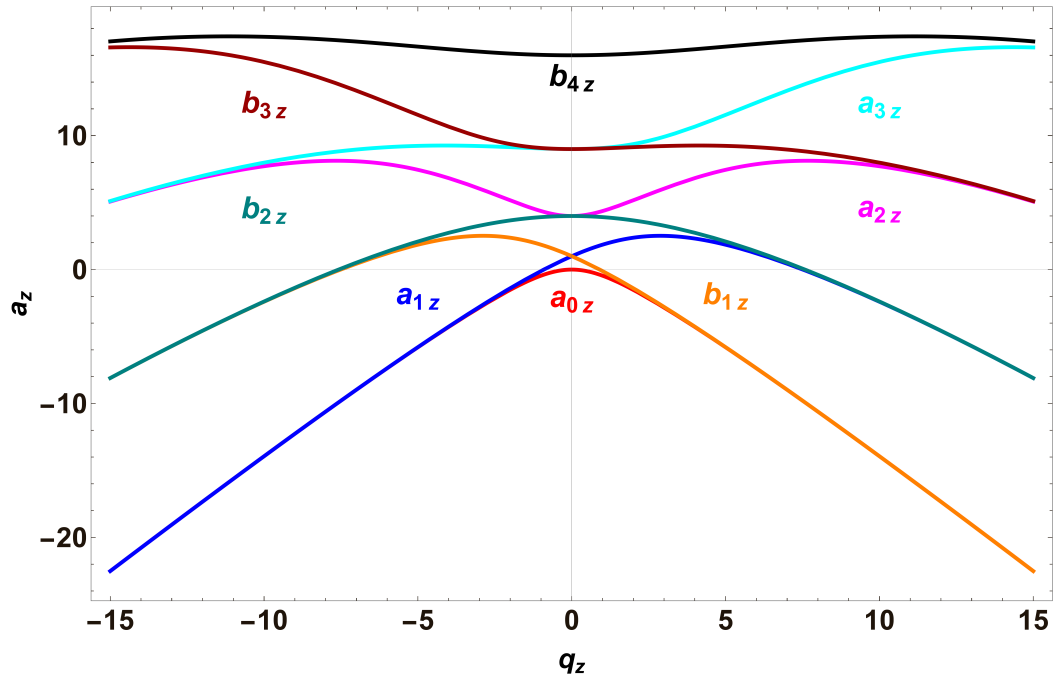


Fig. 2.3.: Stability diagram for equation 2.19 in z—direction. The stability plot has been generated using the inbuilt function in Mathematica [148]

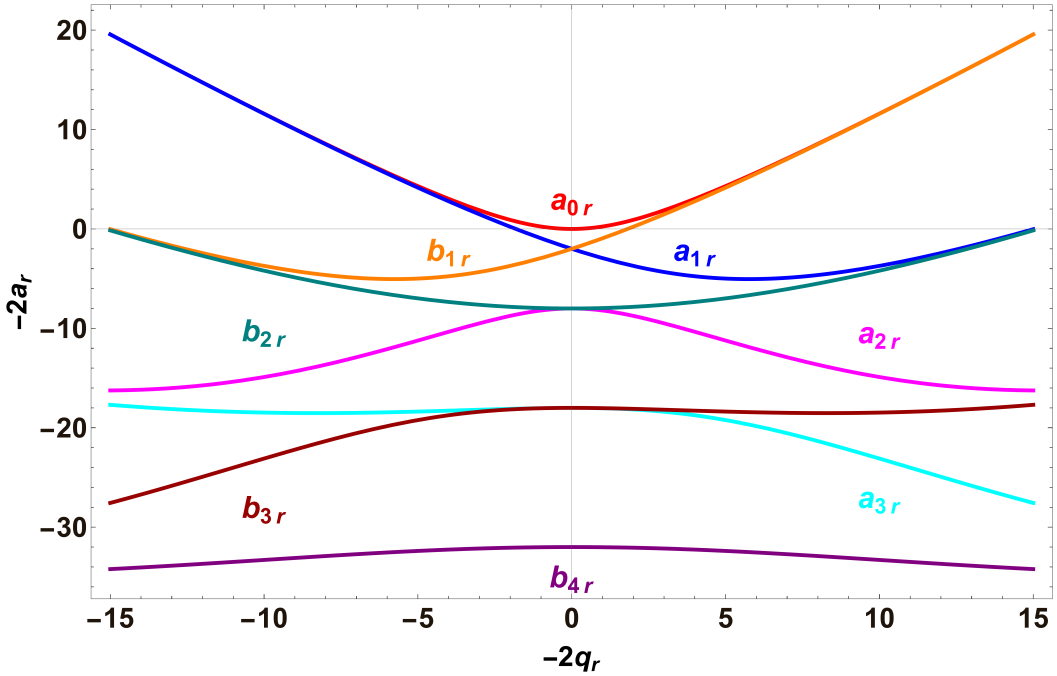


Fig. 2.4.: Stability diagram for equation 2.19 in x and y directions. The stability plot has been generated using the inbuilt function in Mathematica [148]

the stability region of equation 2.19. We are mainly interested in the lowest stability region of the equation 2.19 in the $r-z$ plane, where almost all ion trapping is done. For this, we will plot the stability curve of both planes on the same axis, and the intersection region of the curves will give us a combined stability region as shown in figure 2.5 . Equation 2.21 gives the motional frequency of the trapped particles.

$$\omega_{j,n} = (2n \pm \beta_j)\tau; n \geq 0, \tag{2.28}$$

using equation 2.18, we get the following relation:

$$\omega_{j,n} = (2n \pm \beta_j)\frac{\Omega t}{2}; n \geq 0. \tag{2.29}$$

The fundamental frequency for the ion motion will be

$$\omega_0 = \beta\Omega/2. \tag{2.30}$$

In the adiabatic approximation, $a, q \ll 1$ and the stability parameter β can be approximated to

$$\beta_j^2 \approx a_j + \frac{q_j^2}{2}. \tag{2.31}$$

In this scenario, coefficients, $A_{2n\pm\beta_j}$ and $B_{2n\pm\beta_j}$ decrease rapidly with increasing n. So we neglect all the terms for $n > 1$, and the solution in this adiabatic approximation is

$$u_j(t) = G(1 - \frac{q_j}{2}\cos(\Omega t))\cos(\omega_j t) \tag{2.32}$$

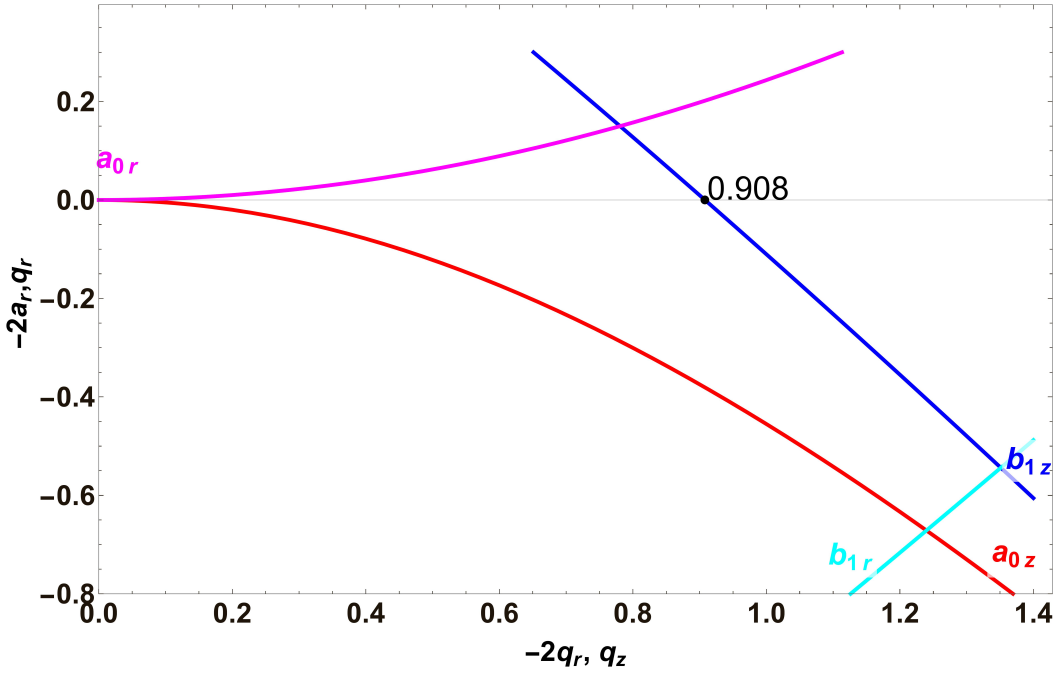


Fig. 2.5.: Lowest stability zone of equation 2.19 in $r-z$ plane formed by intersection of individual stability curves in r and z directions.

Here, G depends on the initial conditions. This is similar to the motion of an oscillator of frequency ω whose amplitude is modulated with the drive frequency Ω. Slow-frequency motion is called secular or macromotion, and the frequency is called secular frequency.

2.4 Linear Paul Trap

In a linear Paul trap [121], a time-varying electric field is applied in 2 directions and a static field is applied in the third direction to achieve confinement. In this type of trap configuration, trapping volume increases, and there is no micromotion along the direction of the static field. It helps to trap a long chain of ion crystals [149, 150]. There are different geometrical variations of linear Paul traps. $2n$ circular rods (poles) of diameter d are placed on a circle of radius r_0 in a linear Paul trap. They are named $2n$-pole trap depending on the number of electrodes. Electrode configuration for a quadrupolar or 4-pole trap is shown in figure 2.8. A cross-sectional view of 4-pole, 6-pole, 8-pole and 10-pole traps with voltage configuration is shown in figure 2.9. The form of the trapping potential generated by configurations shown in figure 2.9 is given in table 2.1. The equation of motion of a trapped charged particle for different configurations can be derived by putting the form of the potential in the equation 2.3.

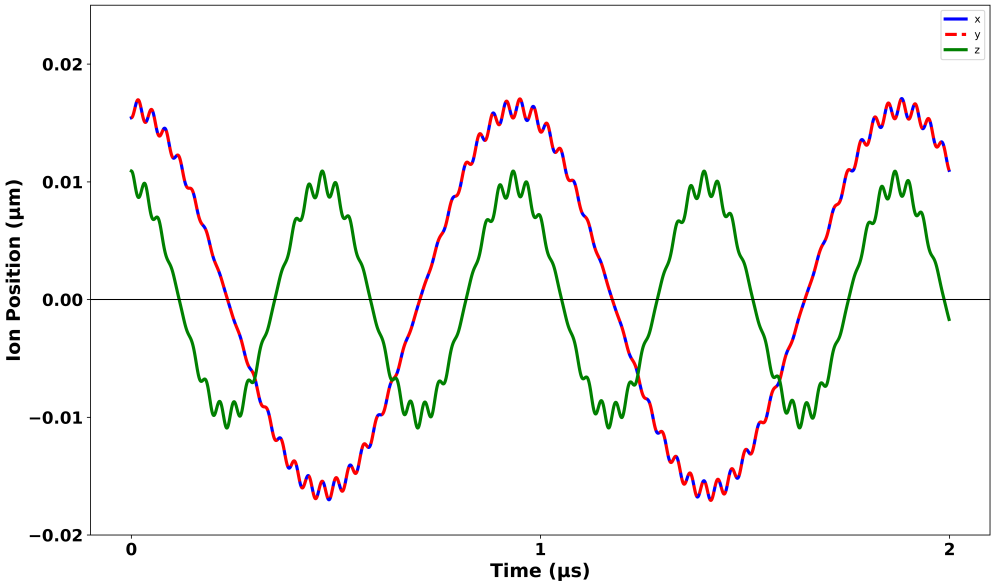


Fig. 2.6.: Position of a trapped calcium ion in ideal Paul trap geometry for $q_x = 0.1$, $\Omega_{rf} = 2\pi \times 30$ MHz

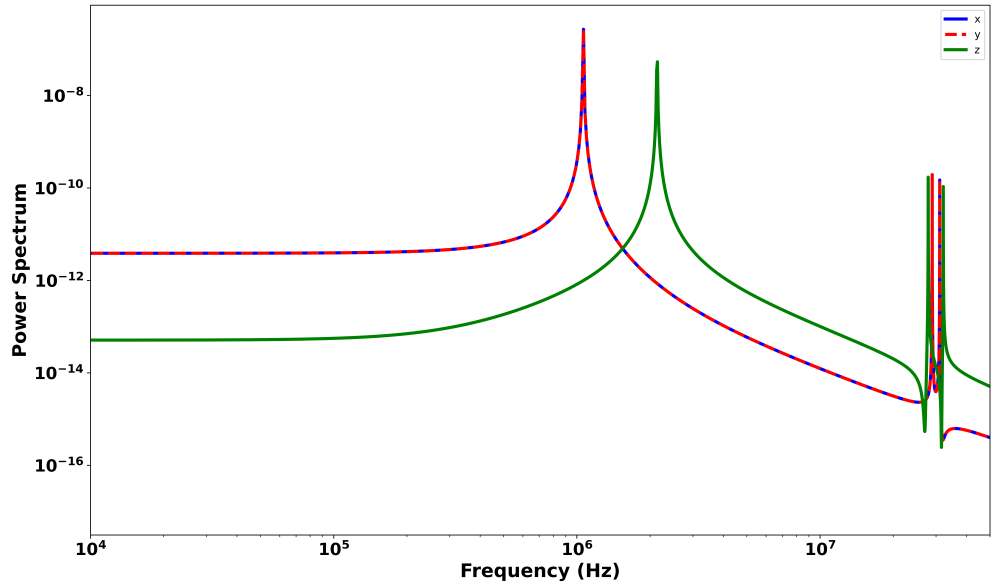


Fig. 2.7.: Power spectrum of the ion position in time and peaks are at the fundamental frequency, first and second harmonics.

Table 2.1.: Form of the potential for different linear Paul trap configuration.

Quadrupole Trap ($n = 2$)	Hexapole Trap ($n = 3$)	Octupole Trap ($n = 4$)	Decapole Trap ($n = 5$)
$V_0(t)\frac{x^2-y^2}{r_0^2}$	$V_0(t)\frac{x^3-3xy^2}{r_0^3}$	$V_0(t)\frac{x^4-6x^2y^2+y^4}{r_0^4}$	$V_0(t)\frac{x^5-10x^3y^2+5xy^4}{r_0^5}$

The equation of motion for 4-pole trap is very simple and has the following form:

$$\begin{aligned} \frac{d^2x}{dt^2} - \frac{8QV_0}{mr_0^2\Omega^2}\cos(\Omega t)x &= 0 \\ \frac{d^2y}{dt^2} + \frac{8QV_0}{mr_0^2\Omega^2}\cos(\Omega t)y &= 0 \end{aligned} \tag{2.33}$$

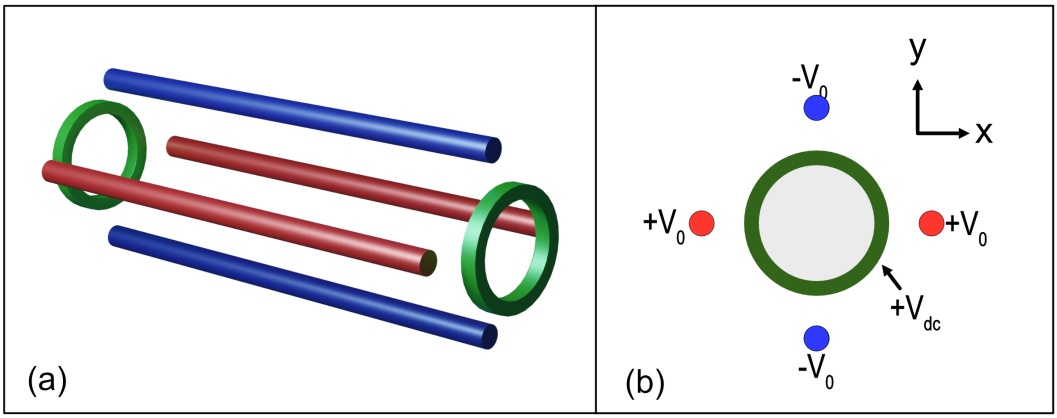


Fig. 2.8.: (a) 3D view of linear Paul trap (4 pole), RF field is applied on cylindrical rods to achieve confinement in 2 directions and static field is applied on ring electrodes to provide confinement in the remaining direction. (b) View of the trap in the x-y plane with voltage configuration of electrodes.

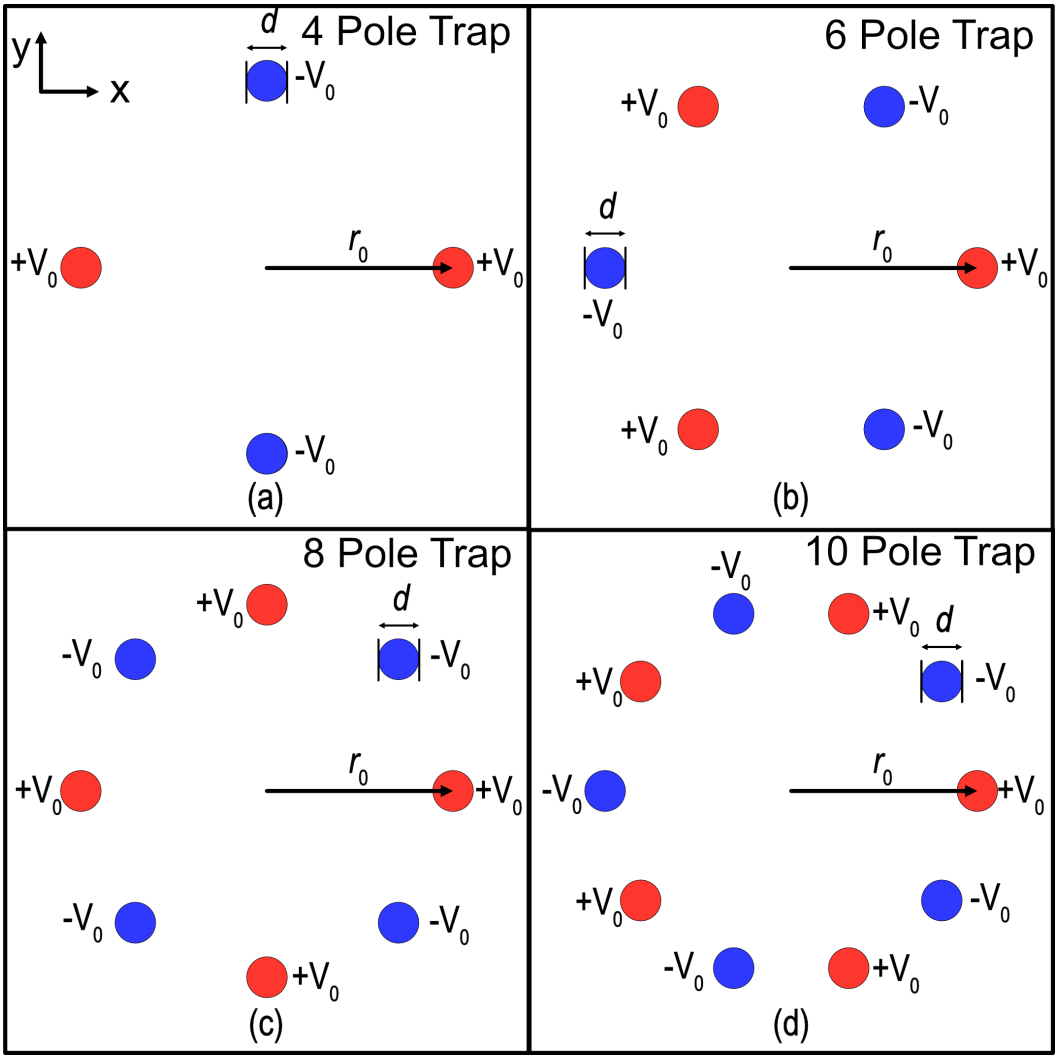


Fig. 2.9.: 2D view of electrode and voltage configuration of different multipole traps. Only RF voltage-carrying electrodes are shown for clarity.

Table 2.2.: Parameters for trajectory simulation of a charged particle in 2n pole traps

	Quadrupole Trap ($n=2$)	Hexapole Trap ($n=3$)	Octupole Trap ($n=4$)
q_n	0.1	0.1	0.1
Ω_{rf} (MHz)	$2\pi*5$	$2\pi*5$	$2\pi*5$
r_0 (cm)	0.707	0.707	0.707

The solution of equations 2.33 is given by equation 2.32. For the hexapole or other higher-order pole case, the equation of motion is not separable due to the presence of $x^m y^n$ term in the trapping potential. Although the equation of motion is not separable, it is still possible to derive the form of the effective potential for the multipolar trap case using equation 2.12. The form of the effective potential is written as

$$\phi_{eff} = \frac{n^2}{4}\frac{Q^2}{m\Omega^2}\frac{\phi_0^2}{r_0^2}(\frac{r}{r_0})^{2n-2}. \tag{2.34}$$

Similarly, it is also possible to derive the adiabaticity parameter, η, for which the motion of the trapped ion is stable

$$\eta = 2n(n-1)\frac{Q\phi_0}{m\Omega^2 r_0^2}(\frac{r}{r_0})^{n-2}. \tag{2.35}$$

A detailed derivation of the adiabaticity parameter and effective potential for multipolar traps can be found in Gerlich *et al.* [142]. It can be shown that for the case of the 4 pole trap, η is equal to the Mathieu dimensionless parameter, q, defined in equation 2.18. For the higher-order pole traps, η depends on the maximum displacement of the trapped ion. We try to define a generalised Mathieu parameter q_n for the multipolar traps as,

$$q_n = 2n(n-1)\frac{Q\phi_0}{m\Omega^2 r_0^2}. \tag{2.36}$$

The generalized Mathieu parameter is a further simplification that helps to analyze stability in $a-q$ space. We will use it to ensure similar trapping parameters in multipolar traps to study the effect of ion trapping potential on the energy of the ion-atom system during a collision.

Since the equation of motion of a trapped charged particle is not separable beyond 4-pole trap, there is no analytical expression for the particle trajectories and secular frequencies. To understand the trajectory and frequency of motion of trapped particles for different trap configurations, we numerically solve the equation of motion, plot it, and find characteristic frequencies of motion. In this thesis, all simulations are performed for $^{40}Ca^{+}$. Simulations are done in Mathematica [148] using "NDSOLVE" function. The initial condition for the simulation of ion's position in the 4 pole case is mentioned in table 2.3. Position of $^{40}Ca^{+}$ in time for parameters mentioned in table 2.2

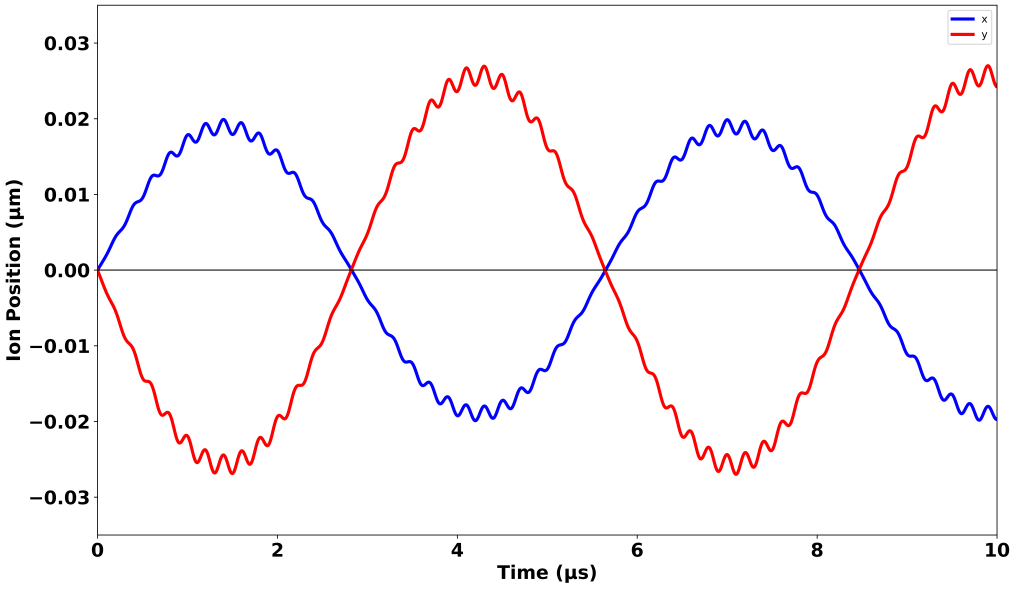


Fig. 2.10.: Position of a trapped $^{40}Ca^{+}$ in time for 4 pole trap for the initial condition mentioned in table 2.3

Table 2.3.: Initial parameters used for trajectory simulation in 4 pole trap. $x(0), y(0)$ are position of ion in x and y directions, respectively. $x^{'}(0), y^{'}(0)$ initial velocity in x and y directions, respectively.

Trapping potential ($\phi(r,t)$)	$x(0)$	$y(0)$	$x^{'}(0)$	$y^{'}(0)$
$V_0 \frac{x^2-y^2}{r_0^2} cos(\Omega_{rf} t)$	0 m	0 m	2×10^{-2} m/s	-3×10^{-2} m/s

and initial conditions mentioned in table 2.3 is shown in figure 2.10. Fourier transform of particles position data in time gives the frequency of periodic oscillations present into the motion. To sample all the frequencies present in the spectrum, we need to keep the sampling frequency according to the Nyquist-Shannon sampling theorem [151]. In the present case, the trap drive frequency is 5 MHz. Since the equation of motion of the trapped particle is a stiff differential equation, to accurately determine the particle's position in time, we sample trajectory at 50 MHz or more. To obtain the frequency close to its true values, we should also simulate the trajectory for a sufficiently long time. The frequency resolution is inversely proportional to the total time length used for simulation. Simulation for a long time comes at the cost of memory. The discrete Fourier transform of the ion's motion as a function of time in the 4 pole trap is shown in figure 2.11. The initial condition for trajectory simulation in 6 pole trap is mentioned in table 2.4. The position in time of a trapped ion in a 6-pole trap for the initial conditions, mentioned in table 2.4, is shown in figure 2.12. It is interesting because the equation of motion is not separable, and there is no analytical solution.

The discrete Fourier transform of the ion's position is shown in figure 2.13. The

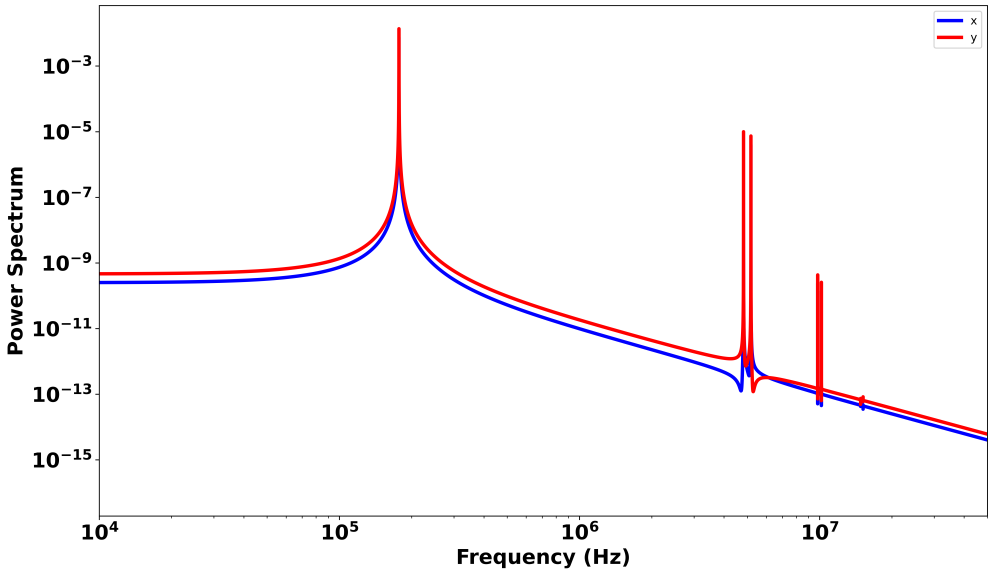


Fig. 2.11.: Discrete transform of the ion's position shown in figure 2.10. The peak at 1.77×10^5 Hz corresponds to the secular frequency mentioned in equation 2.30, and other peaks are higher harmonics mentioned in equation 2.29.

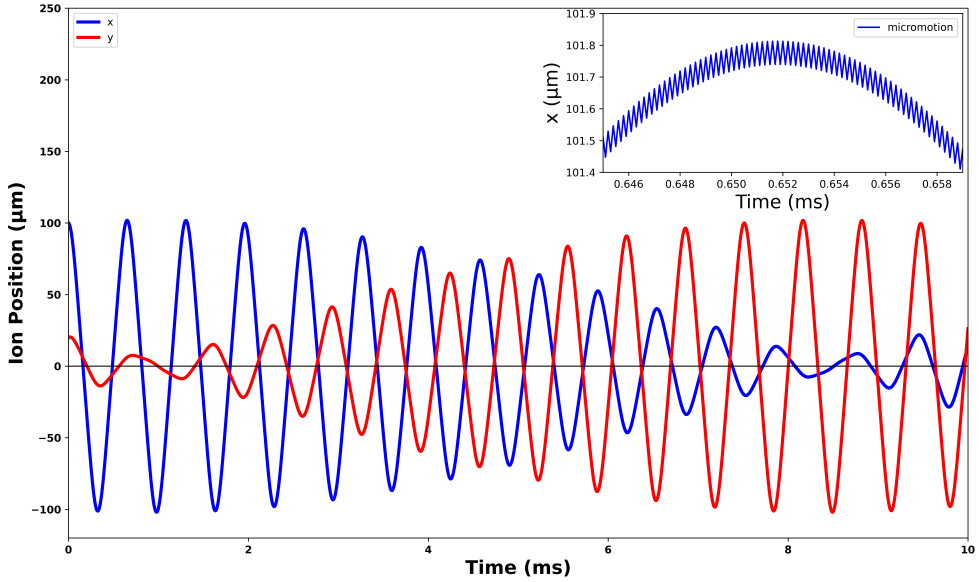


Fig. 2.12.: Position of a trapped $^{40}Ca^{+}$ in time in 6 pole trap for the initial condition mentioned in table 2.4
. Inset shows how micromotion trajectory looks in the 6-pole trap. The shape of the trajectory is not a result of undersampling of the data points used to plot it.

initial condition for trajectory simulation in 8 pole trap is mentioned in table 2.5 The position of a trapped ion for the initial conditions given in the table 2.5 is shown in figure 2.14 The discrete Fourier transform of the position of the trapped particle in the 8-pole configuration is shown in figure 2.15. The nature of the orbit in the x-y

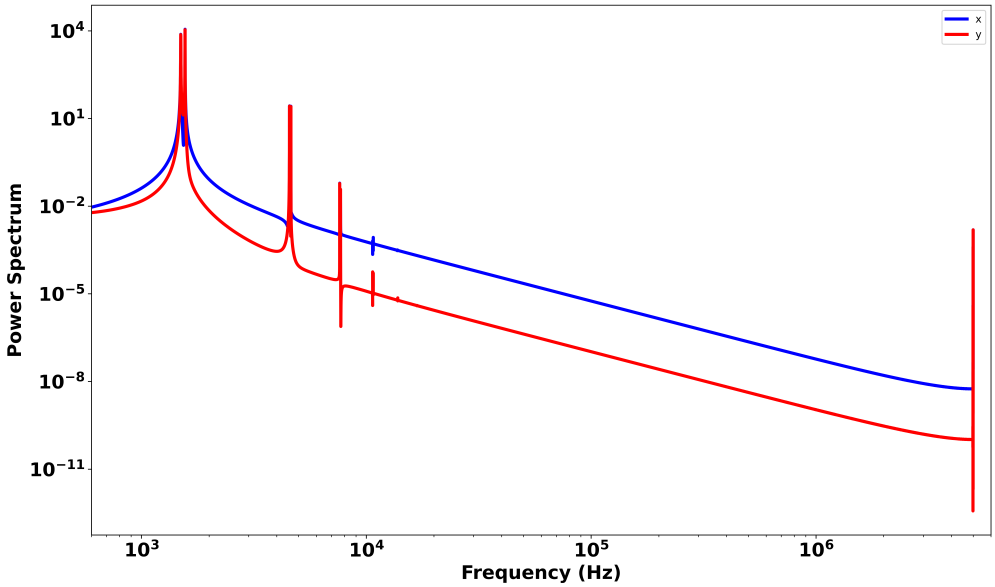


Fig. 2.13.: Discrete transform of the ion's position shown in figure 2.12

plane follows the predictions of classical mechanics. According to Bertrand's theorem [152], the closed orbit is formed in case of potential of the form of $1/r^2$ and r^2. So, we observed a closed orbit for the 4-pole trap only, as shown in figure 2.16. Also, the time-averaged angular momentum is conserved, and a particle starting with non-zero angular momentum never samples the origin.

Table 2.4.: Initial parameters used for trajectory simulation in 6 pole trap. $x(0), y(0)$ are position of ion in x and y directions, respectively. $x^{'}(0), y^{'}(0)$ initial velocity in x and y directions, respectively.

Trapping potential $(\phi(r,t))$	$x(0)$	$y(0)$	$x^{'}(0)$	$y^{'}(0)$
$V_0 \frac{x^3-3xy^2}{r_0^3} cos(\Omega_{rf} t)$	10^{-4} m	$2*10^{-5}$ m	$-28 * 10^{-3}$ m/s	$42 * 10^{-3}$ m/s

Table 2.5.: Initial parameters used for trajectory simulation in 8 pole trap. $x(0), y(0)$ are position of ion in x and y directions, respectively. $x^{'}(0), y^{'}(0)$ initial velocity in x and y directions, respectively.

Trapping potential $(\phi(r,t))$	$x(0)$	$y(0)$	$x^{'}(0)$	$y^{'}(0)$
$V_0 \frac{x^4-6x^2y^2+y^4}{r_0^4} cos(\Omega_{rf} t)$	10^{-4} m	10^{-4} m	$28 * 10^{-3}$ m/s	$-14 * 10^{-3}$ m/s

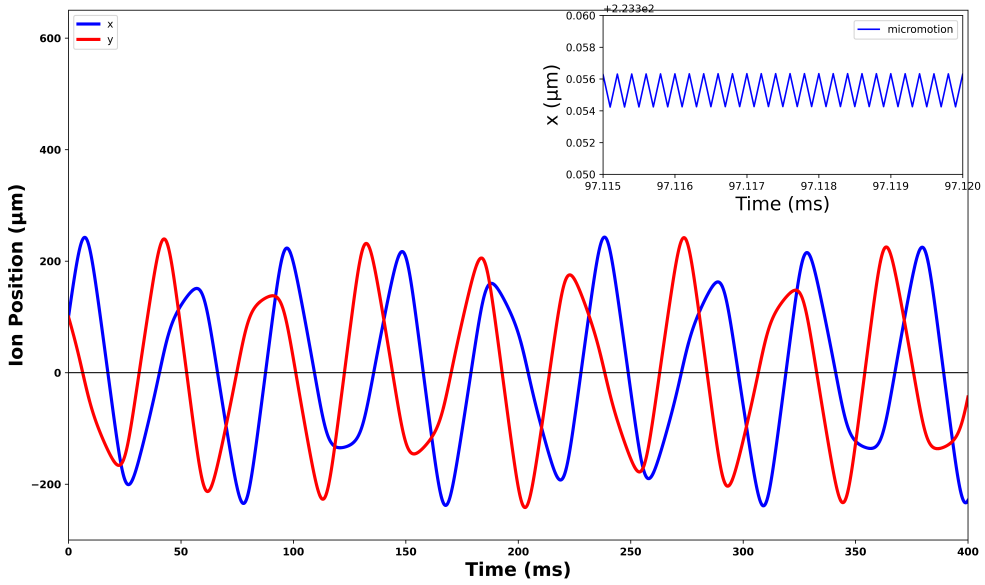


Fig. 2.14.: Position of a trapped ion in 8 pole trap.

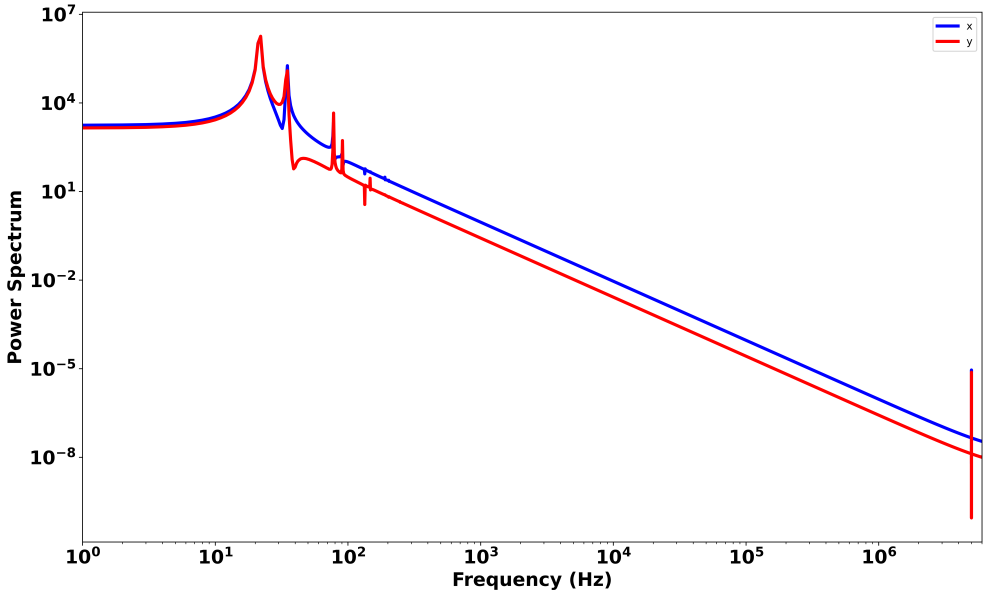


Fig. 2.15.: Discrete transform of the ion's position data in time shown in figure 2.14

2.5 Ion-Atom collision in Linear Paul Trap

There are two energy-pumping mechanisms during ion atom collision in a perfectly compensated ion trap. The first one is the interruption of the micromotion [119] of an ion due to collision with an atom at different phases of the trapping potential, and the second one is the non-adiabatic motion of the ion relative to the trapping potential under the influence of ion-atom interaction potential. It has been shown that the second one is the dominant heating mechanism [61], and it sets the sympathetic cooling limit

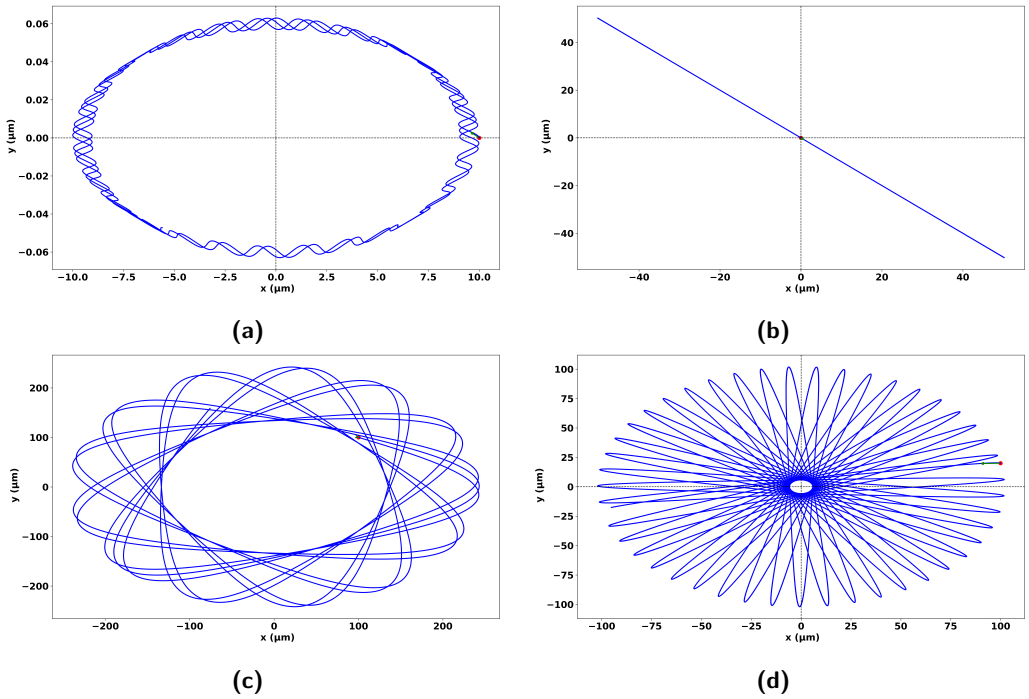


Fig. 2.16.: Orbit of a trapped calcium ion in different trap geometries for different initial conditions. (a) Orbit in a 4-pole trap; it is closed except for micromotion. Angular momentum is non-zero, so the particle never samples the origin. (b) Orbit in a 6-pole trap for zero angular momentum. (c) Orbit in an 8-pole trap for non-zero angular momentum. The orbit is not closed, and the particle never samples the origin. (d) Orbit in an 8-pole trap for non-zero angular momentum. The orbit is not closed, and the particle never samples the origin.

Table 2.6.: Parameters for simulation of rf heating

Trapping potential ($\phi(x,t)$)	q	$x(0)$	$x^{'}(0)$	Ω_{rf}
$V_0 \frac{x^2}{r_0^2} cos(\Omega_{rf} t)$	0.1	1 μm	0 m/s	2π×5 MHz

and the equilibrium energy limit. In this work, the effect of the second mechanism is simulated for linear multipolar traps. To differentiate the two cases, we first show the effect of interruption of micromotion in a 4-pole trap. In the later part, heating due to the non-adiabatic motion of the ion is presented, and the same formalism is extended to calculate the effect of non-adiabatic motion on ion-atom energy during collision in multipolar traps and the trap presented in this thesis.

For the qualitative understanding of the effect of micromotion interruption on an ion's energy, we simulate the trajectory of an ion in 1 dimension with a given initial condition. A head-on collision occurs with an atom at rest at different times. At the point of collision, we exchange the velocity of the ion and atom and continue the simulation. Trap parameters and the initial condition for the simulation are mentioned in table 2.6. This simulation is performed for collision at 2 different time instances. The ion's actual

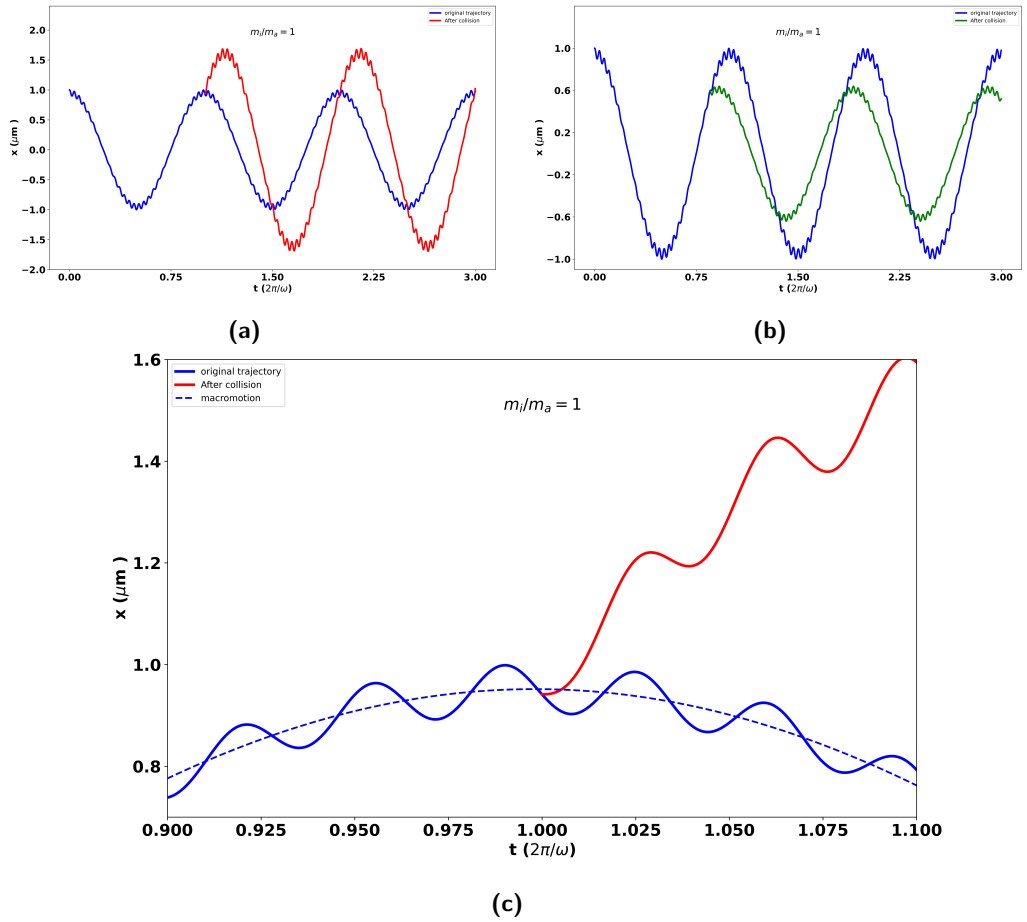


Fig. 2.17.: Change in the trajectory of an ion due to micromotion interruption. (a) Original and modified trajectory of an ion after collision with an atom at rest. Here, a collision takes place at a point where the rf force is directed away from the trap centre. (b) Collision with an atom away from the turning point. (c) zoomed view of the instance of collision shown in (a)

trajectory and the effect of collision with an atom on the ion's trajectory are shown in figure 2.17. The collision of an ion with an atom at rest momentarily brings the ion to rest. Still, depending on the direction of force due to the rf field, energy is pumped to the ion and its macromotion amplitude increases. It is known as rf heating.

We first replicate the results presented by Cetina *et al.* [61] for 1-dimensional ion-atom collision. According to Cetina *et al.* [61], a classical model is considered to simulate the effect of the non-adiabatic motion of ion on the total energy of the system during collision. We start with an ion at the centre of a compensated Paul trap and an atom at rest at infinity. At sufficiently low energies, the angular momentum barrier will be far away from the collision point, and once the atom crosses this barrier, its trajectory will be a straight line. So, collisions are considered to be head on and one-dimensional. First, the case for one-dimensional collision is presented. It is easy to derive an analytical expression for energy change in the system in some particular cases. In the derivation of analytical expression, we only take the effect of the non-adiabatic motion of ion to

its trapping potential. In the simulation, the effect of micromotion interruption and non-adiabatic motion both are taken, and the simulation results are in good agreement with the analytical expression derived for non-adiabatic motion. This shows that the non-adiabatic motion is the dominant energy pumping mechanism.
To derive the analytical expression for energy pumped into the system, let's consider the form of RF trapping potential,

$$V(r_i, t) = \frac{g}{2} * r_i^2 \cos(\Omega t + \phi), \tag{2.37}$$

and the form of the ion-atom interaction potential energy is

$$U(r) = -C_4/(2r^4), \tag{2.38}$$

where r is the distance between the atom and the ion. Dimension of C_4 is ML^6T^{-2}. When the atom is far away or in the absence of the atom, the ion will execute a slow motion with secular frequency, $\omega = \frac{q\Omega}{2\sqrt{2}}$, and $q = 2Qg/m_i\Omega^2$. For ease of calculation and simulation, we can scale the relevant quantities by defining characteristic length, time scale and energy scale. It is defined as

$$R = C_4^{1/6}/(m_i\omega^2)^{1/6}, \quad E_R = \frac{1}{2}m_i\omega^2R^2 \quad \text{and} \quad T = 2\pi/\omega. \tag{2.39}$$

In the case of a lighter atom and a heavier ion, initially, the atom will move towards the ion under the influence of ion-atom interaction potential. Distance between the ion-atom will governed by the motion of the atom in the ion-atom interaction potential. In the center of mass frame, the equation of motion of the reduced mass is

$$\mu\frac{d^2r}{dt^2} = -2\frac{C_4}{r^5} \tag{2.40}$$

where, $\mu = m_i m_a/(m_i + m_a)$. In the case of heavier ions and lighter atoms, reduced mass, μ, is almost equal to the atom's mass and $r(t)$ will give the approximate position of the atom. If the collision is taking place at $t = 0$, we can integrate the equation 2.40 to find the position of the atom. It has the following form:

$$r(t) \approx (9C_4/\mu)^{1/6}\,|t|^{1/3}\,. \tag{2.41}$$

The change in the ion's position during the collision can be calculated by integrating the effect of $2C_4/r^5$ force on an ion trapped in its secular potential. The equation of motion ion in secular potential in the presence of ion-atom interaction force is

$$m_i\frac{d^2r_i}{dt^2} = -m_i\omega^2r_i - \frac{2C_4}{r^5}. \tag{2.42}$$

Dividing both sides of the equation 2.42 by $m_i\omega^2R$ and replacing ωt by τ, the equation

becomes

$$\frac{d^2\widetilde{r}}{d\tau^2} + \widetilde{r} = -\frac{2}{9^{5/6}}\widetilde{m}\frac{1}{|\tau|^{5/3}}, \tag{2.43}$$

where $\widetilde{m} = m_a/m_i$, $\widetilde{r} = r_i/R$. To solve the equation 2.43, we need to find the Green's function [153] of the following equation

$$\frac{d^2\widetilde{r}}{d\tau^2} + \widetilde{r} = \delta(t_{coll} - t^{'}) \tag{2.44}$$

The solution of the equation 2.44 is

$$G(t_{coll}, t) = -\sin(t_{coll} - t^{'}). \tag{2.45}$$

Hence, the solution of the equation 2.43 will have the following form

$$\widetilde{r_c} = \int_{-\infty}^{t_{coll}} \sin(t_{coll} - t^{'})\frac{2}{9^{5/6}}\widetilde{m}\frac{1}{|t_{coll} - t^{'}|^{5/3}}dt^{'}. \tag{2.46}$$

Integrating the equation 2.46 from $-\infty$ to t_{coll}, we get the ion's displacement from the trap center at the time of the collision.

$$\widetilde{r_c} \approx 1.11\widetilde{m}^{5/6}. \tag{2.47}$$

During non-adiabatic motion, the ion moves against its trapping field, and the field acts as a perturbation on the ion-atom system. Work done by the trapping field can be written as

$$W = \int_{-t_1}^{t_1} \vec{F}.\frac{d\vec{r}_i}{dt}dt, \tag{2.48}$$

where $\vec{F}$ is the force on the ion due to its trapping field and $\frac{d\vec{r}_i}{dt}$ is the ion's velocity. During non-adiabatic motion, ion trajectory evolves under the influence of ion-atom interaction potential, and we neglect the effect of the trapping field on the ion's trajectory to calculated its approximated position. The approximated ion position will be

$$r_i \approx r_c - \frac{m_a r}{m_a + m_i}. \tag{2.49}$$

Inserting the form of the force from equation 2.37 and ion's position expression from equation 2.49 into equation 2.48 gives the following

$$W = \int_{-t_1}^{t_1} Qg\cos(\Omega t + \phi)\vec{r}_i.\frac{d\vec{r}_i}{dt}dt \tag{2.50}$$

Where, $r_c = R\widetilde{r_c}$. Since the direction of $d\vec{r}/dt$ changes after the collision, we can break the integral into two parts to simplify the expression for the work done. Before the

collision, $\vec{r}_i$ and $d\vec{r}/dt$ are parallel, and after the collision, they are antiparallel.

$$\begin{aligned} W = &\cos(\Omega t+\phi)\left(\int_{-t_1}^{0} Qg(\vec{r}_c - \frac{m_a\vec{r}}{m_a+m_i}).(-\frac{m_a d\vec{r}/dt}{m_a+m_i})\right)dt \\ &+\cos(\Omega t+\phi)\left(\int_{0}^{t_1} Qg(\vec{r}_c - \frac{m_a\vec{r}}{m_a+m_i}).(\frac{m_a d\vec{r}/dt}{m_a+m_i})\right)dt \end{aligned} \tag{2.51}$$

After taking dot products and expanding $\cos(\Omega t+\phi)$, the expression for work done is

$$\begin{aligned} W = &(\cos(\Omega t)\cos(\phi)-\sin(\Omega t)\sin(\phi))\left(-\int_{-t_1}^{0} Qg\alpha|\vec{r_c}|\left|\frac{d\vec{r}}{dt}\right| + \int_{-t_1}^{0} Qg\alpha^2|\vec{r}|\left|\frac{d\vec{r}}{dt}\right|\right)dt \\ &+(\cos(\Omega t)\cos(\phi)-\sin(\Omega t)\sin(\phi))\left(\int_{0}^{t_1} Qg\alpha|\vec{r_c}||\vec{r}| - \int_{0}^{t_1} Qg\alpha^2|\vec{r}|\left|\frac{d\vec{r}}{dt}\right|\right)dt \\ &\alpha = \frac{m_a}{m_a+m_i} \end{aligned} \tag{2.52}$$

From equation 2.41, dr/dt becomes,

$$\frac{dr}{dt} = -\frac{1}{3}\frac{(9C_4/\mu)^{1/6}}{|t|^{2/3}}. \tag{2.53}$$

Since dr/dt depends on the absolute value of time, $\cos(\Omega t)$ is an even function, and contributions from integrals in the limit $-t_1$ to 0 and 0 to t_1 are opposite in sign. So, there will be no contribution of coefficients of $\cos(\phi)$ in the work done. Using $r_c = R\tilde{r_c}$, $q = 2Qg/(m_i\omega^2)$ and $\Omega t = \tau$, expression for work done, W, becomes

$$W = 2\left(\frac{m_a}{m_i+m_a}\right)^{5/3}\left(\frac{m_i^2 C_4\omega^2}{q^2}\right)^{1/3}\sin(\phi)\int_{-\Omega t_1}^{\Omega t_1}\left[\left(\frac{1+\tilde{m}}{\tilde{m}}\right)^{5/6}\frac{\sqrt{2}\tilde{r_c}}{(3|\tau|)^{2/3}} - \frac{q^{1/3}}{(3|\tau|)^{1/3}}\right]d\tau. \tag{2.54}$$

For non-adiabatic motion, the velocity of the ion is greater than its average micromotion velocity (v_{mm}), i.e. $|dr_i/dt| > v_{mm}$. This means that $3q\Omega t < (2/\tilde{r_c})^{3/2}$ for $q < 0.5$, and all mass ratios, $1 < \tilde{r_c} < 2$. Hence, $|\Omega t| < 0.8$. As it is verified that changing integration limit from $-\infty$ to ∞ does not change the integral significantly. For ease of calculation, we change the integration limit and it gives an analytical form for the work done, W

$$\widetilde{W} = \frac{4}{q^{2/3}}\left(\frac{\tilde{m}}{1+\tilde{m}}\right)^{5/3}\left(1.82\left(\frac{1+\tilde{m}}{\tilde{m}}\right)^{5/6}\tilde{r_c} - 1.63q^{1/3}\right)\sin(\phi), \tag{2.55}$$

where, $\widetilde{W} = W/E_R$. Expression for the work done is directly proportional to $\sin(\phi)$. Depending on the phase at the time of collision, the ion-atom system will gain or lose energy. For the first collisions between $\pi < \phi < 2\pi$, work done by the field will be negative. We expect more than one collision till the colliding atom gains sufficient energy to escape the ion-atom interaction potential.

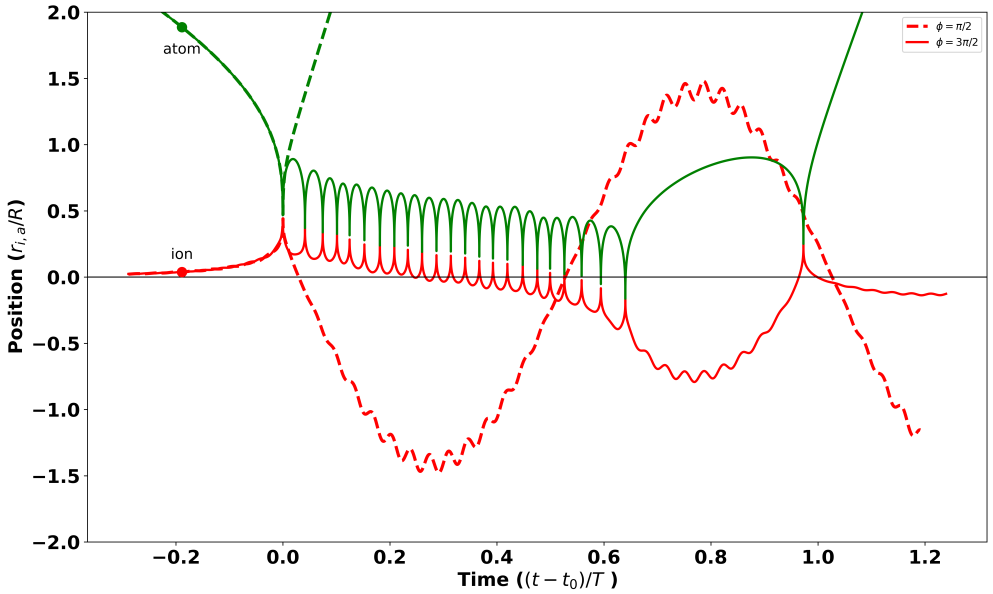


Fig. 2.18.: Trajectory for ion and atom during collision. When the first collision occurs at $\phi = \pi/2$, the energy change is maximum during a single collision, and it is sufficient to knock the atom far away from its starting point. For the first collision at $\phi = 3\pi/2$, the total energy change will be negative. So, more than one collision is required to knock the atom away.

To verify the model, we numerically calculate the trajectory of the ion-atom system under the influence of ion trapping field and ion-atom interaction potential. To simulate the trajectories, we have slightly modified the protocol established in Cetina *et al.* [61]. We started with an ion at the center of a compensated trap and kept the atom at a distance of $3.8\,(1 + m_i/m_a)^{1/3}\,R$ from the ion. The closest approach for the hard-core collision is $10^{-3}\,(1 + m_i/m_a)\,R$. The simulation is stopped once the distance between ion and atom exceeds $2 * 3.8\,(1 + m_i/m_a)^{1/3}\,R$ after collision. These parameters are fixed such that the $U(r)$, atom's kinetic energy and ion's kinetic energy are smaller than 1% of the maximum energy gained in one collision. The secular energy of the ion-atom system is calculated at two instants, first at the start of the simulation and second when the ion atom separates far apart. Total energy change will be the difference between these two energies. Cetina *et al.* [61] holds the ion at the trap centre till the ion-atom interaction potential dominates the trap potential while they let the atom evolve. In our case, we have let the ion and atom evolve from the start of the simulation. This modification should not impact the energy change significantly because, at the start, mainly the atom is displaced toward the ion. Total energy change will be phase dependent, and more than one collision will happen when the first collision takes between $\pi < \phi < 2\pi$. We first simulate the ion-atom trajectory to verify the predictions for 1-dimension. $q = 0.1$ and $\widetilde{m} = 0.5$ for this case. Ion atom collision trajectory for two phases $\pi/2$ and $3\pi/2$ is shown in figure 2.18. The total energy change after the completion of the collision process is shown in figure 2.19. The energy change after the first collision for phases between 0 and π agrees with the model proposed by Cetina *et al* [61].

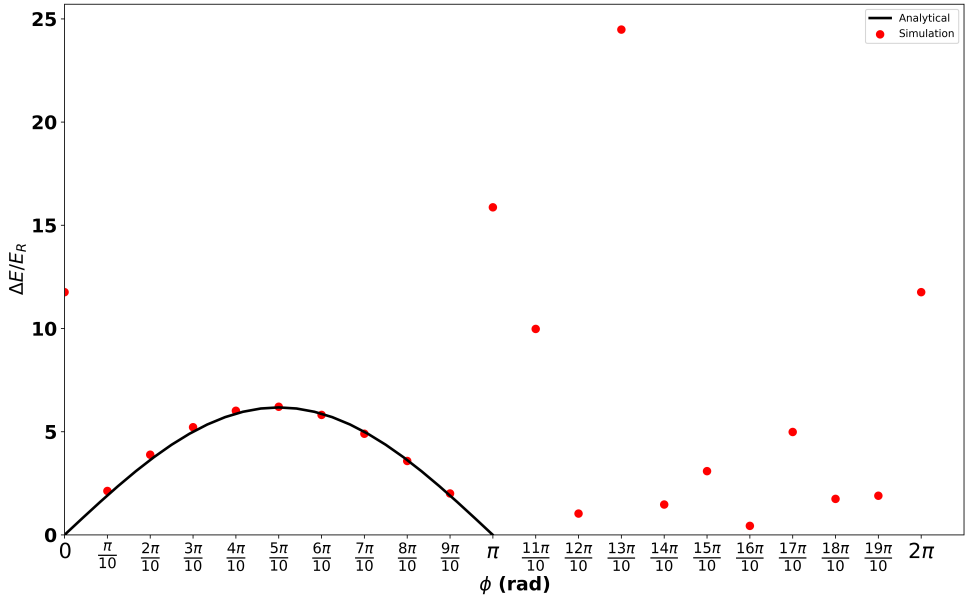


Fig. 2.19.: Change in total secular energy as a function of the phase of trapping field ϕ.

We have extended this model to study the effect of trapping potential on the total energy of the ion-atom system after collisions for multipolar Paul traps and the end-cap type of type presented in this thesis. For the 4-pole trap and end-cap type trap, we start with atom sufficiently far away from the trap center such that the ion-atom interaction energy is very small compared to relevant energy scales in the system. For a fixed generalized Mathieu q value, as the number of poles increases in a multipolar trap, potential becomes flat around the center and starts resembling box-shape potential. In this scenario, if we apply the initial condition mentioned for 4-pole trap, $r_{i-a} = 3.8\,(1 + m_i/m_a)^{1/3}\,R$, co-evolution of ion-atom does not takes place due to large separation between ion and atom. Hence, we fix initial distance between the ion and atom in higher pole traps to be $\approx R$. Due to the flat shape of potential around the trap center, the ion will be mostly under ion-atom interaction potential as the number of poles increases. Hence, the energy pumped to the system will decrease as the number of poles increases. In the case of an end-cap type trap, an RF field is applied in all 3 directions and energy pumped to the system will be maximum for same trap parameters. Parameters for numerical calculation of the collision trajectory and energy change to the system are the following: The case of an end-cap type trap is slightly different; we keep $q = 0.1$ but $\Omega_{rf} = 2\pi \times 20$ MHz because the drive frequency of the end-cap type discussed in this thesis is $2\pi \times 20$ MHz. Trajectory ion and atom, and kinetic energy of ion during collision is shown in figure 2.20. Change in the secular energy of the ion-atom system after the collision process is shown in figure 2.21. It is according to our expectations because potential starts becoming like a step potential that is flat around the trap centre and becomes like a step closer to the trap electrodes.

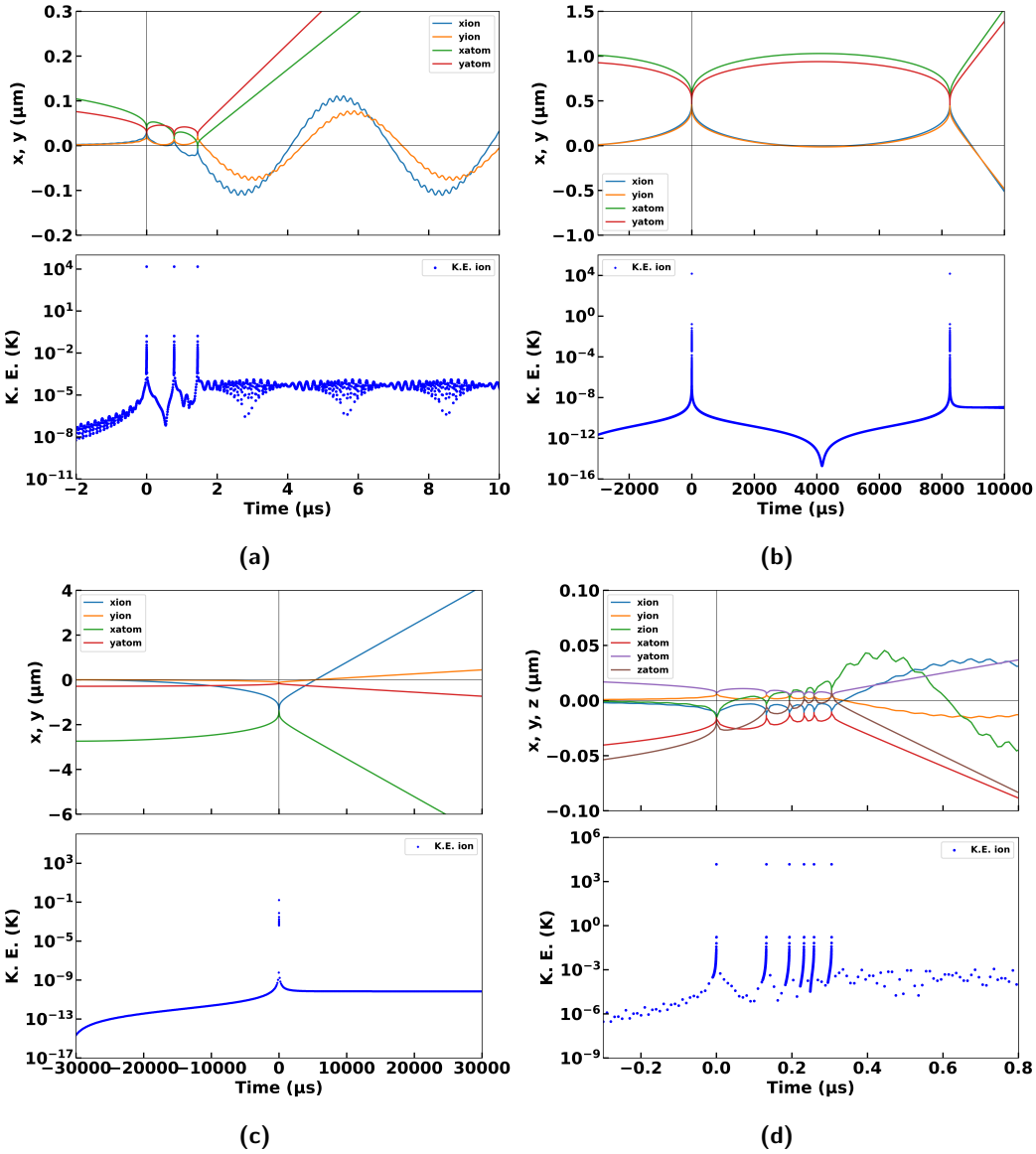


Fig. 2.20.: (Top Panel) Position of ion and atom during collision process, (Bottom Panel) Kinetic energy of ion during the process. (a) 4-pole trap, (b) 6-pole trap, (c) 8-pole trap, (d)End-cap type trap.

Table 2.7.: Parameters for ion-atom collision trajectory simulation in 2n pole traps. Here, r_{i-a} is the initial separation between atom and ion, r_{max} is the maximum separation between atom and ion, r_{min} is the distance of minimum approach between atom and ion, ϕ_1 is the angle atom makes with the x-axis at the start of the simulation.

	Quadrupole Trap ($n = 2$)	Hexapole Trap ($n = 3$)	Octupole Trap ($n = 4$)
q_n	0.1	0.1	0.1
Ω_{rf} (MHz)	$2\pi*5$	$2\pi*5$	$2\pi*5$
$r_{i-a}(\mu m)$	≈ 0.32	≈ 1.38	≈ 1.38
$r_{min}()$	2.86	2.86	2.86
$r_{max}(\mu m)$	4	4	4
ϕ_1(rad)	0.63	0.74	3.25

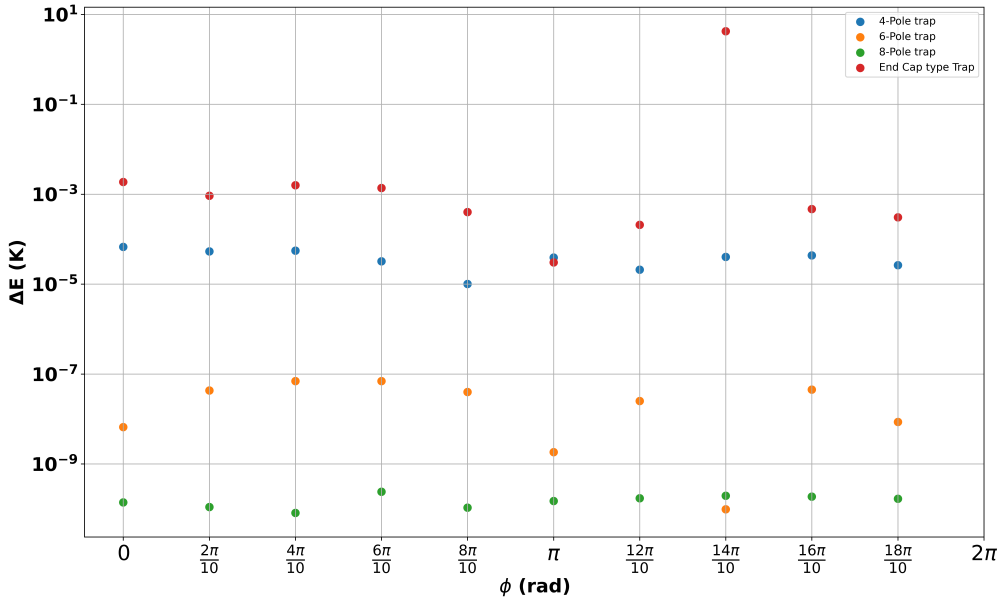


Fig. 2.21.: Change in secular energy of the ion-atom system with respect to the phase of the trapping field at the time of collision.

2.6 Discussion

We discussed the basics of ion trapping in this chapter. It guides the design parameters of the trap discussed in the thesis. Second, it is important to understand the theory of Paul traps to do the numerical simulation of the ion-atom collision trajectory. It has already been established that the work done by the trapping field due to the non-adiabatic motion of the ion dominates the sudden interruption of micromotion. So, the same model is extended to study this effect in multipolar traps. Since we are starting with an ion at the trap center with zero energy, there is no energy scale common to all traps. To compare the collision effect in different traps, we set a common generalized Mathieu parameter, q_n for all traps. Results (figure 2.21) show that the energy gain to the ion-atom system decreases as the number of poles increases. At the same time,

higher-order pole traps suffer from other problems, like trap depth decreases with an increase in the number of poles while the ratio of mean kinetic energy to mean potential energy increases which can be understood by applying the virial theorem as discussed in our paper [62]. It is therefore hard to form ion crystals in multipolar traps for $n > 2$. We infer from our analysis that the flat nature of trap potential around the trap's center makes it hard to localize an ion and study its interaction with a cloud of localized atoms. Keeping these points in mind, we opt for a quadrupole trap to study controlled interaction between trapped ion-atom systems.

3 Why A New Experiment

3.1 Why a New Experiment

One of the leading research interests of our group is the study of ion-atom interactions in different energy regimes. There are three working hybrid ion-atom experiments [37, 39, 154–158]. These experiments have given interesting physics results [37, 44, 46, 48, 55, 117, 159]. In a hybrid ion-atom experiment, co-trapping of ions and atoms and controlling them separately is feasible. Hence, we can control the initial state and energy of the system and study interaction processes in different energy regimes. Some interesting physics results of the previous studies are the sympathetic cooling of homo-nuclear ions and cooling by resonant charge exchange [37, 48, 55, 117] and the cooling of co-trapped lighter ions by heavier atoms [46, 118]. Ion traps in the previous experiment are not designed for the ground state cooling of the trapped ions. We have a parallel interest in precision spectroscopy, frequency standards and thermodynamics of small systems. This new setup is designed to meet our parallel interest and long-term goal of studying interaction between co-trapped ions and atoms. These kinds of physics experiments have been mainly performed with Group I atoms and ions. Group I ions are not laser-coolable. We aim to probe interactions in the quantum regime [160], so the lighter laser-coolable ion species are the most suitable candidates. Beryllium (Be) is the lightest laser-coolable ion species; the next one is magnesium (Mg), but no work has been reported in the area of Be atom trapping due to cooling transition in the deep ultraviolet region. The cooling transition for Mg atoms is in the deep ultraviolet region too. So, we decided to work with calcium atoms. It is a promising candidate for frequency standards and is suitable for our long-term goals.

3.2 Experimental Setup Requirements

This setup is designed for dual purposes: first, spectroscopy, thermodynamics of small systems, etc., and second, study of ion-atom interactions in cold and ultracold regimes. Here we will analyze the setup requirements in the order of increasing complexity. The system requirements for the first part are much simpler; we need a well-characterized and compensated ion trap system with good optical access where

ground-state cooling of the trapped ion is possible. For the co-trapping of atoms and ions, we require a cold atomic cloud at the center of the ion trap. Since our group is working on co-trapping of alkali atoms and ions, we will translate our knowledge from the past to the new setup where we plan to co-trap alkaline atoms and ions. The first step in this direction is to understand the limitations of our older setups, divide the new setup design into small, complete experimental setups, and integrate them later. The ion traps used in the previous experiments [37, 39, 158] are linear Paul traps [121], and the distance between the nearest electrodes is approximately 10 mm or more. High voltage is required to drive the trap to achieve the Lamb-Dicke regime ($\eta^2(2n+1) \ll 1$) [161]. To meet the conditions for the Lamb-Dicke regime, several kilovolts are required to drive the already installed traps. So we need to modify the present design or choose a different one. In almost all such experiments atoms are trapped using the 3-D magneto-optical trap (MOT) [162, 163]. The source of the atom is an atom dispenser, and the magnetic field gradient required for alkali atoms is in the range of $10-30$ G/cm. The magnetic field gradient required to trap calcium atoms is $\sim$ 60 to 100 G/cm. In addition, due to the large divergence of the atom source, we can not use an atom dispenser to load ions, see chapter 4. These two challenges require special attention. Given the above constraints, the experimental setup is divided into two independent experiments: ion trap design and experimental implementation and the atom trapping schematic and its implementation. The final part is the integration of two independent experiments. We started with the design of the integrated system and then started pursuing the first part of it. The deciding factors of the complete setups are a cold and collimated source of atoms to load 3D MOT, ion trap design, good optical access for the ion trap, and overlap of trapped ions and atoms. Zeeman slower [164] and 2D MOT [66, 165] are two commonly used alternatives to produce a collimated and cold atomic beam. To produce such a high magnetic field gradient, we must increase the current or turns in the magnetic coil and cool the coil continuously. The ion trap design will decide how to overlap ions and atoms in an experiment. According to the initial plans, the final experimental setup will be a two-chamber experiment. In the top chamber, a a collimated atomic beam to load the 3D MOT will be produced and transferred to the bottom chamber. The bottom chamber is the main experimental chamber where atoms and ions will be trapped and overlapped according to experimental requirements.

The ion trap design and assembly are paramount for precision spectroscopy and thermodynamics of small systems and an important step in our long-term goal. Here, we have a few options: first, either miniaturize the linear Paul trap [97]; second, opt for a blade trap [166]; third, go for an end-cap type trap [60]. We opted for the third option because it is suitable for frequency standards. Merits and details of the trap will be discussed in chapter 5.

4 Low Divergence Atomic Source

4.1 Introduction

Miniaturized ion traps [1, 60, 115, 166–168] are very sensitive to patch potential. These develop due to the deposition of heterogeneous material on the surface of trap electrodes. It deforms the trapping potential and heats the trapped ions. The main reason behind the development of patch potential is the deposition of atomic beam used to load the trap, which in time forms irregular patches on the surface, corrupting the trap potential over time. To minimize the patch potential, we need to decrease the divergence of the atomic beam such that it should not get deposited on the electrodes closest to the trapped ions. The most common method of the divergence reduction is to put a collimation aperture in the path of the atomic beam. This collimation aperture can be a separate entity aligned in the path of the beam [168–170], or it can be an integral part of the beam source. In our case, it is an integral part of the beam source. This chapter will discuss the design, building, alignment, and testing of a low divergence source in detail. This kind of oven is already reported by L Sharma *et al.* [171]. We will also discuss the progress made by us to decrease divergence and increase the robustness of the system. This work is published in Rev Sci Instrum. 2024 Mar 1;95(3):033202 [172].

4.2 Design Details and Alignment

In a cold-wall oven [171], collimation aperture used to reduce the divergence, of the outgoing beam, is an integral part of the oven. Only a part of the oven is heated directly, and the remaining part is relatively colder. The cold part acts as a collimator and reduces the divergence of the source. This oven has been designed for the trap geometry mentioned in the chapter 5 of this thesis. The design parameters of the trap are important in deciding the oven's parameters. Divergence of the source depends on the distance of the coldest part from the hot region and its diameter. The gap between the trap electrodes, in our case, is $\approx$ 1 mm. The operating distance of the oven from the trap centre is 15 mm. A stainless steel (ss-316) capillary tube of 160 mm in length, an inner diameter of 0.9 mm, and an outer diameter of 1.25 mm is used for the oven.

One end of the capillary is sealed by spot welding a copper wire. Using a copper sleeve, another copper wire is attached at 117 mm from the spot-welded end. The diameter of the copper wire used for connection is ≈ 1.2 mm; we can also use a thinner wire, but it will increase the heat dissipated across the connecting wires and may not be rated for the current required to heat the oven. Initially, we used nichrome wires for connection. The resistivity of the nichrome wire is higher than that of the copper wire of the same thickness. Hence, connecting wires heats up much faster than the oven body and break during operation. The oven is resistively heated by passing current through its connections. During operation, the part of the needle which is between the connector and the feedthrough is at a higher temperature than the remaining part. The colder part of the oven adsorbs the beam and thus acts like a collimator for the beam coming out of the oven.

Calcium is hard and not easy to cut using a knife. To load calcium into a narrow diameter tube, calcium chunk is held between two clean ss plates and converted into a thin strip of desired thickness using an Arbor press. After that, it is cut into thin slices using a knife to fill inside the capillary tube. Approximately 50 mg of calcium is filled inside the oven. The knife to cut calcium strips into slices is made at the RRI workshop. The top layer of calcium chunk gets oxidized during the whole process, and prolonged heating of the oven is required to start the atomic beam for the first time. We have not observed any significant time delay in the oven's response in successive operations due to oxidation. No fluorescence is observed even after prolonged heating if the metal chunk oxidizes beyond a limit. So, it is necessary to store the opened metal sample in an inert environment. We were able to preserve the opened sample for an year by storing it in a desiccator and evacuating it at intervals of approximately 3 weeks.

The oven is integrated into a vacuum chamber (Kimball Physics: MCF450-SphOct-E2A8). It is mechanically constrained at two points to direct flux to the centre of the chamber. The oven is mounted on a CF16 feedthrough (Model no: EFT02V5602) using a Macor block. The Macor block is aligned with respect to the pins of the feedthrough, and the oven passes through the centre of the block. This is the first point of alignment. An image of the oven mounted on the feedthrough with the electrical connection is shown in figure 4.1. We have ensured that connecting wire do not put any stress on the oven after mounting it on the feedthrough flange. This measure will prevent bending of the oven during operation. The second point of alignment is a Macor tube fixed inside the chamber. The cylindrical Macor tube of an inner diameter of 1.3 mm is aligned concentrically to the chamber 1.33" port. The alignment of the Macor tube inside the chamber depends on the alignment of the groove grabber and plate used to mount the trap and hold the Macor tube inside the chamber. Brass pieces with a hole of diameter 1.3 mm at the center are used as a reference for the 1.33" port. These brass pieces slight fit the 1.33" port. They are placed in the 1.33" port and held with non-sticky tape. Next,

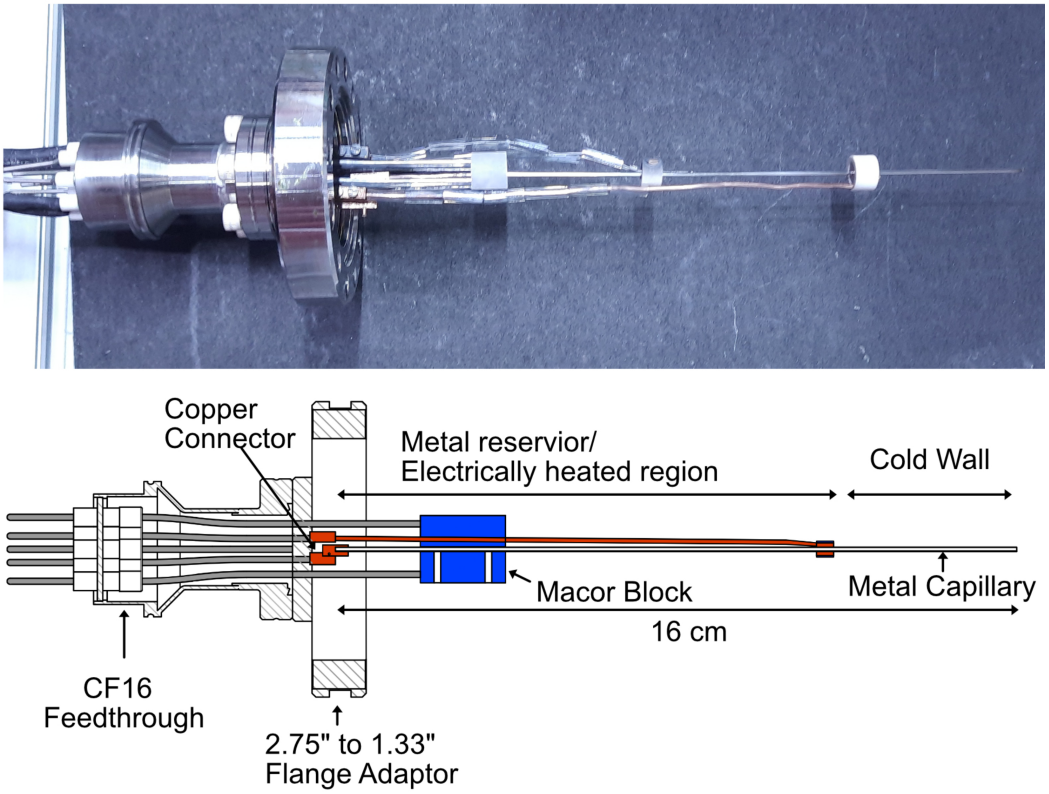


Fig. 4.1.: (Top panel) Image of the oven mounted on the feedthrough using a Macor block. This oven is used for the characterization presented in this chapter. (Bottom panel) 2D schematic diagram of the oven assembly

we mount the groove grabber with the ss plate that holds the oven on one side. Then, try to pass a long capillary identical to the oven's capillary through the brass pieces and hole at the center of the plate. If the tube passes smoothly through the center of the brass pieces and ss plate, it is aligned; otherwise, shift the position of the ss plate accordingly. A similar approach will be used to align the groove grabber on the other side. The dimensions of the ss plates, brass pieces, and the position of holes for holding them are decided by integrating them with the chamber in the 3D design software CATIA. They are machined in the in-house workshop once we finalize their dimensions. An image of the aligned ss plate inside the chamber is shown in figure 4.2. A combination of CF40 to CF16 reducer and CF16 nipple is used to accommodate the length of the oven. CF16 feedthrough is connected to CF40 to CF16 reducer using an adaptor. The reducer provides sufficient space for connectors near the CF16 feedthrough. Copper wire is insulated using glass beads, and a Macor sleeve is put on the copper connector near the cold wall to avoid any electrical contact between the oven and its housing.

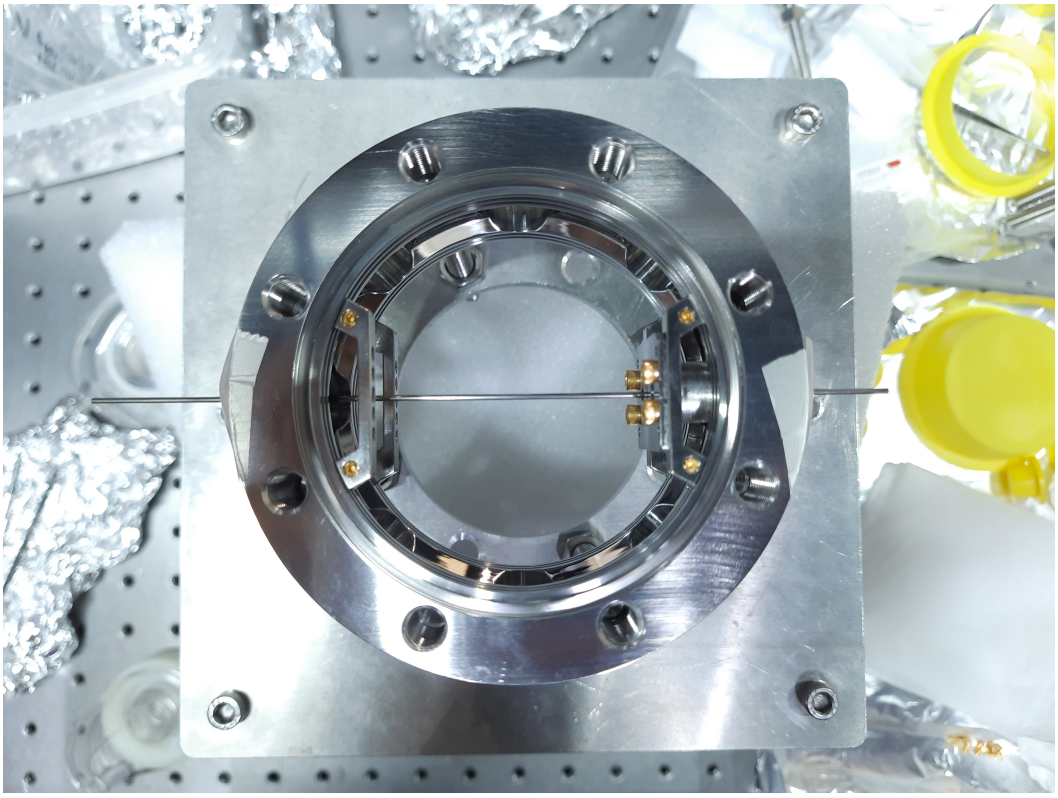


Fig. 4.2.: An image of aligned groove grabber with ss plate inside the vacuum chamber. The needle shown in the images passes smoothly through the brass plate (not visible in the image), and the ss plate is mounted via groove grabbers.

4.3 Experimental Details

After integrating the oven into the system, the chamber is pumped out using a turbo-molecular pump to a pressure of approximately 10^{-8} mbar. The oven is slowly heated by increasing the current in steps of 0.2 A up to a current of 7 A. It is left at 7 A till the fluorescence is observed due to the orthogonal laser beam. This slow heating process is repeated a few more times to cure capillary by heat treatment. We have observed that this prevents the capillary from bending during operations when the current is switched on rapidly. The setup for characterizing the oven is shown in figure 4.3. For complete characterisation of the oven, two laser beams, L1 and L2, are aligned perpendicular and at an angle of 45° with respect to the direction of the atomic beam, respectively. Schematic of laser beams, L1 and L2, and their position with respect to the chamber and the oven is shown in figure 4.4. These beams pass through the geometric centre of the chamber and ≈ 15 mm away from the oven. It is aligned with the help of jigs on CF40 viewports shown in figure 4.3. Atomic fluorescence is collected in the direction perpendicular to both the atomic and laser beams. The measurements to characterise the oven's performance are performed using resonance fluorescence detection and imaging. A Toptica DLC pro laser addresses the $4s - 4p$ transition (≈ 423 nm) of the calcium atoms. Its frequency is scanned by varying piezoelectric transducer (piezo) voltage

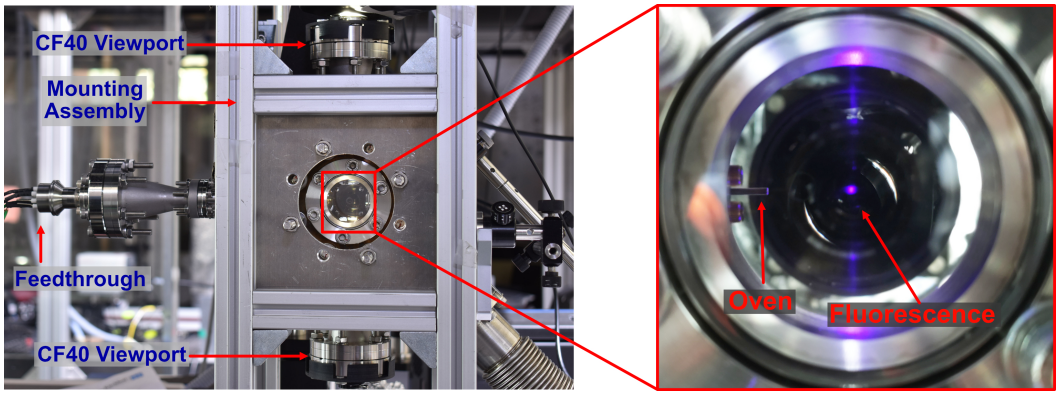


Fig. 4.3.: (Left Panel)Experimental setup with mounting assembly. (Right Panel) Fluorescence at the centre of the chamber due to the interaction of the atomic beam with a laser beam (L1).

using the built-in function to control the voltage range and scan rate. The frequency is monitored using a calibrated wavemeter (WSU-2). A low-noise CCD camera (great eyes ElSEi) is used to image atomic fluorescence. An intensity-calibrated photomultiplier tube (PMT), R758-10, is used to record real-time fluorescence.

4.4 Results

4.4.1 Divergence

To measure the divergence of the atomic beam at the centre of the chamber, the 423 nm laser beam is focused to a waist of $\approx 100\ \mu$m, as shown in figure 4.4. The laser frequency is scanned over 1 GHz across the resonance at a rate of 2 Hz to address the transverse velocity profile of the atomic beam. An imaging system of magnification ≈ 1.52 collects the fluorescence on the CCD camera. The camera's exposure time is set to 20 s, so it is much larger than the scan rate of the laser. The fluorescence image of the beam is shown in figure 4.5. A Gaussian distribution is fitted along the central pixel of the fluorescence image. Estimated $1/e^2$ diameter of the beam is 1.6 ± 0.17 mm. The theoretical estimate of the angular divergence is 10 mrad, while the measured angular divergence is 14 mrad. At the higher oven currents, the divergence of the beam increases further. The heated region of the oven is in direct contact with the cold wall region. Hence, there is a temperature gradient across the cold wall, and it decreases the effective length of the cold wall region.

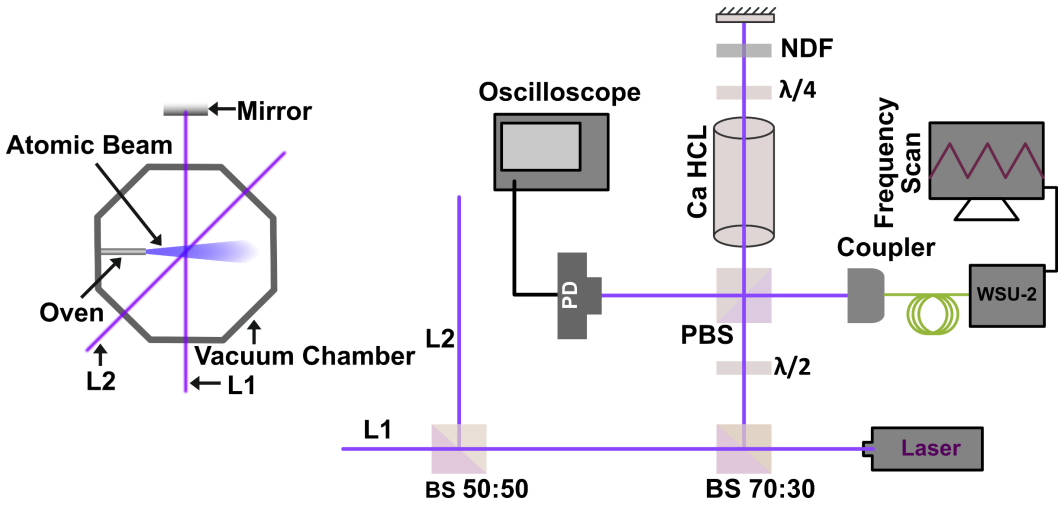


Fig. 4.4.: (Left Panel) Schematic diagram showing the alignment of the oven and laser beams with respect to the vacuum chamber. (Right Panel) Optical setup showing the arrangement for the frequency, scan range measurement and the beam division for spectroscopy of the oven's atomic beam where WSU-2 is the wavemeter used to measure the scan range, BS 70 : 30 is the beam splitter, which divides the incoming beam in the ratio of 70 and 30, Ca HCL is calcium hollow cathode lamp, PBS is a polarising beam splitter, PD is the photodiode, $\lambda/4$ is quarter waveplate, and NDF is neutral density filter.

4.4.2 Temperature and Flow Rate

The temperature of the atoms coming out of the oven can be determined by measuring the shift in the fluorescence spectrum of atoms due to the beam at a known angle $\theta \neq 90°$ with respect to the orthogonal beam fluorescence spectrum. The 423 nm beam is expanded to a diameter of $\phi = 2.3$ mm to address the whole atomic beam in the region of interrogation and then split into two beams (L1, L2) with intensities of 350 μm and 2.3 mW. The beams are aligned such that they address the atomic beam at angles of 90° and 45°, respectively, as shown in figure 4.4. The laser is scanned over 4 GHz across the $4s^2\ {}^1S_0 \rightarrow 4s4p\ {}^1P_1$ transition to cover the full range of the longitudinal Doppler profile. Fluorescence due to both beams is collected simultaneously on a PMT.

The L1 beam will interrogate the transverse velocity distribution of the Ca atomic beam. The fluorescence spectrum has Lorentzian distribution due to the finite lifetime of the excited state and Gaussian distribution due to Doppler broadening. Thus, the observed fluorescence spectrum is expected to follow the convolution of Lorentzian and Gaussian distribution, i.e. Voigt distribution in equation 4.1

$$V(x;\sigma_t,\gamma) = \int_{-\infty}^{\infty} G(x';\sigma_t)L(x-x';\gamma)dx', \tag{4.1}$$

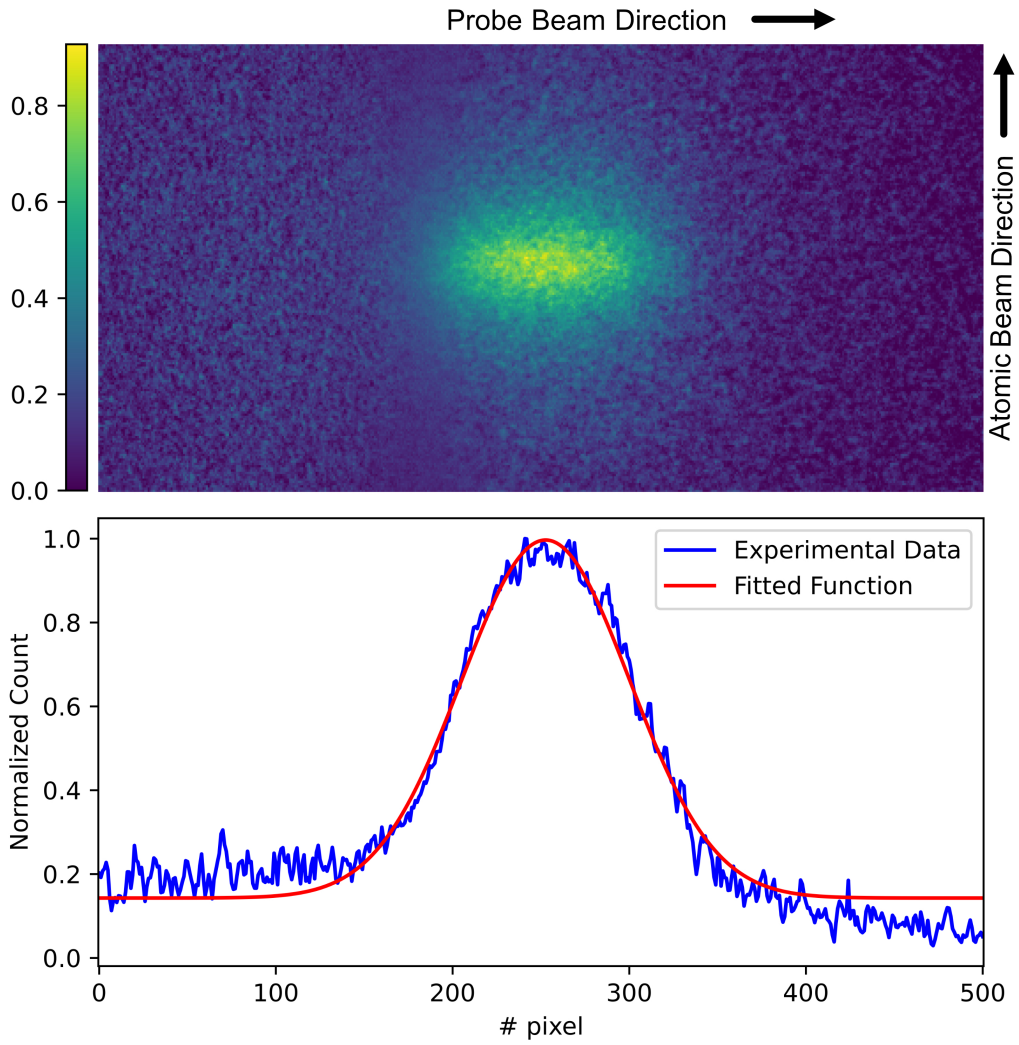


Fig. 4.5.: (Top Panel) The averaged fluorescence image captured on the CCD camera and (Bottom Panel) the experimental data along the centre line of the above image with Gaussian fit.

where

$$G(x;\sigma_t) = \frac{1}{\sigma_t\sqrt{2\pi}}\exp\left(-\frac{x^2}{2\sigma_t^2}\right), \tag{4.2}$$

σ_t is the standard deviation of the Gaussian function $G(x;\sigma_t)$; which specifies the transverse velocity spread of atoms, and

$$L(x;\gamma) = \frac{\gamma}{\pi(x^2+\gamma^2)}, \tag{4.3}$$

γ is a scale parameter that specifies half width at half maximum of the natural Lorentzian lineshape. Laser L2 will sample both the transverse and longitudinal velocities of the atoms in the atomic beam. The normalised longitudinal velocity distribution of the flux

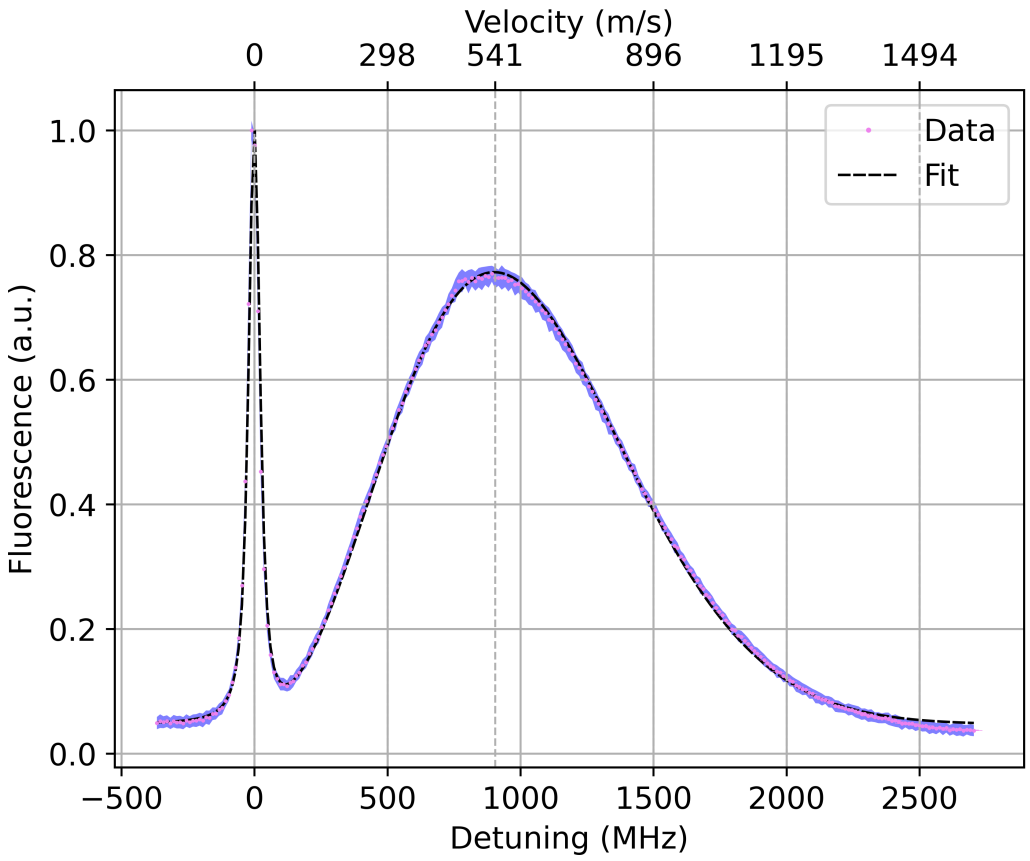


Fig. 4.6.: Experimental data and fit function corresponding to the L1 and L2 beams (Voigt + MBD) for 4.5 A. Purple colour are actual data points, Violet colour is showing error bar corresponding to the data points, and black is the fitted function.

of atoms out of the oven is given by [173]

$$f(v)dv = \frac{2v_l^3}{a^4}\exp(-v_l^2/a^2)dv; \qquad a = \sqrt{\frac{2k_BT}{m}}, \tag{4.4}$$

where T is the temperature of the source and m is the atom's mass.

When the laser beam L2 addresses the atomic beam with a longitudinal velocity v_l, the fluorescence signal of the atomic beam depends on the laser and atomic beam overlap volume, transit time ($t_{\text{trans}} = \frac{\phi}{v_l}$) of the atoms through the beam L2. Therefore, the number of atoms that fluoresce in the interaction volume of the L2 laser beam and the atomic beam has a velocity distribution given by flux multiplied by transit time. The fluorescence signal measured by the PMT is hence proportional to the velocity distribution of the number density of atoms [174], which is given by the Maxwell-Boltzmann distribution (MBD) equation (4.5)

$$f(v)dv = \frac{4v_l^2}{\sqrt{\pi}a^3}\exp(-v_l^2/a^2)dv. \tag{4.5}$$

The fluorescence signal obtained from L1 and L2 is fit to an incoherent sum of equation 4.1 and equation 4.5. For the Voigt distribution, we fit for the Lorentzian scale parameter, γ, and Gaussian scale parameter, σ_t. For the Doppler peak, we fit for the parameter a in equation 4.5, which quantifies the most probable velocity of MBD. When fitting the incoherent sum, we fit for two independent amplitudes for Voigt and MBD, and an overall offset. Figure 4.6 shows the normalised fluorescence data for 4.5 A oven current and fit function plotted against relative detuning of the laser with respect to the Voigt line centre. The relative detuning of the Doppler peak (δ) with respect to the Voigt can be converted to the velocity as

$$\delta = \frac{v_{beam}\cos(45^\circ)}{\lambda}. \tag{4.6}$$

$v_{\text{beam}} = \sqrt{\frac{3k_BT}{m}}$, is the most probable longitudinal speed. The measured shift in the peak position is $\sim$ 900MHz, and the oven temperature corresponding to this shift is 702 ± 7K. For the estimation of the temperature and all other parameters, the data is averaged over multiple shots, and the error corresponding to temperature and other parameters is the standard deviation of the averaged values.

The atomic flow rate,Φ, from the peak fluorescence power $\mathrm{P_{max}}$ due to the L1 beam can be written as [169, 175].

$$\begin{aligned}\Phi = \quad & \frac{1}{V_{\text{int}}} \times \frac{1}{\Omega_{\text{PMT}}} \times \mathrm{P_{max}} \\ & \times \left(\frac{h\omega_0\Gamma s}{2\sigma_t(2\pi)^{3/2}} \int_{-\infty}^{\infty} \frac{\exp(-v^2/2\sigma_t^2)}{1+4(|k|v_t/\Gamma^2)} dv_t\right)^{-1} \\ & \times v_{\text{beam}} \times \pi r^2,\end{aligned} \tag{4.7}$$

where $V_{\text{int}} = \pi(\frac{\phi}{2})^2 2r$, Ω_{PMT} is the solid angle for fluorescence collection by PMT, $r = 0.45$ mm is the radius of the aperture at the end of the cold wall, Γ is the natural linewidth of the state $4s4p\,^1P_1$, $s = I/I_{\text{sat}}$ is the saturation parameter, $k = \frac{2\pi}{\lambda}$ and σ_t is the standard deviation of velocity of the atomic beam in the transverse direction. The term under integral in equation 4.7 is due to the Voigt lineshape of the absorption spectrum of the atomic beam due to the beam L1. Flow rate is the number of atoms emerging from the oven per second. For a given oven temperature, T, the vapour pressure of Ca inside the capillary is given by equation 4.8 [176]

$$\log(P(\mathrm{Pa})) = 15.133 - \frac{9517}{T(\mathrm{K})} - 1.4030\log(T(\mathrm{K})). \tag{4.8}$$

The number of atoms emitted per second within the solid angle of capture, Ω_c, is[165]

$$\Phi_{\text{theory}} \approx n_0 \bar{v} A \frac{\Omega_c}{4\pi}, \tag{4.9}$$

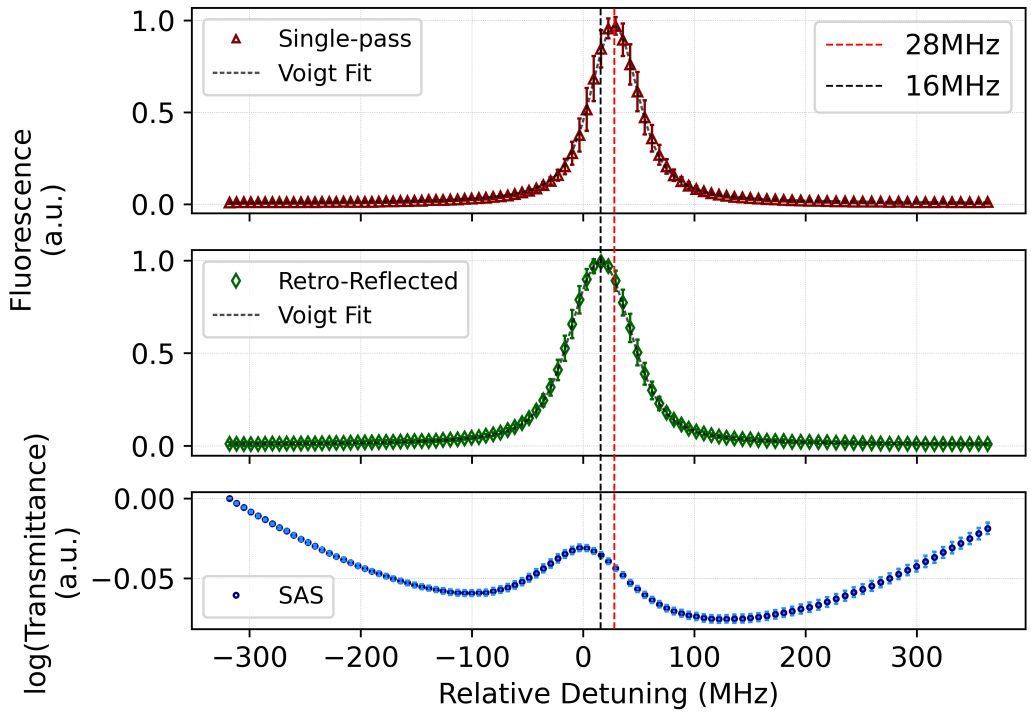


Fig. 4.7.: Fluorescence spectrum of the atoms emitted from the oven when addressed by a resonant laser in single-pass (top panel) and retro-reflected configurations (mid panel), with reference to the SAS transmittance (bottom panel).

where A is the area of the aperture at the end of the cold wall, $\bar{v} = \sqrt{\frac{8k_BT}{\pi m}}$ the mean thermal speed, n_0 is atomic density, $\Omega_c = \frac{\pi A}{l^2}$ where $l = 58$ mm is the distance between the orifice at the edge of the hot wall of the oven and the centre of the interaction region. The calculated theoretical flow rate, using Eq. 4.9, at 4.5A(702 ± 7k) is $2.2 \pm 0.6 \times 10^9$ atoms s^{-1}. The flow rate determined experimentally from equation 4.7 is by substituting the measured value is $1.5 \pm 0.2 \times 10^9$ atoms s^{-1}.

4.4.3 Characterizing the Alignment of Atomic Beam

We perform orthogonal cross-beam spectroscopy of the $4s^2\,^1S_0 \rightarrow 4s4p\,^1P_1$ transition at $\lambda \sim 423$nm to characterize and quantify the alignment of the capillary with respect to the vacuum chamber assembly. Two apertures guide a laser beam with an intensity of 54 μW and diameter of 0.9 mm ($I/I_{sat} = 1.4 \times 10^{-3}$) through the centre of the chamber. We perform beam walking to ensure that the laser beam is aligned to within 1 mrad with respect to the geometrical axis of the vacuum windows. Any misalignment of the capillary with respect to the chamber, and thus the laser beam, will result in a slightly asymmetric and broadened fluorescence spectrum. By retro-reflecting the laser beam, we record the sum of spectra due to counter-propagating beams. The shift in the fluorescence peak due to a single laser beam with respect to the fluorescence peak due to two counter-propagating laser beams will determine both the direction and

the degree of misalignment of the atomic beam with respect to the chamber.

The 423nm laser frequency is scanned at a rate of 90 MHz/s, and its frequency is monitored using the wavemeter. We perform saturation absorption spectroscopy (SAS) on a calcium hollow cathode lamp (Hamamatsu Model no. L2783) as a reference to match the frequency axis of the single-pass and retro-reflected spectra shown in figure 4.7. To account for the atomic beam's divergence, we fit Voigt profiles for both spectra by fitting for the line centre, Lorentzian FWHM, Gaussian FWHM, total amplitude, and offset. From the fits, we find the single-pass fluorescence peak is blue-detuned by ∼12 MHz with respect to the retro-reflected fluorescence peak. The top of the transmission peak observed in the Doppler-free SAS signal is red-detuned by ∼ 16 MHz due to collision with the neon buffer gas [177]. The measured Doppler shift of ∼ 12 MHz implies that the misalignment of the oven, following the best practice for alignment, is around 9 mrad (0.5°).

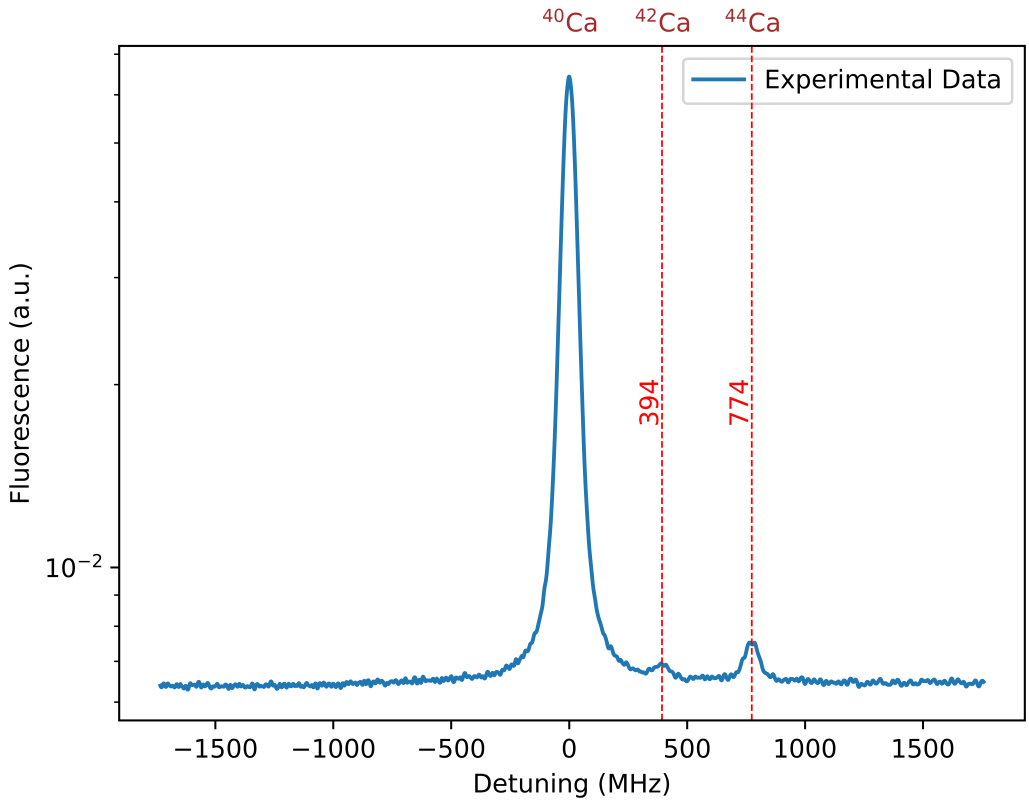


Fig. 4.8.: Averaged fluorescence signal showing the peaks for ^{40}Ca, ^{42}Ca and ^{44}Ca. The dotted lines mark the isotope shifts of ^{42}Ca and ^{44}Ca with respect to ^{40}Ca peak [178].

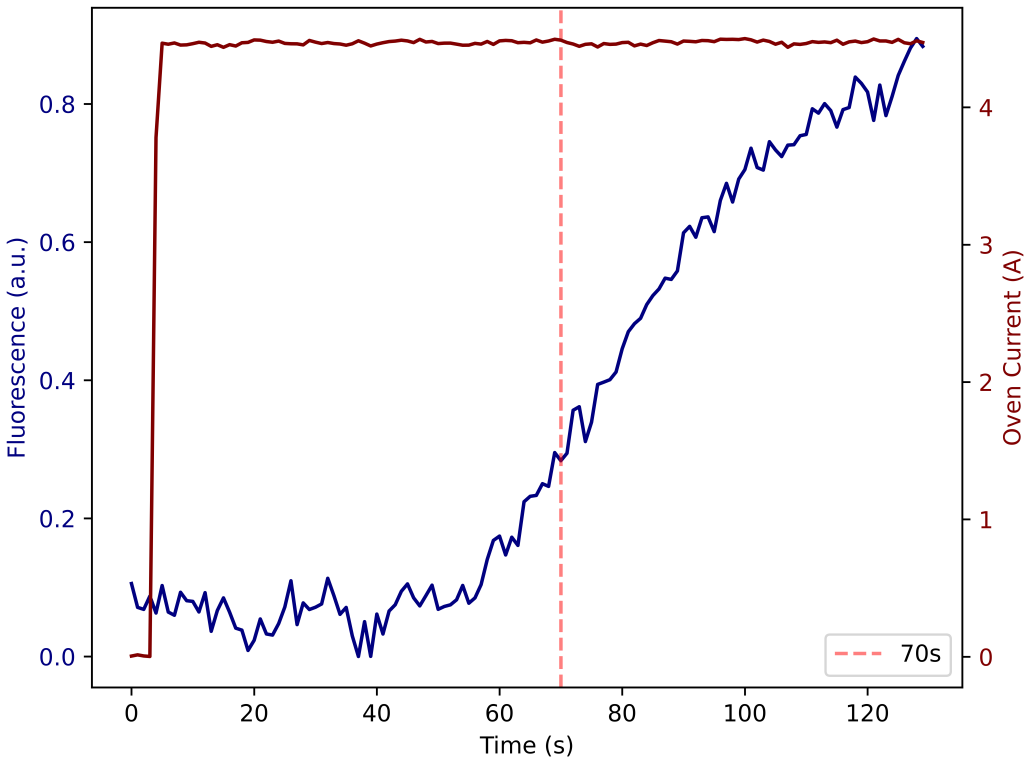


Fig. 4.9.: Fluorescence signal of the oven after switching on the heating current, and temporal evolution of the signal. Here, the red curve shows the change in oven current, and the blue curve represents the fluorescence signal.

4.4.4 Observation of Ca Isotopes

The cross laser beam (L1) frequency is scanned around 5GHz across the $4s^2\,{}^1S_0 \rightarrow 4s4p\,{}^1P_1$ transition of ^{40}Ca to observe the spectrum of the beam coming out of the oven, and the fluorescence is collected on a PMT. By averaging the fluorescence over ∼180 scans, we can observe the fluorescence from the isotopes ^{42}Ca and ^{44}Ca as shown in figure 4.8. The isotopes have been identified using the relative detuning of the fluorescence peaks with respect to the ^{40}Ca transition due to isotope shift [175, 178].

4.4.5 Response Time of the Oven

We observe the atomic fluorescence on PMT within ∼ 70 seconds after switching on the oven, as shown in figure 4.9.

4.5 Conclusion

We started with an aim of designing, building and characterization of low divergence cold wall oven. It is very close to our initial idea specially in terms of its divergence alignment with respect to the vacuum chamber, response time and robustness during operation. Ideally the divergence of the outgoing beam can be further reduced by decreasing the inner diameter of the ss tube used for oven but reducing diameter will increase difficulty in calcium filling. The oven is already 16 cm long, if we increase the length of cold wall further then long length can leading to bending of the oven during initial operation. The same argument is true if we reduce the wall thickness of the oven's wall. Another better option is to replace the ss tube by tantalum tube of smaller wall thickness.

5 Ion Trap Design and Fabrication

5.1 Introduction

In Chapter 2, we discussed the basics of ion trapping, the potential's ideal form, and the corresponding geometry. Any modification of geometry leads to change in the form of trapping potential. A geometrical variation of the ideal trap is used for our experimental setup. In the first part of this chapter, we will discuss the design and simulation details of trap geometry, material selection, change in the form of trapping potential and relate it to the basics of ion trapping discussed in Chapter 2. Machining, characterization of individual parts and alignment details are discussed in the second part.

5.2 The End Cap Trap

Real Paul traps are different from ideal Paul traps due to curvature of the electrode's surface and misalignment of geometry or due to deliberate modifications of geometry for convenience of machining and experimental requirements. Some of the geometrical modifications of the Paul trap are linear Paul trap, microfabricated trap, stylus ion trap, end cap trap, etc. [1, 20, 60, 120, 121, 179–181].

The form of the ideal potential is given by equation 2.15. We introduce a $2a_{2,0}$ factor in front of the ideal potential to quantify the deviation from it. Value of $a_{2,0}$ for the ideal quadrupolar trap is 0.5. The modified form of the potential [60] becomes:

$$\phi(x,y,z,t) = 2a_{2,0}\frac{2z^2-x^2-y^2}{4z_0^2}\phi(t), \tag{5.1}$$

where $\phi(t)$ is the time-varying potential applied on the electrodes. We have used the relation mentioned in equation 2.15 and replaced d by z_0. Only the value of z_0 is determined in the modified end cap type geometry.

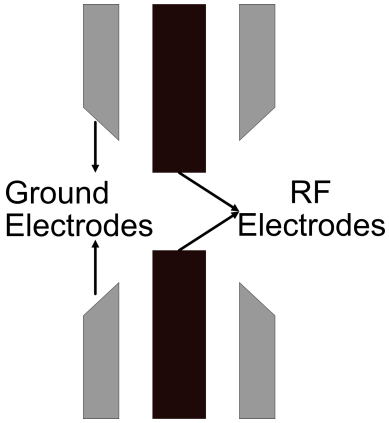


Fig. 5.1.: 2D schematic of electrode configuration in End cap type trap

The expression for a and q parameters in Mathieu equation then change to

$$\begin{aligned} -2a_x = -2a_y = a_z &= \frac{8a_{2,0}QU_0}{mz_0^2\Omega^2} \\ -2q_x = -2q_y = q_z &= \frac{4a_{2,0}QV_0}{mz_0^2\Omega^2}. \end{aligned} \tag{5.2}$$

As we depart from the ideal Paul trap configuration, higher-order harmonic and anharmonic terms start appearing in the trapping potential generated by the modified configuration. To analyze the contribution of higher-order terms, we expand the potential in terms of spherical harmonics [145, 182] around the trap's center. This method is similar to solving the Laplace equation, equation 2.1, inside spherical geometries [183, 184]. The potential generated by the trap configuration can be written as,

$$\Phi(V_t) = V_t \sum_{l=0}^{\infty} \sum_{m=-l}^{m=l} a_{lm} A_{lm}(r, \theta, \phi), \tag{5.3}$$

where,

$$A_{lm} = \sqrt{\frac{4\pi}{2l+1}} (\frac{r}{z_0})^l Y_{lm}(\theta, \phi)$$

$$Y_{lm} = \begin{cases} Y'_{0,0} & m = 0, \\ \sqrt{2}(Y'_{l,m} + (-1)^m Y'_{l,-m}) & m > 0, . \\ \sqrt{2}(-iY'_{l,m} + i(-1)^m Y'_{l,-m}) & m < 0 \end{cases}$$

Y'_{lm} is the spherical harmonics in complex form. The above form of potential simplifies depending on the symmetries present in the system. The end-cap type trap, 5.1, usually has $D_{\infty h}$ (rotational and planar) symmetry. Due to rotational symmetry, only the $m = 0$ term contributes to the expansion, and the planar symmetry restricts the l to even values. The form of potential for the traps having the planar and rotational symmetry has the

Table 5.1.: Relation between multipole coefficients and fitted coefficients

Fitted coefficient	c2	c4	c6	c8	c10
Multipole coefficient	$\frac{a_{2,0}}{2z_0^2}$	$\frac{a_{4,0}}{8z_0^4}$	$\frac{a_{6,0}}{16z_0^6}$	$\frac{a_{8,0}}{128z_0^8}$	$\frac{a_{10,0}}{256z_0^{10}}$

following form:

$$\begin{aligned}\phi(r,z) =& c0 + c2(2z^2 - r^2) + c4(8z^4 + 3r^4 - 24r^2z^2) + c6(16z^6 - 5r^6 \\ & - 120r^2z^4 + 90r^4z^2) \\ & + c8(128z^8 + 35r^8 - 1792z^6r^2 + 3360z^4r^4 - 1120z^2r^6) \\ & + c10(256z^{10} - 63r^{10} - 5760z^8r^2 + 20160z^6r^4 - 16800z^4r^6 \\ & - 3150z^2r^8),\end{aligned}$$

where $r^2 = x^2 + y^2$. The relation between the fitted coefficients and the multipolar terms is mentioned in table 5.1. In the actual case, when accounting for the entire trap geometry (figure 5.2), we should start from equation 5.3 to understand and predict the effect of the trap frame and other parts. As shown in figure 5.2, the trap geometry is still symmetric about $z = 0$ and $y = 0$ planes. This means that the basis used to expand the simulated potential will not have any odd power terms in y and z. In other words, for all even m, only positive and even l terms will contribute. In our case, the protrusion in the forks (figure 5.2) is ≈ 15 mm away from the trap center, so we will consider the effect of symmetry breaking in only quadrupole terms. The form of the potential used to fit the simulated potential becomes:

$$\begin{aligned}\phi(x,y,z) =& c0 + c2(2z^2 - (1-\epsilon)x^2) + c4(8z^4 + 3r^4 - 24r^2z^2) + c6(16z^6 - 5r^6 \\ & - 120r^2z^4 + 90r^4z^2) + c8(128z^8 + 35r^8 - 1792z^6r^2 + 3360z^4r^4 - 1120z^2r^6) \\ & + c10(256z^{10} - 63r^{10} - 5760z^8r^2 + 20160z^6r^4 - 16800z^4r^6 - 3150z^2r^8),\end{aligned}$$

where $\epsilon = \sqrt{3}\frac{a_{2,2}}{a_{2,0}}$ and the relation between the fitting coefficients and multipole coefficients are the same as in table 5.1. Due to symmetry breaking about $x = 0$ plane, expression for Mathieu parameters a_x, q_x, a_y, and q_y further changes to

$$\begin{aligned}-2a_y &= \frac{8a_{2,0}QU_0(1+\epsilon)}{mz_0^2\Omega^2}; \quad -2a_x = \frac{8a_{2,0}QU_0(1-\epsilon)}{mz_0^2\Omega^2} \\ -2q_y &= \frac{4a_{2,0}QV_0(1+\epsilon)}{mz_0^2\Omega^2}; \quad -2q_x = \frac{4a_{2,0}QV_0(1-\epsilon)}{mz_0^2\Omega^2}.\end{aligned} \tag{5.4}$$

Our objectives with this trap are oriented towards frequency standard, precision spectroscopy, and thermodynamics of small systems, as well as study of ion atom interaction in low energy regimes. Our trap design requirements are specific. We require

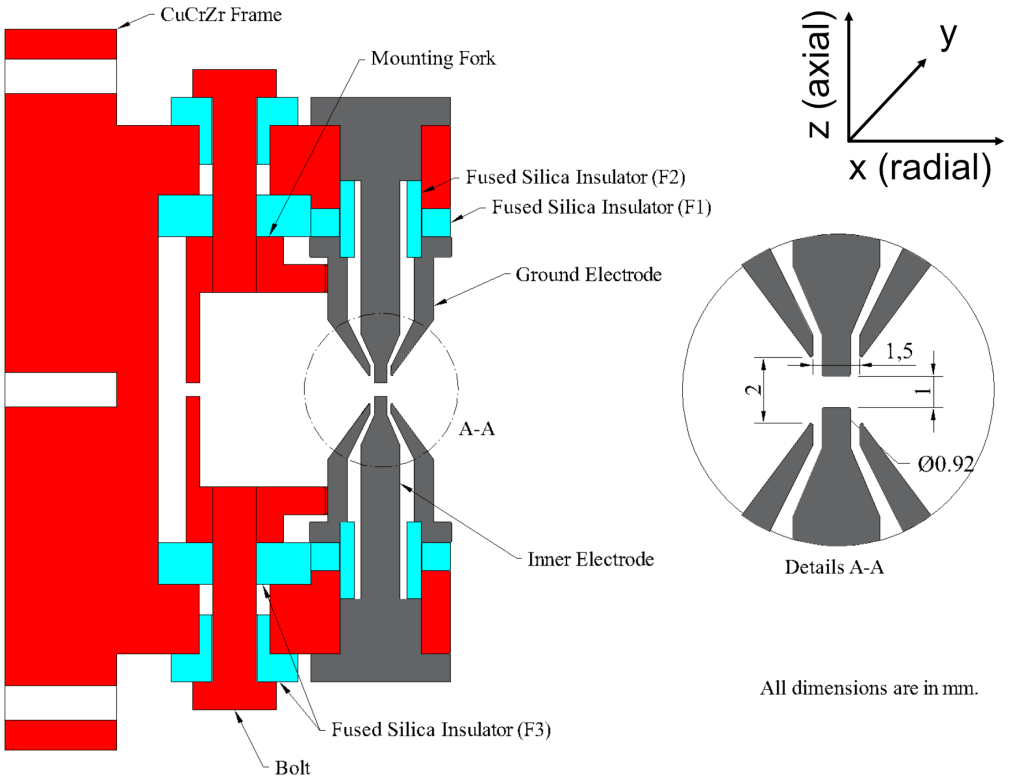


Fig. 5.2.: Central plane cut view of the final ion trap assembly.

better optical access, strong confinement, sensitivity to perturbation and higher drive frequency. To increase the stiffness of the trapping potential and drive it at a higher frequency, keeping the q parameter around 0.1, we have to either increase the applied voltage or decrease the gap between the electrodes. We opted for compact geometry, and among the various options, decided to go for the end cap trap due to its suitability for optical frequency standards. This type of trap was first experimentally demonstrated by Schrama *et al.* [60] and then further modified and used for precision spectroscopy by Universitat Hannover [181], NPL UK [1], and NMI Finland [185]. An identical replica of this trap will be installed at NPL (Delhi), IUCAA (Pune), and IIT (Tirupati) for precision metrology and optical frequency standard experiments.

The end cap trap geometry has two concentric cylindrical electrodes, as shown in figure 5.1. The inner electrode carries rf voltage; the outer electrode is usually at ground potential or some constant voltage. This kind of trap has rotational symmetry as well as planar symmetry. The gap and relative position of the outer electrode with respect to the inner electrode is guided by the capacitance and quadrupole coefficient of the whole system.

The journey of the trap assembly from theoretical design to experimental implementation can be divided into the following parts:

- Design details
- Material selection
- Assembly process
- Integration of the trap in the experimental setup
- Testing and characterization

5.2.1 Design Details and Potential Analysis

5.2.1.1 Geometry

Machining constraints, assembly feasibility, and alignment mainly guide the design. A 2D schematic of the main parts of the trap assembly is shown in figure 5.2. First, we started by deciding the gap between the inner electrodes. This gap depends mainly on the voltage requirement, oven's divergence, and size of the cooling, repump, and diagnosis laser beam. While deciding the gap, we considered the heating due to thermal electronic noise in the trap electrodes and the trap drive electronics. The heating rate of a trapped ion is reported to be $T_a d^{-2}$ [186, 187], where T_a is the temperature of the trap surface closest to the ion, and d is the distance between the trapped ion and the trap electrode. The FWHM of the atomic beam used to create ions is approximately 0.96 mm. To avoid coating heterogeneous material on the electrodes' surface as much as possible, the gap between the closest electrodes is $\approx$ 1 mm. The coating of heterogeneous material develops patch potential and heats the trapped ion.

The second point is the diameter of the inner electrode. It is decided mainly by the machining constraints and the inner diameter of the ground (outer/conical) electrode. In our design, the gap between both electrodes is also adjusted to avoid electrical breakdown due to the ground electrode's machining imperfection and to decrease the system's capacitance.

The third point is positioning of the outer electrode with respect to the inner electrode. Simulations show that if we keep both electrodes on the same level in the axial direction, the quadrupole coefficient for the trap geometry is maximum. However, it comes at the cost of a higher contribution of other multipole coefficients. So, in the present design, we have recessed the outer electrode in the axial direction till the change in higher order multipole is minimal for further adjustment [116]. This modification also decreases the quadrupole coefficients. The ion trap setup has been simulated using the commercial software Comsol 6 [188]. In the final phase of design optimization, for a fixed diameter of the inner electrode at the tip, other dimensions of the outer and inner electrodes are varied to optimize the contribution of the quadrupole coefficient and minimize the contribution of higher-order multipoles. In the optimization process, the strength of the components for machining and the capacitance of the entire trap

assembly plays a crucial role. The final machining drawing of every element of the trap assembly is attached in the A.

5.2.1.2 Simulation

As mentioned in the previous section, commercial software Comsol is used for analysis and optimization. Only the inner and outer electrode geometries are considered in the initial phase, with appropriate boundary conditions. Poisson's equation, $\nabla^2\phi = \rho/\epsilon_0$, is solved for the whole geometry. Stepwise details of the process are as follows:

- Select Model Wizard (3D)
- Select Electrostatics (es) interface under Physics module AC/DC
- Draw a 2D/3D model using geometry functions.
- Define the metal, insulators, and other components
- Assign the boundary condition
- Mesh the whole geometry. To avoid meshing errors in the full assembly analysis (5.3), first, mesh the entire surface using a free triangular mesh and then use a tetrahedral mesh to mesh the volume.
- Solve it.
- Extract the potential of the desired plane.

5.2.1.3 Result

We have done the simulation for the complete trap geometry, shown in figure 5.2. The extracted potential has been fitted with equation 5.4 in Mathematica. The contour plot of the simulated potential is shown in figure 5.4. We have also simulated the geometry mentioned in Schrama *et al* [60] and Stein's PhD thesis [181] to benchmark the simulation method and compare the contribution of quadruple and octopole terms. In the verification of the simulation of the models by Schrama *et al.* [60] and Stein's PhD thesis [181], only electrodes are considered. Mounting assembly for the electrodes is excluded in their original work. Due to absence of complete electrode dimensions, the model by Nisbet-Jones *et al.* [1] is not simulated but is included in the comparison table 5.2. At this point, the $a_{2,0}$ coefficient has been optimized for our situation. A

Table 5.2.: Comparison of multipole coefficients for different trap geometries. We have simulated already published trap geometries similar to our design and compared the values of multipole coefficients with their literature values.

	Schrama [60] (sim./lit.)	Stein [181] (sim./ lit.)	Nisbet-jones [1] (lit.)	RRI (sim.)
$a_{2,0}$	0.31/0.29	0.217/ 0.218	0.335	0.283
$a_{4,0}$	0.0013/...	0/0	...	0.003
$a_{6,0}$	0.03/...	0/0.00016	...	0.028
$a_{8,0}$	0.001/...	0.003/0.003	...	0.005
$a_{10,0}$	0/...	0/...	...	0
ϵ	...	.../0.01	...	0.001

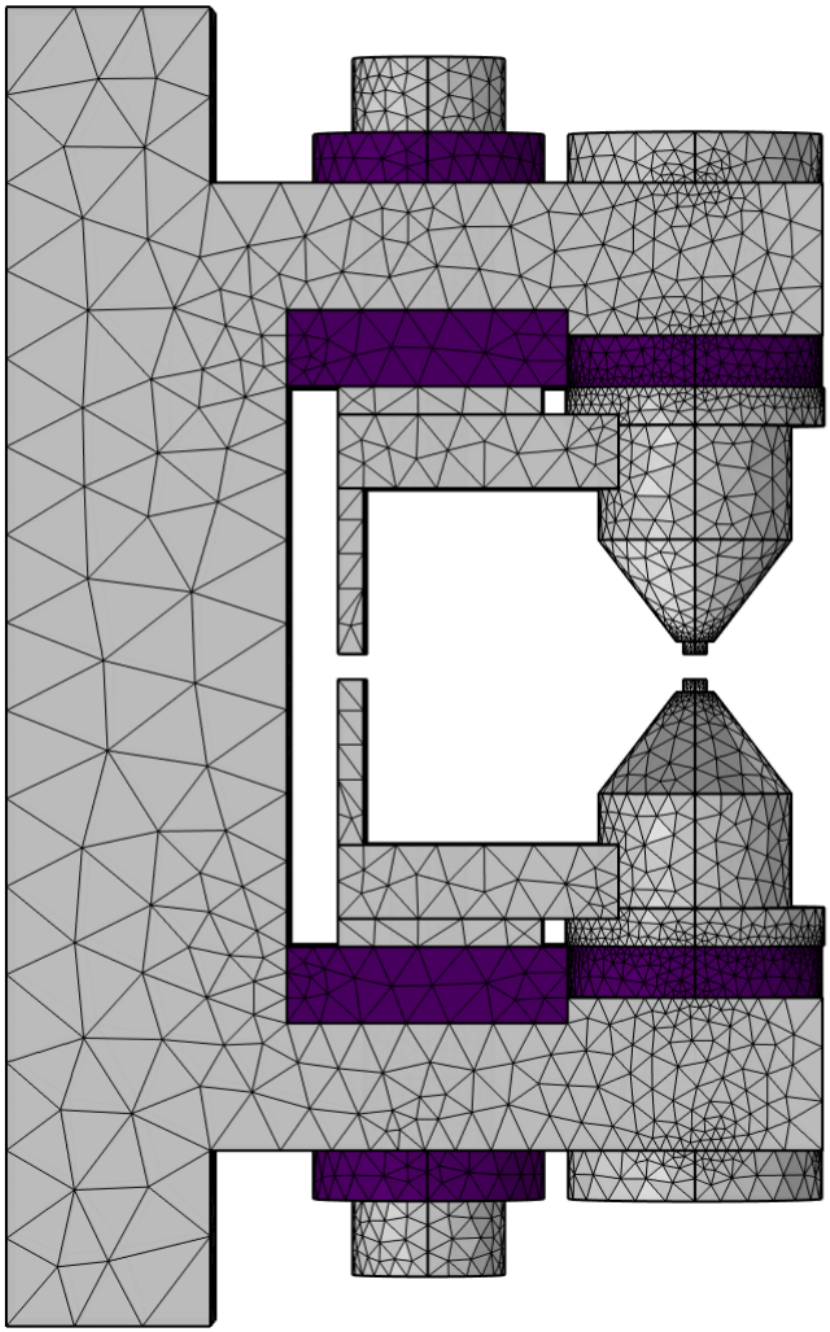


Fig. 5.3.: Screenshot of Comsol interface showing the mesh for complete and final trap model with all components to solve Poisson's equation with appropriate boundary condition. Insulators and metal parts are shown in different colours.

higher $a_{2,0}$ comes at the cost of the increased contribution of other multiple terms. Since we are new to precision spectroscopy or other experiments where a higher value of multipole coefficients has an adverse effect, we decided to go with the presented design and incorporate feedback from experiments in the next version.

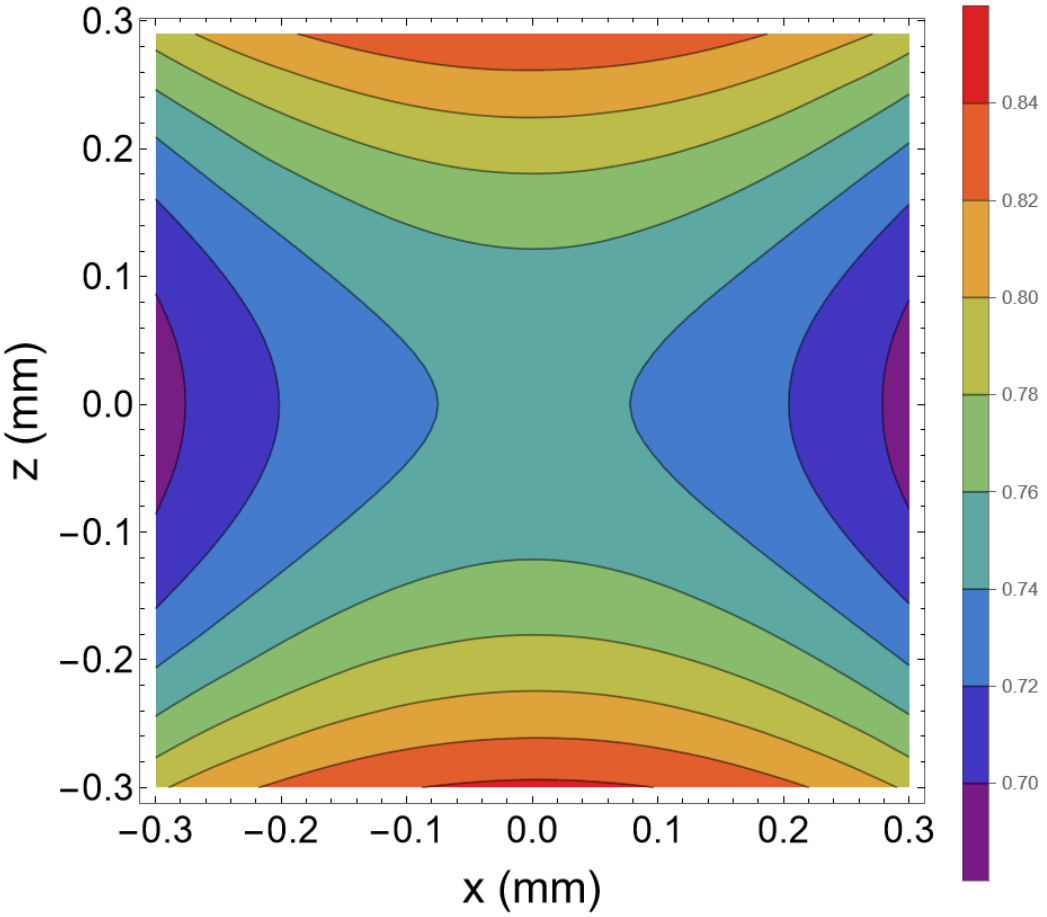


Fig. 5.4.: Contour plot of trap potential in the region of interest around the trap centre.

There is another important point that we should pay attention to: the shape of the fork used to mount the outer electrodes in case of Stein *et al.* [181] and Nisbet-Jones *et al.* [1] is different. We have followed Nisbet-Jones *et al.* [1] because the protrusion of the fork body, parallel to the trap, nullifies the effect of the rf field generated by the trap body. The contour plot of the potential generated by the complete trap geometry is shown in figure 5.5.

5.2.2 Material Selection

The second phase of the design starts with search of metal and insulators suitable for the trap. Deciding factor for the electrode material is the availability of pure materials, machinability in India, strength, thermal conductivity, resistivity, and work function differences between the electrode material and the parent atom of the ion to be trapped. For insulators, machinability, low dielectric constant and low dielectric loss tangent at the drive frequency range of our interest are more important. Considering the strength, machinability and resistivity, we selected Molybdenum (Mo), Copper-

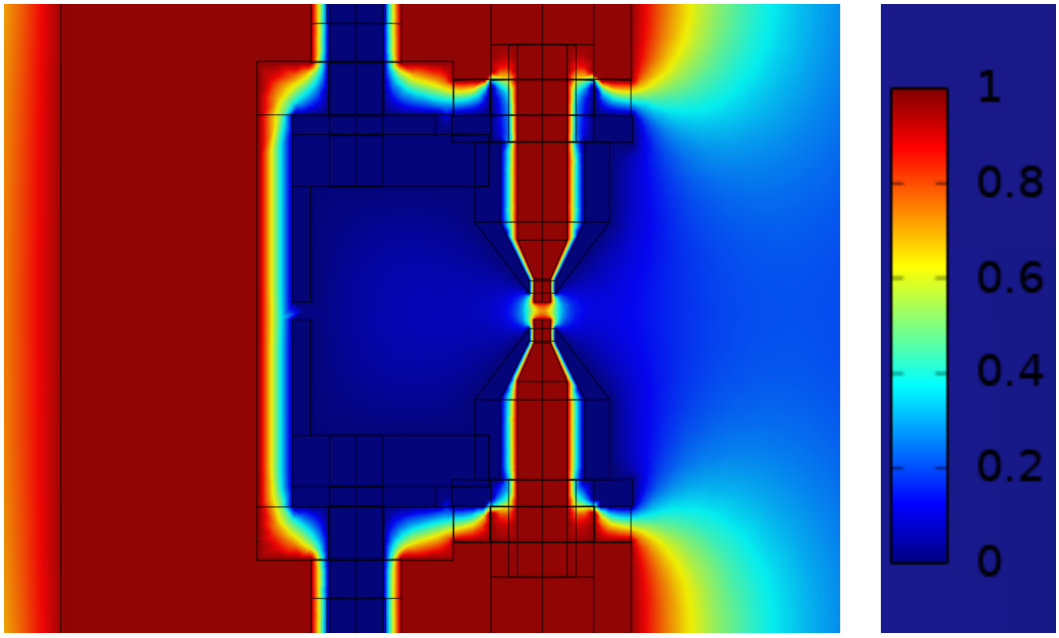


Fig. 5.5.: Effect of the fork's shape on potential generated by full trap assembly at the centre.

Chromium-Zirconium (CuCrZr) and fused silica as materials for electrodes, trap frame and insulator, respectively. A detailed comparison of material properties is available in Dolezal *et al.* [189].

5.2.3 Machining and Alignment

Machining and alignment of the complete geometry is the most critical and challenging part. It took us three years and at least ten iterations to reach the final phase, and still, there is possible room for improvement. To make a trap very close to the designed geometry, we require a strict tolerance on the inner electrodes, outer electrodes, and holes in the frame to align it. We first started with an over-enthusiastic aim of aligning the whole geometry within a tolerance of 1 μm from the simulated geometry, but it proved impossible. Initially, we did not wish to use an insulator to align and adjust the height of the outer electrode with respect to the inner electrode to keep the capacitance of the trap as low as possible. The result of the first attempted prototype of the trap at RRI is shown in figure 5.6.

In the next step, we started to look for machining facilities outside RRI for metal parts. After consulting with our workshop [190] and engineers at Central Manufacturing Technology Institute [191], we realized we had to relax the tolerances to fabricate and align the trap in India. We increased tolerances on the inner and the outer electrodes to 10 μm. This is not detrimental to the performance of the trap, as properly matched pieces with relaxed tolerances can still yield a high-quality trap. Simultaneously, we began to modify the design to place insulators to constrain the position of the outer

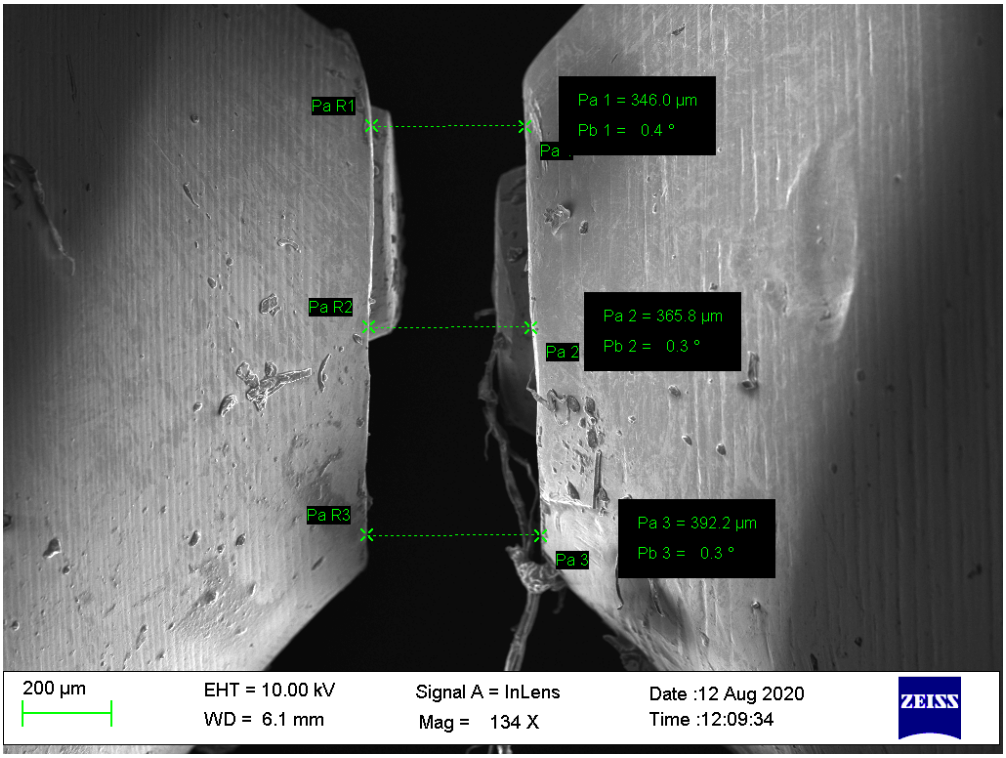


Fig. 5.6.: Scanning Electron Microscope (SEM) image of the first trap prototype built at RRI workshop. We have used stainless steel to make all the parts. It is evident from the image that we need better machining precision and methods to constrain the position of electrodes with respect to the frame. The strands are residue of the lens cleaning tissues.

electrode with respect to the inner electrode. Design modifications in this stage were the following:

- The alignment procedure is guided by the co-axiality of the holes in the CuCrZr frame to arrest the inner electrodes. Check figure 5.2
- The hole in the trap frame will guide fused silica insulators (F1), which will guide the outer electrode. Check figure 5.2
- Another insulator, F2, adjusts the height of the conical electrode with respect to the inner electrode. Check figure 5.2
- Earlier, the mounting fork was an integral part of the outer electrode. Now, it is divided into two parts. It eases the machining of the outer electrode. Check figure 5.2
- Interference fit will be used to fix the inner electrodes in the frame.

To observe the effect of the above mentioned modifications on a coarser level, we again machined a trap assembly at RRI and aligned it to observe the effect of the guiding insulator. Since it is a prototype to understand the effect of modifications on the alignment of the electrodes, electrodes are made from SS316, and teflon is used as an insulator. Results are shown and discussed in figures 5.7 and 5.8.

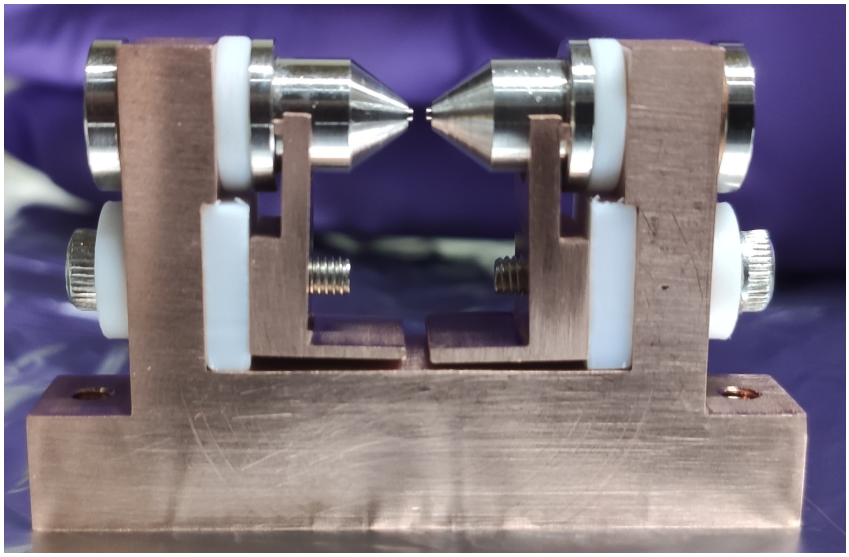


Fig. 5.7.: Image of the modified trap assembly to align the outer electrode. The frame is made from CuCrZr, the electrodes are made from stainless steel, and Teflon is used as an insulator.

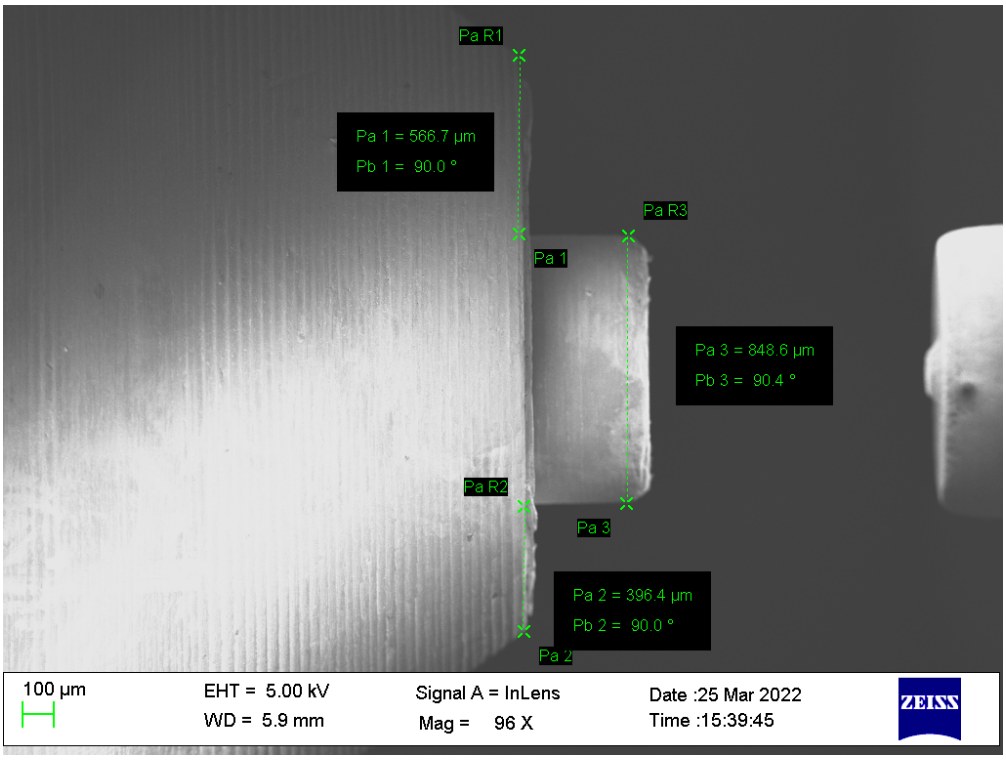


Fig. 5.8.: SEM image of the one side of the trap electrodes. We observe a positive impact of the guiding insulators on alignment.

Our next task is to check the possibility and effectiveness of the interference fit to fix the inner electrodes. First, we present the result and analyze the reasons for the failure of interference fit. It is evident from figure 5.9 that interference fit has not produced results as per our expectation. There can be two reasons for this. First, the co-axiality of the holes in the frame is not up to the specifications. Second, we don't

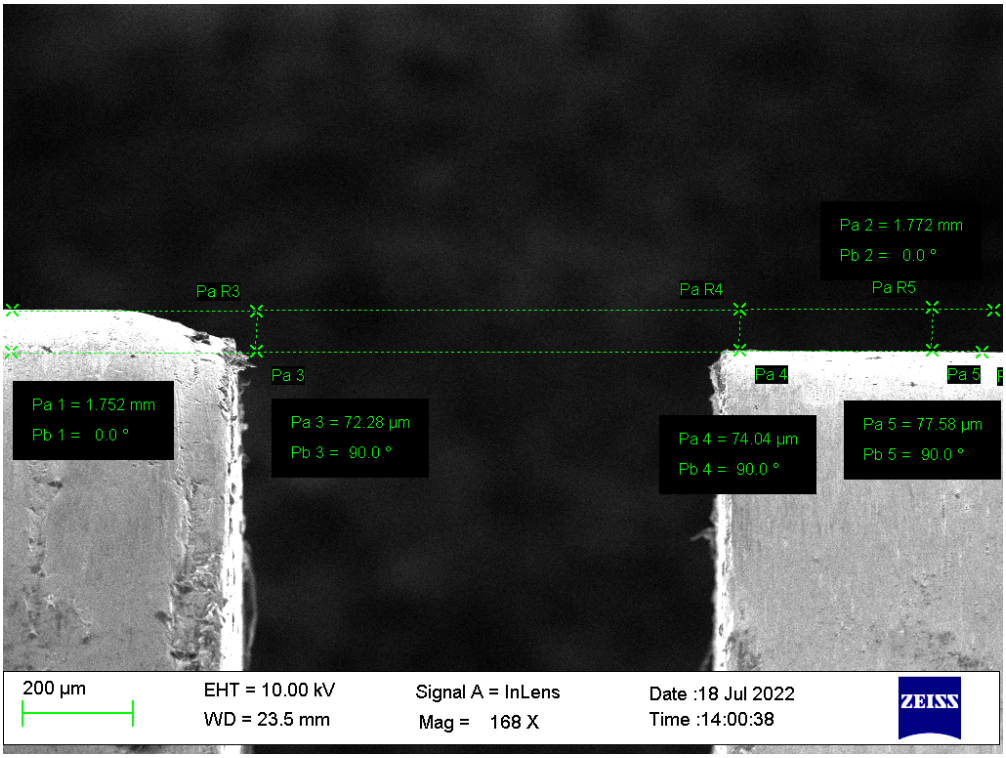


Fig. 5.9.: SEM image of the inner electrode for the case of interference fit trail.

have complete control over the fitting process, and if the electrode goes at an angle with respect to the hole in the frame, it will be misaligned. We have additional problems like water drops freezing on the inner electrode surface when we remove it from the liquid nitrogen. Due to the small size of the electrodes, they thermalize with the environment quickly and regain their dimensions before the fitting process is complete. We don't have a source to uniformly heat the holes in the frame to fit the inner electrodes. Hence, we have to devise a different strategy to align the electrodes. In the final phase, we planned to use the transition fit to fix the inner electrodes in the frame.

We have chosen fused silica for insulators, and the final alignment is ultimately limited by its machining tolerance. There are three groups of insulators, as shown in figure 5.2. The first one, F1, adjusts the height of the outer conical electrode with respect to the inner electrode on each side. The thickness of this insulator is very critical. The second one, F2, is used to make the ground electrode concentric with respect to the inner electrode. It is guided by the hole for the inner electrode in the CuCrZr frame. F2 has a significant overlap (1.5 mm) with the outer electrode to arrest it. The outer diameter of this insulator is very critical. It is the primary source of misalignment because of tolerances in the hole dimension, the outer electrodes' diameter at the base, and the outer diameter of F2 must be in a very narrow range. The F3 isolates the mount and electrical connector of the outer electrode from the trap body.

5.2.4 Characterization of Final Assembly Parts and The Aligned Assembly

After several iterations, we found that the degree of uniformity in the manufacturing of the metal electrodes is much higher than that for the fused silica. We therefore changed the strategy and started with the machining of fused silica parts first and then adjusted the metallic electrodes for precision fitting. Tolerances of guiding insulators (F1) and height-adjusting insulators (F2) were up to 15 μm. It is beyond our initial demand for fused silica tolerances, but since this was unavoidable, we used these pieces and adapted the metallic pieces to maintain the overall alignment and design integrity of the trap.

Machining of metal parts is done at the Government Tool Room and Training Center, Bangalore [192]. A coordinate measuring machine (CMM) and SEM are used to characterize the dimensions of the different parts of the trap assembly, including the CuCrZr frame. The first task is to characterize the co-axiality of the holes in the CuCrZr frame, and it is found that the holes are misaligned by 6 μm and 20 μm in the radial directions. To maintain the co-axiality of the inner electrode and compensate for the machining error in the co-axiality of holes in the frame, we made a slot in the arms of the CuCrZr frame on one side and thread for the M2 grub screw on the other side as shown in figure 5.10. The next part is the characterization of the diameter and surface quality of the inner electrodes. The diameter of the inner electrode in theoretical simulation is 920 μm; after machining, the measured diameter is 905 μm and 908 μm. SEM images of the inner electrodes are shown in figure 5.11. It is very good and close to our expectations. Atomic force microscopy (AFM) is used to analyze the surface quality of the top surface of the inner electrodes. Initially, all the rough patches were

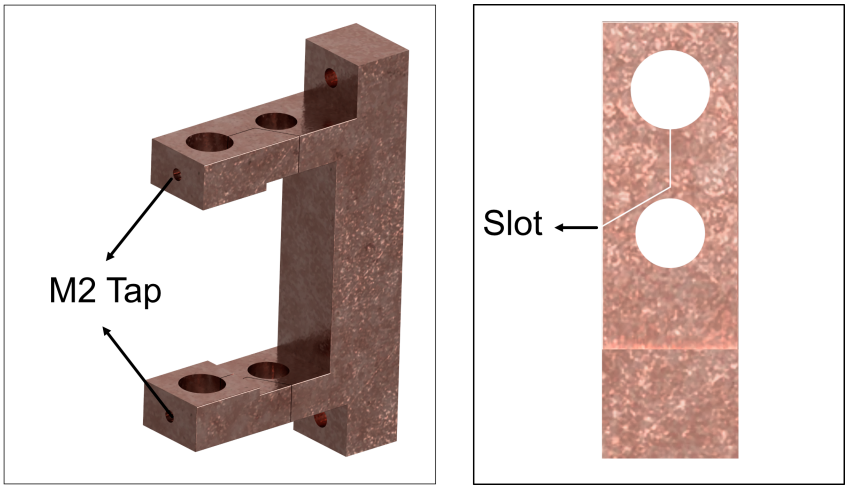


Fig. 5.10.: The Left image shows the M2 tap and slot to align the inner electrode. The right image is showing the top view of the top arm.

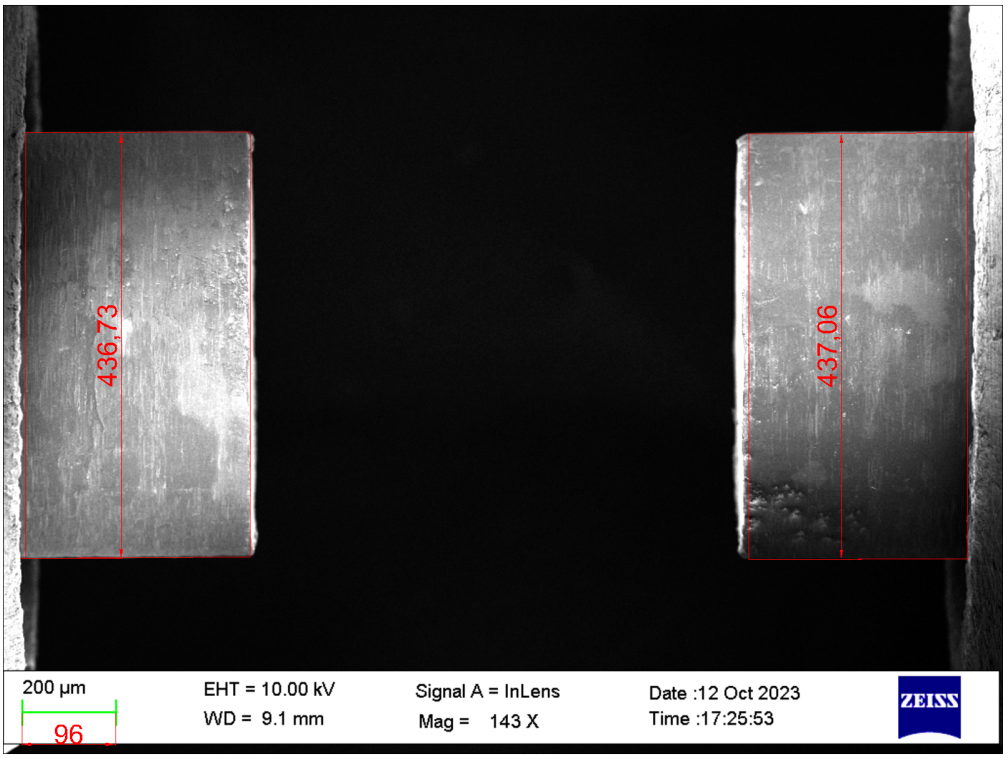


Fig. 5.11.: SEM image of the inner electrodes. The diameter of the inner electrodes is 905 μm and 908 μm.

identified and scanned in a region of 100 μm × 100μm around all the patches on both electrodes.

An AFM image of one of the patches and the corresponding surface texture along different lines on both electrode surfaces are shown in figure 5.12. The surface roughness of the second electrode is better compared to the surface roughness of the first electrode, but both are within design specifications. Once the characterization of the inner electrodes is over and they are up to specification, we move to the characterization of the outer electrode. The inner diameter of the outer cone at the tip is 1.5 mm in simulation, and the same for the machined parts are 1.48 mm and 1.5 mm. SEM images of the outer electrodes are shown in figure 5.13. It is evident from the SEM image that the inner edges of both the cones are circular, but the outer edges are slightly elliptical. It limits our alignment in terms of co-axiality of the outer electrodes with respect to the inner electrodes. For the inspection of other dimensions, we have relied on CMM only.

We started the assembly process once the individual parts were within the best possible tolerance limit. The steps for the assembly process are as follows:

- First, insert the guiding insulator (F1).

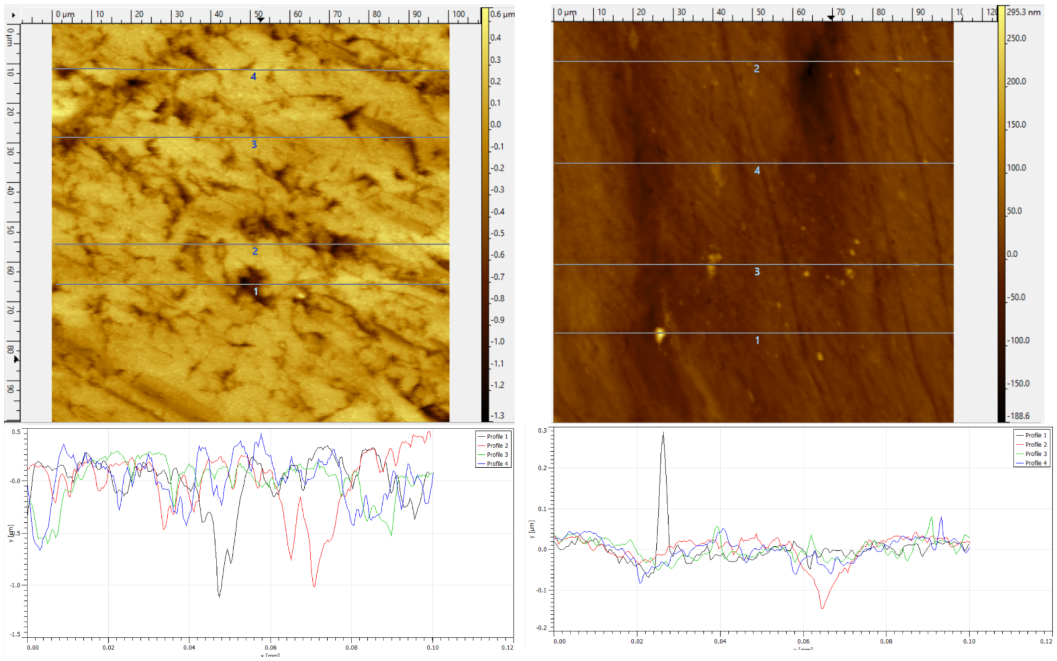
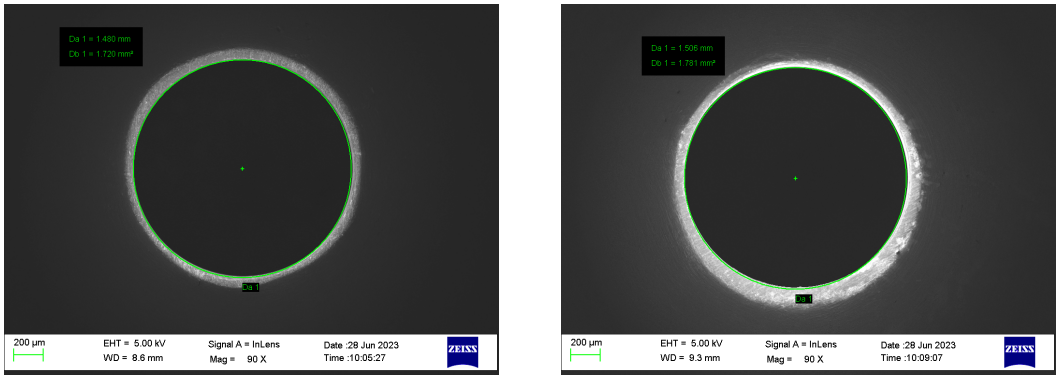


Fig. 5.12.: Left Panel: (Top) AFM image of the top surface of the inner electrode 1, (Bottom) Corresponding surface undulation along the lines marked in the top image. RMS roughness, in this case, is approximately 208 nm. Right Panel: (Top) AFM image of the top surface of the inner electrode 2, (Bottom) Corresponding surface undulation along the lines marked in the top image. RMS roughness, in this case, is approximately 26 nm



(a) **(b)**

Fig. 5.13.: (a) SEM image of the top portion of the conical electrode 1. It is almost circular on the inner as well as the outer side. (b) SEM image of the top portion of the conical electrode 2. It is almost circular inside, but the outer side has a significant deviation. We will observe the effect of this distortion in the final assembly.

- Mount the outer electrode in the place.
- Insert the inner electrodes.
- Check this assembly under a high-resolution optical system and align it using the slot and M2 grub. The slot and M2 threaded hole are shown in figure 5.10
- Inspect the whole system using SEM
- Apply very small quantity of Torrseal [193] where the base of the inner electrode

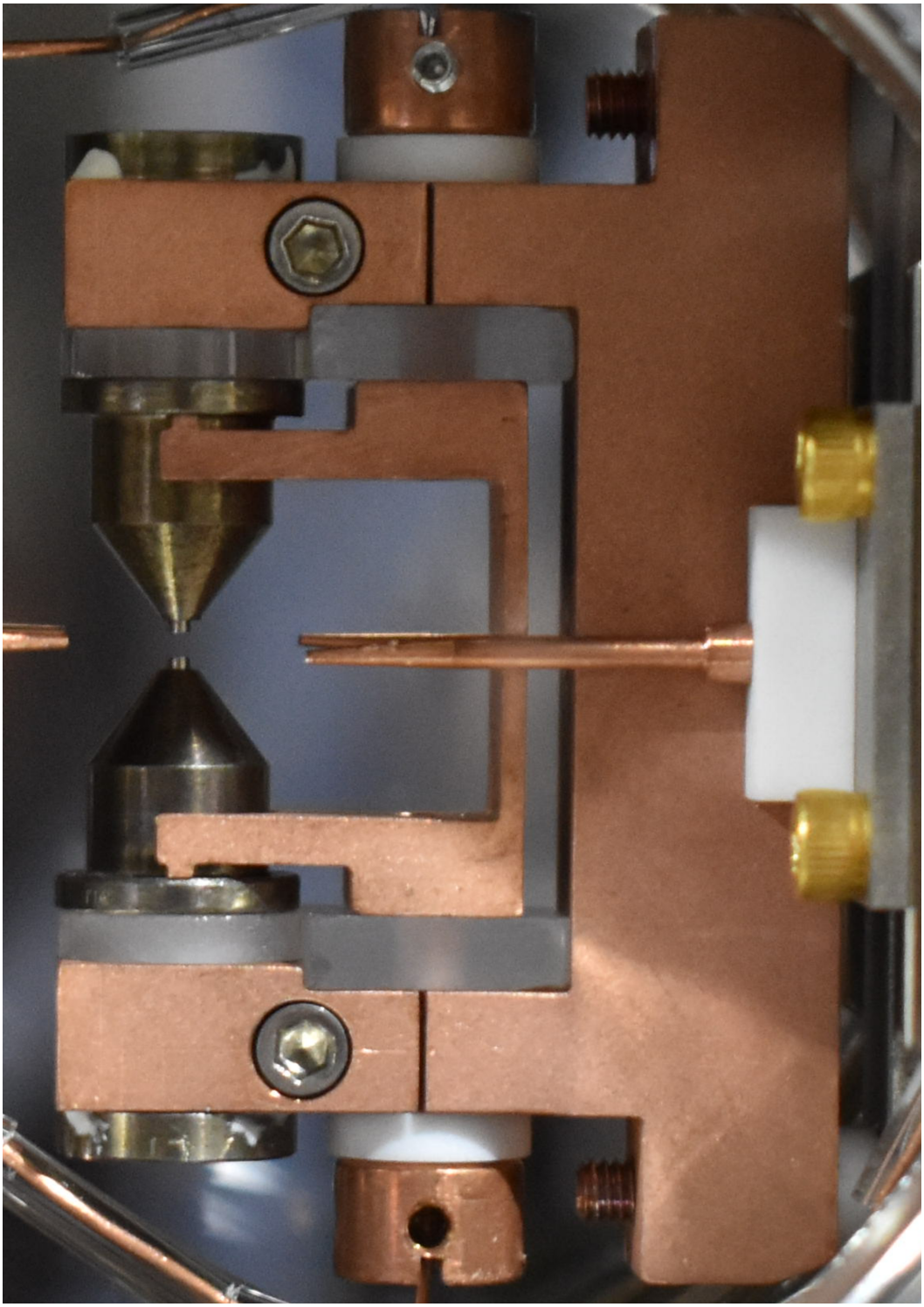


Fig. 5.14.: Close view of the aligned trap assembly installed inside the vacuum chamber.

is flush with the CuCrZr frame. It will help to maintain the alignment during the baking process to obtain UHV.

SEM images of the assembled trap in different orientations are shown in figure 5.15. A comparison table of the ideal and the achieved geometry is presented in table

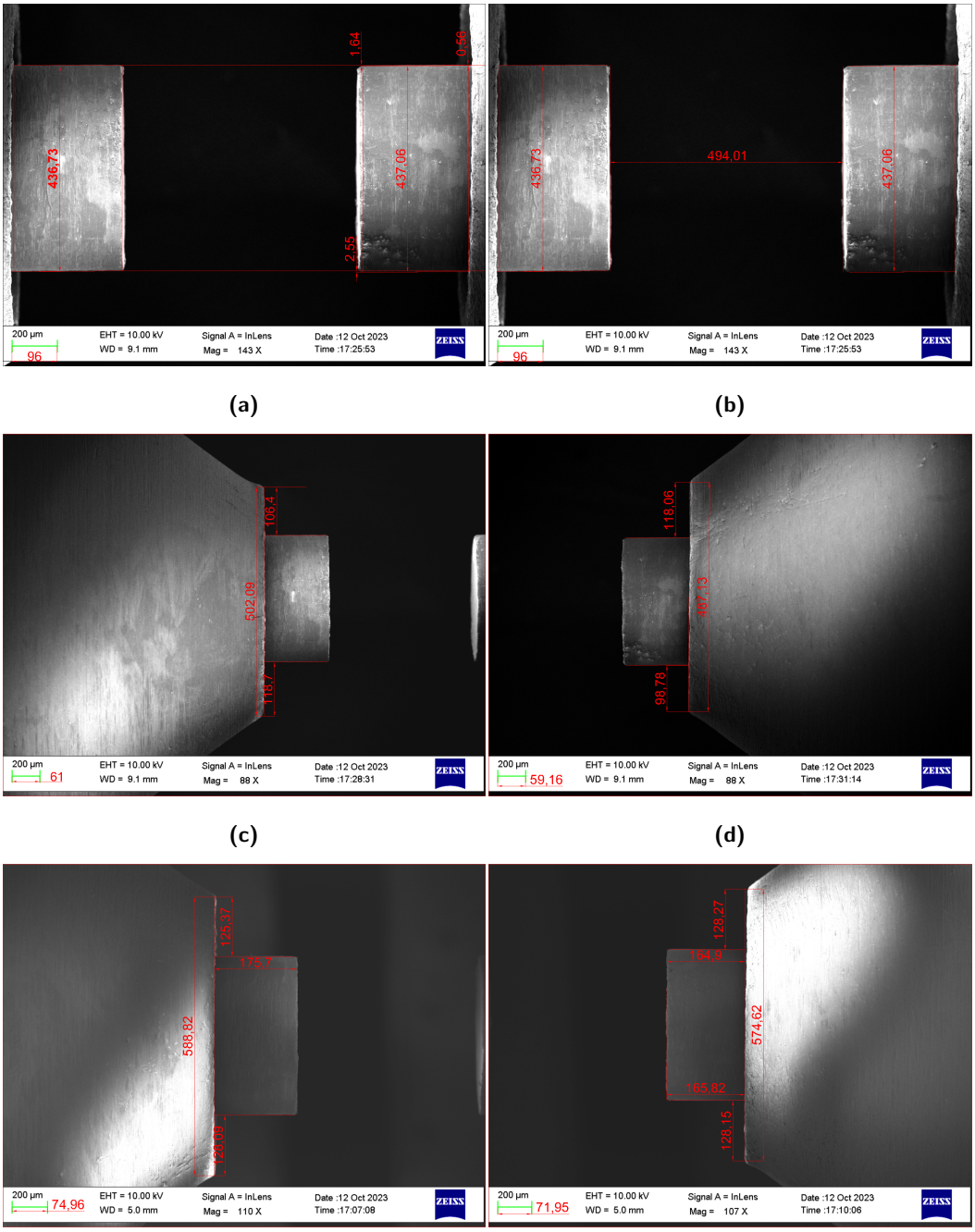


Fig. 5.15.: SEM image of the aligned assembly. (a) Co-axial deviation between the inner electrodes. (b) Distance between the inner electrodes. (c) Alignment of the conical electrode 1 with respect to the pin electrode shown in (a). (d) Alignment of the conical electrode 2 with respect to the pin electrode shown in (b). (e) Alignment of the conical electrode 1 with respect to the pin electrode shown in (a) in the orthogonal direction shown in (c). (f) Alignment of the conical electrode 2 with respect to the pin electrode shown in (b) in the orthogonal direction shown in (d). The length scale of individual images is shown at the bottom of the image.

Table 5.3.: This table presents the alignment analysis of the SEM images shown in figure 5.15. From the 5th row onwards, all the rows represent the outer diameter of the conical electrode and the gap between the inner electrode and conical electrodes on both sides. All the dimensions mentioned in the table are in mm.

Parameters	Model	Assembly
figure 5.15a (Inner electrode diameter)	0.92, 0.92	0.908, 0.905
figure 5.13 (Inner diameter of conical electrodes)	1.5, 1.5	1.48, 1.51
figure 5.15a (Misalignment of inner electrodes)	0, 0	0.0034, 0.0053
figure 5.15b (Distance between inner electrodes)	1.0	1.029
figure 5.15c (Outer diameter of the outer electrode, Gap between outer and inner electrodes on both sides)	1.6, 0.34, 0.34	1.646, 0.389, 0.347
figure 5.15d (Outer diameter of the outer electrode, Gap between outer and inner electrodes on both sides)	1.6, 0.34, 0.34	1.646, 0.334, 0.399
figure 5.15e (Outer diameter of the outer electrode, Gap between outer and inner electrodes on both sides)	1.6, 0.34, 0.34	1.57, 0.342, 0.334
figure 5.15f (Outer diameter of the outer electrode, Gap between outer and inner electrodes on both sides)	1.6, 0.34, 0.34	1.597, 0.356, 0.356
figure 5.15e (Distance between outer and inner electrodes in axial direction)	0.5	0.468
figure 5.15f (Distance between outer and inner electrodes in axial direction)	0.5	0.460

5.3. To quantify the coaxiality of the inner electrodes, the outer edge of one of the electrodes has been taken as the reference and extended up to the other electrode to find the distance between the edges. Coaxial alignment of the outer electrode with respect to the inner electrode is measured with respect to the outer edge of the conical electrode. The elliptical or deformed cross-section of the outer edge of the outer electrode limits the alignment process. A lot of care has been taken during image analysis to detect the boundaries of electrodes. The resolution always limits us, and a difference of a single

pixel in edge detection will result in a change of dimension by $\sim 2\ \mu$m.

5.3 Conclusion

In this chapter, we have followed the details of the design process. One part is the effect of trapping potential on trapped ions, and the other part is factors like machining, alignment, and tolerances. Taking care of both factors, we arrived at a suitable model for our starting design. In principle, this is not the optimal design. Still, if we consider the machining and alignment viability of components, it is excellent for the given constraints. Considering our end goals, after initial characterization, the heating rate due to patch potential, the black body radiation shifts due to surface roughness will be most critical part. It will enable us to evaluate and understand the effect of machining imperfections and patch potential in our experiments. Considering the multipole coefficients of similar trap geometries implemented at different places, this is a good starting point towards characterization and preliminary experiments. Trap installation and details of the vacuum system will be discussed in the next chapter.

6 Experimental Setup

6.1 Introduction

A good ultra-high vacuum (UHV) setup is one of the prerequisites for the experiments where a low background collision rate is required. Along with this, a good overlap of the oven's beam with the trap center, proper optical access for imaging and laser beams, mounting of the whole setup with ease and selection of appropriate ion pump, gauge, and Titanium sublimation pump (TSP) play a crucial role during the design process of this kind of experiment. Proper care during the assembly, cleaning, and baking process helps to achieve a good vacuum. A high-voltage source at high frequency, circuits for connection, and probe circuits to measure voltage across the trap are required to run the ion trap. This chapter deals with the process of design, assembly, drive circuits, lasers, and detection systems to trap and detect ions.

6.2 System Design and Components Details

6.2.1 System Design

The size of the ion trap, its mounting ease, and the alignment of the oven and the compensation electrodes with respect to the trap center are some of the primary factors that help in choosing a vacuum chamber. The second important point is the high collection efficiency of the fluorescence signal emitted from the trapped ions. It helps to image and detect the single ion with a very good signal-to-noise ratio. Collection efficiency depends on the solid angle available for fluorescence collection, transmission of vacuum windows, and numerical aperture of the imaging system. The gap between the trap's inner electrodes and the imaging system's numerical aperture limits the solid angle for collecting scattered light from the trapped ion. It gets partially fixed once we fix the gap between the trap electrodes. The numerical aperture of the imaging system mainly depends on the focal length and diameter of the optics used for light collection. For the standard available options of the lenses, we needed to minimize the distance between the trap center and the first lens used for the fluorescence collection. The

selection of the chamber fixes the minimum distance between the trap center and the imaging system. The next factor is the transmittance of the windows used for imaging. Here, we have two options: either go for anti-reflection coated windows in the regime of our interest or select one with very high transmittance throughout the range of our interest; we opted for the second one.

After taking care of the above facts, once we decide on the chamber and windows, our next task is to design the mounting assembly to hold the chamber in position. The chamber is mounted on an 8 mm thick aluminium plate of appropriate dimensions using the tapped holes on 4.5" sealing surface of the chamber. The plate is held using an aluminium profile channel. We have used a non-evaporable getter (NEG) ion pump, NEXTORR 100-D, to achieve UHV. Additionally, a TSP is also installed in the system. A hot cathode ion gauge is used to measure the pressure inside the chamber. The rest of the vacuum hardware parts are selected according to the dimensions of the other components like the gauge, pump, TSP, etc. An all-metal stainless steel valve is used to connect the turbo pump to the chamber for the initial vacuum. All the parts are first assembled into a 3D design software, CATIA, to check the feasibility of the assembly procedure. A rendered image of the full assembly and a zoomed view of the chamber and the trap assembly, rendered in the 3D software FUSION 360, are shown in figure 6.1.

6.2.2 Components Detail

A spherical octagon chamber from Kimball Physics, model no: *MCF450-SphOct-E2A8*, is used to mount the trap assembly. The oven assembly is integrated into the chamber using a conical reducer and a full nipple in series. To mount the trap inside the chamber, first, it is mounted on an in-house made SS plate using copper screws, and Macor® spacer is used to isolate it from the plate as shown in figure 6.2. The SS plate is mounted using a pair of groove grabbers. These groove grabbers are held by grabber grooves made on the inner side of the 4.5" sealing surface. The RF connection to the trap is provided using a high-voltage feedthrough from VACOM, CF16-HV20S-1-CE-CU24. Compensation electrodes of the trap side are mounted on the same plate, their distance from the trap center is 5mm, and the angle between their tips is 60°. A pair of compensation electrodes counter to the first one is mounted on the oven side. Feedthroughs used for connecting compensation electrodes are from VACOM, and their part numbers are CF16-HV2-4-CE-CU081 and CF16-HV2-8-CE-CU081. We have used VACOM viewports, model no: VPCF63DUVQ-L-316L, made from Corning® HPFS® 7980. Reflection from each surface of the window is approximately 5.25%, and internal transmission is almost 100%. A Pfeiffer turbo molecular pump, TMU047, backed by a diaphragm pump, model no: MVP 015-2, is used to achieve high vacuum. A

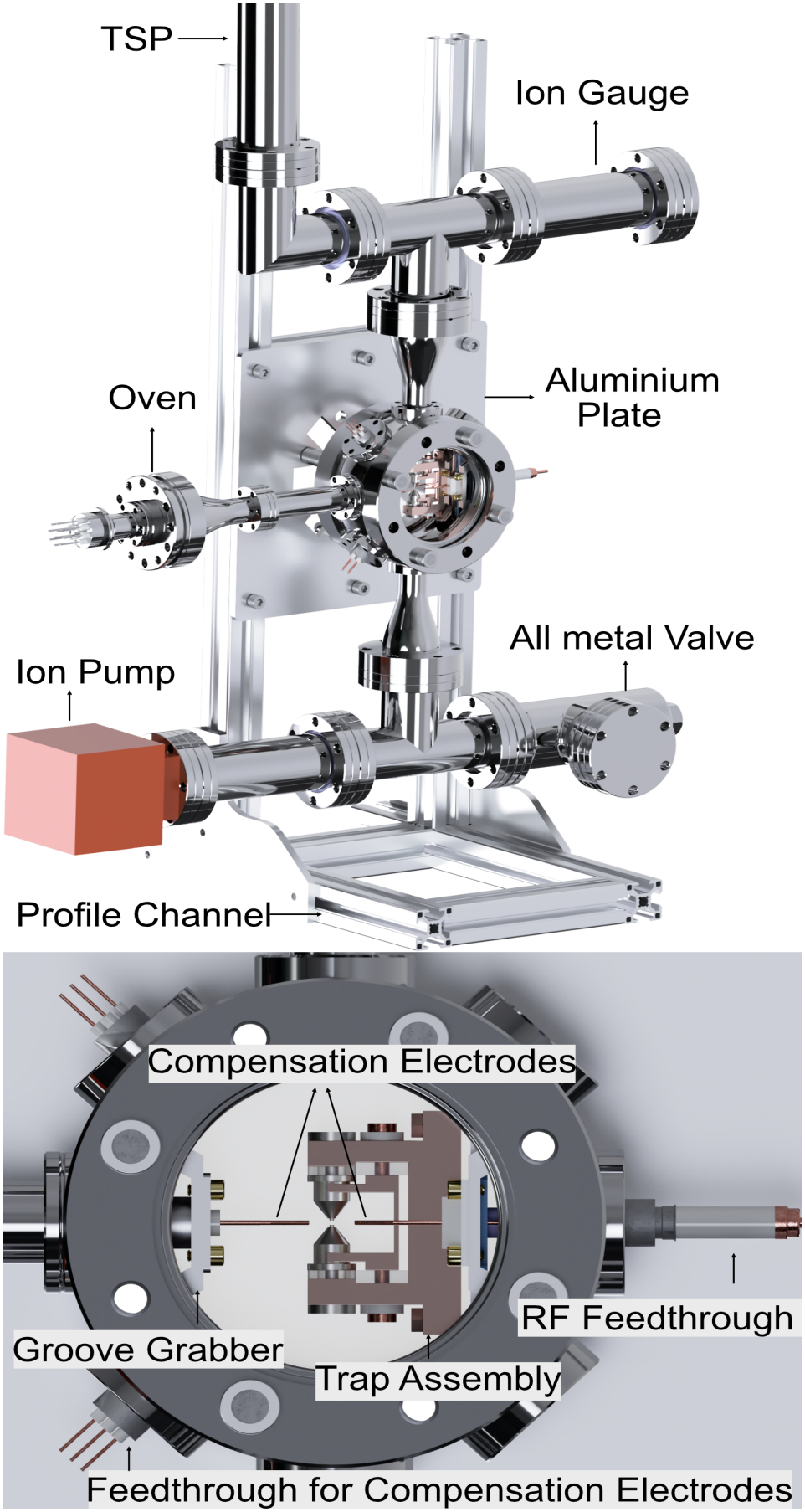
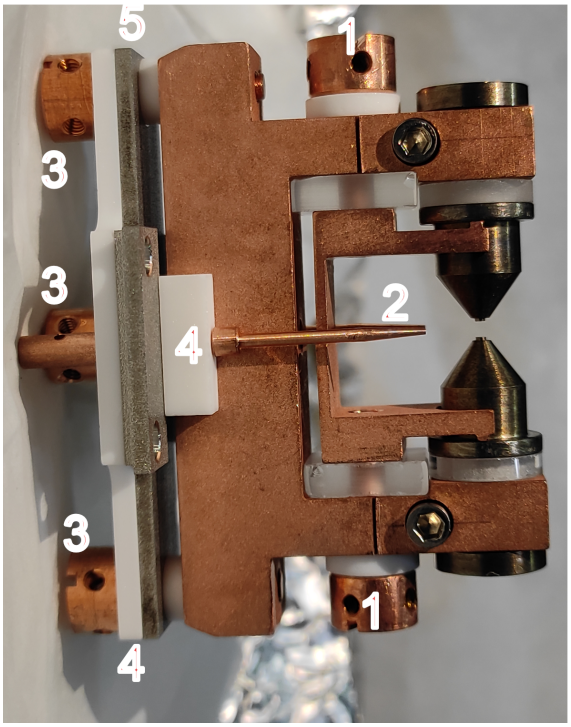


Fig. 6.1.: (Top) Rendered image of the full assembly setup with all critical components and mounting frame made using aluminium profile channels and plate to hold the vacuum chamber in place. (Bottom) Detailed view of the trap mounting structure and feedthroughs for connection.



1. Copper Bolt 1
2. Compensation Electrodes
3. Copper Bolt 2
4. Macor Spacer
5. SS Plate

Fig. 6.2.: Mounting assembly for the trap, to mount the whole setup inside the chamber, showing SS plate, insulator and Copper bolts. Copper Bolt 1 is used to provide the electrical connection to the outer electrode. The middle bolt in copper bolt 2 is used to provide the RF connection to the trap; counter sink screws replace the other two bolts in copper bolt 2 to avoid any contact of the mounting assembly to the chamber. Macor® plate and spacers isolate the copper bolts and the trap from the SS plate, respectively. Machining design details of the plate and other parts are given in **??**. The trap shown in the image is not the aligned trap.

SAES-100D NEG ion pump is used to achieve UHV, and a UHV-24 Bayard-Alpert gauge from Agilent is used to measure the pressure inside the chamber. A TSP cartridge is also installed to increase pumping efficiency in the UHV regime. To mount the chamber in the configuration as shown in figure 6.1, 4 homemade 5/16" bolts of suitable length are used to mount the chamber on an 8 mm thick aluminium plate. A 30 mm aluminium profile channel is used to form a support structure for the plate holding the chamber assembly.

6.3 Cleaning, Assembly and Bake out

6.3.1 Cleaning and Assembly

The first part of the vacuum assembly building process is cleaning of the components that are going to be installed inside the vacuum chamber. The cleaning process is performed separately for the chamber and its accessories, windows, and trap components.

The trap and its accessories are manufactured at different workshops in Bengaluru; oil and coolants are adsorbed on the surface of machined parts. The cleaning process of these components involves the following steps.

- Clean all the components using soap-water.
- Clean it with normal water twice and let it dry naturally, or use a cold air gun to dry the components.
- Clean it with demineralized water and dry it after taking it out.
- Clean it using iso-propanol and dry it.
- Wrap inside an aluminium foil and store in a clean box.
- Copper parts are cleaned using lemon water after the first step to remove the oxide layer from the surface, and then the rest of the process is completed.
- Similarly, other metal parts are cleaned using ortho-phosphoric acid or lemon water after the first step, and then the further cleaning process is performed.
- All the cleaning steps are performed using a sonicator bath for at least 15 minutes.

According to the information provided by VACOM, we have used oil-free dry nitrogen to remove dirt or lint from the window surfaces, if present. The chamber and the other vacuum accessories supplier companies claim that the components are ready to assemble in a UHV setup but recommend cleaning before installing them into the system. Since we do not have a big sonicator bath, we manually cleaned the edges of the components using a lint-free tissue soaked in iso-propanol after removing the cap. During the whole cleaning and assembly process, all the members working on it wore masks, hair nets, and powder-free gloves to avoid contamination of the cleaned components.

The second part is fixing the groove grabbers, SS plates, aligned trap assembly inside the chamber and mounting other components like windows, reducer nipples, pumps and hardware parts. The procedure to fix the position and alignment of the groove grabbers and the SS plate is already discussed in Chapter 4. The trap alignment procedure is discussed in Chapter 5. The aligned trap is then mounted on the SS plate using copper screws and insulators as shown in figure 6.2. Then wires are connected to the copper bolt 1 and trap side compensation electrodes to provide the electrical connection. The plate with the trap is mounted inside the chamber using groove grabbers. A similar procedure is followed for the other pair of compensation electrodes. Next, the feedthrough for the electrical connections is mounted and in-house machined copper connectors connect the feedthrough leads to the wires coming out from different electrodes. Finally, the viewports are mounted to seal the CF63 ports. All bolts are tightened using a torque wrench in a criss-cross pattern, as a good vacuum practice. All the bolts used to fix any components with the chamber are either silver-plated or copper-greased. After this, the chamber is fixed to the support structure. In the last phase, hardware assembly with TSP and ion gauge on the top side and all metal angle

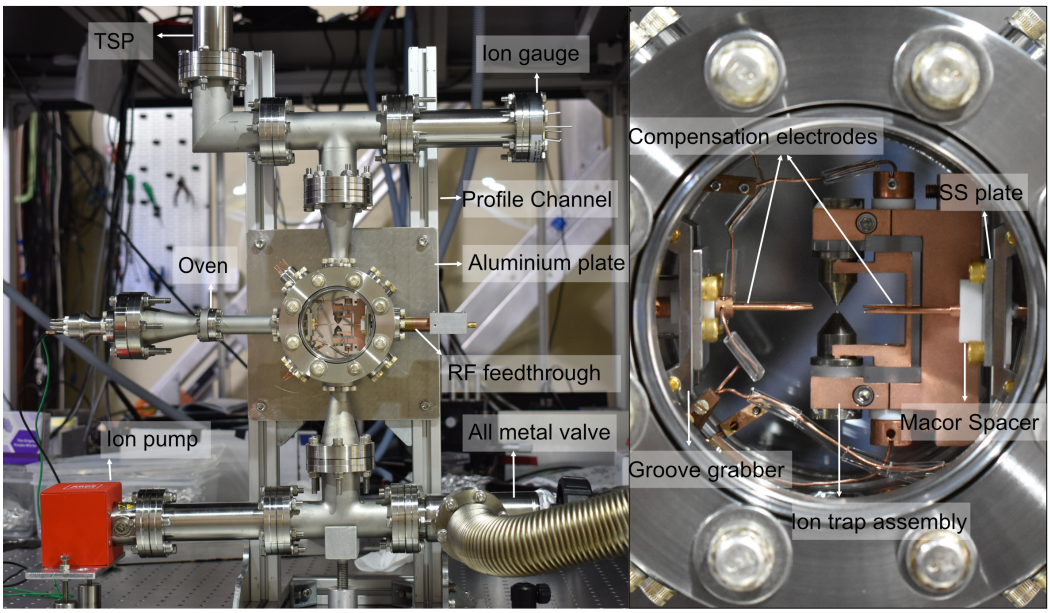


Fig. 6.3.: (a) Image of the complete assembly mounted on an optical table in the lab. (b) Zoomed view of the components inside the chamber.

valves on the bottom are connected to the chamber. In the end, the ion pump and the turbo pump are connected at their respective position.

6.3.2 Baking

After sealing all the surfaces, we used the backing pump of the turbomolecular pump to create a rough vacuum of approximately 10^{-2} mbar. Then, we switched on the turbomolecular pump to create high vacuum. Once the pressure on the turbo pump gauge dropped to 3×10^{-8} mbar, we started preparation for the baking process. K-type thermocouples are stuck on the chamber assembly surface at 12 different points, and their temperatures are regularly monitored. First, the ion gauge and filaments of TSP are degassed. An Agilent controller controls the ion gauge and has an inbuilt function for degassing. TSP filaments are degassed by passing 40 A current for 1 min each. During the degassing process, the pressure inside the chamber reached $\sim 4 \times 10^{-6}$ mbar and dropped afterwards. Vacuum viewports are covered with crushed aluminium foil of window size for uniform conduction of heat across the window. The chamber assembly, ion pump and the bellow connecting turbo pump are wrapped with a heater tape. The whole assembly is loosely covered with aluminium foil to reduce the heat loss to the environment during the baking process. Setup ready for baking is shown in figure 6.4. The temperature of all the thermocouples is noted before switching on the current of the heater coil. During the baking process, the current in the coil is increased very slowly to keep the temperature change slow. Temperature change of the viewports at higher rates than the specified values can develop leaks. The temperature of all the thermocouples is



Fig. 6.4.: Image of the setup ready for the baking process. Yellow wires are k-type thermocouples attached to the surface of the vacuum assembly at different points.

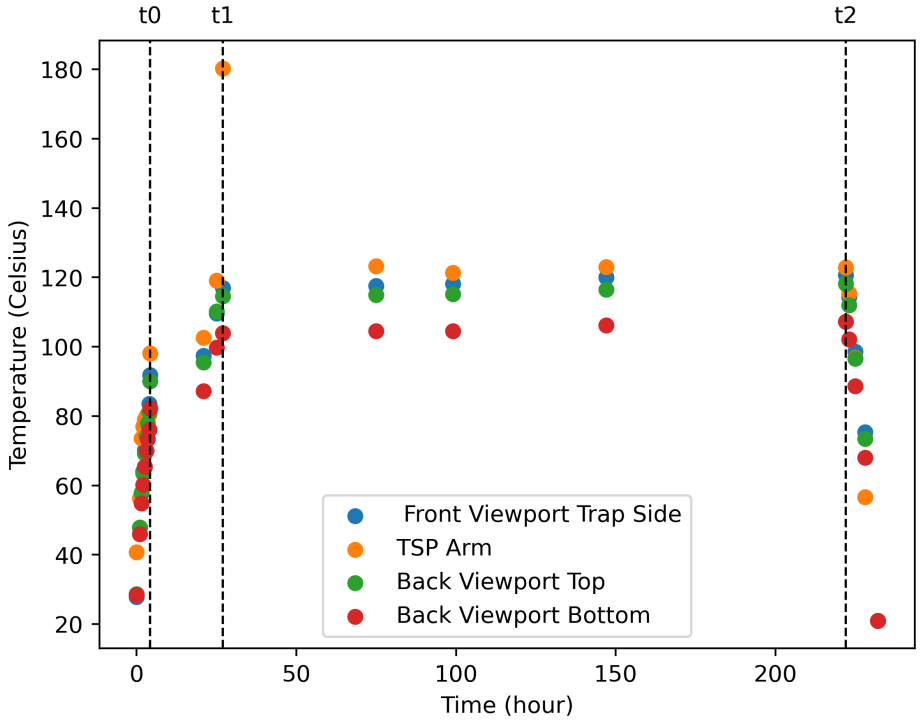


Fig. 6.5.: Change in temperature of the thermocouples with time during the baking process. Temperature variation of 4 thermocouples are shown in the figure, out of which three are installed on the chamber body near viewports, and the 4th is installed on the TSP cartridge arm. At t_0, we stopped increasing the current in the heater coil on day 1. At t_1, on the next day, we stopped increasing the current in the heater coil and left the system unperturbed till time t_2. After t_2, we started decreasing current in the heater coil.

monitored at intervals of 30 minutes. Since the thermocouples are not calibrated, they may read slightly different temperatures during the heating process. Figure 6.5 shows temperature variation in different parts of the assembly during the complete baking and cooling process. Once the temperature of all parts of the assembly reached above 100 degrees Celsius, we stopped increasing the current in the heating tape. The system is left at this temperature for approximately 200 hours and then cooled down slowly. The ion gauge pressure reading before, during, and after baking is shown in figure 6.6. Once we stop increasing the heater coils' current, we degas the ion gauge and TSP filament. This time, all the TSP filaments were operated at 30 A for 15 minutes. We again degassed the filaments of the ion gauge three times, and the final reading of the gauge at the end of baking was 3.8×10^{-9} mbar. The NEG element of the ion pump is activated after the completion of the baking. There is a built-in function on the controller for activation of the NEG. Maximum pressure during activation on the ion gauge reached 1.8×10^{-4} mbar, and the pressure reached 4.4×10^{-9} mbar in the next 120 minutes. Next, the turbo pump was detached after closing the metal valve. The ion gauge filament was degassed again and fired TSP filament3 for 3 minutes at 50 A. Pressure on the ion gauge

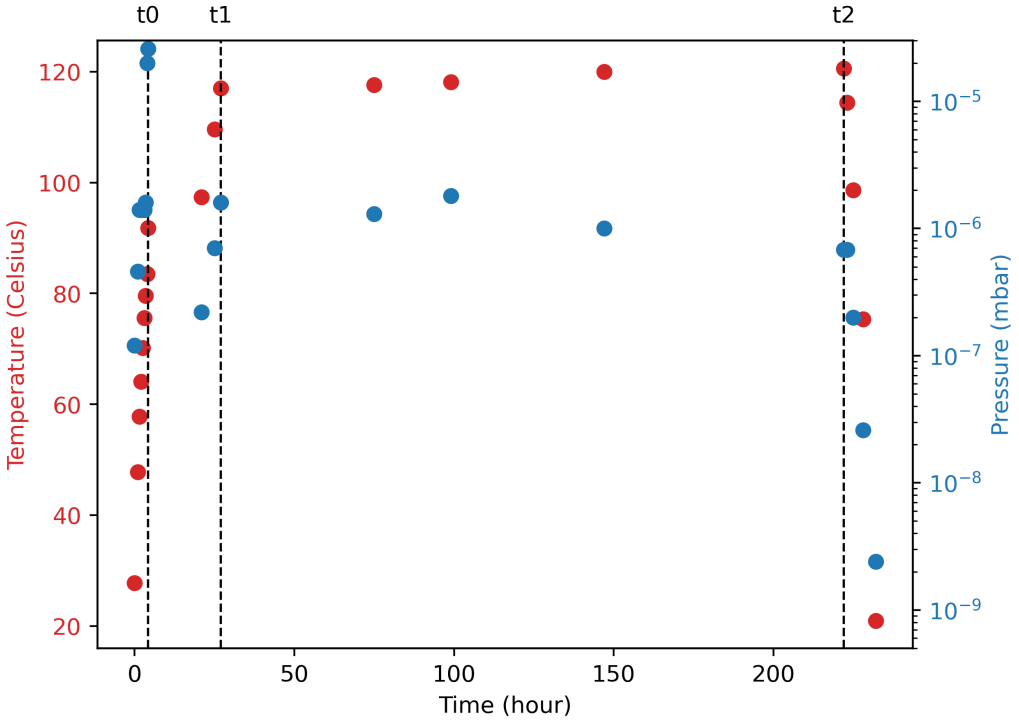


Fig. 6.6.: Change in Pressure on the ion gauge and temperature of the Front viewport trap side with time during the baking process. The current in the heating tape is constant between the time t_1 and t_2

by the end of the day was 3.3×10^{-10} mbar. The next day, pressure on the gauge was 2×10^{-10} mbar. The atomic oven was heated at different currents for a long time for the next few days so that the pressure inside the chamber would not rise significantly when the oven current was up to 3 A. After this, we fired the TSP filament3 for 3 days for 1 min at 50 A. The final pressure on the gauge was 1.3×10^{-10} mbar on the 4th day. We generally keep the ion gauge off. During experiments, we observe pressure using the ion pump's gauge. The pressure inside the chamber increases if we operate the oven at 5.5 A and drops down very fast after switching off the oven. At our normal operating oven current, 4 A, we don't notice any pressure change on the ion pump controller because the change is below the measurable range of the gauge attached to the ion pump.

We should perform some important checks before and after the baking process to ensure the proper functioning of the experiment. A few of them are the oven's performance, integrity of the electrical connections and the trap's characteristics. To ensure the oven's performance, we operate it for long times, like up to 20 hours, in different time stretches and days. We note the minimum current at which we can observe the oven's fluorescence using an ordinary mobile phone camera. After completing the baking process, we operated the oven at the minimum current to observe fluorescence. We checked the oven's fluorescence before and after the trap center to ensure the

alignment. One way to check the integrity of the electrical connections is to measure the capacitance of the trap and other connected electrodes and repeat this process after baking. The capacitance of the trap is in the picofarad (pF) range, and we don't have an impedance analyzer. So, we operated the trap before baking, loaded an ion cloud and noted the resonance frequency of the trap. After baking, we repeated the same process and ensured all the connections were fine.

6.4 Trap Drive Electronics

6.4.1 Helical Resonator and Voltage Probe

To drive the trap, a voltage source of several hundred volts at MHz frequency is required. This type of source with a variable output impedance is not available on demand. Impedance matching is required to transfer maximum voltage to the load. In the absence of impedance matching, unnecessary power will be lost in the transmission line, and interference of the applied pulse with the reflected pulse will distort the applied waveform. To solve the issue of impedance matching, the ion-trapping community generally uses a helical resonator in the path. Radiofrequency signal is derived from a low-power signal generator, passed through an RF amplifier of desired gain, and applied across the trap with a resonator in the path before the trap to tune the impedance. A helical resonator consists of two helical coils: the bigger coil is called the main coil, and the smaller coil is called the antenna coil. The coils are co-axially aligned and housed inside a bigger shield as shown in figure 6.7. The initial parameters of the helical resonator are based on the trap's capacitance and the system's target-loaded frequency. The paper by Macalpine *et al.* [194] is followed to fix the number of turns, diameter, and pitch of the primary coil, diameter, and length of the outer shield of the coil housing. The drive circuit, including the RF source, trap, and helical resonator, can be represented by a lumped circuit model (figure 6.8). It helps to represent the drive circuit plus the trap system as a *LCR* circuit and calculate the resonant frequency and Q factor of the system. The LCR model presented here closely follows the description in the paper by Siverns *et al.* [195]. The resonant frequency of the lumped circuit representation in the unloaded case is

$$f_0 = \frac{1}{2\pi\sqrt{L_h(C_h + C_s + C_w)}}. \tag{6.1}$$

Q factor of the system is defined as

$$Q = \frac{1}{R}\sqrt{\frac{L_h}{C_h + C_s + C_w}}. \tag{6.2}$$

Here, the source of resistance, R, is the sum of the resistance of the wire used to wind the coil, the resistance of the outer shield of the resonators, the joints to connect any

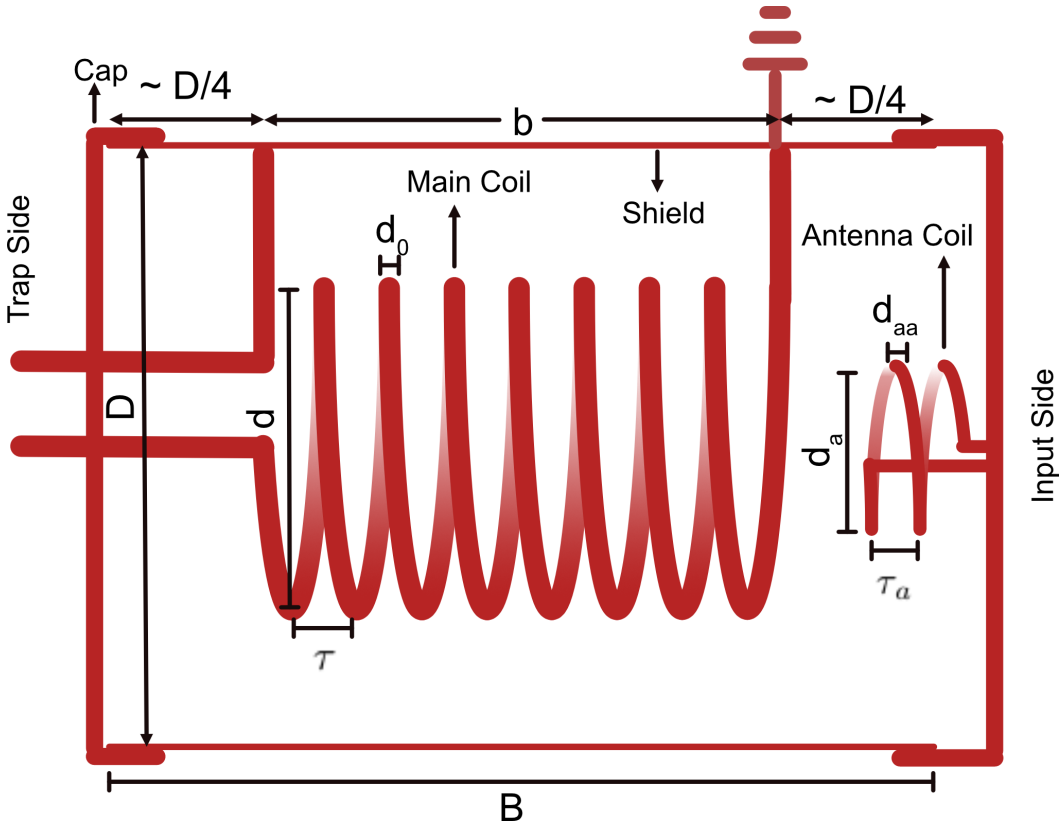


Fig. 6.7.: Schematic diagram of a helical resonator showing the position of coils and other parts.

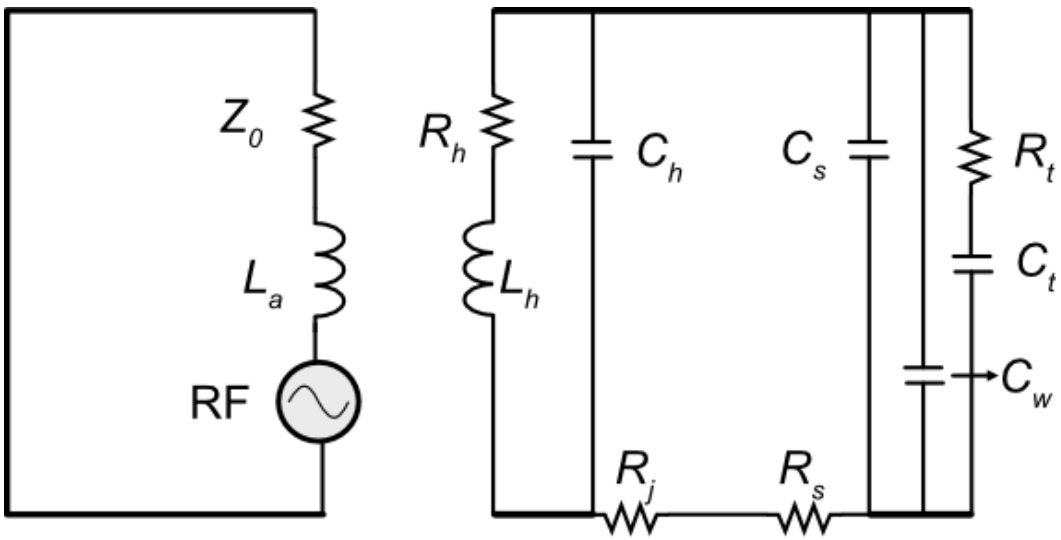


Fig. 6.8.: Lump circuit model of RF source, helical resonator, trap and other connecting parts. L_a is the inductance of the antenna coil, L_h is the inductance of the main coil, R_h is the resistance of the main coil, C_h is the capacitance of the main coil, R_j is the resistance of the main coil to the shield joint,R_s is the resistance of shield, C_s is the capacitance between the shield and the main coil, C_w is the capacitance of wire used to connect the resonator to the trap, C_t is the capacitance of the trap and R_t is the resistance of the trap.

two components, the wires to connect the trap, resistance of the trap body. Since we don't have any way to measure the resistance of joints at high frequencies, we ignore it in the design phase. The Q factor of an underdamped oscillator is also defined as the ratio of the center frequency, f_{res}, to the full width at the half-maximum, δf, of the power transmitted at the resonator output.

$$Q = \frac{f_{res}}{\delta f} = \frac{f_{res}}{f_{-3dB}}. \tag{6.3}$$

The self capacitance of the main coil, C_h, is calculated using empirical formula[195]

$$C_h \approx (0.1126\frac{b}{d} + 0.08 + \frac{0.27}{\sqrt{\frac{b}{d}}}) * 10^{-10} \text{ F}. \tag{6.4}$$

The capacitance between the main coil and the shield is given by

$$C_s \approx 39.37\frac{0.75b}{\log(D/d)} \text{ F}. \tag{6.5}$$

The inductance of a coil inside a shield, for the case where $\frac{b}{d} > 1$, is given empirically by

$$L_h \approx 39.37b\frac{0.025d^2(1-(d/D)^2)}{\tau^2} \text{ H}. \tag{6.6}$$

Sankalpa Banerjee from IUCAA, Pune, has fixed the initial parameters of the resonator assembly. The resonant frequency and Q factor in the loaded and unloaded cases were calculated and experimentally verified at RRI. The initial parameters of our main coil are the following:

D	d	b	B	τ	N	d_0
90 mm	53 mm	80 mm	135 mm	10 mm	8	6 mm

The initial parameters of the antenna coil are the following:

N_a	d_a	τ_a	d_{aa}
3	31 mm	5 mm	2 mm

The thickness of the shield is 3mm. Based on the initial parameters, the calculated values of capacitance, inductance, and resonant frequency of the system are the following:

C_h	C_s	L_h	C_t	f_0	f_{load}
2.5 pF	4.6 pF	1.4 μ H	14 pF	$\approx$ 50 MHz	$\approx$ 28.9 MHz

Details of connectors will be mentioned while discussing the different phases of Q factor optimization. The following procedure has been followed to experimentally verify the resonant frequency in the loaded and unloaded case. A bidirectional coupler, model no: ZFBDC20-62HP-S+, is added between the resonator and source (model no: ED8257D (Agilent Technologies)). CPL out of the bidirectional coupler is monitored using a signal analyzer, model N9010A (KEYSIGHT). The frequency corresponding to the minimum reflection gives the resonant frequency. Figure 6.9 shows the schematic of the setup. CPL IN port of the bidirectional coupler is terminated using a 50 Ω resistance. Experimentally finding the Q factor and resonant frequency and its optimization is an iterative process. It has taken several iterations. We will report the key iterations where we achieved a higher Q factor. We match the impedance of the source and the system by altering the distance between the antenna and the main coil [195–197]. In the first step, we mounted the coils received from the manufacturer and made all the connections including grounding using a BNC connector. For the loaded condition, the trap's initial prototype (figure 5.7) is connected after the resonator. Frequency is swept across the region of interest for a fixed RF amplitude to record the reflected voltage. Since we are working with the reflected voltage, we must find the f_{-3dB} point on the transmitted voltage and relate it to the reflected voltage. Normalized transmission spectrum is related to the reflected spectrum by

$$T = 1 - R, \tag{6.7}$$

corresponding f_{-3dB} point on transmitted voltage is $T_{max}/\sqrt{2}$. For the reflected voltage it will be

$$R_{-3dB} = 1 - T_{-3dB}. \tag{6.8}$$

T_{max} will correspond to R_{min} on the reflected spectrum. so the formula for f_{-3dB} point becomes

$$R_{-3dB} = 1 - \frac{1 - R_{min}}{\sqrt{2}}. \tag{6.9}$$

For the loaded case, the reflection spectrum for the unloaded and loaded cases are shown in figure 6.10, respectively. This modification led to an increase in the Q factor as well as the resonant frequency. In the next step, BNC connectors for grounding were replaced by brazing. It provides direct copper-to-copper contact. SMA connectors replace BNC connectors in other places. The resonant frequency, Q factor of the resonator in the unloaded and loaded cases are ≈ 48.3 MHz, 1208 and ≈ 26.3 MHz, 154.5, respectively. A copper screw can also be used for grounding purposes.Figure 6.11 shows this iteration's results. The resonant frequency, Q factor of the resonator in the unloaded and loaded cases are ≈ 45 MHz, 36 and ≈ 25.8 MHz, 36.8, respectively. The resonant frequency of the manufactured resonator system is close to the designed value, but the Q value is off. The theoretical Q value of the unloaded resonator is approximately 1200. It also confirms that the capacitance of the bare trap assembly is very close to that of the simulated one. The low Q can be due to impedance mismatch and high resistance at connection joints. The reason for impedance mismatch can be an insufficient gap

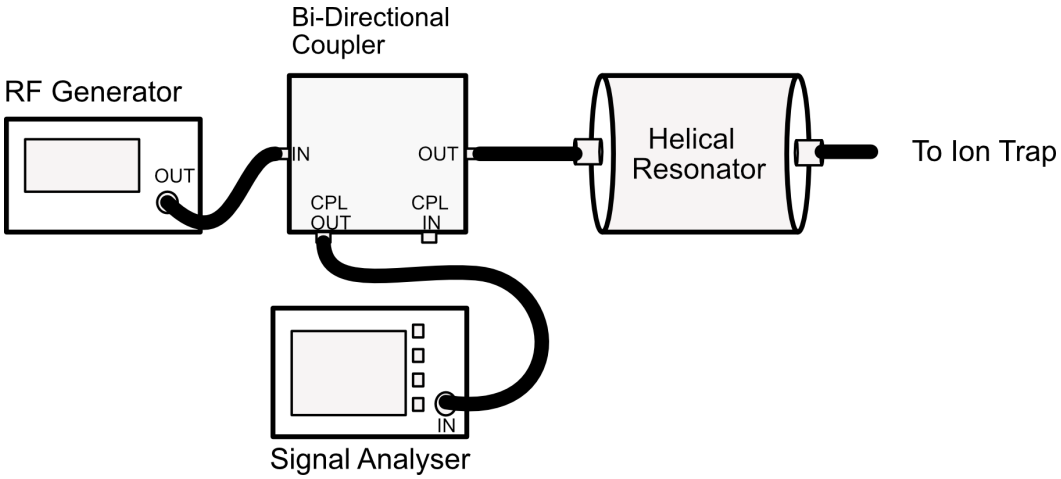


Fig. 6.9.: Schematic of experimental setup for measurement of Q factor

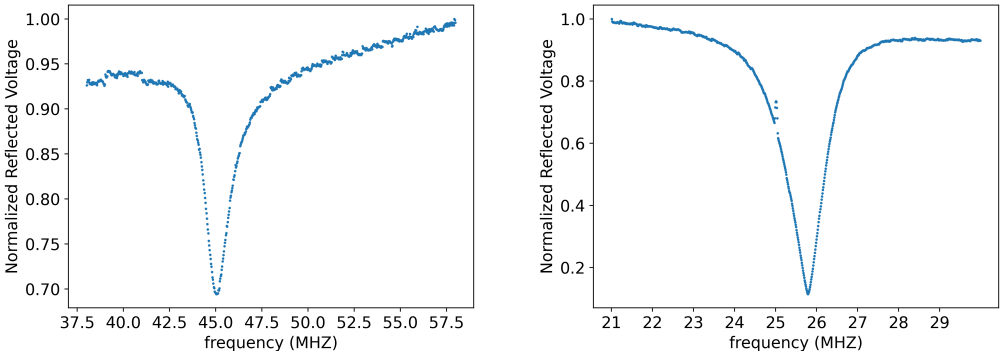


Fig. 6.10.: (a) Normalized reflection spectrum for the unloaded case. (b) Normalized reflection spectrum for the loaded case

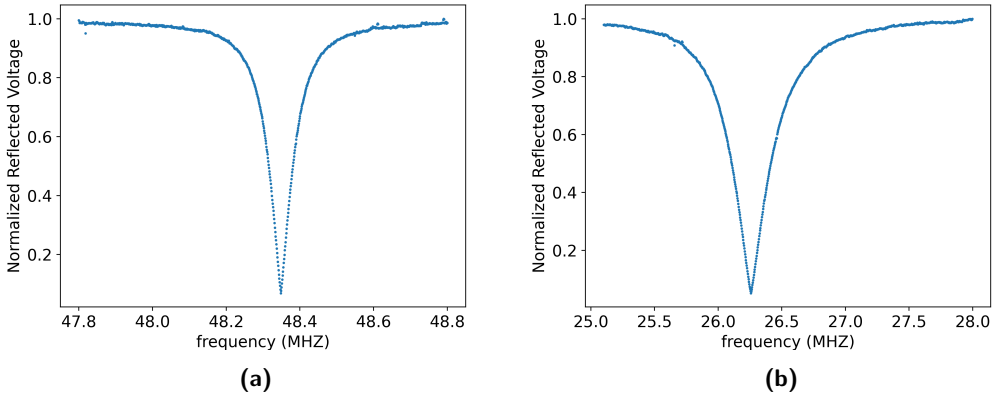


Fig. 6.11.: (a) Normalized reflection spectrum for the unloaded case. (b) Normalized reflection spectrum for the loaded case

between the main and antenna coil and the pitch of the antenna coil. To address it, we first made a new cap (depth 40 mm) for the antenna coil mount to increase the gap

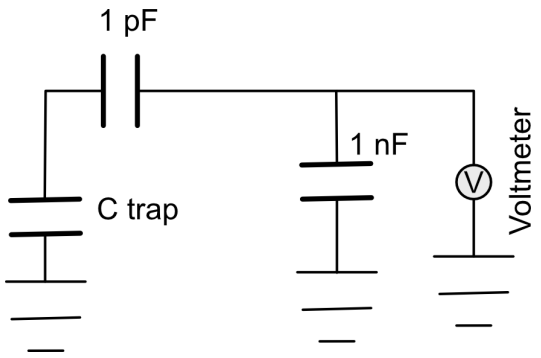


Fig. 6.12.: Schematic of probe circuit and details of components

between the coils and reduce the number of turns in the antenna coil to 2. The new cap is made from aluminium.

Our next task was integration of the resonator system with the aligned trap mounted in the vacuum assembly. The capacitance of the mounted trap assembly will be higher than the bare one, so with the present value of the Q factor, it was challenging to minimize the drop in the Q value with a drop-in resonance frequency. There was another task to add a probe circuit in parallel to the trap to sample the applied voltage across the trap. The probe will help to characterize the trap. It should be ideal in nature so that it does not alter the properties of the trap and the resonator system. In this scenario, the probe will be added in parallel to the trap, and its capacitance should be very small. Details of the components of the probe and its position in the circuit are shown in figure 6.12. Here, the capacitors in the probe circuit are selected such that their combined capacitance is negligible to the trap's capacitance, and any voltage probe across the 1 nF capacitor should not change the voltage ratio across the capacitors. Details of the probe circuit are described in Park *et al.* [198]. In order to find the voltage ratio across the 1 nF capacitor, the probe circuit is calibrated using a signal generator and the spectrum analyzer mentioned previously. The calibration curve for the source and probe is shown in figure 6.13. The calibration ratio for the probe is $\approx 990 \pm 5$. The signal generator should be operated in High Z mode for calibration. To tackle the increased capacitance due to the mounting assembly of the trap inside the chamber, we kept the resonator next to the trap feedthrough outside the chamber. An image of the vacuum chamber assembly with the electrical connection is shown in figure 6.21. We used a PCB and SMA connector to connect it. It has helped us to achieve a reasonable Q value for operating the trap. The transmission spectrum of the resonator assembly integrated with the mounted trap inside the chamber before baking is shown in figure 6.14. Ideally, the probe should not change the resonance frequency of the system, but due to extra connectors required to place the probe, an old PCB leads to a change in the resonant frequency. While removing the RF connection to the trap for baking preparation, we damaged the PCB used for the connection. After baking, we put a new PCB and removed one SMA female-to-female connector from the path. It leads to an increase in the resonance frequency of the system

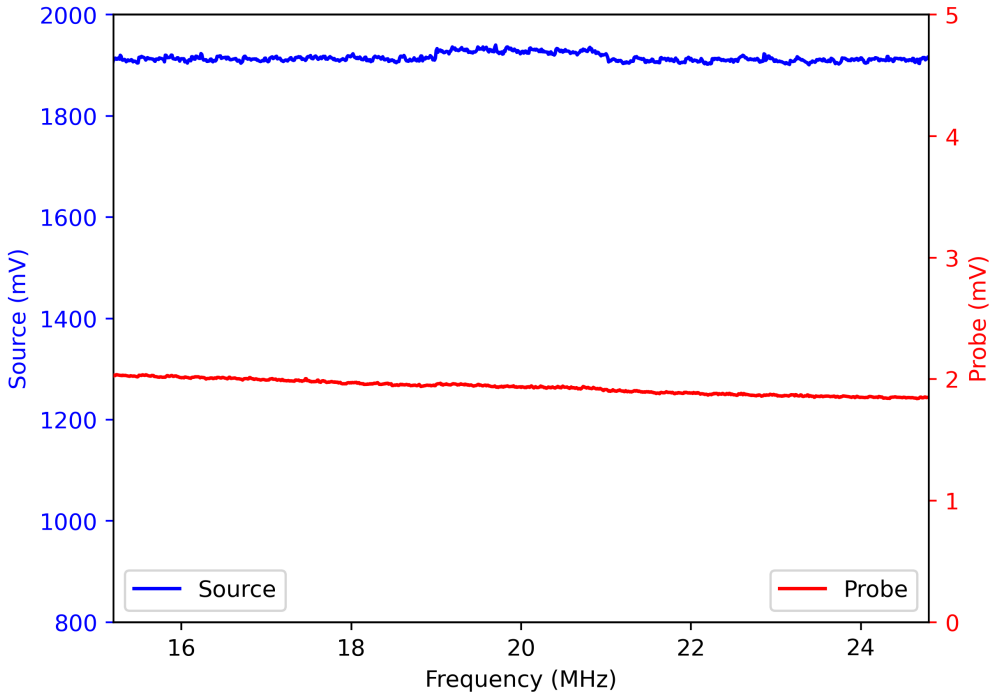


Fig. 6.13.: Calibration curve for the source and the probe. The set voltage on the source is 2000 mV.

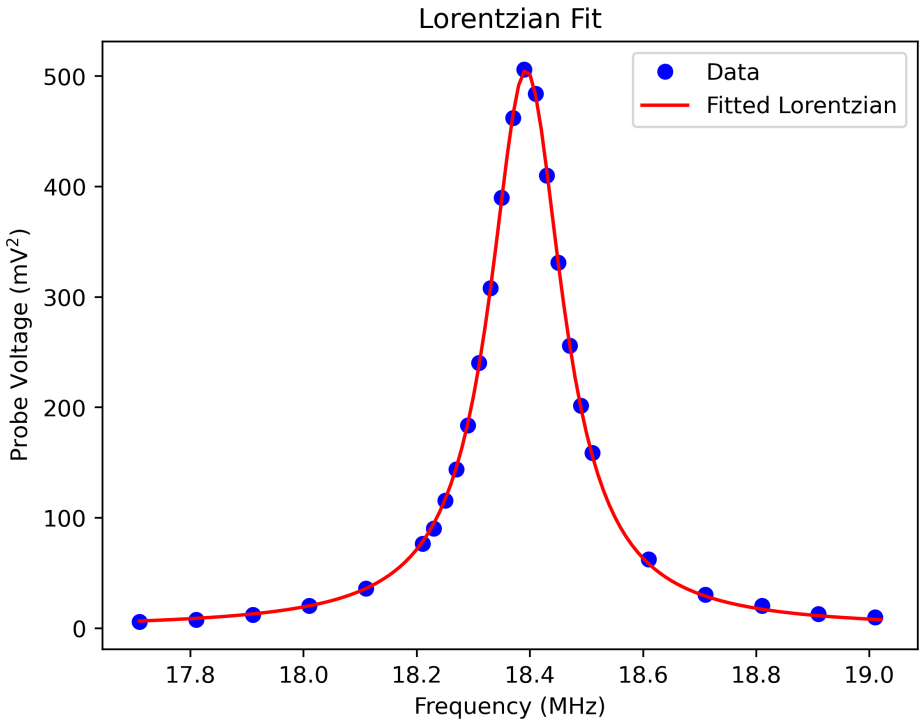


Fig. 6.14.: Transmission spectrum of the resonator integrated with the trap mounted inside the chamber before baking. Resonance frequency is $\approx$ 18.4 MHZ and Q is $\approx$ 115

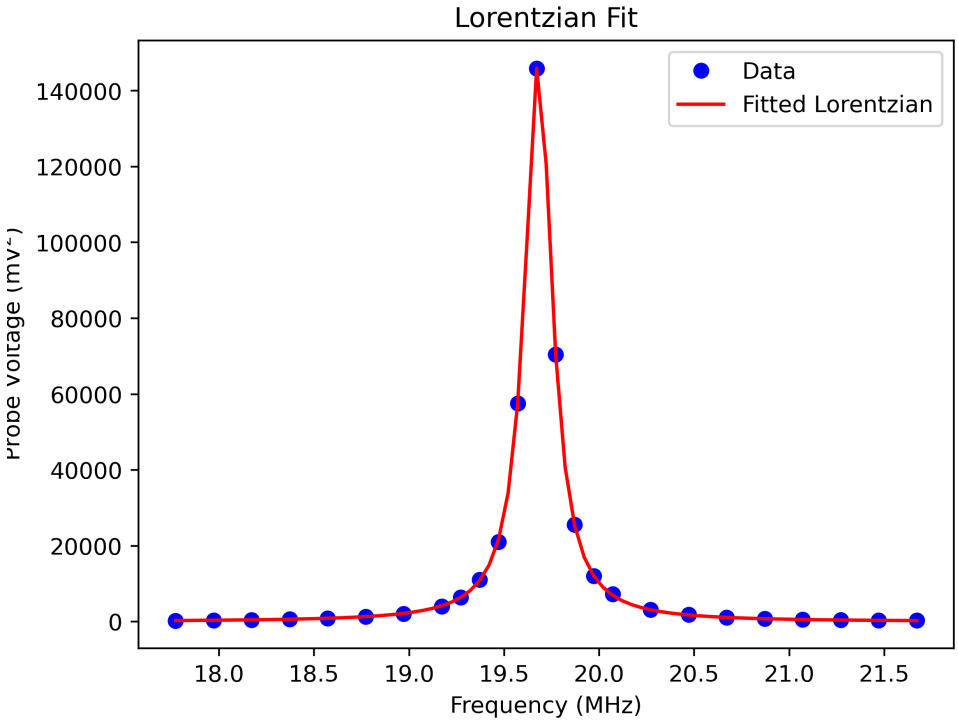


Fig. 6.15.: Transmission spectrum of the resonator integrated with the trap mounted inside the chamber before baking. Resonance frequency is ≈ 19.67 MHZ and Q is ≈ 114

but almost no increase in the Q factor (figure 6.15).

6.4.2 Filter circuits

Neighboring compensation and ground electrodes act as an antenna; they pick up the voltage applied to the trap and re-radiate in off phase. It will lead to excess micromotion. In order to discharge the pick-up voltage or minimize its effect, all the ground or DC electrodes are capacitively grounded using a parallel combination of 1 pF and 0.1 pF. It will allow us to provide DC bias to these electrodes and ground the pick-up voltage simultaneously. An R-C filter (100KΩ and 100 nF) followed by a Pi filter(100 nF and 22 μH (Coil craft)) is put at the output of the DC sources, as shown in figure 6.16, to filter the noise of DC output. It is used to provide DC bias to compensation and ground electrodes. It provides ≈ 70 dB voltage attenuation in the range of our interest. The transmission spectrum of the RC and Pi filter combination is simulated by Keerthipriya S from Electrical Engineering Group (EEG), RRI. All the capacitors used above have a very low effective series resistance in the range of our interest and are rated for the applied voltages. Another critical issue is the grounding of the chamber and all other components with respect to the ground of the RF source. Although there is a common ground for all the instruments and the optical table in the lab, it is still

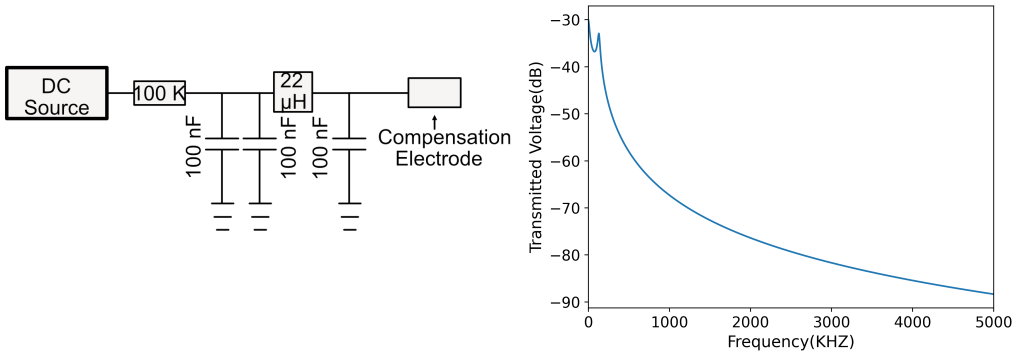


Fig. 6.16.: (a) Schematic showing RC and Pi filters used to filter the noise of DC output and their position in the setup. (b) Transmission spectrum of the filter.

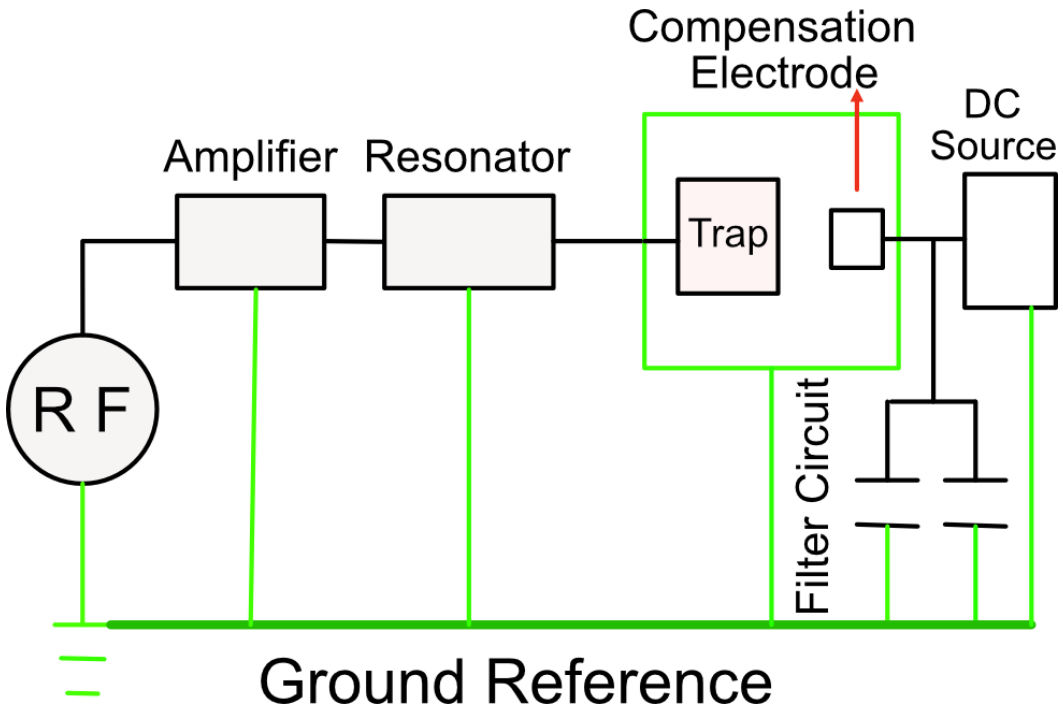


Fig. 6.17.: Schematic diagram showing the grounding arrangement of the system

insufficient when a high-voltage RF is applied to the trap. Earlier, when the chamber and the filter circuits were grounded with respect to the optical table, there was a high pick-up voltage on compensation and ground electrodes up to 10 V peak-peak. To resolve this, a ground wire is directly connected to the ground of the RF amplifier. The chamber was grounded by connecting a wire from the amplifier ground and the filter circuits were grounded with respect to the chamber. The schematic diagram showing the grounding arrangement of the system is shown in figure 6.17.

6.5 Laser and Detection System

6.5.1 Laser System

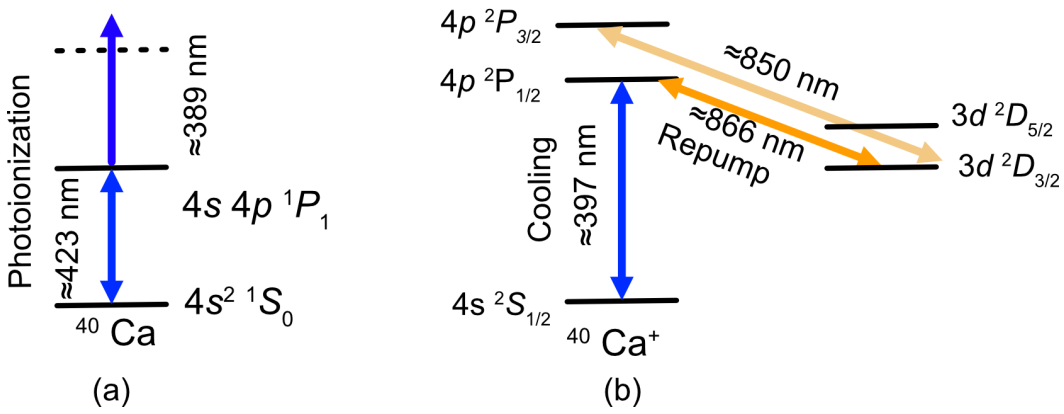


Fig. 6.18.: Relevant energy levels and corresponding transition wavelengths of Ca and Ca^+

We have used a two-photon ionization scheme to create calcium ions at the trap center. The first photon addresses $4s^2\ {}^1S_0 \rightarrow 4s4p\ {}^1P_1$ transition, and the second photon takes the electron from the excited state to the continuum. The first photon is derived from the Toptica DL Pro laser, and any source below 389 nm is sufficient for the second photon. In our case, we are using fiber-coupled LED, 365 nm, from Thorlabs, model no: MF365FP1. For cooling of calcium ions, $4^2S_{1/2} \rightarrow 4^2P_{1/2}$ transition is used. This is an electric dipole transition, and the wavelength corresponding to this transition is $\approx$ 397 nm. The excited state decays to the ground state and $3^2D_{3/2}$. A repump laser at ≈866 nm is used to bring the ions back into the cooling cycle. The repump laser addresses $3^2D_{3/2} \rightarrow 4^2P_{1/2}$. The cooling and repump lasers are derived from Toptica DL Pro and Toptica DL 100 lasers, respectively. Quantum jump signal is used to detect the number of trapped ions. A home-built ECDL at ≈850 nm addresses $3^2D_{3/2} \rightarrow 4^2P_{1/2}$ transition and the excited state decays back to $3^2D_{3/2}$ and $3^2D_{5/2}$. No laser beam is used to address the second state, and the lower-lying states are connected by quadrupole transition. Hence, the trapped ions go dark for a long time, and the signal drops in steps depending on the number of trapped ions. Relevant transitions for ionization of calcium atoms and cooling, repump, and detection of calcium ions are shown in figure 6.18. All these lasers are referenced using a wavemeter, WSU-8. A more precise value for the relevant transition is mentioned in Muller *et al.* [199]. We have followed the frequency data for all relevant transitions mentioned in Muller *et al.* [199] to set initial frequency values on the wavemeter throughout the experiments.

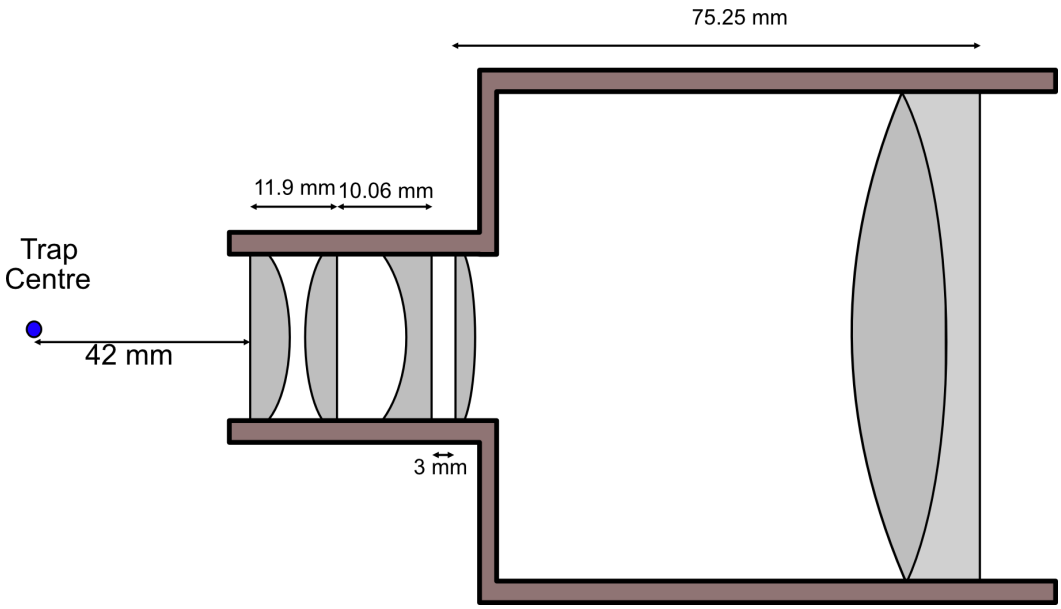


Fig. 6.19.: Schematic diagram of the optics assembly used to collect fluorescence from the trapped ions. The focal length of the lenses from left to right is 60 mm, 75 mm, -50 mm, 100 mm and 1000 mm.

6.5.2 Detection System

An imaging system is designed by Akhil V, a doctoral student working on the same project at RRI, using commercially available lenses for fluorescence collection from the trapped ions. The working distance of the lens system is 42 mm, magnification 22, and numerical aperture 0.13. A schematic diagram of the imaging system is shown in figure 6.19. We can use PMT and EMCCD simultaneously to detect the trapped ions or use one of them at a time. To use both the detectors simultaneously, we place a 70 : 30 beamsplitter at the end of the imaging system. A single photon detector, model n0: H10682-210, is used for the photon signal detection coming from the trapped ions and an Andor iXon 897 EMCCD is used for imaging it.

6.6 Initial Test

We were working for the first time on loading an ion trap from an atomic beam and cooling it using a laser beam. The drive voltage and frequency of the system were also very high. It requires a lot of care and testing to ensure that the assembly, electrical connections and other parameters are fine. To be sure that the atomic beam is shooting in the right direction, electrical connections are right, and the trap is working, we tested the loading of the trap at high vacuum, $\approx 10^{-8}$ mbar and recorded the critical parameters like resonant frequency, pick up voltage on compensation electrodes. It guides us in figuring out any change in the electrical connection inside the chamber after baking.

The initial test is performed in the following steps:

- Applying RF voltage and checking pick-up voltage on other electrodes will ensure that all the electrical connections are fine. If all connections are proper, all compensation electrodes will pick up some voltage. If the pick-up voltage changes with time or is dependent on the connections of other electrodes, either the grounding is improper or the connection is loose.
- Check the fluorescence from the atomic beam before and after the trap center to ensure that the beam passes through the center of the trap. It also gives a check that the oven is working. The fluorescence signal can be observed manually using a mobile phone camera.
- Align the cooling, repump, and ionization beam such that it passes through the trap center. Keep the first ionization beam, here 423 nm, perpendicular to the atomic beam. It will help to load selective isotopes. The most important benefit is that there will be no Doppler effect for the perpendicular beam, and a fixed detuning of the 423 nm laser beam will be sufficient for all oven currents.
- Install the imaging system with the help of any ordinary camera such that it is looking at the trap center. Fix the single photon PMT at the end of the imaging system with a spectral filter on its front.
- Switch on all the lasers, and keep detuning the cooling laser beam around 400 - 600 MHZ on the red side of the transition; the repump laser will be close to its transition, 100 - 200 MHZ detuned on the red side of the resonance. Apply RF voltage to the trap, monitor it using the probe and set the voltage such that the q_z is around 0.2.
- Try to check the PMT signal. If you do not observe any change in signal after switching on and off the trap, start tweaking the alignment of the beams and imaging system. The parameter to tweak in the imaging system is its focus, and it should be translated in all three directions. All the laser beams should overlap at the center of the trap, which can be manually changed to see the change in fluorescence. Starting from the crude alignment, it can take up to a few hours to a day to observe the signal.

An image of the experimental setup, with helical resonator and RF amplifier connected in position, PCB connecting compensation electrodes, and laser beam, is shown in figure 6.21. The signal from a trapped cloud at a high vacuum is shown in figure 6.20. After the baking process is completed, as mentioned in the earlier section of this chapter, we followed the same method mentioned in this section to observe the ion loading signal. Details will be mentioned in the next chapter.

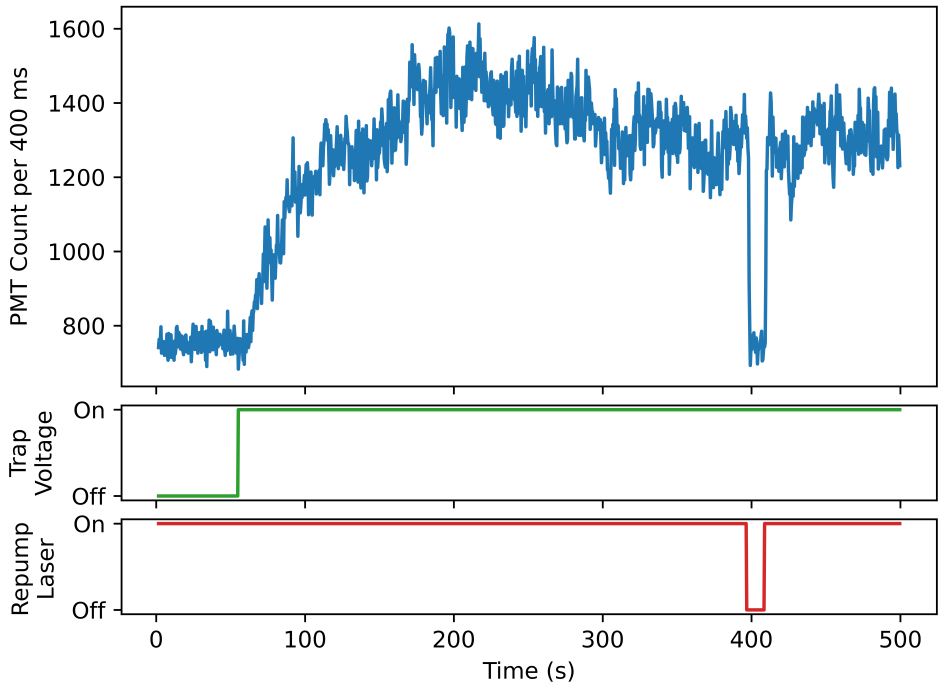


Fig. 6.20.: Signal observed on PMT from trapped ion cloud. The Change in signal with the trap voltage and repump laser status confirms that the signal is real.

6.7 Conclusion

In this chapter, we have discussed the experimental setup's planning, implementation, and initial results. Although this system is working according to the initial planning, there are some limitations and shortcomings that can be easily addressed in the next version without any practical difficulties. I will discuss them one by one by one and suggest some alternatives. The chamber in this setup is not the most suitable for achieving the best vacuum and optical access for imaging ions and sending beams. All the pumps are connected using the CF16 ports, which reduces the effective pumping speed. The position of the first lens used for imaging the trapped ion is 42 mm away from the trap center, and it can hardly be reduced further in this setup. All the optical windows used for collecting or sending light are not anti-reflection (AR) coated in the range of desired wavelength. The Q factor of the helical resonator used in this system is ≈ 115. The probe circuit is changing the capacitance of the system, ideally it should not. Customization of the vacuum chamber can easily solve the first three issues. These windows were ordered with the overall goal of the thesis in mind, but if somebody wants to use them for precision spectroscopy, they can easily get AR-coated windows. The helical resonator can be coated with gold to reduce resistance and increase the Q factor. The miniature and compact circuit board has already been ordered to reduce the

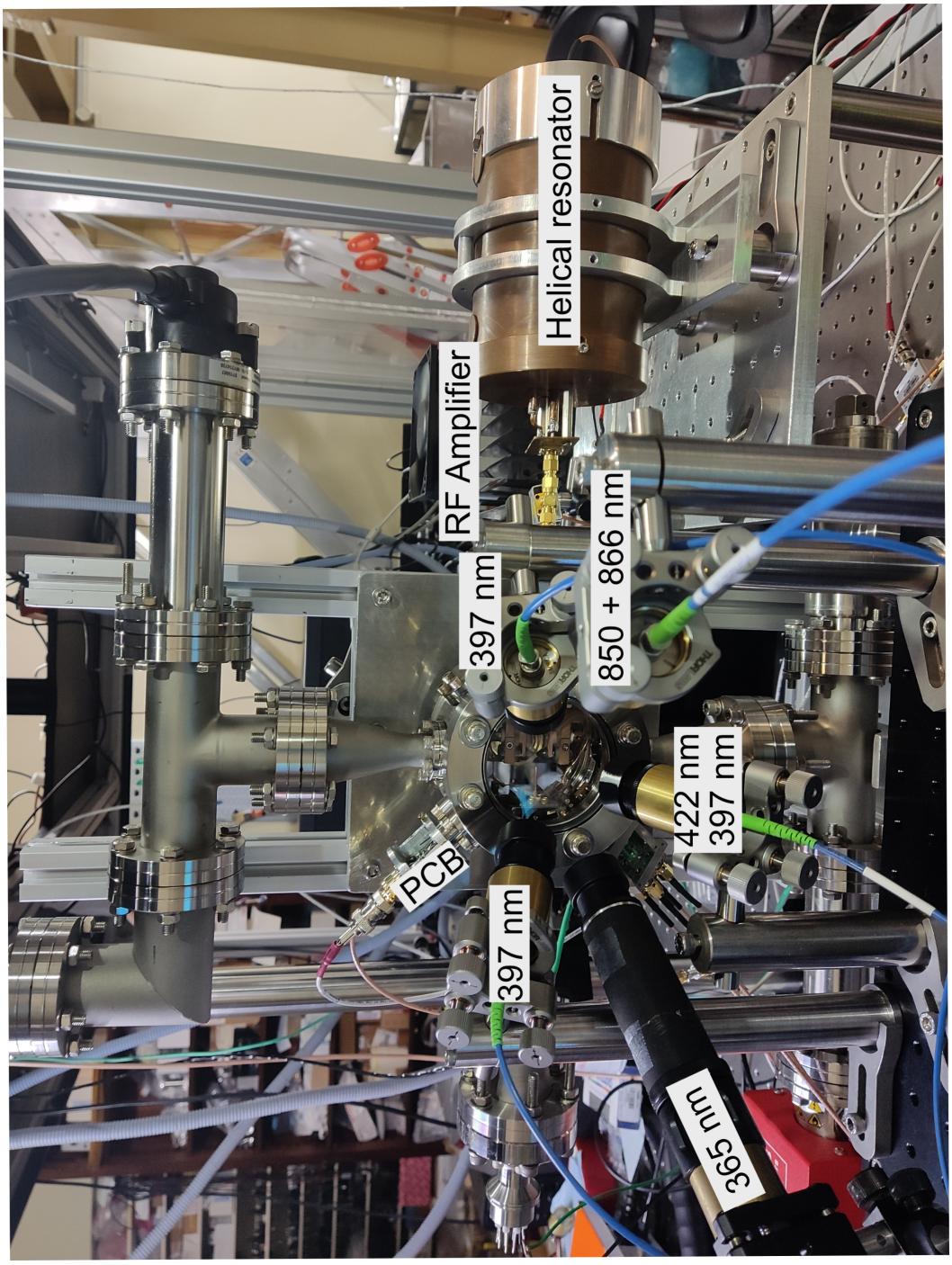


Fig. 6.21.: Functioning experimental setup.

effect of the probe circuit on the system. Due to the delay in delivery, it has not been integrated into the system.

Despite the above-mentioned limitations, this setup is suitable for precision spectroscopy, understanding and exploring its basics, and a wide variety of basic physics problems.

7 Trap Characterization and Initial Experiments

7.1 Introduction

In the previous two chapters, we have looked into the trap design and assembly process in detail. Our next task is to characterize the trap parameters against the designed values.

7.2 Trap Characterization

7.2.1 Trap Loading

After completion of the baking process, we follow the procedures mentioned in section 6.6 of chapter 6 to ensure that all the electrical connections are fine. We then align the cooling, repump, and ionization beams and set up the detection system. The cooling and repump beams are focused at the trap center to reduce scattering from the trap electrodes. $1/e^2$ diameter of the focused beam is $\approx 40\mu$m, which is measured using a beam profiler. The beam size is measured outside the vacuum chamber at an approximate distance corresponding to the experimental situation. A 70 : 30 beam splitter is placed at the end of the imaging system to split the collected fluorescence to PMT and camera. First, we load an ion cloud and image it on the EMCCD camera. The cooling beam is detuned by -250 to -350 MHz from the resonant transition to load an ion cloud [200], and the repump laser is detuned by less than -100 MHz from the transition. The trap voltage amplitude is set around 250 V. To observe the first fluorescence signal, we tweak the cooling and repump beams and imaging system to focus it at the trap's center. Once we observed a faint fluorescence signal from the trapped cloud on PMT, optimizing the fluorescence count from the ion cloud took an hour. Figure 7.1 shows one of the initially loaded cloud images.

Our next task is to control the loading of ions and detect the number of loaded ions. For controlled loading of ions, the oven current is set to 4.1 A, power in the 422

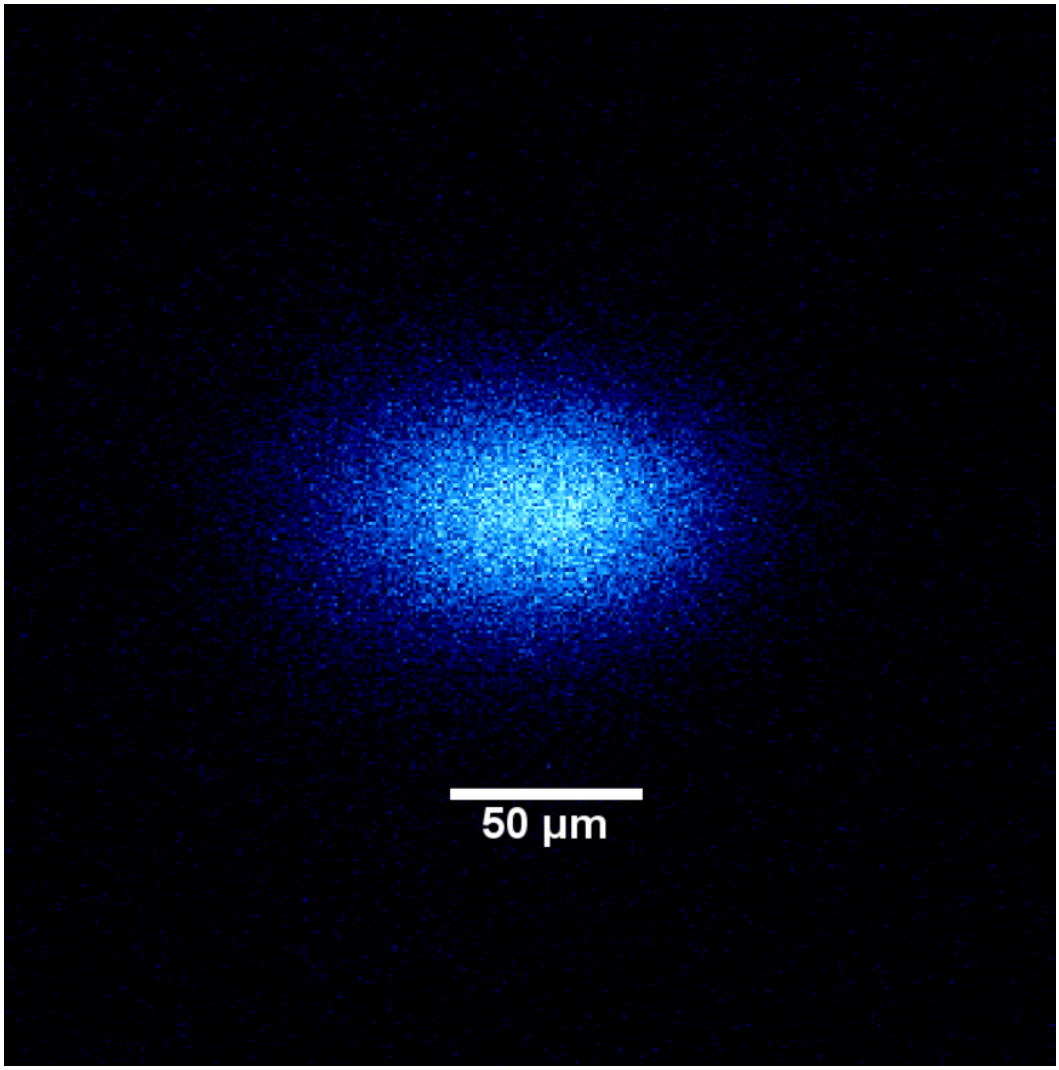


Fig. 7.1.: False colour image of the ion clouded loaded in the trap. The cloud shape is elliptical because the trap is stiffer in $z-$ direction compared to the x and y directions, $\omega_z \approx 2\omega_x$.

nm laser beam is reduced to 80 μW or even lower, cooling laser, at ∼397 nm, is detuned approximately −60 MHz from the resonance, the repump laser, at ∼866 nm is on the resonance or ≈ −10 MHz from the resonance and power in the ionisation LED is < 15 μW. All the lasers are locked using a WSU-8 wavemeter. The wavemeter is calibrated using a reference laser having wavelength 852.356686 nm in vacuum. The reference laser is locked on $F(4) \rightarrow F^{'}(4,5)$ crossover of D_2 transition using saturation absorption spectroscopy on a cesium vapour cell. Reference data for all the transitions are taken from Muller *et al.* [199]. Loading of the first ion takes 3 minutes on average at 4.1 A oven current because the oven takes time to heat from room temperature. Subsequent ions get loaded much faster with intervals of a few seconds. This allows us to precisely control the number of loaded ions in the trap by switching off the ionization beam at specific times. Control over the number of loaded ions is crucial for future experiments. For every loaded ion in the trap, we observe a jump in the fluorescence signal observed

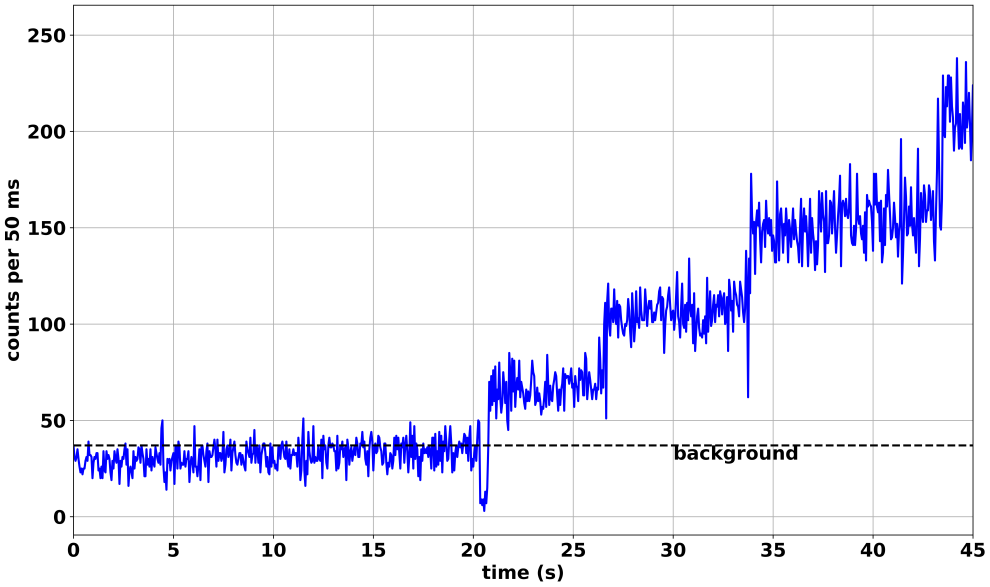


Fig. 7.2.: Ion loading signal observed on PMT. This data is taken at 4.1 A oven current. Initially the fluorescence signal is at the background level. The fluorescence signal increases after loading of every ion in the trap. Wait time to load the first ion is not shown in the image.

on the PMT. PMT signal for multiple ion loading cases is shown in figure 7.2. To reduce the waiting for ion loading after switching on the oven's current, we keep the oven at 2 A after loading ions.

7.2.2 Quantum Jumps

During interaction with light, an atom undergoes instantaneous changes of its internal state upon absorption or emission of a photon. This is known as quantum jumps [105–107, 201, 202]. Every transition after absorption and emission of a photon is a quantum jump but it is very hard to observe them in the case of short lifetime states ($\sim$ ns). It is easy to observe the jumps in the case of transition to metastable states. Quantum jump signal can be used to detect the number of trapped ions. Cooling, repump and other relevant transitions are shown in figure 7.3. In the regular cases, the 397 nm and 866 nm beams continuously addresses the trapped ions. The 397 nm beam drives $4S_{1/2} \rightarrow 4P_{1/2}$ transition. It decays back into $4S_{1/2}$ and $3D_{3/2}$ with the branching ratio of $\sim 15:1$. The 866 nm laser drives $3D_{3/2} \rightarrow P_{1/2}$ transition. Hence, we observe a continuous fluorescence on the PMT, and the ion doesn't go dark.

To observe the phenomenon of quantum jumps, we switch on another beam at 850 nm; it couples $3D_{3/2} \rightarrow 4P_{3/2}$. The excited state decays back to $4S_{1/2}$ and $3D_{5/2}$ states with the branching ratio of $18:1$. $3D_{5/2}$ is a metastable state having mean life time ≈ 1.16 seconds [203, 204]. So, in the case of a single ion, the PMT signal goes to the

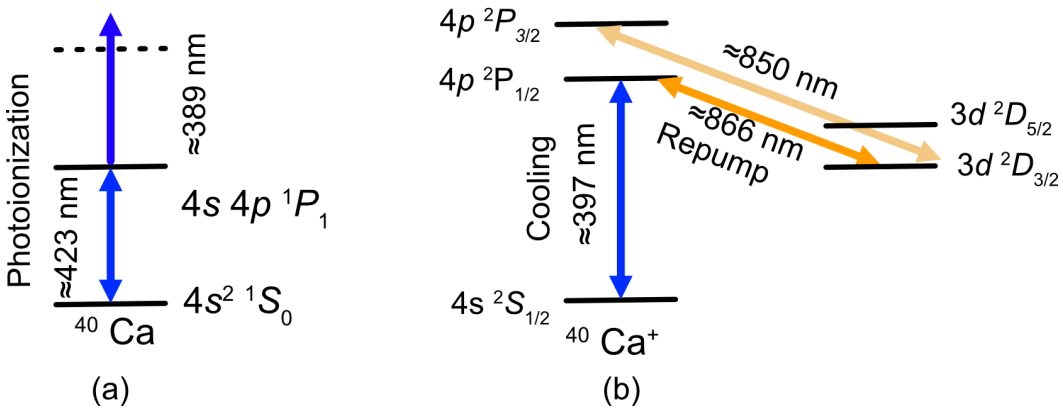


Fig. 7.3.: Energy levels of $^{40}Ca^{+}$ showing cooling transition, 397 nm, repump transition, 866 nm, and 850 nm transition used to observe quantum jumps.

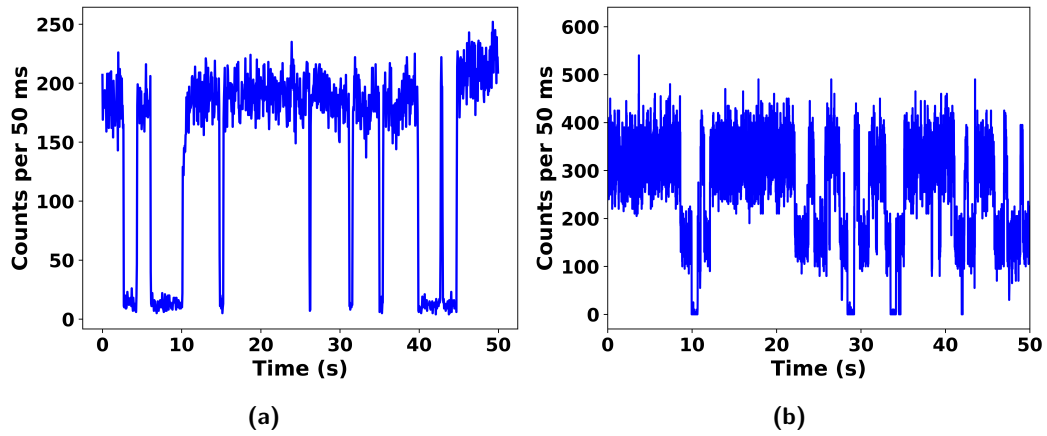


Fig. 7.4.: (a) Quantum jumps signal for single ion. When the electron is shelved into $3D_{5/2}$ metastable stable, PMT fluorescence goes to the background level. (b) When one ion goes to metastable $3D_{5/2}$, the fluorescence signal decreases to half, and when both go to $3D_{5/2}$, the fluorescence signal drops to the background level. The number of steps in the fluorescence signal equals the number of trapped ions.

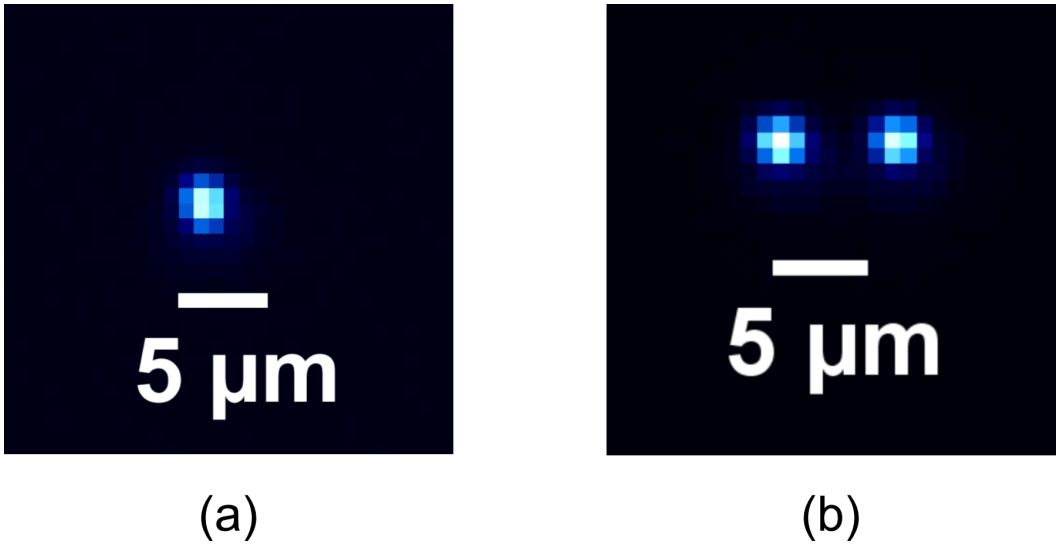


Fig. 7.5.: (a) Image of a single loaded and cooled ion in the trap (b) Image of two loaded and cooled ions in the trap. These ions are loaded at 4.1 A oven current.

background level and returns to the previous level after it spontaneously decays to $4S_{1/2}$ state. Depending on the number of trapped ions, we observe steps in the fluorescence signal. We keep the intensity of the 850 nm beam very low so as not to saturate the transition. In our case, the intensity of 850 nm is 4 nW. Quantum jump for 1 and 2 ions are shown in figure 7.4. Image of control loaded 1 and 2 ions observed on EMCCD camera is shown in figure 7.5.

7.2.3 Determination of Quadrupole coefficient ($a_{2,0}$)

The experimental determination of $a_{2,0}$ is essential to assess how close our trap geometry is to the designed parameters. If we know the secular frequency, rf, and dc voltages applied on the trap, using equation 2.30 and equation 5.4 $a_{2,0}$ coefficient can be determined. To determine the voltage applied to the trap, we added a probe circuit parallel to the trap as discussed in section 6.4 of chapter 6. dc voltage can be directly applied to both the end caps, or it can added directly after the helical resonator using RF chokes. We have both options for dc voltage addition in our system, but we mostly use the second option to provide dc voltage to the trap. To find the secular frequency of the trapped ions at a given trap configuration, we apply a small voltage on one of the outer electrodes and scan the frequency of the applied voltage around the theoretical secular frequency. Very close to the secular frequency, the ion cloud starts gaining energy, and its fluorescence decreases as shown in figure 7.6. This method is similar to forced oscillation [143], where energy gain is maximum when the drive frequency matches the system's natural frequency. Another method is parametric excitation [143], where we modulate one of the system's parameters, which is not discussed here.

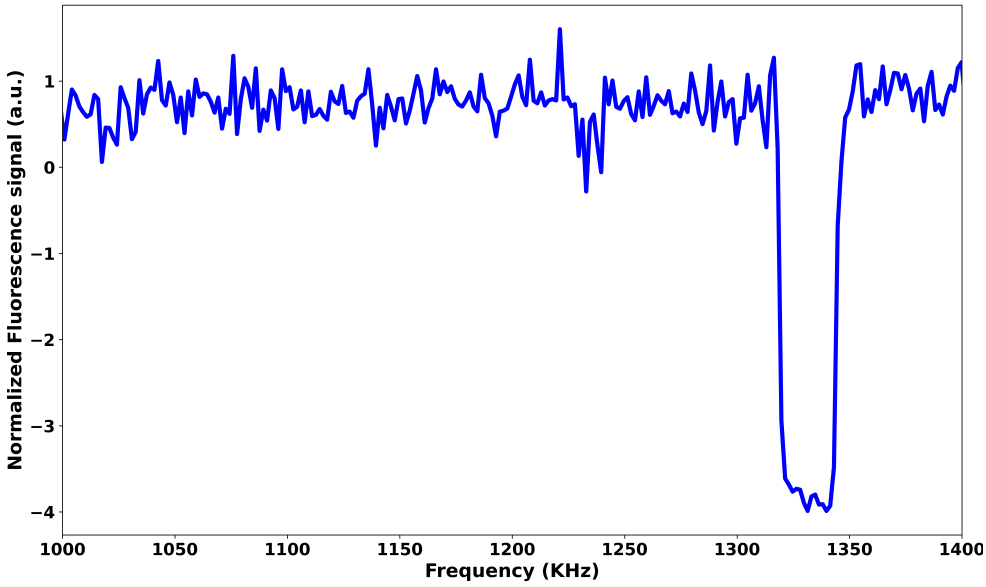


Fig. 7.6.: Dip observed in the fluorescence signal of ion cloud during forced oscillation. Trap drive voltage is 300 V and dc offset is −5 V.

We use the forced oscillation method to determine the secular frequency at different trap voltages. The resonant trap drive frequency, in this case, is 18.24 MHz. Tickle voltage is applied at upper end cap electrode. The fork used to mount the outer electrodes breaks the symmetry in the radial plane as discussed in section 5.2 of Chapter 5. We have introduced a parameter ϵ to quantify it. According to the simulation, ϵ is 0.001. So, we don't expect a clear symmetry breaking in x and y directions. A frequency scan of the tickle voltage is performed in forward and reverse direction to find the lower and upper limit of secular frequency, . Parameters for which secular frequency data is collected are mentioned in table 7.1. To fit the secular frequency versus trap parameters using equation 2.30, we have considered the all data point simultaneously to fit using global parameters $a_{2,0}$, ϵ. New variables are introduced to account for errors in the probe voltage measurement and dc voltage offset. The values of the fitted parameters are given in table 7.2 and the errors mentioned are standard deviation in the values of the fitted parameters. Experimental secular frequencies and best fit corresponding to a give q_z and different a_z are shown in figure 7.7.

The observed discrepancy between the simulated value and experimentally derived values of the quadrupole coefficient can be due to misalignment of the geometry and change in the position of the outer electrode with respect to the inner electrode. We attribute the observed change in the quadrupole coefficient to decrease in the distance between the tips of the outer electrode and the inner electrodes. It is observed in the simulations that this decrease in the distance increases the quadrupole efficiency as well higher order terms [116].

Table 7.1.: Parameters for secular frequency experimental data. According to our simulation, difference between secular frequency in x and y direction will be very small, so the parameters for forced oscillation are same in x and y directions are same.

	V_{DC} (V)	U_{mod} (V)	V_{probe} (mV)	Scan Range	Scan Time (S)
x/z	-1	10/4.5	200,250,300	0.5-0.9/0.8-2 MHz	30
x/z	0	10/5	200,250,300	0.4-0.9/1-2 MHz	30
x/z	1	10/5	200,250,300	0.4-0.8/1-2 MHz	30
z	-5	5	200,250,300	0.5-1.5 MHz	30

Table 7.2.: Fitted parameters for forced oscillation case.

$a_{2,0}$	ϵ	DC offset error (V)	probe voltage error (%)
0.319 ± 0.015	0.002 ± 0.016	0.321 ± 0.131	8

At this point, only the contribution of the quadrupole coefficient is experimentally determined. It is close to the one designed and agrees with the realized trap. We have to perform further experiments to determine the effect of surface roughness of the inner electrodes, patch potential, and the higher-order multipoles. We need to cool the ion further to determine the heating rate of the ion cooled to the motional ground state. As we shall see in the following few sections, the Doppler cooling limit and excess micromotion currently limit us from performing further diagnostics.

7.3 Excess Micromotion Compensation

Micromotion is an inherent property of the motion of the trapped ions in Paul trap. It can be only decreased by cooling the trapped ion but can not be completely eliminated. It affects the line shapes of the transition, trapping time, and introduces systematic shift in the frequency measurement. It will affect the accuracy of the measurement of the clocks based on trapped ions. If the null points of the rF field in the 3D Paul trap and stray field due to various sources do not coincide at a single point in the space, it introduces excess micromotion. The excess micromotion can not be reduced by cooling because it is driven motion. So, it is imperative to reduce the excess micromotion to use the trap for high accuracy measurements. To understand the excess micromotion and its effect, let us consider the Mathieu equation for a trapped charged particle in 1-dimension subjected to uniform static dc field, E_{dc}

$$\frac{d^2u}{dt^2} + [a + 2q\cos(\Omega t)]\frac{\Omega^2}{4}u = \frac{QE_{dc}}{m}. \tag{7.1}$$

Solution of equation 7.1 is following:

$$u(t) \cong [u_0 + u_1 \cos(\omega t + \phi_s)][1 + \frac{q}{2}\cos(\Omega t)], \tag{7.2}$$

where

$$u_0 \cong \frac{QE_{dc}}{m\omega^2}.$$

Kinetic energy averaged over an rf period will be

$$E_{KE} \cong \frac{1}{4}mu_1(\omega^2 + \frac{1}{8}q^2\Omega^2) + \frac{4}{m}\left(\frac{QqE_{dc}}{(2a+q^2)\Omega}\right)^2. \tag{7.3}$$

Excess micromotion can induce first and second order Doppler effect by altering the excitation spectrum of the atom. The electric field of the laser beam used to excite the atom is E_0, frequency, ω_l, phase, ϕ_l and wave vector, k. All the calculations are done for 1-dimension and can be extended to 3-dimensions. In the rest frame of the ion, the electric field of the laser becomes

$$\begin{aligned} E(t) &\cong Re\{E_0 \exp[iku - i\omega_l t + \phi_l]\} \\ &\cong Re\{E_0 \exp[ik(u_0 + u') - i\omega_l t + \phi_l]\}. \end{aligned} \tag{7.4}$$

It can be re-written as

$$E(t) = Re\{E_0 \exp[iku_0] \sum_{-\infty}^{\infty} J_n(\beta) \times \exp[-i\omega_l t + \phi_l + in(\Omega t + \pi/2)\}, \tag{7.5}$$

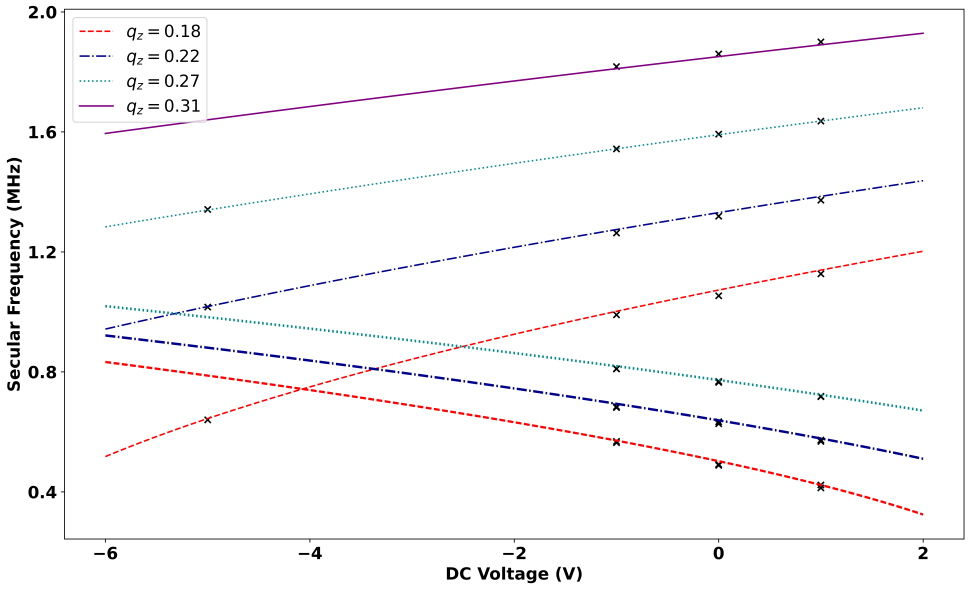


Fig. 7.7.: Secular frequency of the trap for different trap parameters measured by forced oscillation method. Discrete data points are experimentally obtained value and line are best fit for a given q_z value and various dc offsets. x and y directions are degenerate, so we get two very close points on the graph for secular frequencies along these directions.

where

$$ku^{'}(t) = \beta\cos(\Omega t)$$

Fourier transform of the equation 7.5 gives [205],

$$E(\omega) \propto J_0(\beta)\delta(\omega-\omega_l)+J_1\left(\delta(\omega-\omega_l+\Omega)\exp(-i\pi/2)+\delta(\omega-\omega_l-\Omega)\exp(-i\pi/2)\right). \tag{7.6}$$

Excess micromotion, inherent micromotion and secular motion induces 2nd order Doppler shift [206] given by,

$$\frac{\Delta\nu}{\nu} = -\frac{\langle K.E.\rangle}{mc^2}. \tag{7.7}$$

Here, $\langle K.E.\rangle$, is average kinetic energy. Using equation 7.3, equation 7.7 can be written as

$$\left(\frac{\Delta\nu}{\nu}\right) \approx -\frac{1}{mc^2}\frac{1}{4}mu_1(\omega^2+\frac{1}{8}q^2\Omega^2)+\frac{4}{m}\left(\frac{QqE_{dc}}{(2a+q^2)\Omega}\right)^2. \tag{7.8}$$

Excess micromotion also give gives 2nd-order Stark shift [206] due to non-vanishing mean square electric field at the position of the ion

$$\left(\frac{\Delta\nu}{\nu}\right) = \sigma\langle E^2\rangle, \tag{7.9}$$

where σ is differential static polarizability of the involved state and $\langle E^2\rangle$ is mean square electric field at the position of ion.

There are several methods to determine the excess micromotion and compensate for it. The use of different methods is dependent on the experimental condition like drive frequency of the trap, Ω, and linewidth, γ of the state used for the fluorescence detection. Complete details of these methods are discussed and compared for different conditions by Berkeland *et al.* [206] and Keller *et al.* [10]. In this thesis, the photon-correlation method is used to detect and compensate for excess micromotion. Here, we will discuss the theoretical basis of the method briefly, which is discussed in detail by Keller *et al.* [10]. This method uses the fact that driven motion has a fixed phase relation to the trap voltage. It gives rise to the correlation between fluorescence modulation due to excess micromotion and the trap drive voltage. It is recorded by measuring the time delay between the arrival of a photon and zero crossing of the RF voltage and when measured gives a histogram that has the following form

$$S = S_0 + \Delta S\cos(\Omega t-\phi), \tag{7.10}$$

where, S_0 is mean fluorescence, which depends on observation bin size. $\Delta S/S_0$ and ϕ gives amplitude and phase of micromotion. Once we know the amplitude and phase of micromotion, the magnitude of stray fields can be determined in different directions and can be compensated. To do this, we need to know the angle of the laser beam, which is sampling the excess micromotion, with respect to the trap axis. In our case, it is difficult

to determine the angle between the laser beam and the trap axis. So, we aligned two non parallel beams in the radial plane and a third beam samples axial as well as radial directions as shown in figure 6.21. The beam on the RF amplifier side is called resonator beam, the beam on the oven side is called oven beam, and the beam carrying 422 nm and 397 nm light is called ionization beam. The resonator and the oven beam mostly samples the radial plane, while the ionization beam sample the radial as well as the axial plane. We try to minimize the amplitude of the photon correlation signal for each beam independently by manually changing the voltages on compensation electrodes. To acquire the correlation data, we use Swabian Instruments Time Tagger 20. It can directly generate the correlation signal using the start and stop signals. The start signal is provided by the photon counter and the stop signal is generated using a Schmidt trigger. The input for the Schmidt trigger is the probe voltage. Our Schmidt trigger is not generating a stop pulse at either negative or positive zero crossing but it is generating a stop signal around maximum value of the probe voltage. If we want to find a correlation, Schmidt trigger should generate the stop signal at a fixed phase in all rf cycles. First, we measure the photon-correlation signal for each beam to get the modulation amplitude, $\Delta S/S_0$. The plot for the uncompensated correlation signal is shown in figure 7.8. The laser and trap parameters for data acquisition for the uncompensated case is mentioned in table 7.3. The first attempt at compensation is tried at the same laser and trap parameters as mentioned in table 7.3, and the plot for photon correlation signal is shown in figure 7.9.

For our kind of condition where trap drive frequency is very close to the linewidth, γ, of the state used for fluorescence detection, $\Delta S/S_0$ has better sensitivity around $\approx 1.4\gamma$ [10]. We next attempted to compensate the excess micromotion at detuning

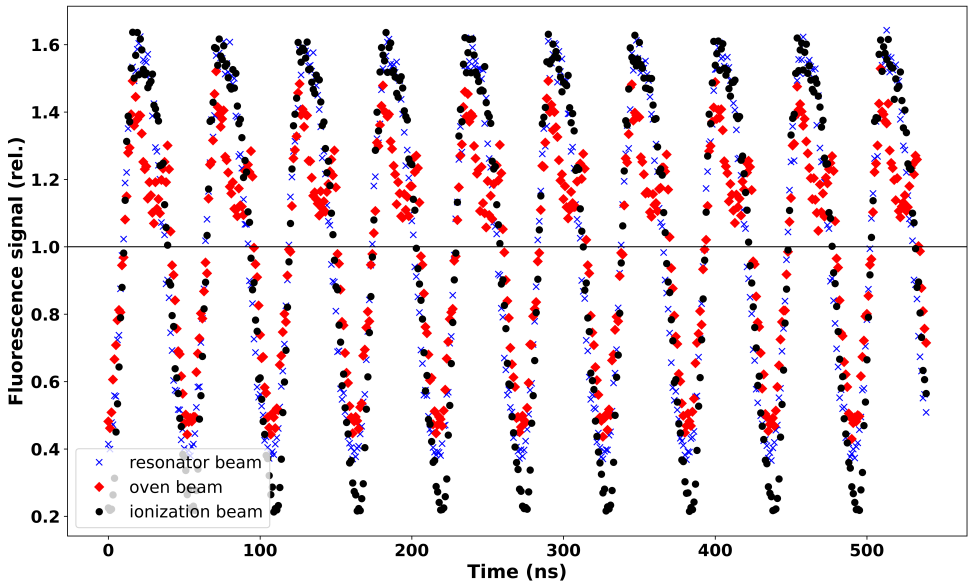


Fig. 7.8.: Photon correlation signal of an uncompensated ion.

Table 7.3.: Laser and trap parameters for correlation signal acquisition in uncompensated case.

Ω (MHz)	397 nm laser detuning (MHz)	Resonator beam power (μw)	Oven beam power (μw)	ionization beam power (μw)
$2\pi \times 18.26$	≈ -20	0.53	0.62	1.3

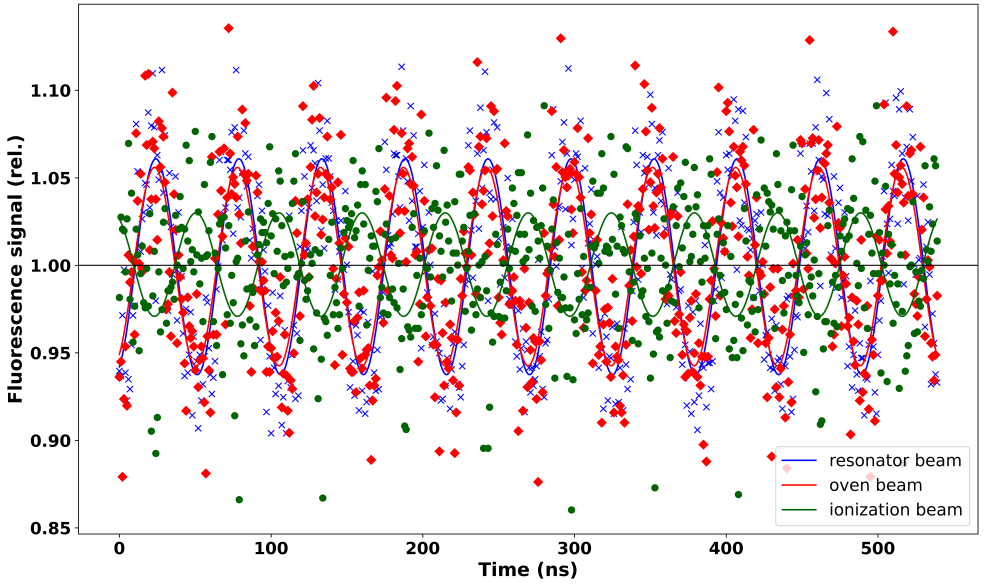


Fig. 7.9.: Photon correlation signal of a compensated ion. $\Delta S/S_0$ for resonator, oven and ionization beams are -.06,-0.06 and 0.03 respectively.

Table 7.4.: Compensation voltage on the different electrodes for the case shown in figure 7.10

oven beam	oven img	img resonator	bottom end cap
-5.35 V	55.2 V	-1.64 V	-0.17 V

of −30 MHz. Results of the compensation are shown in figure 7.10. Powers in the resonator, oven and ionization beams are 1.1, 2.2 and 1.5 μW respectively. Voltage on the compensation electrodes are mentioned in table 7.4 for the case shown in figure 7.10. All other compensation electrodes are grounded. It has been observed that the compensation voltages are varying over time. In particular instance, we have observed the correlation function in morning around 10:00 AM and it had visibly changed in the evening around 5:00 PM. We are looking into the possible reasons for deterioration of the compensation voltage with time. This compensation attempt is also preliminary in the sense that we are not actively stabilizing the power of the cooling laser used to collect fluorescence.

After compensating for the dc stray field at the trap center, we were able to trap the a single for more than 8 hours with cooling beams on. In case of absence of cooling beam, ion's hold time was ≈ 15 min as shown in figure 7.11

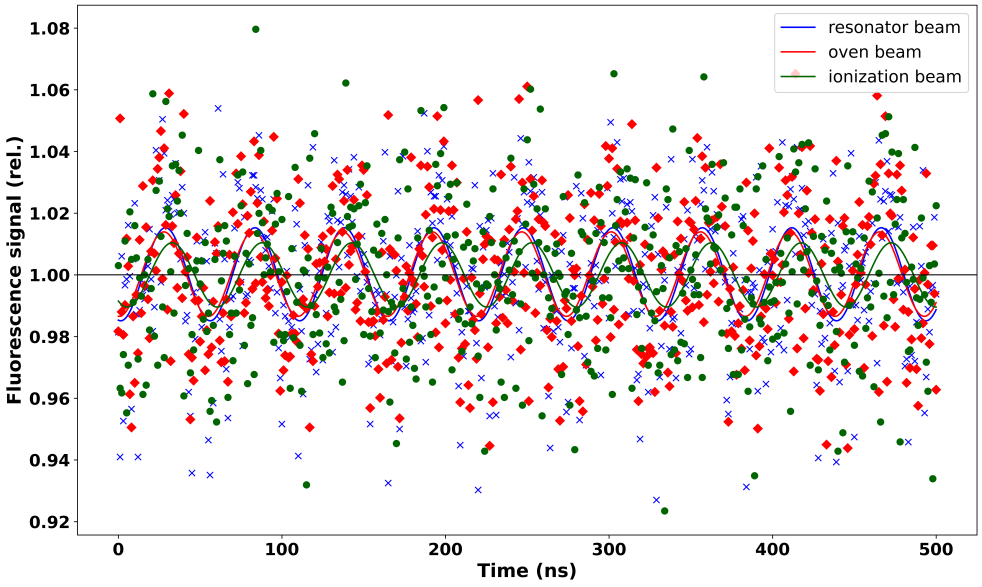


Fig. 7.10.: Photon correlation signal of a compensated ion. $\Delta S/S_0$ for resonator, oven and ionization beams are .015,0.014 and 0.01 respectively.

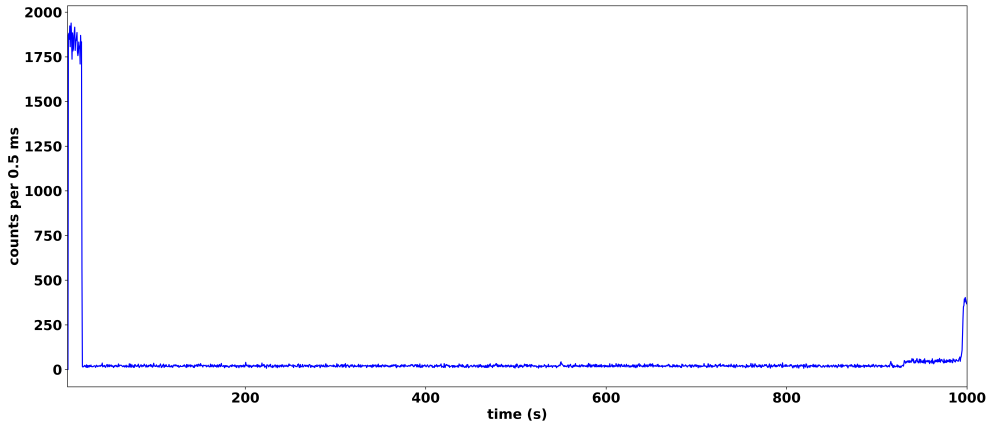


Fig. 7.11.: Ion hold time without cooling laser.

7.4 Temperature of a Single Ion and Trapping Life Time

Temperature of a trapped single ion can be determined using spectral broadening of the fluorescence observed from $S_{1/2}$ to $P_{1/2}$ transition [200]. Spectral signal depends on the number of atoms in the excited state in the steady state. The steady state population of the atoms in the excited state is determined by equilibrium between radiative excitation and relaxation processes like spontaneous emission, collisional relaxation. The solution of the optical Bloch equation [207] for a 2-level system in the

non-perturbative approach has the following form

$$N_e = \frac{N}{2}\left(\frac{\Omega_1^2}{\Delta^2 + \Omega_1^2 + \gamma^2}\right). \tag{7.11}$$

The above solution is for N atoms, where N_e is number of atoms in the excited state, Ω_1 is the Rabi frequency, γ is the natural linewidth of the excited state, and Δ is detuning of the laser driving the transition. Ω_1^2 is directly proportional to the intensity of the laser used to drive the transition. In the low intensity case, $\Omega_1^2 \ll (\Delta^2 + \gamma^2)$, lineshape of transition is Lorentzian with Full Width Half Maximum (FWHM) 2γ. At higher intensities, lineshape of the transition is still Lorentzian but FWHM changes to $2\sqrt{\gamma^2(1 + \Omega_1^2/\gamma^2)}$. It is called power broadening. So, if we experimentally determine the FWHM for different intensity of laser and plot the square of FWHM with respect to the power/intensity, we will get a straight line and intercept of the line on the y-axis will give the natural linewidth of the spectral line. According to the formalism if the atom has high temperature then lineshape will not be Lorentzian, so there is an implicit assumption that the atom is cold enough to not change the lineshape significantly. In this case, we are assuming that the contribution due to Doppler effect is accounted for in the modified Lorentzian lineshape and formula for relation between Lorentzian, Gaussian and Voigt lineshape can be used to determine the Gaussian linewidth, which has information on the temperature of the trapped ion. To the best of our understanding, the most precise formula for the lineshape relation [208] is the following:

$$f_V \approx 0.5346 f_L + \sqrt{0.2166 f_L^2 + f_G^2}, \tag{7.12}$$

where $f_V, f_L,$ and f_G are FWHM of Voigt, Lorentzian and Gaussian distribution. Powers for which data are taken are $0.22, 0.35, 0.78, 0.95, 1.32, 2, 3.35, 16.56, 23.4, 49, 65.3, 92, 128.5$ μW. The detuning versus fluorescence for all data is fitted to half Lorentzian shape to determine the FWHM. The plot for normalized fluorescence versus detuning for 0.22μW laser power is shown in figure 7.12. Finally the FWHM square versus laser power is fitted to find the intercept. For executing the fit, the fitted data points have assigned weight inversely proportional to power. This process reduces the effect of systematic shifts due to higher powers. The intercept on the γ'^2 axis is used to find the f_G, which is converted into ion's temperature using following relation

$$T = \frac{mc^2}{k_B}\left(\frac{FWHM}{\nu_0 2\sqrt{2\ln(2)}}\right)^2, \tag{7.13}$$

where m is the mass of the atom, c is the speed of light, k_B is Boltzmann's constant, ν_0 is resonant transition frequency. The fit and the data points for the FWHM square versus power is shown in figure 7.13 and the derived temperature of the ion is ≈ 34 mK.

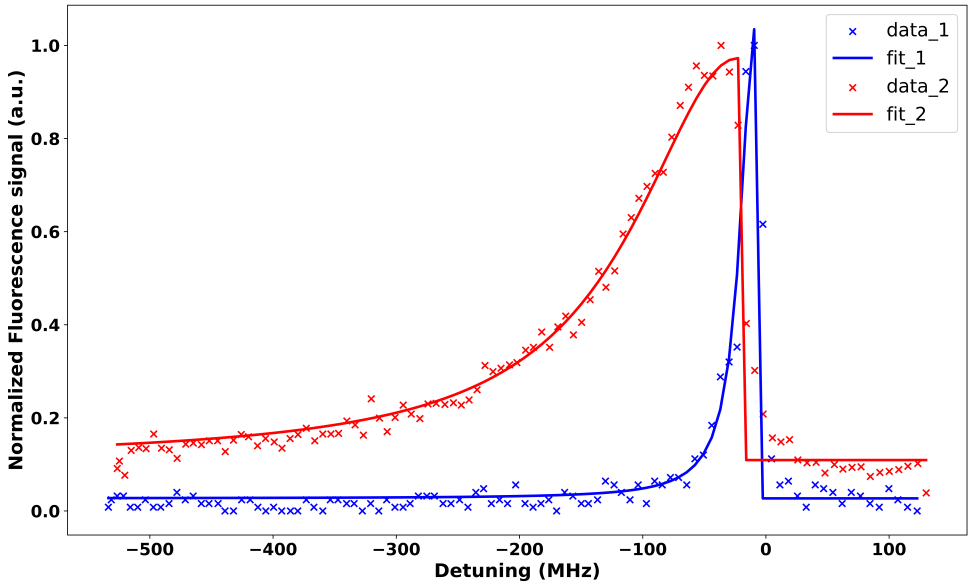


Fig. 7.12.: Normalized fluorescence rate versus laser detuning for a single trapped ion. Laser power for data$_1$ is 0.22μW and for the data$_2$ is 65.3 μW.

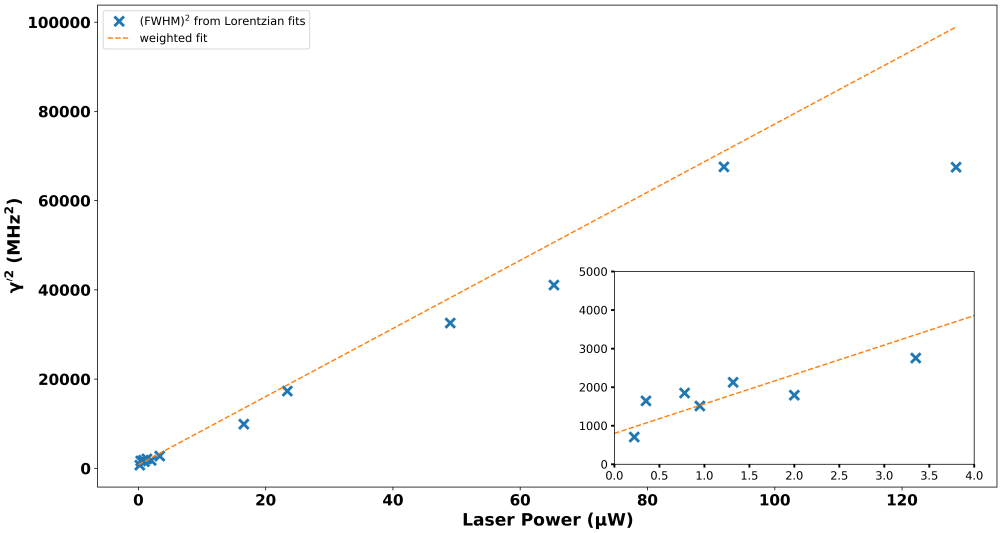


Fig. 7.13.: Weighted fit and data points for different laser powers. x-axis is scaled laser power because we measure the power outside the vacuum chamber. The value of intercept on the γ'^2 is ≈ 801.

7.5 Lifetime of Metastable State

The lifetime measurement of a metastable state is one of the precision measurements performed on a single trapped ion. It is determined by performing statistical analysis for the dark periods associated with the quantum jumps. The lifetime of a metastable state gets affected by laser frequencies close to the neighboring transitions from the metastable state, collision with background gas, and RF heating. Metastable

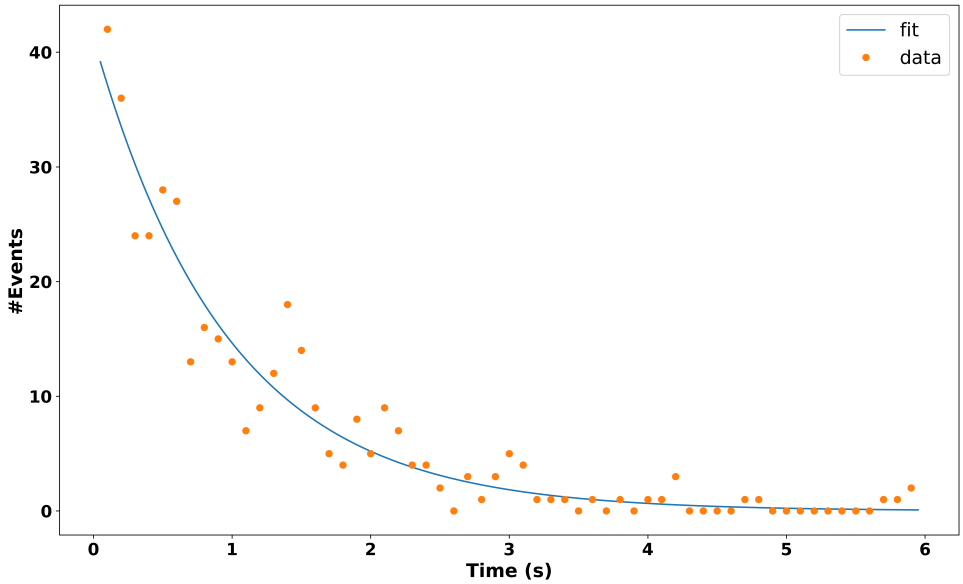


Fig. 7.14.: Fitted function and experimental data for lifetime determination of metastable state $D_{5/2}$.

Table 7.5.: Lifetime of $D_{5/2}$ state reported in previous experiments

	Knoop *et al.* [209]	Ritter *et al.* [210]	Block *et al.* [211]	Barton *et al.* [203]
Lifetime	994 ± 38 ms V	969 ± 21 ms	1100 ± 18 ms	1168 ± 7 ms

states are also important from the point of view of optical frequency standard. Lifetime measurement of the metastable state helps to identify and control the effects that may reduce the lifetime and contribute to the broadening of the clock transition. In the past, there are several experimental reports where the lifetime of $D_{5/2}$ state has been determined [203, 209–211], where the assessment of the systematic errors has improved with time. This is the reason why we quote lifetime of the $D_{5/2}$ to be ≈ 1.16 s. Experimentally determined lifetime by Knoop *et al.*, Ritter *et al.*, Block *et al.*, and Barton *et al.* is quoted in table 7.5. In our case, the lifetime measurement of a single trapped ion is a preliminary exercise without taking account of the systematic effects. Since we do not have the complete gauge of the systematic errors like change in lifetime due to RF heating, and level coupling due to 866nm and 850 nm lasers, this measurement is very preliminary.

Data acquisition: Initially, the 397nm and 866nm lasers are on for ion cooling. Energy diagram of $^{40}Ca^{+}$ is shown in figure 7.3. The 850nm laser is unblocked to observe quantum jumps. Initially, when only 397nm and 866nm lasers are on, ion decaying to the $D_{3/2}$ level is going to the $P_{1/2}$ level, and it is continuously in the cooling cycle. Once we unblock the 850nm laser, ion decaying to the $D_{3/2}$ level can go to the $P_{1/2}$ and the $P_{3/2}$. Ion going to the $P_{3/2}$ level can decay back to the $S_{1/2}$ and $D_{5/2}$. Once the ion decays

to the $D_{5/2}$, it is out of the cooling cycle and becomes dark. It decays to the ground state by spontaneous emission and comes back to the cooling cycle again. The probability of finding the ion in the $D_{5/2}$ state at time t is $\exp(-t/\tau)$. Ion's fluorescence statistics shown here is collected for 2 hours using a single photon PMT binned in intervals of 10 ms.

Data analysis: First, we need to set a threshold fluorescence value on the collected data to classify a bin as dark or bright. The threshold level is set to $s_{bright}/5$, where s_{bright} is the averaged fluorescence of the bright level. The threshold level is decided by looking at the raw data. There is a threshold on the number of continuous dark bins to classify it as a dark state, and it is 5. The whole data is binned in the histogram of bin size 50 ms. It is fitted using an exponential decay function, $F(t) = A\exp(-t/\tau)$. The fitted function and histogram data are shown in figure 7.14. The determined lifetime from the fitted function is 966 ± 60 ms. The error reported here is fitting error.

The lifetime numbers reported by us is in good agreement with Knoop *et al.* [209] and Ritter *et al.* [210]. In these measurements, they have accounted for some systematic effect. The agreement of the numbers reported by us without taking care of systematic effects shows that our trap is performing as per requirement. In this measurement, we are not blocking the 850nm laser once the ion goes to the dark state. The effect of the 866nm laser, collision with background gas and RF heating is not taken care of. We can extend this measurement for multiple ion case to figure out the effect of presence of another ion on quantum jumps statistics in a two ion system. The lifetime measurement experiment is still under process and will be reported in detail in the future.

7.6 RF Heating and Cloud to Coulomb Crystal Transition

For a single trapped ion, time dependent potential generates a time averaged conservative confining potential. This is not always true for more than one ion system in Paul traps. In the cloud phase, Coulomb interaction between the ions pumps energy into the ion cloud. This is known as RF heating. The mechanisms of energy pumping is similar to the one discussed in chapter 2 for the ion-atom system. It has been experimentally and numerically observed that for small ion clouds, RF heating increases with the trap voltage [30, 149, 212–214]. RF heating rate is negligible for ion crystals due to decoupling of micromotion and secular motion in a fully compensated trap [145, 213–215]. Understanding of RF heating and optimal laser cooling parameters for fast recrystallization are essential for the experiments where ion crystals are used for different operations and measurements.

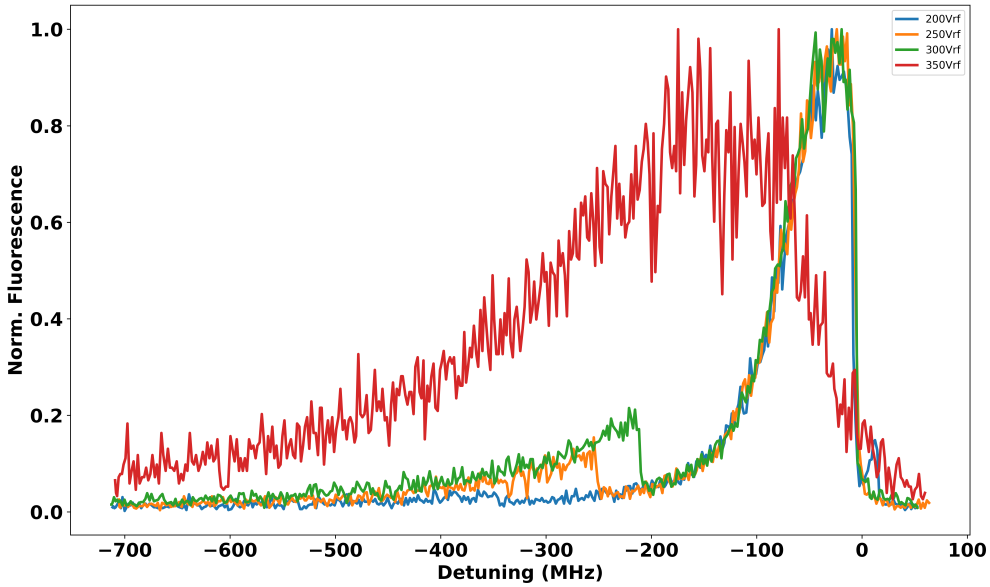


Fig. 7.15.: Cloud to crystal transition of 4 ions for different trapping voltages.

One component plasmas are characterized by the Coulomb parameter, Γ. It is defined as

$$\Gamma = \frac{Q^2}{4\pi\epsilon_0 a_{WS} k_B T}, \tag{7.14}$$

where a_{WS} is the Weigner-Seitz radius defined by $\left(\frac{4\pi}{3} n_0 a_{WS}^3\right) = 1$, n_0 is the particle number density and k_B is Boltzmann's constant. Γ is the ratio of the electrostatic energy of the neighboring charges to the thermal energy $k_B T$. It has been numerically established that $\Gamma \gg 174$ corresponds to crystalline phase [216, 217]. When the frequency of the cooling laser is swept from the red side of the transition to the resonance, a kink is observed in the fluorescence of the trapped ion cloud. The kink is characteristic of the transition to the crystal phase from the cloud. Cooling must overcome RF heating to achieve crystallization. The force due to cooling laser is proportional to $-\left(\frac{\delta\gamma}{\delta^2+\gamma^2}\vec{v}\right)$, where δ is the detuning of the cooling beam, and $\vec{v}$ is velocity of the ion. This expression is for the case when the ion's velocity is anti-parallel to the cooling beam's propagation direction. The cooling force is maximum at $\gamma/2$. It has been observed that as the trapping voltage increases, cloud to crystal transition point shifts towards the resonance frequency and beyond a certain trapping voltage, crystallization is never observed [30, 149]. We also observe a similar kind of feature in the phase transition point as the trapping voltage is increased. The cloud fluorescence signal with respect to the detuning of the cooling laser is shown in figure 7.15.

It has been predicted by Weiss *et al.* that the lifetime of metastable state during cloud to crystal transition follows power law, $\tau_m \sim (\kappa - \kappa_c)^{-\zeta}$, where τ_m is average lifetime of metastable cloud, κ is damping constant, κ_c is critical damping constant and exponent ζ depends on a and q parameters of the trap and independent of the number

of ions present in the system. In the future, we plan to perform experiments to verify the power law.

7.7 Observation of Ion Crystals

Since the observation of Coulomb crystals in the 3D Paul traps [30, 149], its application in studying different kinds of systems has increased rapidly. Apart from the quantum computation, simulation [19–22, 69–75] and precision spectroscopy [2–4, 76] ion crystals are ideal for study of non linear dynamics [218–221] due to non linear nature of the Coulomb interaction between the charged particles, topological defect formation and their dependence on the trap parameters, impurities [31, 222], statistical physics and thermodynamics like thermal diffusion of impurities, quantum heat transport, nano-friction etc. [31, 223–226].

Coulomb crystals have been studied extensively in the linear Paul trap [31, 223–227]. Still there are very few experiments [30, 149, 212] where crystal morphologies for multiple ions are studied in the 3D Paul traps. The 3D Paul traps are more fundamental in the sense that only a and q parameters are required to control the trap stiffness in all three directions, but in the linear Paul trap, three parameters are required, one in the axial direction and two in the radial direction. So the 3D Paul trap is the ideal system to study the effectiveness of pseudo potential derived in the chapter 2. Ursekar *et al.* [228] has numerically shown that the pseudo potential derived using the first-order approximation is not always valid. It fails to predict crystal morphologies for multiple ions and their transition points correctly in the $a-q$ space. Inadequacy of the first order pseudo potential has been first shown by Dantan *et al.* [229]. The work for derivation of improved pseudo potential for 3 and 4 ions is extended by Ursekar *et al.* [228] and predicted crystal morphologies and their transition points in $a-q$ space which has not been reported experimentally yet.

These crystal configurations provide an ideal platform to test our 3D Paul trap, verify the validity of improved pseudo potential approximation, and observe the predicted crystal morphology for 3 and 4 ions. In our case, at present, we can not go above $q_z > 0.4$ but still can observe the predicted morphology for $q_z < 0.4$.

Orientation of the crystal depends on the balance between the Coulomb forces acting between the ions and the force due to trapping field on the individual ions. In case of 2 ions, initially, ions will be aligned along the weakest axis in a line (rod geometry). In our case, $\omega_x \approx \omega_y$, so the ion will be aligned along a line in the radial plane as shown in figure 7.16a. Since we can image only $y = 0$ plane and ions can be oriented at any polar angle in the radial plane due to degeneracy, we are not able to resolve the

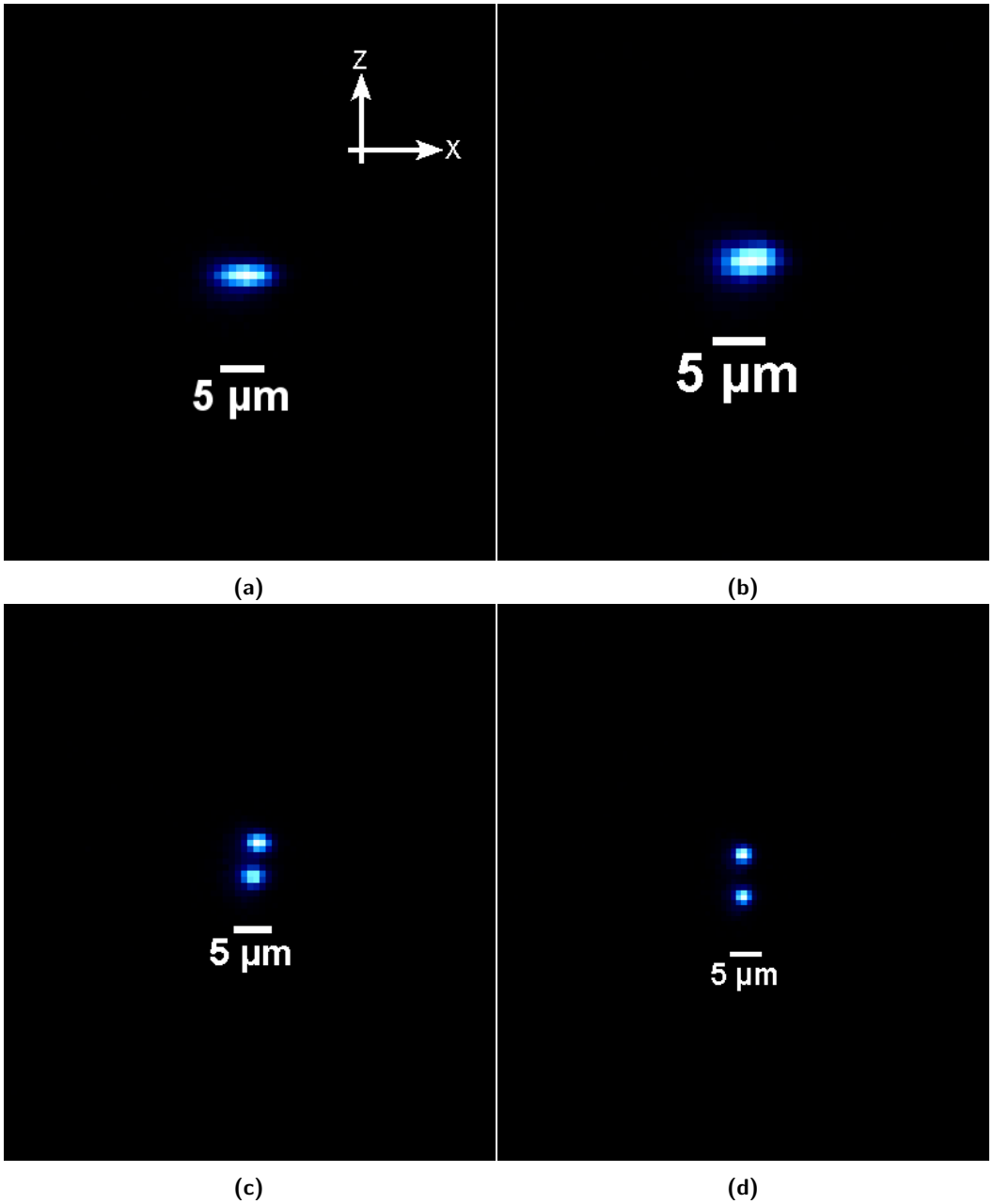


Fig. 7.16.: Image of 2 ion crystal, RF voltage applied to the trap is ≈ 310 V and the RF drive frequency is $2\pi \times 18.63$ MHz. (a) Rod configuration, ions are aligned along a line in the radial plane, dc offset is 0 V (b) pop out phase, dc offset is −9 V. (c) pop out configuration, dc offset is −10 V. (d) Rod phase, aligned along z−axis, dc offset is −13 V.

ions. Because of degeneracy and radiation force due to the cooling laser, they can be continuously rotating in the radial plane. As we start increasing the dc offset applied to trap in negative, radial axes will start becoming strong and the axial axis will start becoming weak. At a certain dc offset, one of the ions will pop out from the radial plane to the z-direction as shown in figure 7.16b and 7.16c. Further changing of the dc offset in the same direction will make the z-axis weakest and the ions will align along it in rod geometry (figure 7.16d). Nomenclature for the morphologies is taken from Ursekar *et*

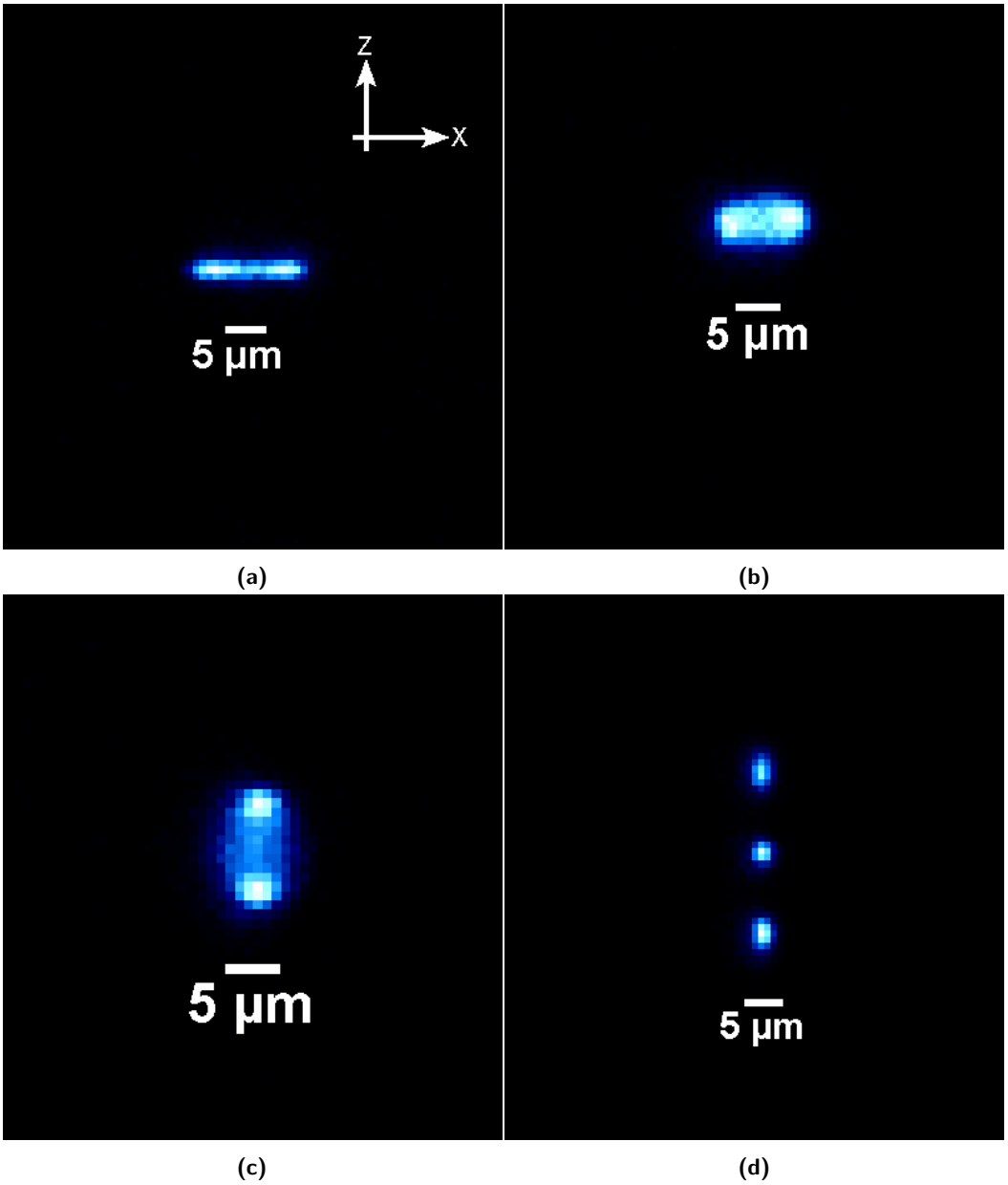


Fig. 7.17.: Image of 3 ion crystal, RF voltage applied to the trap is ≈ 250 V and the RF drive frequency is $2\pi \times 18.63$ MHz. (a) Rod configuration, ions are aligned along a line in the radial plane, dc offset is 0 V (b) planar configuration, dc offset is −6 V. (c) pop out phase, dc offset is −7 V. (d) Rod configuration, aligned along z−axis, dc voltage in this case is −12 V.

al. [228].

For the three ion crystal case, initially the ion is aligned along a line, rod configuration (figure 7.18a). As we start increasing the dc offset in negative direction, one ion pops out of the line but remains in radial plane as shown in figure 7.18b. Image of all three ions are not clear in this case but the spread of the ion image has decreased along x-axis but the spread is unchanged along the z-axis, it confirms that all three ions are in the plane. Further increase of the dc offset in the negative direction makes z-axis weaker

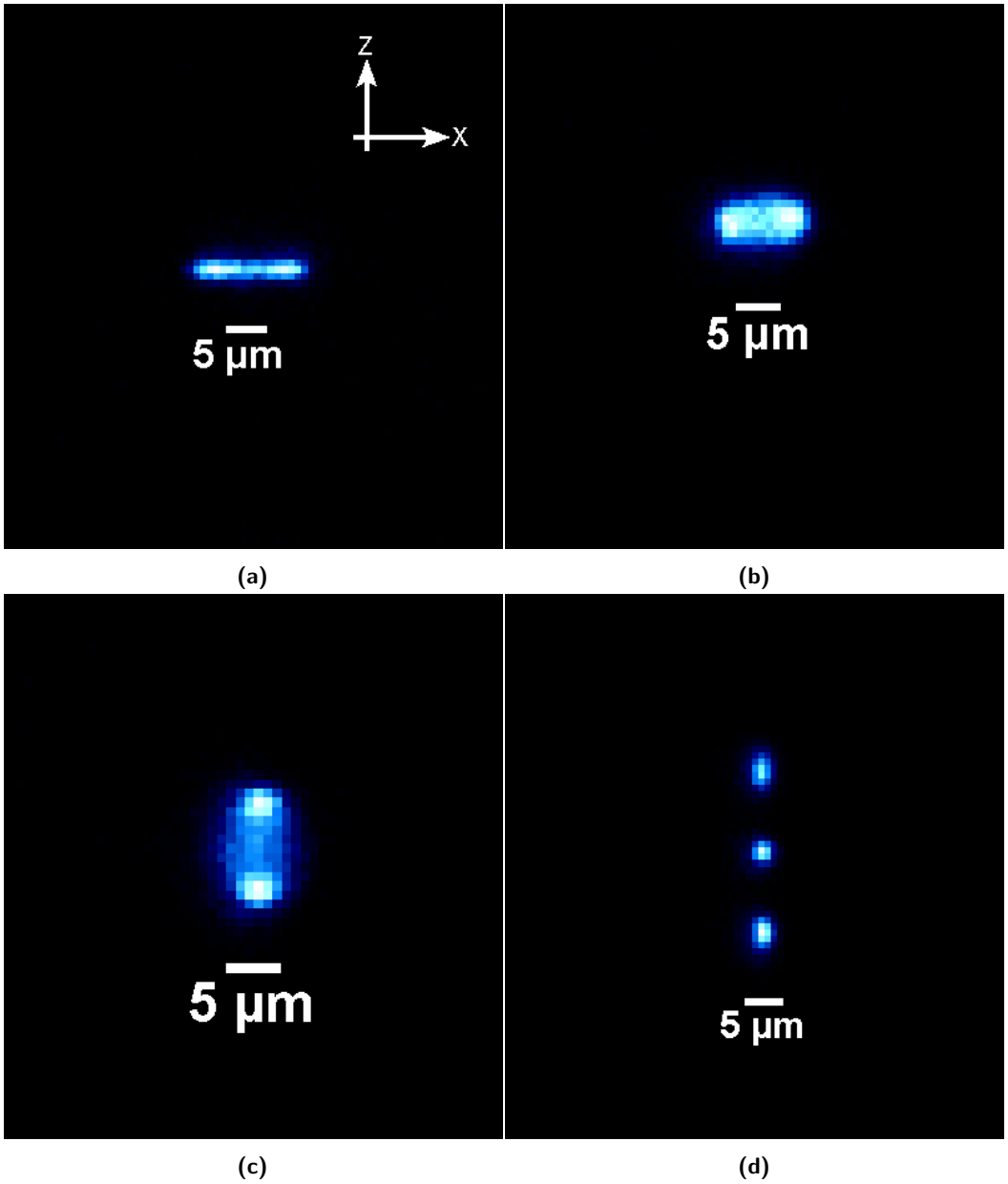


Fig. 7.18.: Image of 3 ion crystal, RF voltage applied to the trap is ≈ 250 V and the RF drive frequency is $2\pi \times 18.63$ MHz. (a) Rod configuration, ions are aligned along a line in the radial plane, dc offset is 0 V (b) planar configuration, dc offset is −6 V. (c) pop out phase, dc offset is −7 V. (d) Rod configuration, aligned along z−axis, dc voltage in this case is −12 V.

and two ions are along the z-axis and third one is in the radial plane (figure 7.18c). There is another orientation predicted by Ursekar *et al.* [228] between the planar and pop out configuration, where the ion is not along any of the defined axes in the image. Currently, due to positioning of high resolution imaging system we can not verify this phase. Beyond a certain dc offset z-axis becomes the weakest axis and ions align along the z-axis in rod shape (figure 7.18d).

For the 4-ion case, initially the ions are along a line in the radial plane, rod

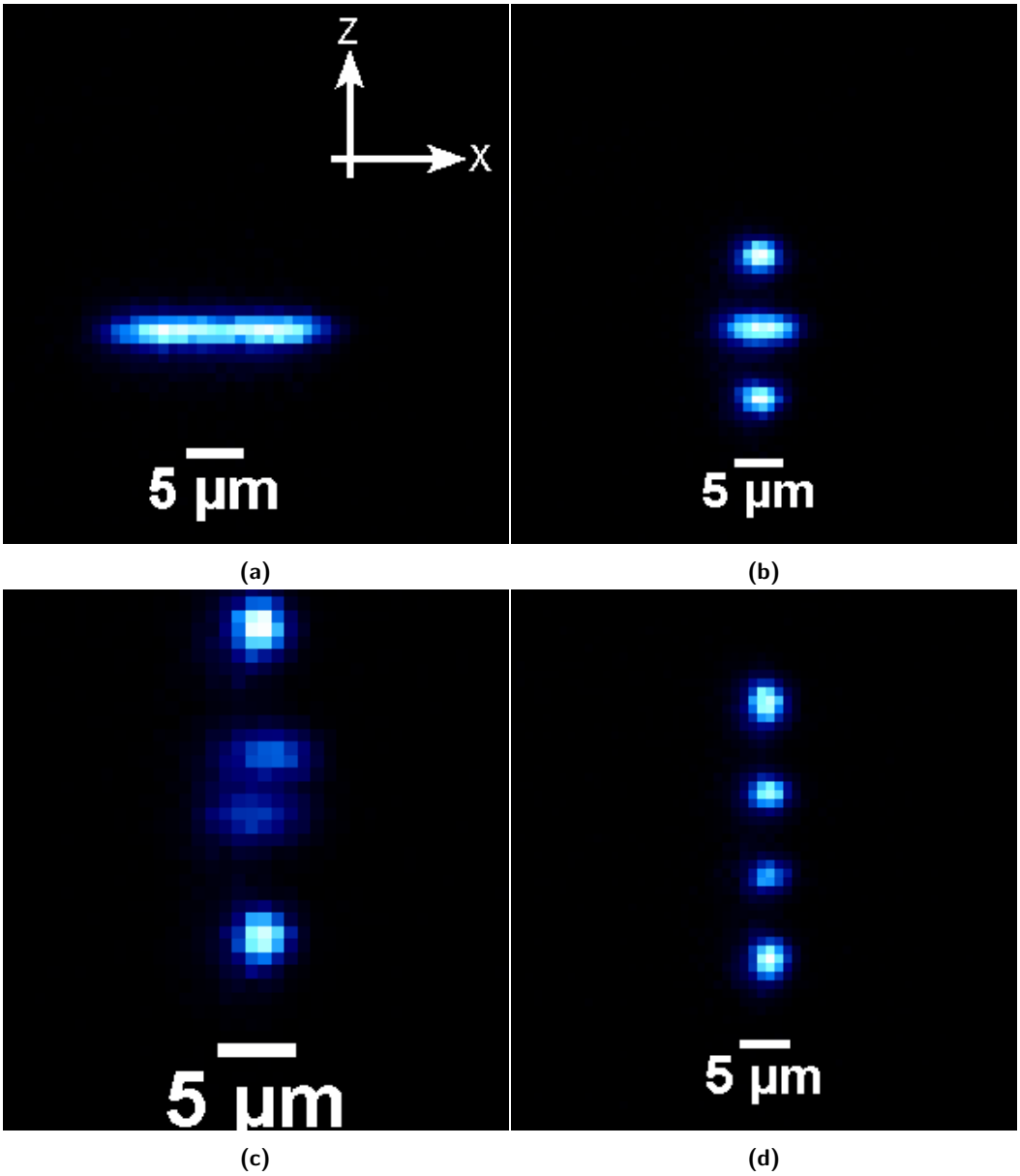
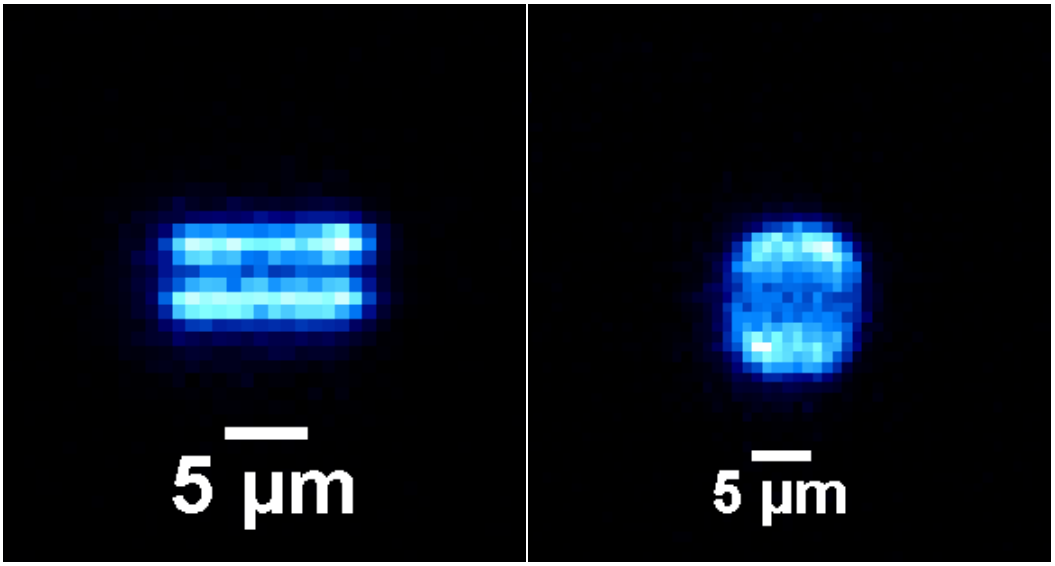


Fig. 7.19.: Image of 4 ion crystal, RF voltage applied to the trap is ≈ 225 V and the RF drive frequency is $2\pi \times 18.63$ MHz. (a) Rod phase, ions are aligned along a line in the radial plane, dc offset is 0 V (b) pop out configuration, dc offset is −7 V. (c) Zig-zag configuration, dc offset is −8.4 V. (d) Rod configuration, aligned along z—axis, dc voltage in this case is −9 V.

geometry (figure 7.19a). As we increase the dc offset in the negative direction, planar and tilt configurations come, these configuration are not resolved in our image (figure 7.20a and 7.20b). Then comes the pop out geometry (figure 7.19b) where ions are mostly aligned along the z-axis and a few are popped in the radial direction. After this zig-zag configuration (figure 7.19c) comes. Beyond a certain dc offset all ions align along the z-axis, rod geometry.

Observation of different crystal morphologies is just one part of the predictions



(a) (b)

Fig. 7.20.: Image of 4 ion crystal, RF voltage applied to the trap is ≈ 225 V and the RF drive frequency is $2\pi \times 18.63$ MHz. (a) A possible tilt phase configuration, ions are aligned along a line in the radial plane, dc offset is −4.4 V (b) A possible configuration, dc offset is −6 V. Due to imaging limitations, these phases can not be identified to a particular tilt phase.

made by Ursekar *et al.* [228]. Classification of the transition boundaries between two configuration not completed yet due to the limitations of the imaging system and voltage applied to the trap. This is ongoing work.

7.8 Conclusion

Our experiments shows that we are very close to the initially designed trap. The trap and other parts are working according to our expectations. In order to proceed towards elimination of the systematic effects, we need to do better compensation of excess micromotion as well as resolved sideband cooling of the ion to the motional ground state of the potential. At this point, this trap can be used for study of ion crystal morphology, life time of cloud to crystal transition states, and RF heating in crystals and cloud.

8 Summary and Future Prospects

8.1 Summary

We started with the idea of setting up a new experiment which can be used for precision spectroscopy, study of Coulomb crystals, and ion-atom interaction. This kind of experimental setup requires a trap geometry suitable for the above mentioned goal, a source to load ions, the laser system for creation and cooling of ions, and a detection system. The complete experimental setup design has been divided into smaller and independent experiments for the ease of building, characterization and integration.

For precision spectroscopy, miniaturized linear Paul traps and the end cap type trap are most preferable geometries. To decide that which kind of trap is more suitable for ion-atom collision experiments, a numerical study is performed to calculate the effect of trapping potential on the energy of the ion-atom system. It was found that for a given set of trap parameters and similar initial conditions for the ion-atom system, energy gain to the ion-atom system is minimum in an 8-pole trap. The numerical simulation is performed for the end cap type trap discussed in the thesis, 4-pole, 6-pole and 8-pole traps. Given the same trap parameters, the 8-pole trap is favourable from the energy gain point of view, but it does not provide a stiff potential to achieve confinement of the trapped ions near the trap center. In this scenario, cooling of ions to a much lower temperature (below mK) is required to confine the particle at the trap center and observe Coulomb crystal in the case of multiple ions. The Doppler cooling limit of calcium ion is 0.5 mK. So, higher order pole traps (above 4-pole) are not suitable for studying interaction of a localized ion with a cloud of atoms. Among the quadrupolar traps, we choose the end cap trap because of better optical access, a promising candidate for optical frequency standards, and possibility of integration with cold atom system to study interactions in the near future.

After deciding on the trap geometry, we started the trap design process. The trap design process begins with fixing the trap geometry and the gap between the electrodes to optimize the quadrupole coefficient and minimize the higher-order pole contributions. Once the gap between the trap electrodes is fixed, design, building, and characterization of atomic source start. The gap between the inner electrodes, in our case, is 1 mm. We

build and characterize an atomic source which has FWHM divergence of ~ 0.96 mm at the trap center, flow rate, $\sim 1.5 \times 10^9$ atoms s^{-1}. Signal of calcium isotopes ^{42}Ca and ^{44}Ca is also present in the beam coming out of the oven. At the front of the trap design process, the next task was selecting insulators, machining, and aligning the trap assembly. The final trap geometry is very close to the one designed. Results of machining and alignment analysis are shown in chapter 5.

During the trap design process, vacuum chamber, vacuum windows, ions pumps, drive circuit to provide high RF voltage to the trap and other accessories suitable for our kind of experiment are fixed. The aligned trap and the oven are mounted inside the vacuum chamber, and the complete experimental setup was prepared for the baking process to achieve UHV. The final pressure in our system is 1.3×10^{-10} mbar.

Characterization of the trap starts with the loading of an ion cloud, it helps us to test that all parts of the setup are working. Ions are loaded with complete control over their number in the trap. Control of the ion loading process is very important for all the experiments performed with this trap. The forced oscillation method is used to determine the secular frequency of the trap at a given operating parameters. Using the relation between secular frequencies with trap parameters, the quadrupole coefficient, $a_{2,0}$ is determined. The value of the simulated $a_{2,0}$ coefficient is 0.283 and the experimentally determined value of $a_{2,0}$ is 0.319. In the initial experiments, lifetime measurement of metastable state $D_{5/2}$ is performed, and Coulomb crystals for multiple ions are observed. According to our understanding, this is the first time that crystal morphologies for multiple ions have been experimentally reported. Predictions of exotic ion crystals for 3 and 4 have been made by Ursekar *et al.* [228]. We have observed the geometries predicted by Ursekar *et al* [228]. We are in the process of determining the morphologies of the imaged ion crystals through a combination of optical imaging and numerical analysis. Initial experimental results suggest the trap is very close to the one designed. Hence, it can be used for the proposed experiments at the start of the thesis, with further characterization depending on the experimental requirements.

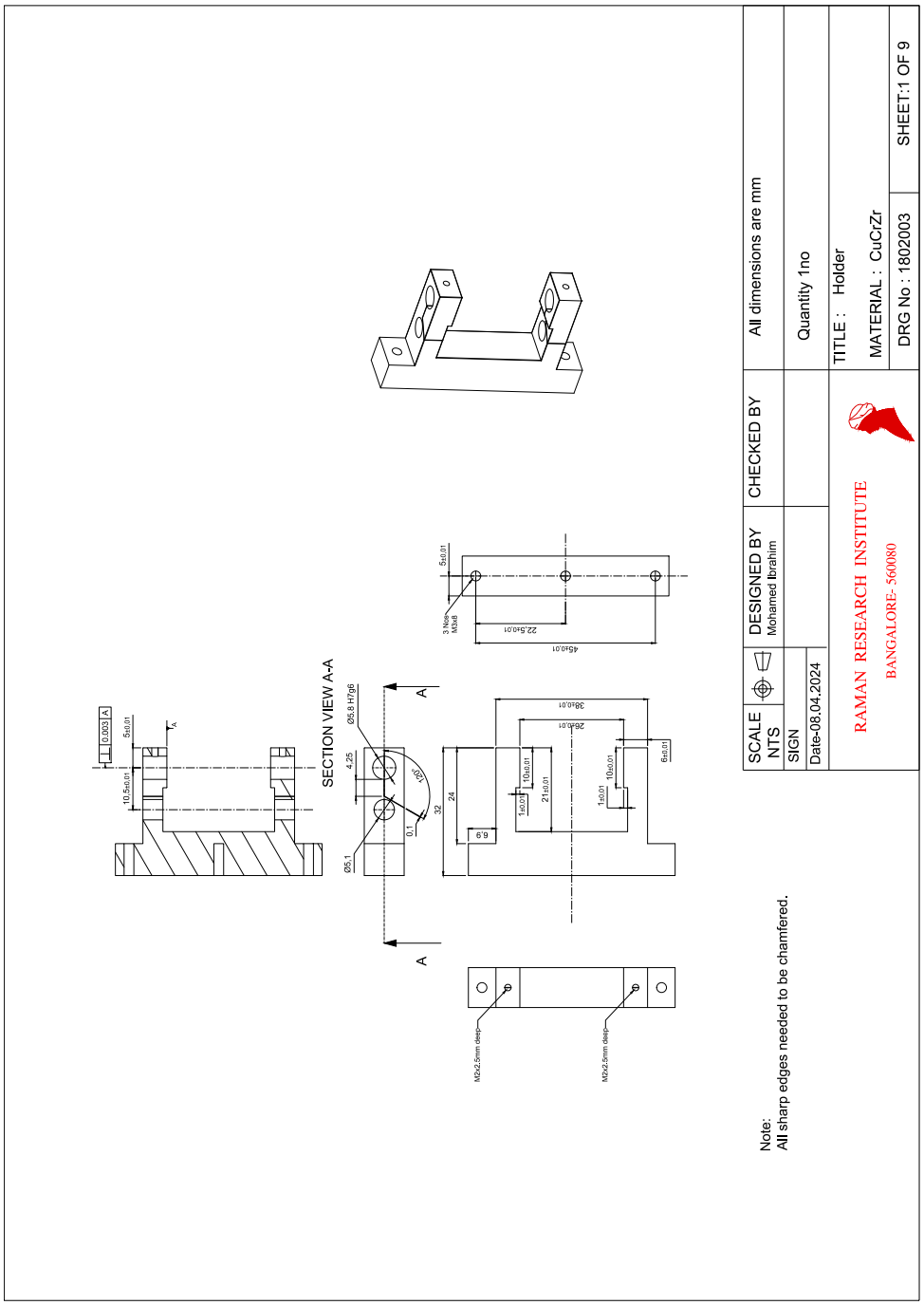
8.2 Future Prospect

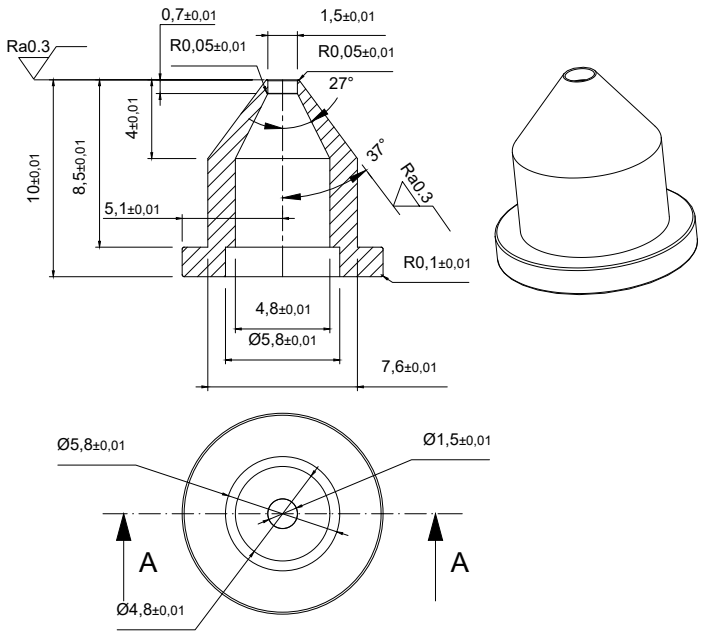
This trap has been designed with the idea of using it for trapped ion optical frequency standards in the future. The trapped ion frequency standard is a very long project that requires a well-characterized and reliable ion trap setup. However, this is a good start in terms of success in ion trapping and characterization of $a_{2,0}$ coefficient. Hence, experiments with this trap geometry can be continued to figure out the contribution of higher-order multipoles, ion heating rate due to interaction with the environment, excess micromotion minimization and its effect on 2nd-order Doppler shift, and the

effect of patch potential in the long run.

At this point, this system is suitable for studying ion crystal morphologies, the validity of adiabatic approximation of pseudopotential, RF heating, statistics of quantum jumps in interacting multiparticle systems, and precision measurement of the lifetime of metastable states and atomic clock operations. A few of these are ongoing. For the study of ion-atom interaction, this system needs to be integrated with a trapped atom system.

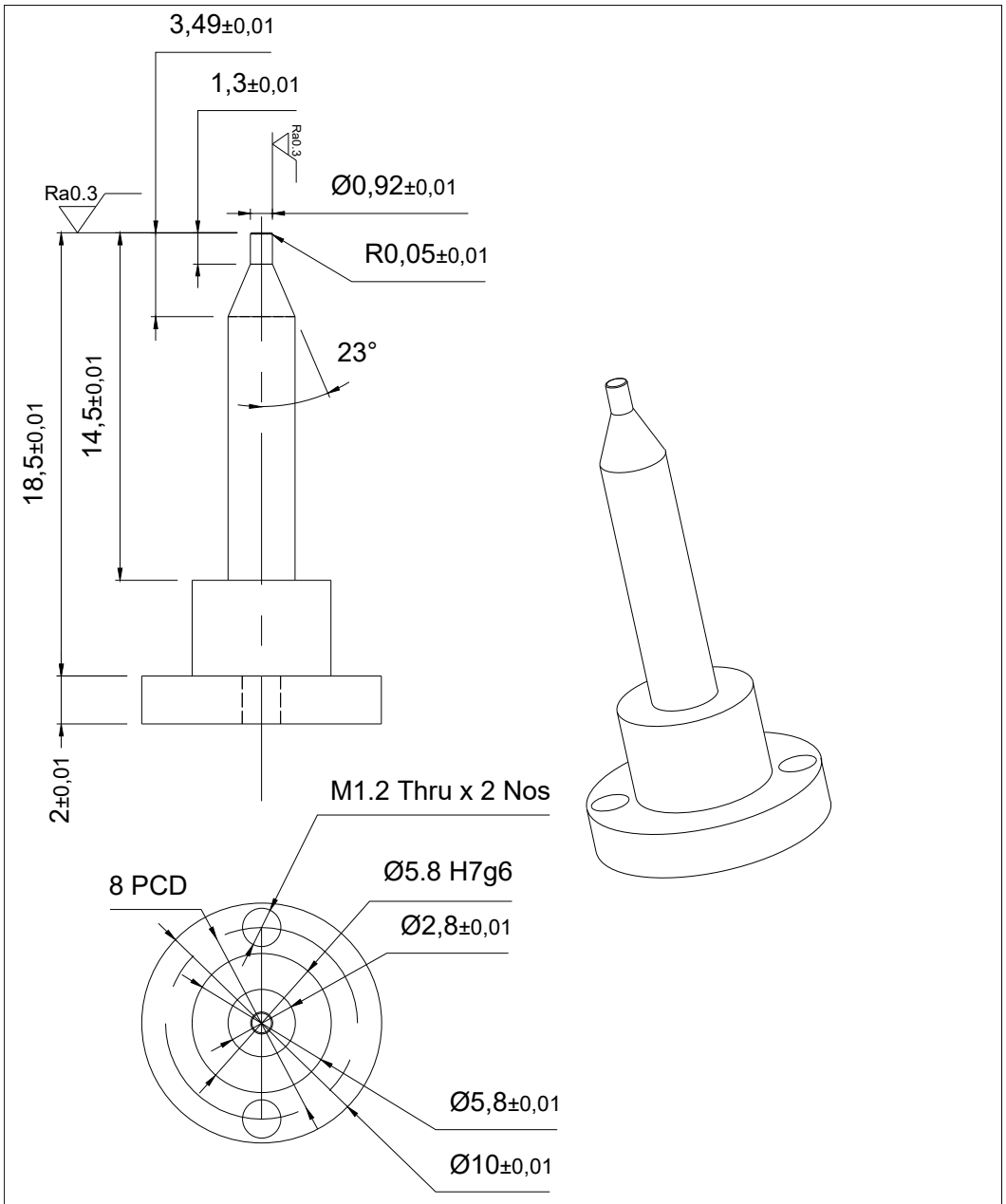
Trap Design


SECTION VIEW A-A
All dimensions are mm
Quantity 1no
TITLE : Holder
MATERIAL : CuCrZr
DRG No : 1802003
SHEET:1 OF 9
DESIGNED BY
Mohamed Ibrahim
CHECKED BY
SCALE
NTS
SIGN
Date-08.04.2024
RAMAN RESEARCH INSTITUTE
BANGALORE- 560080
Note:
All sharp edges needed to be chamfered.

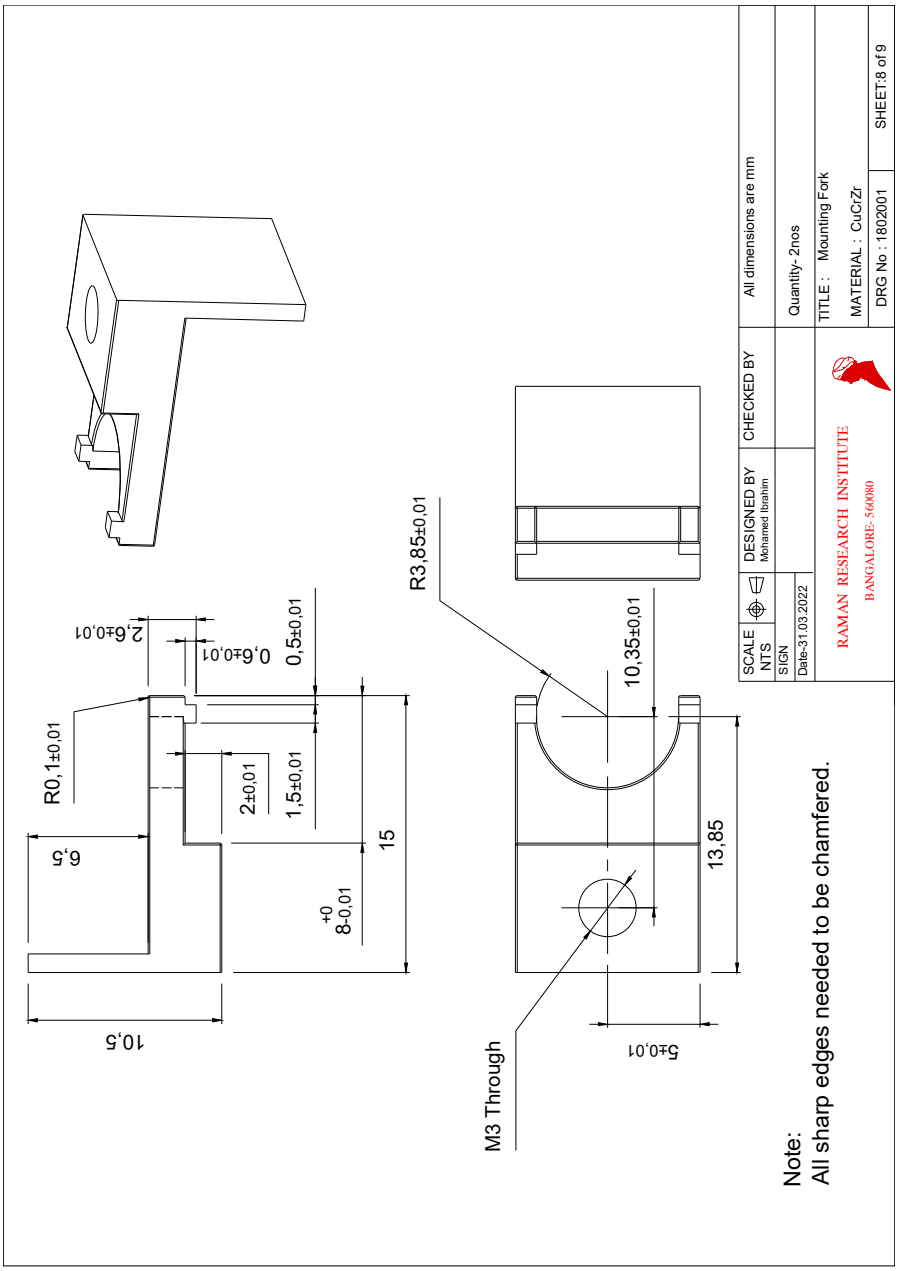


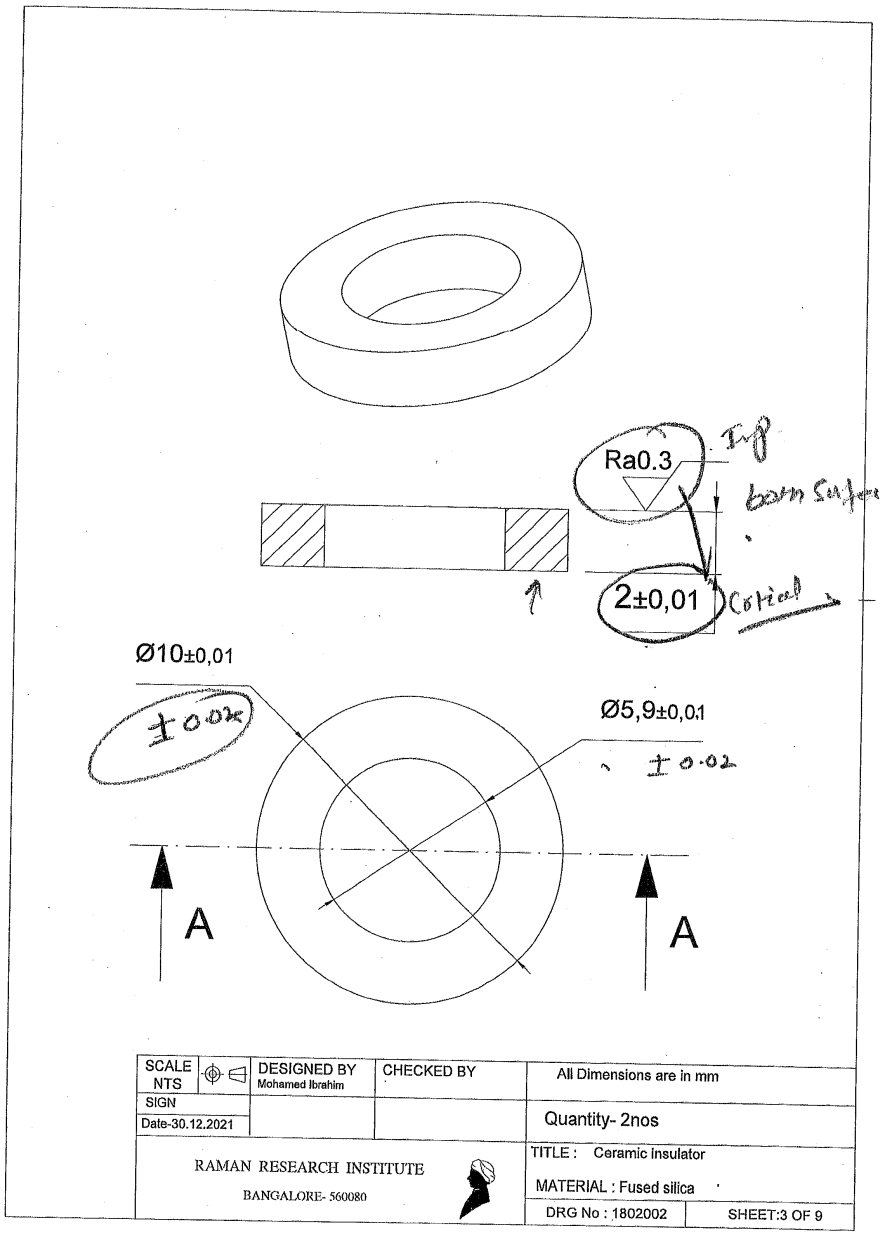
Note:
Unless mentioned all the sharp edges needed to be chamfered.

SCALE NTS	DESIGNED BY Mohamed Ibrahim	CHECKED BY	All Dimensions are in mm
SIGN			Quantity- 2nos
Date-30.12.2021			
RAMAN RESEARCH INSTITUTE BANGALORE- 560080			TITLE : Outer Electrode MATERIAL : Molybdenum
			DRG No : 1802002 / SHEET:2 OF 9

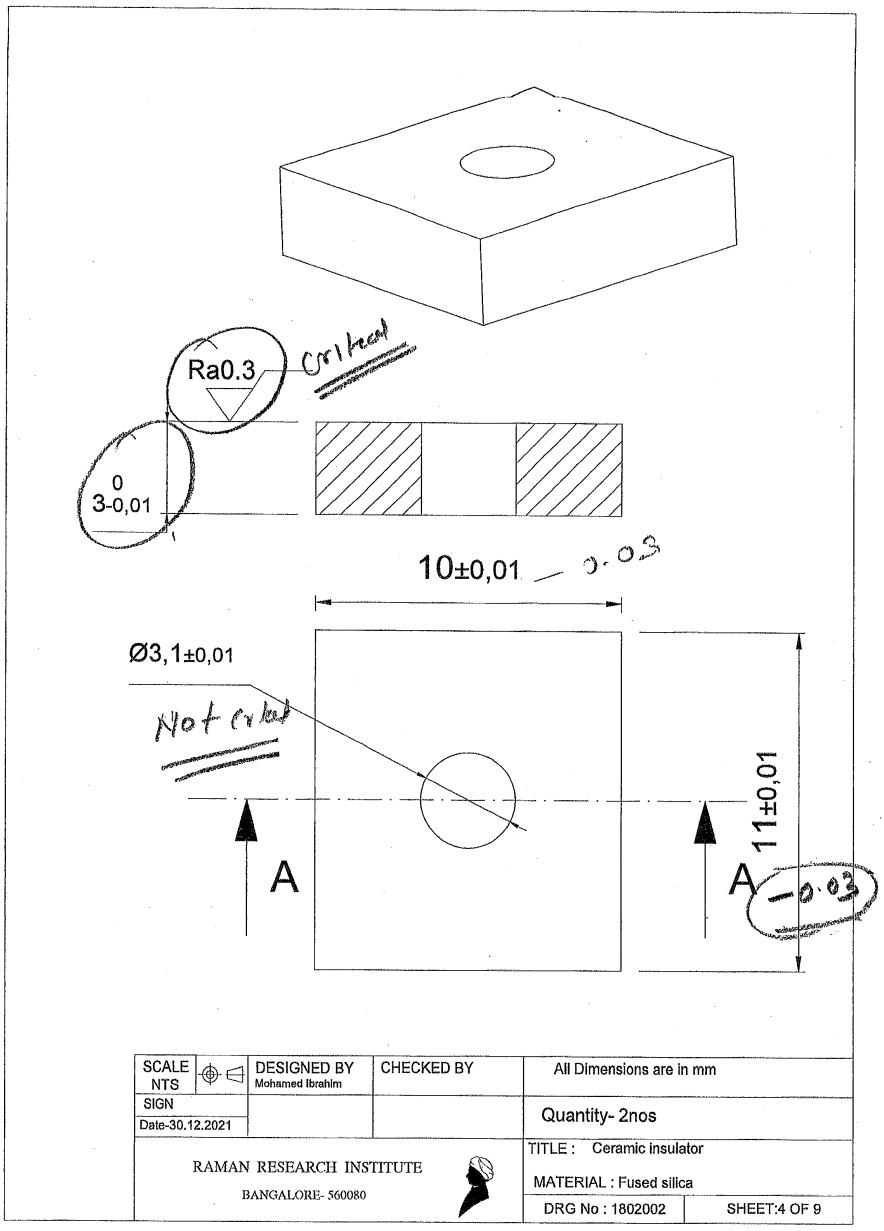


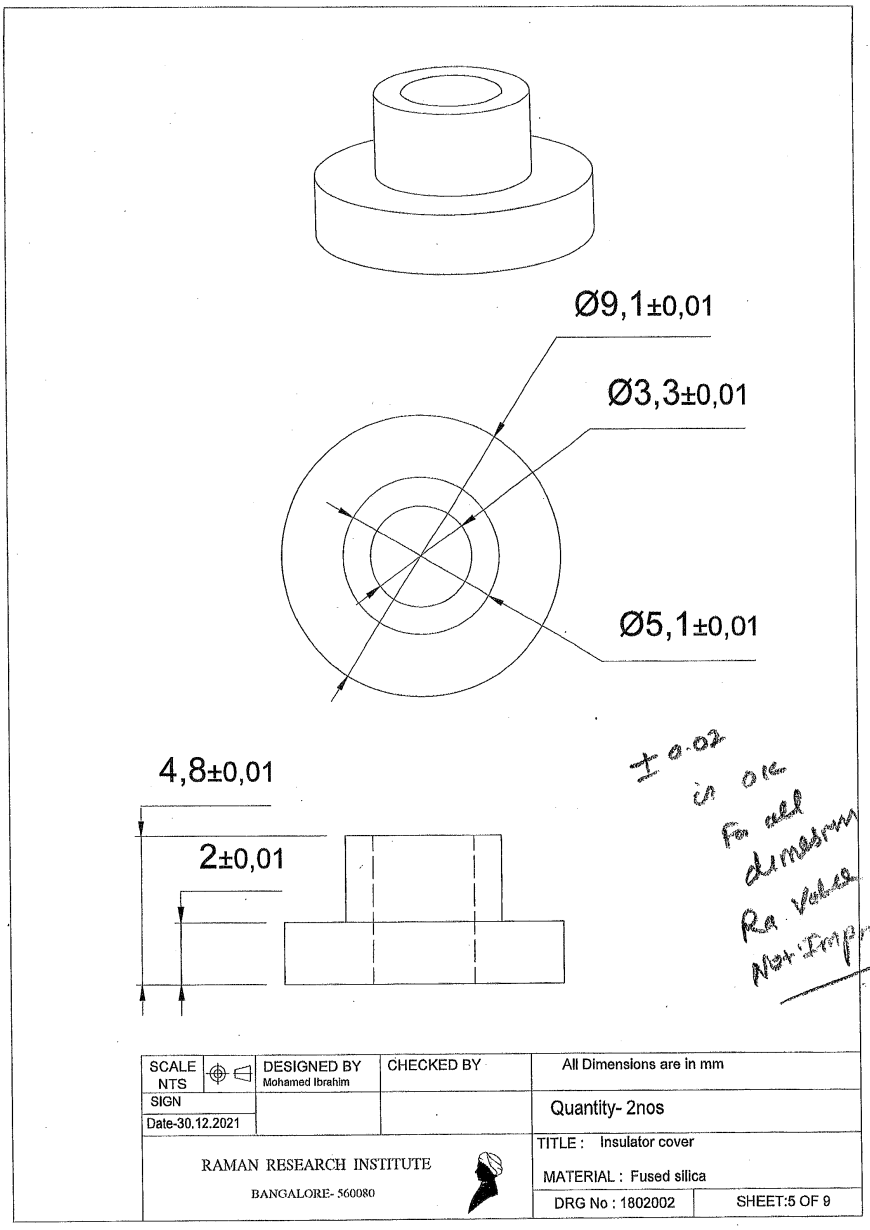
SCALE NTS	DESIGNED BY Mohamed Ibrahim	CHECKED BY	All Dimensions are in mm
SIGN Date-31.03.2022			Quantity- 2nos
RAMAN RESEARCH INSTITUTE BANGALORE- 560080			TITLE : Inner Electrode MATERIAL : Molybdenum
			DRG No : 1802002 / SHEET:7 OF 9


R0,1±0,01
6,5
10,5
2,6±0,01
0,6±0,01
0,5±0,01
2±0,01
1,5±0,01
15
8+0-0,01
R3,85±0,01
10,35±0,01
13,85
5±0,01
M3 Through
Note:
All sharp edges needed to be chamfered.
SCALE NTS
SIGN
Date-31.03.2022
DESIGNED BY Mohamed Ibrahim
CHECKED BY
All dimensions are mm
Quantity- 2nos
TITLE : Mounting Fork
MATERIAL : CuCrZr
DRG No : 1802001
SHEET:8 of 9
RAMAN RESEARCH INSTITUTE
BANGALORE- 560080

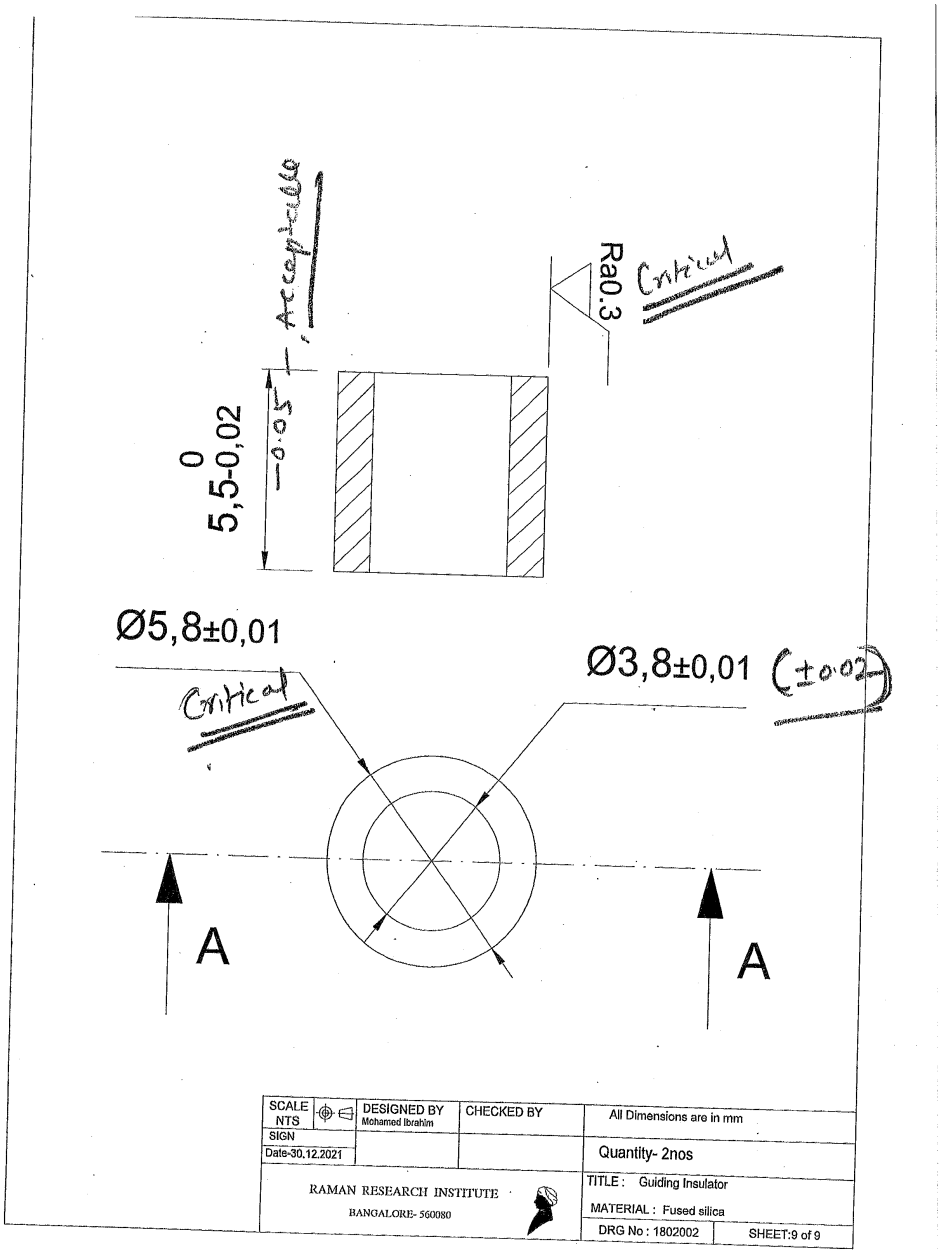


SCALE NTS	DESIGNED BY Mohamed Ibrahim	CHECKED BY	All Dimensions are in mm
SIGN			
Date-30.12.2021			Quantity- 2nos
RAMAN RESEARCH INSTITUTE BANGALORE- 560080			TITLE : Ceramic insulator
			MATERIAL : Fused silica
			DRG No : 1802002 SHEET:3 OF 9


Ra0.3
Critical
0
3-0,01
10±0,01
Ø3,1±0,01
Not critical
A
A
11±0,01
SCALE NTS
DESIGNED BY Mohamed Ibrahim
CHECKED BY
All Dimensions are in mm
SIGN
Date-30.12.2021
Quantity- 2nos
RAMAN RESEARCH INSTITUTE
BANGALORE- 560080
TITLE : Ceramic insulator
MATERIAL : Fused silica
DRG No : 1802002
SHEET:4 OF 9



SCALE NTS	DESIGNED BY Mohamed Ibrahim	CHECKED BY	All Dimensions are in mm
SIGN			Quantity- 2nos
Date-30.12.2021			
RAMAN RESEARCH INSTITUTE BANGALORE- 560080			TITLE : Insulator cover MATERIAL : Fused silica DRG No : 1802002 SHEET:5 OF 9


Acceptable
Ra0.3
Critical
5,5-0,02
0
-0.05
Ø5,8±0,01
Critical
Ø3,8±0,01 (±0.02)
A
A
SCALE NTS
DESIGNED BY Mohamed Ibrahim
CHECKED BY
All Dimensions are in mm
SIGN
Date-30.12.2021
Quantity- 2nos
RAMAN RESEARCH INSTITUTE
BANGALORE- 560080
TITLE : Guiding Insulator
MATERIAL : Fused silica
DRG No : 1802002
SHEET:9 of 9

B

Trap Mounting Accessories

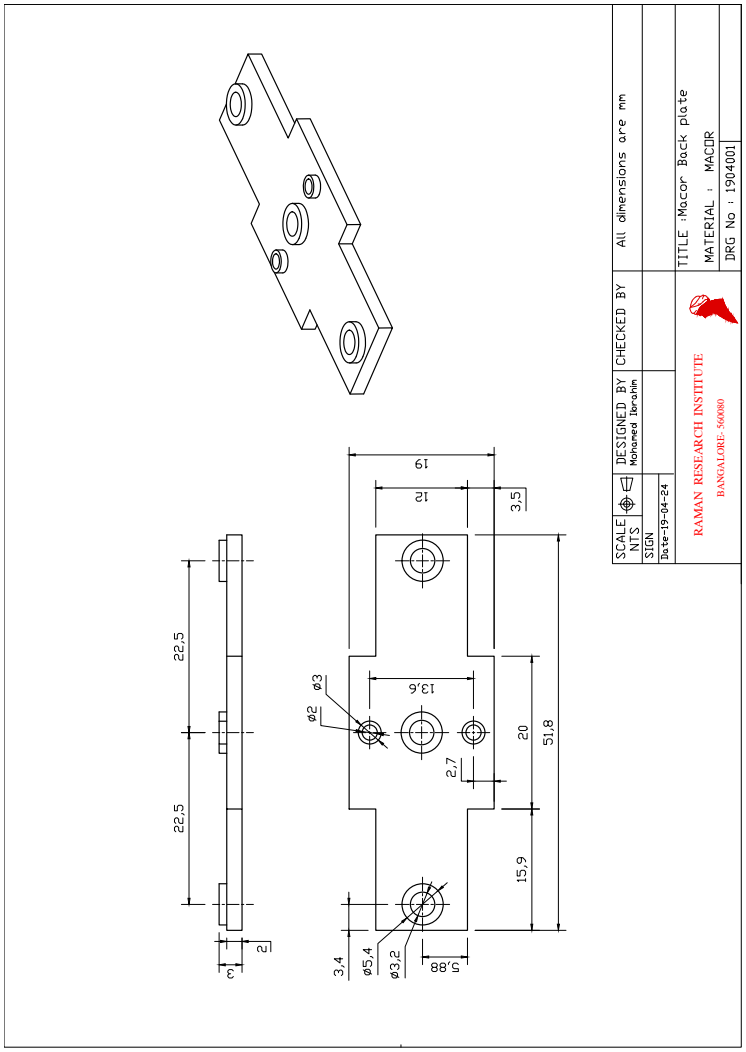


Fig. B.1.: Macor spacer present behind the ss plate. It is used to isolate the screws for electrical connection from the ss plate.

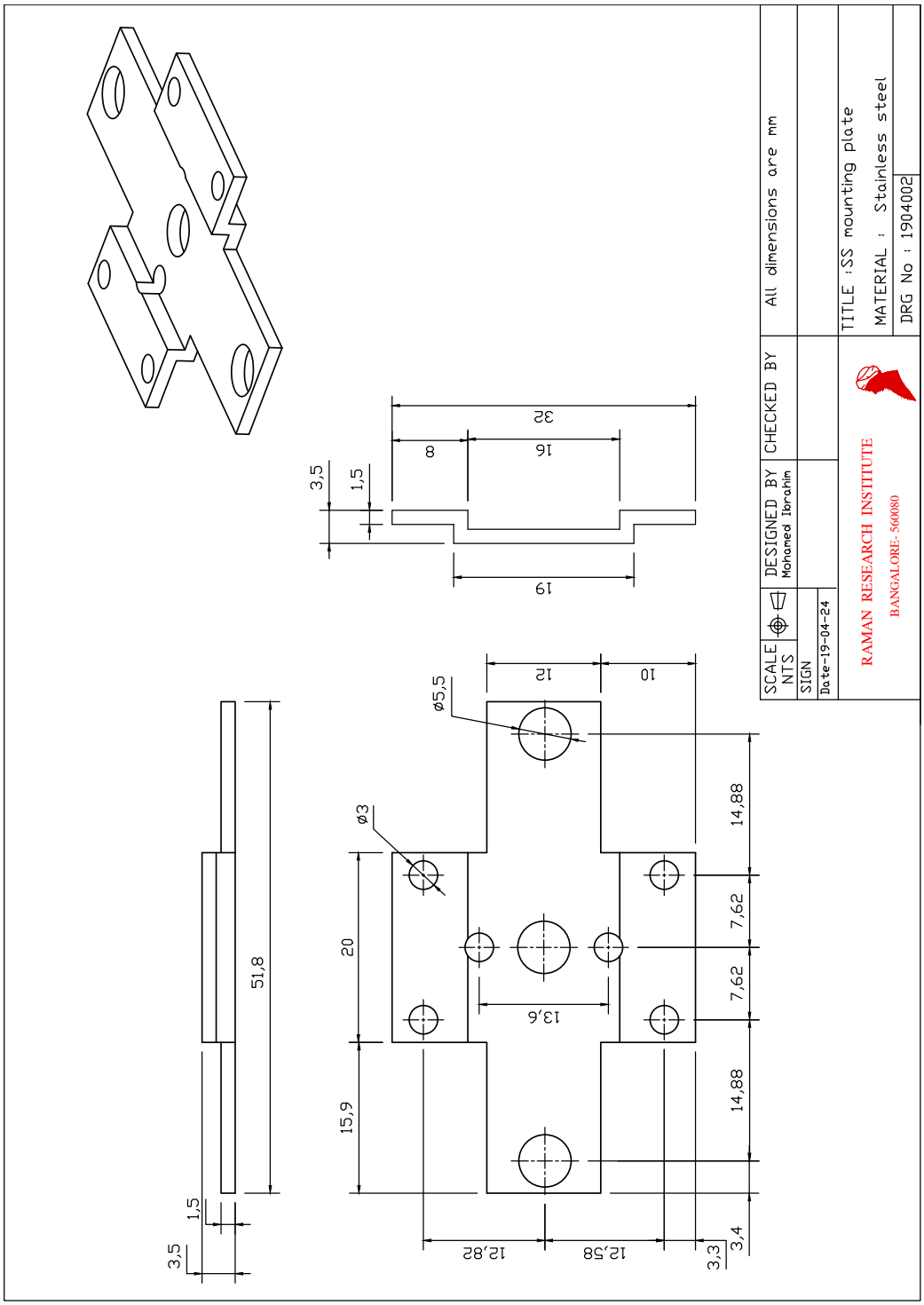


Fig. B.2.: SS plate for mounting trap with respect to the groove grabbers.

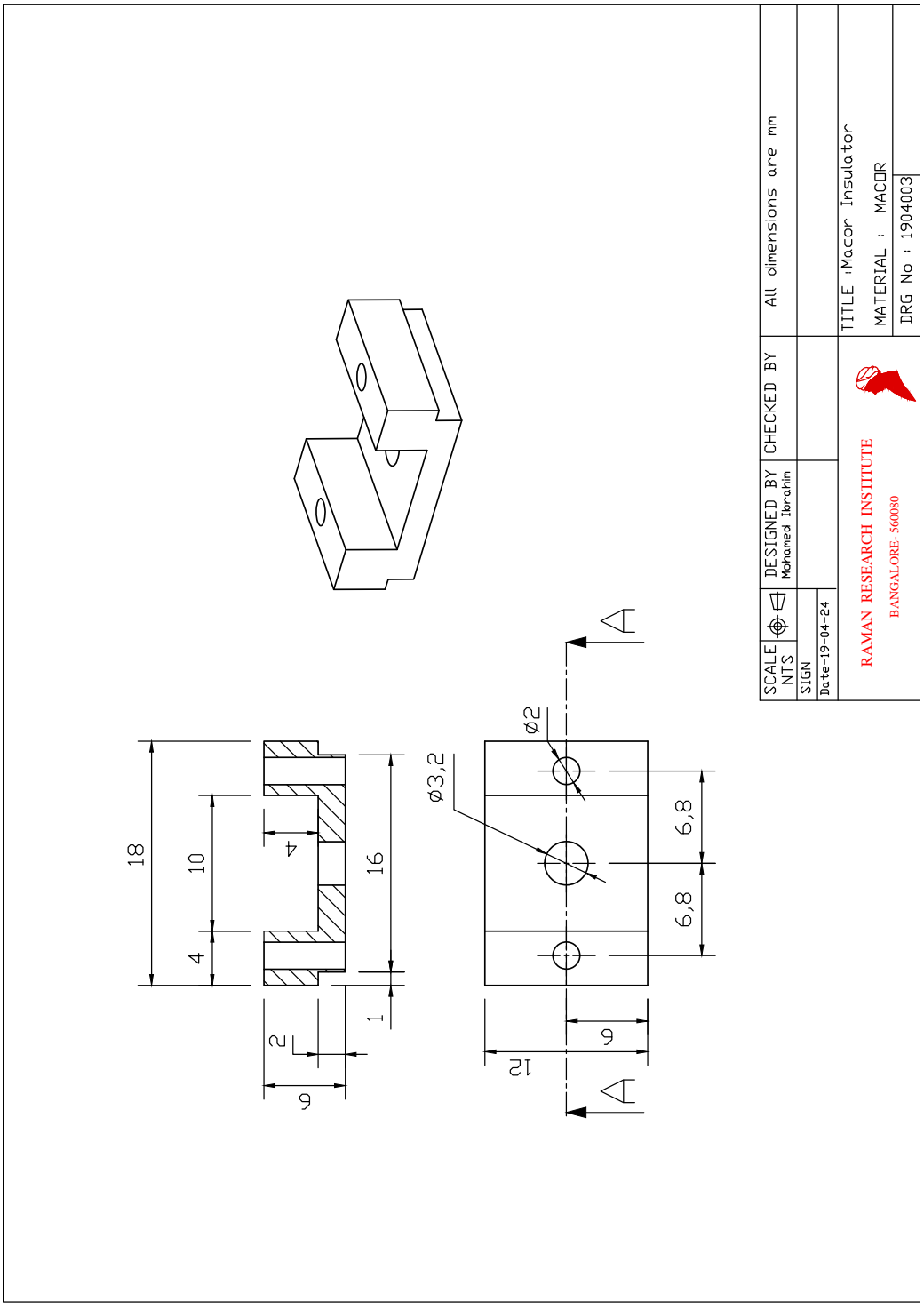


Fig. B.3.: Macor spacer used to isolate the trap from the ss plate.

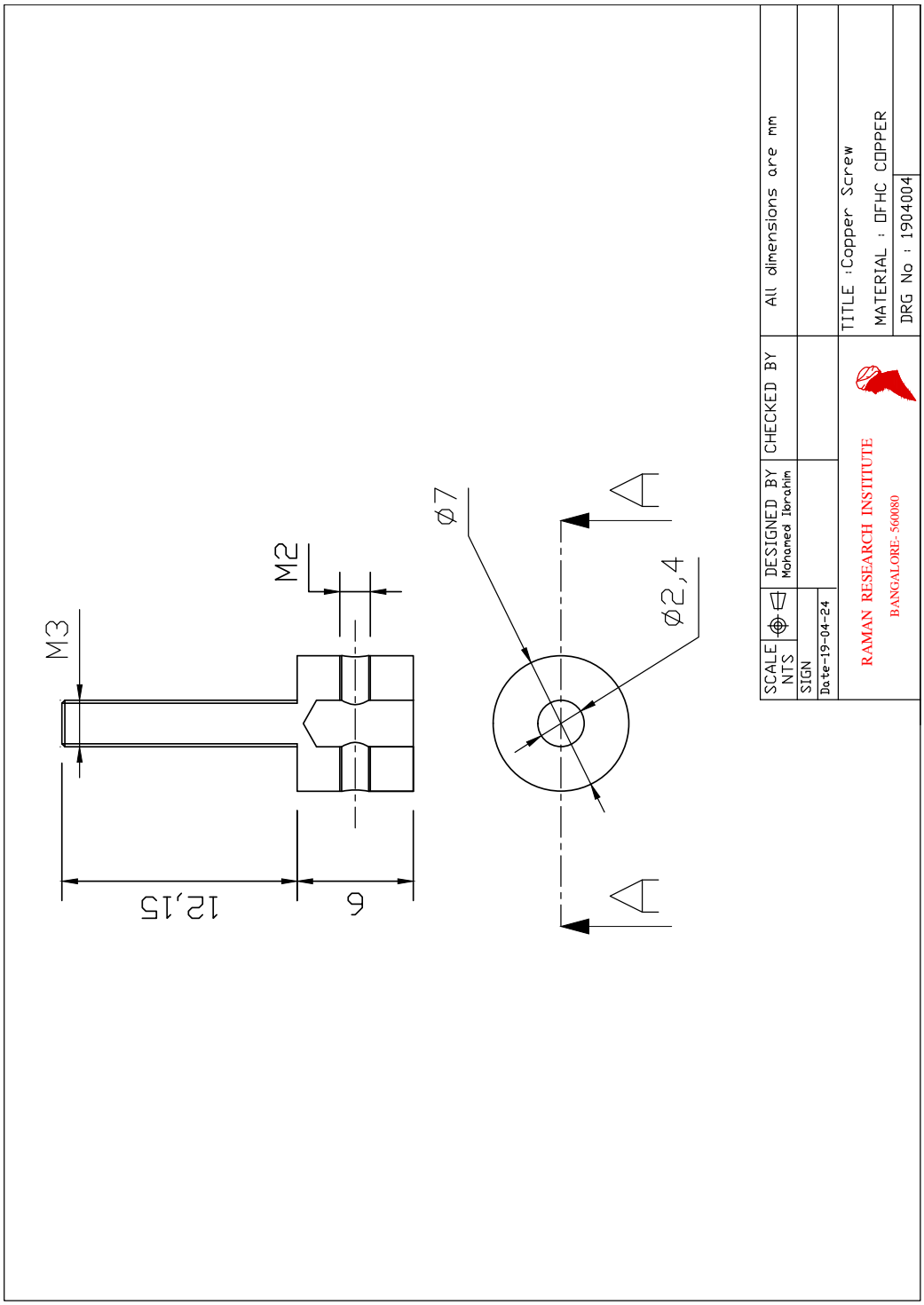


Fig. B.4.: Screw used to provide electrical connection to the trap. Feedthrough fits into the circular hole at the head of the screw and hold in place using M2 screws.

Bibliography

[1] P. B. R. Nisbet-Jones, S. A. King, J. M. Jones, et al., "A single-ion trap with minimized ion–environment interactions", Applied Physics B **122**, 57 (2016).

[2] W. M. Itano, J. C. Bergquist, and D. J. Wineland, "Laser Spectroscopy of Trapped Atomic Ions", Science **237**, 612–617 (1987).

[3] D. J. Wineland, J. J. Bollinger, W. M. Itano, and D. J. Heinzen, "Squeezed atomic states and projection noise in spectroscopy", Physical Review A **50**, 67–88 (1994).

[4] R. Lange, A. A. Peshkov, N. Huntemann, et al., "Lifetime of the F 7 / 2 2 Level in Yb + for Spontaneous Emission of Electric Octupole Radiation", Physical Review Letters **127**, 213001 (2021).

[5] D. J. Wineland, W. M. Itano, J. C. Bergquist, and R. G. Hulet, "Laser-cooling limits and single-ion spectroscopy", Physical Review A **36**, 2220–2232 (1987).

[6] D. J. Berkeland, J. D. Miller, J. C. Bergquist, W. M. Itano, and D. J. Wineland, "Laser-Cooled Mercury Ion Frequency Standard", Physical Review Letters **80**, 2089–2092 (1998).

[7] T. Rosenband, D. B. Hume, P. O. Schmidt, et al., "Frequency Ratio of Al^+ and Hg^+ Single-Ion Optical Clocks; Metrology at the 17th Decimal Place", Science **319**, 1808–1812 (2008).

[8] C. Chou, D. Hume, J. Koelemeij, D. Wineland, and T. Rosenband, "Frequency Comparison of Two High-Accuracy Al + Optical Clocks", Physical Review Letters **104**, 070802 (2010).

[9] C. Tamm, B. Lipphardt, S. Weyers, et al., "$^{171}Yb^+$ single-ion optical frequency standards", in CPEM 2010 (June 2010), pp. 20–21.

[10] J. Keller, T. Burgermeister, D. Kalincev, et al., "Controlling systematic frequency uncertainties at the 10 - 19 level in linear Coulomb crystals", Physical Review A **99**, 013405 (2019).

[11] J. Keller, T. Burgermeister, D. Kalincev, J. Kiethe, and T. E. Mehlstäubler, "Evaluation of trap-induced systematic frequency shifts for a multi-ion optical clock at the 10^{-19} level", Journal of Physics: Conference Series **723**, 012027 (2016).

[12] J. Keller, D. Kalincev, T. Burgermeister, et al., "Probing Time Dilation in Coulomb Crystals in a High-Precision Ion Trap", Physical Review Applied **11**, 011002 (2019).

[13] E. Jordan, M. Brinkmann, A. Didier, et al., "Trapped ions for quantum metrology", in Cold Atoms for Quantum Technologies, edited by S. Franke-Arnold (Oct. 2020), p. 5.

[14] L. S. Dreissen, C.-H. Yeh, H. A. Fürst, K. C. Grensemann, and T. E. Mehlstäubler, "Improved bounds on Lorentz violation from composite pulse Ramsey spectroscopy in a trapped ion", Nature Communications **13**, 7314 (2022).

[15] S. A. Diddams, T. Udem, J. C. Bergquist, et al., "An Optical Clock Based on a Single Trapped ^{199} Hg $^{+}$ Ion", Science **293**, 825–828 (2001).

[16] N. Huntemann, M. Okhapkin, B. Lipphardt, et al., "High-Accuracy Optical Clock Based on the Octupole Transition in Yb + 171", Physical Review Letters **108**, 090801 (2012).

[17] N. Huntemann, C. Sanner, B. Lipphardt, C. Tamm, and E. Peik, "Single-Ion Atomic Clock with 3 × 10 - 18 Systematic Uncertainty", Physical Review Letters **116**, 063001 (2016).

[18] E. A. Burt, J. D. Prestage, R. L. Tjoelker, et al., "Demonstration of a trapped-ion atomic clock in space", Nature **595**, 43–47 (2021).

[19] C. Monroe, D. M. Meekhof, B. E. King, W. M. Itano, and D. J. Wineland, "Demonstration of a Fundamental Quantum Logic Gate", Physical Review Letters **75**, 4714–4717 (1995).

[20] D. Kielpinski, C. Monroe, and D. J. Wineland, "Architecture for a large-scale ion-trap quantum computer", Nature **417**, 709–711 (2002).

[21] J. T. Barreiro, M. Müller, P. Schindler, et al., "An open-system quantum simulator with trapped ions", Nature **470**, 486–491 (2011).

[22] R. Blatt and C. F. Roos, "Quantum simulations with trapped ions", Nature Physics **8**, 277–284 (2012).

[23] G. Higgins, W. Li, F. Pokorny, et al., "Single Strontium Rydberg Ion Confined in a Paul Trap", Physical Review X **7**, 021038 (2017).

[24] F. M. Gambetta, C. Zhang, M. Hennrich, I. Lesanovsky, and W. Li, "Long-Range Multibody Interactions and Three-Body Antiblockade in a Trapped Rydberg Ion Chain", Physical Review Letters **125**, 133602 (2020).

[25] A. Mokhberi, M. Hennrich, and F. Schmidt-Kaler, "Trapped Rydberg ions: A new platform for quantum information processing", in *Advances In Atomic, Molecular, and Optical Physics*, Vol. 69 (Elsevier, 2020), pp. 233–306.

[26] F. M. Gambetta, C. Zhang, M. Hennrich, I. Lesanovsky, and W. Li, "Exploring the Many-Body Dynamics Near a Conical Intersection with Trapped Rydberg Ions", Physical Review Letters **126**, 233404 (2021).

[27] F. Zähringer, G. Kirchmair, R. Gerritsma, et al., "Realization of a Quantum Walk with One and Two Trapped Ions", Physical Review Letters **104**, 100503 (2010).

[28] J. Roßnagel, S. T. Dawkins, K. N. Tolazzi, et al., "A Single-Atom Heat Engine", Science **352**, 325–329 (2016).

[29] N. Van Horne, D. Yum, T. Dutta, et al., "Single-Atom Energy-Conversion Device with a Quantum Load", npj Quantum Information **6**, 37 (2020).

[30] D. J. Wineland, J. C. Bergquist, W. M. Itano, J. J. Bollinger, and C. H. Manney, "Atomic-Ion Coulomb Clusters in an Ion Trap", Physical Review Letters **59**, 2935–2938 (1987).

[31] K. Pyka, J. Keller, H. L. Partner, et al., "Topological Defect Formation and Spontaneous Symmetry Breaking in Ion Coulomb Crystals", Nature Communications **4**, 2291 (2013).

[32] O. Dulieu and S. Willitsch, "Ion Coulomb crystals: from quantum technology to chemistry close to the absolute zero point", Europhysics News **48**, 17–20 (2017).

[33] W. W. Smith, O. P. Makarov, and J. Lin, "Cold ion–neutral collisions in a hybrid trap", Journal of Modern Optics **52**, 2253–2260 (2005).

[34] S. Willitsch, M. T. Bell, A. D. Gingell, S. R. Procter, and T. P. Softley, "Cold Reactive Collisions between Laser-Cooled Ions and Velocity-Selected Neutral Molecules", Physical Review Letters **100**, 043203 (2008).

[35] C. Zipkes, S. Palzer, C. Sias, and M. Köhl, "A trapped single ion inside a Bose–Einstein condensate", Nature **464**, 388–391 (2010).

[36] W. G. Rellergert, S. T. Sullivan, S. Kotochigova, et al., "Measurement of a Large Chemical Reaction Rate between Ultracold Closed-Shell Ca 40 Atoms and Open-Shell Yb + 174 Ions Held in a Hybrid Atom-Ion Trap", Physical Review Letters **107**, 243201 (2011).

[37] K. Ravi, S. Lee, A. Sharma, G. Werth, and S. A. Rangwala, "Combined ion and atom trap for low-temperature ion–atom physics", Applied Physics B **107**, 971–981 (2012).

[38] K. Ravi, S. Lee, A. Sharma, G. Werth, and S. Rangwala, "Cooling and stabilization by collisions in a mixed Ion–Atom system", Nature Communications **3**, 1126 (2012).

[39] T. Ray, S. Jyothi, N. B. Ram, and S. A. Rangwala, "A thin wire ion trap to study ion–atom collisions built within a Fabry–Perot cavity", Applied Physics B **114**, 267–273 (2014).

[40] K. Chen, S. T. Sullivan, and E. R. Hudson, "Neutral Gas Sympathetic Cooling of an Ion in a Paul Trap", Physical Review Letters **112**, 143009 (2014).

[41] I. Rouse and S. Willitsch, "Superstatistical velocity distributions of cold trapped ions in molecular-dynamics simulations", Physical Review A **92**, 053420 (2015).

[42] B. Höltkemeier, P. Weckesser, H. López-Carrera, and M. Weidemüller, "Buffer-Gas Cooling of a Single Ion in a Multipole Radio Frequency Trap Beyond the Critical Mass Ratio", Physical Review Letters **116**, 233003 (2016).

[43] T. Secker, R. Gerritsma, A. W. Glaetzle, and A. Negretti, "Controlled long-range interactions between Rydberg atoms and ions", Physical Review A **94**, 013420 (2016).

[44] S. Jyothi, T. Ray, S. Dutta, et al., "Photodissociation of Trapped Rb 2 + : Implications for Simultaneous Trapping of Atoms and Molecular Ions", Physical Review Letters **117**, 213002 (2016).

[45] J. Joger, H. Fürst, N. Ewald, et al., "Observation of collisions between cold Li atoms and Yb + ions", Physical Review A **96**, 030703 (2017).

[46] S. Dutta, R. Sawant, and S. A. Rangwala, "Collisional Cooling of Light Ions by Cotrapped Heavy Atoms", Physical Review Letters **118**, 113401 (2017).

[47] I. Rouse and S. Willitsch, "Superstatistical Energy Distributions of an Ion in an Ultracold Buffer Gas", Physical Review Letters **118**, 143401 (2017).

[48] S. Dutta and S. A. Rangwala, "Cooling of trapped ions by resonant charge exchange", Physical Review A **97**, 041401 (2018).

[49] I. Rouse and S. Willitsch, "Energy distributions of an ion in a radio-frequency trap immersed in a buffer gas under the influence of additional external forces", Physical Review A **97**, 042712 (2018).

[50] S. Jyothi, K. N. Egodapitiya, B. Bondurant, et al., "A hybrid ion-atom trap with integrated high resolution mass spectrometer", Review of Scientific Instruments **90**, 103201 (2019).

[51] M. Tomza, K. Jachymski, R. Gerritsma, et al., "Cold hybrid ion-atom systems", Reviews of Modern Physics **91**, 035001 (2019).

[52] H. Li, S. Jyothi, M. Li, et al., "Photon-mediated charge exchange reactions between ^{39} K atoms and ^{40} Ca $^{+}$ ions in a hybrid trap", Physical Chemistry Chemical Physics **22**, 10870–10881 (2020).

[53] T. Feldker, H. Fürst, H. Hirzler, et al., "Buffer gas cooling of a trapped ion to the quantum regime", Nature Physics **16**, 413–416 (2020).

[54] L. Wang, M. Deiß, G. Raithel, and J. H. Denschlag, "Optical Control of Atom-Ion Collisions Using a Rydberg State", Journal of Physics B: Atomic, Molecular and Optical Physics **53**, 134005 (2020).

[55] S. Dutta and S. A. Rangwala, "Measurement of collisions between laser-cooled cesium atoms and trapped cesium ions", Physical Review A **102**, 033309 (2020).

[56] H. Hirzler, T. Feldker, H. Fürst, et al., "Experimental setup for studying an ultracold mixture of trapped Yb + – Li 6", Physical Review A **102**, 033109 (2020).

[57] L. Oghittu, M. Johannsen, A. Negretti, and R. Gerritsma, "Dynamics of a trapped ion in a quantum gas: Effects of particle statistics", Physical Review A **104**, 053314 (2021).

[58] M. Deiß, S. Haze, and J. Hecker Denschlag, "Long-Range Atom–Ion Rydberg Molecule: A Novel Molecular Binding Mechanism", Atoms **9**, 34 (2021).

[59] E. Trimby, H. Hirzler, H. Fürst, et al., "Buffer gas cooling of ions in radio-frequency traps using ultracold atoms", New Journal of Physics **24**, 035004 (2022).

[60] C. Schrama, E. Peik, W. Smith, and H. Walther, "Novel miniature ion traps", Optics Communications **101**, 32–36 (1993).

[61] M. Cetina, A. T. Grier, and V. Vuletić, "Micromotion-Induced Limit to Atom-Ion Sympathetic Cooling in Paul Traps", Physical Review Letters **109**, 253201 (2012).

[62] M. Niranjan, A. Prakash, and S. A. Rangwala, "Analysis of Multipolar Linear Paul Traps for Ion–Atom Ultracold Collision Experiments", Atoms **9**, 38 (2021).

[63] W. Neuhauser, M. Hohenstatt, P. Toschek, and H. Dehmelt, "Optical-Sideband Cooling of Visible Atom Cloud Confined in Parabolic Well", Physical Review Letters **41**, 233–236 (1978).

[64] D. J. Wineland, R. E. Drullinger, and F. L. Walls, "Radiation-Pressure Cooling of Bound Resonant Absorbers", Physical Review Letters **40**, 1639–1642 (1978).

[65] W. Neuhauser, M. Hohenstatt, P. E. Toschek, and H. G. Dehmelt, "Visual observation and optical cooling of electrodynamically contained ions", Applied Physics **17**, 123–129 (1978).

[66] K. Dieckmann, R. J. C. Spreeuw, M. Weidemüller, and J. T. M. Walraven, "Two-dimensional magneto-optical trap as a source of slow atoms", Physical Review A **58**, 3891–3895 (1998).

[67] C. Monroe, W. Swann, H. Robinson, and C. Wieman, "Very cold trapped atoms in a vapor cell", Physical Review Letters **65**, 1571–1574 (1990).

[68] K. B. Davis, M. .-. Mewes, M. R. Andrews, et al., "Bose-Einstein Condensation in a Gas of Sodium Atoms", Physical Review Letters **75**, 3969–3973 (1995).

[69] C. Langer, R. Ozeri, J. Jost, et al., "Long-Lived Qubit Memory Using Atomic Ions", Physical Review Letters **95**, 060502 (2005).

[70] H. Haffner, C. Roos, and R. Blatt, "Quantum computing with trapped ions", Physics Reports **469**, 155–203 (2008).

[71] T. D. Ladd, F. Jelezko, R. Laflamme, et al., "Quantum computers", Nature **464**, 45–53 (2010).

[72] A. Bermudez, P. O. Schmidt, M. B. Plenio, and A. Retzker, "Robust trapped-ion quantum logic gates by continuous dynamical decoupling", Physical Review A **85**, 040302 (2012).

[73] T. P. Harty, D. T. C. Allcock, C. J. Ballance, et al., "High-Fidelity Preparation, Gates, Memory, and Readout of a Trapped-Ion Quantum Bit", Physical Review Letters **113**, 220501 (2014).

[74] J. P. Gaebler, T. R. Tan, Y. Lin, et al., "High-Fidelity Universal Gate Set for Be 9 + Ion Qubits", Physical Review Letters **117**, 060505 (2016).

[75] P. Wang, C.-Y. Luan, M. Qiao, et al., "Single ion qubit with estimated coherence time exceeding one hour", Nature Communications **12**, 233 (2021).

[76] P. O. Schmidt, T. Rosenband, C. Langer, et al., "Spectroscopy Using Quantum Logic", Science **309**, 749–752 (2005).

[77] P. Dubé, A. A. Madej, Z. Zhou, and J. E. Bernard, "Evaluation of systematic shifts of the 88 Sr + single-ion optical frequency standard at the 10 - 17 level", Physical Review A **87**, 023806 (2013).

[78] R. M. Godun, P. B. R. Nisbet-Jones, J. M. Jones, et al., "Frequency Ratio of Two Optical Clock Transitions in Yb + 171 and Constraints on the Time Variation of Fundamental Constants", Physical Review Letters **113**, 210801 (2014).

[79] A. D. Ludlow, M. M. Boyd, J. Ye, E. Peik, and P. O. Schmidt, "Optical atomic clocks", Reviews of Modern Physics **87**, 637–701 (2015).

[80] Y. Huang, H. Guan, P. Liu, et al., "Frequency Comparison of Two Ca + 40 Optical Clocks with an Uncertainty at the 10 - 17 Level", Physical Review Letters **116**, 013001 (2016).

[81] J. Cao, P. Zhang, J. Shang, et al., "A compact, transportable single-ion optical clock with 7.8 × 10-17 systematic uncertainty", Applied Physics B **123**, 112 (2017).

[82] S. M. Brewer, J.-S. Chen, A. M. Hankin, et al., "Al + 27 Quantum-Logic Clock with a Systematic Uncertainty below 10 - 18", Physical Review Letters **123**, 033201 (2019).

[83] Z. Zhiqiang, K. J. Arnold, R. Kaewuam, and M. D. Barrett, "^{176} Lu $^{+}$ clock comparison at the 10 $^{-18}$ level via correlation spectroscopy", Science Advances **9**, eadg1971 (2023).

[84] C. F. Roos, R. Gerritsma, G. Kirchmair, et al., "Quantum simulation of relativistic quantum physics with trapped ions", Journal of Physics: Conference Series **264**, 012020 (2011).

[85] S. M. Clark, D. Hayes, D. Hucul, et al., "Trapped ions for testing foundations of quantum theory", in QUANTUM THEORY: RECONSIDERATION OF FOUNDATIONS 6 (2012), pp. 56–60.

[86] J. Broz, B. You, S. Khan, et al., "Test of Causal Nonlinear Quantum Mechanics by Ramsey Interferometry with a Trapped Ion", Physical Review Letters **130**, 200201 (2023).

[87] A. Bjerhammar, "On a relativistic geodesy", Bulletin Géodésique **59**, 207–220 (1985).

[88] T. E. Mehlstäubler, G. Grosche, C. Lisdat, P. O. Schmidt, and H. Denker, "Atomic clocks for geodesy", Reports on Progress in Physics **81**, 064401 (2018).

[89] C. Schneider, D. Porras, and T. Schaetz, "Experimental quantum simulations of many-body physics with trapped ions", Reports on Progress in Physics **75**, 024401 (2012).

[90] Q.-X. Mei, B.-W. Li, Y.-K. Wu, et al., "Experimental Realization of the Rabi-Hubbard Model with Trapped Ions", Physical Review Letters **128**, 160504 (2022).

[91] J. Knörzer, T. Shi, E. Demler, and J. I. Cirac, "Spin-Holstein Models in Trapped-Ion Systems", Physical Review Letters **128**, 120404 (2022).

[92] L. Schmöger, O. O. Versolato, M. Schwarz, et al., "Coulomb crystallization of highly charged ions", Science **347**, 1233–1236 (2015).

[93] G. Werth, T. Beier, S. Djekic, et al., "Precision studies in traps: Measurement of fundamental constants and tests of fundamental theories", Nuclear Instruments and Methods in Physics Research Section B: Beam Interactions with Materials and Atoms **205**, 1–8 (2003).

[94] J.-S. Chen, S. M. Brewer, C. W. Chou, et al., "Sympathetic Ground State Cooling and Time-Dilation Shifts in an Al 27 + Optical Clock", Physical Review Letters **118**, 053002 (2017).

[95] S. Schiller and J.-P. Karr, "Prospects for the determination of fundamental constants with beyond-state-of-the-art uncertainty using molecular hydrogen ion spectroscopy", Physical Review A **109**, 042825 (2024).

[96] J. R. Pierce, *Theory and Design of Electron Beams* ().

[97] W. Paul, "Electromagnetic traps for charged and neutral particles", Reviews of Modern Physics **62**, 531–540 (1990).

[98] H. G. Dehmelt and F. G. Major, "Orientation of (He 4) + Ions by Exchange Collisions with Cesium Atoms", Physical Review Letters **8**, 213–214 (1962).

[99] A. Kastler, “Quelques suggestions concernant la production optique et la détection optique d’une inégalité de population des niveaux de quantifigation spatiale des atomes. Application à l’expérience de Stern et Gerlach et à la résonance magnétique”, Journal de Physique et le Radium **11**, 255–265 (1950).

[100] Y. B. Zel’dovich, “Cooling with the aid of high-frequency energy”, JETP Lett. **19**.

[101] T. Hänsch and A. Schawlow, “Cooling of gases by laser radiation”, Optics Communications **13**, 68–69 (1975).

[102] D. Wineland H. Dehmelt, “Proposed 10 ^ 14 $\Delta\nu/\nu$ laser fluorescence spectroscopy on Tl+ mono-ion oscillator III (side band cooling)”, Bull. Am. Phys. Soc. 20, 637 (1975).

[103] H.G. Dehmelt, “H. G. Dehmelt, "Proposed 10 ^ 14 δV < v laser fluorescence spectroscopy on Tl+ mono-ion oscillator, I and II”, Bull. Am. Phys. Soc. 18, 1521 (1973).

[104] H Dehmelt, “Proposed 1014$\delta\nu/\nu$ laser fluorescence spectroscopy on Tl+ mono-ion oscillator”, Bull. Am. Phys. Soc (1975).

[105] W. Nagourney, J. Sandberg, and H. Dehmelt, “Shelved optical electron amplifier: Observation of quantum jumps”, Physical Review Letters **56**, 2797–2799 (1986).

[106] T. Sauter, W. Neuhauser, R. Blatt, and P. E. Toschek, “Observation of Quantum Jumps”, Physical Review Letters **57**, 1696–1698 (1986).

[107] J. C. Bergquist, R. G. Hulet, W. M. Itano, and D. J. Wineland, “Observation of Quantum Jumps in a Single Atom”, Physical Review Letters **57**, 1699–1702 (1986).

[108] R. J. Rafac, B. C. Young, J. A. Beall, et al., “Sub-dekahertz Ultraviolet Spectroscopy of 199 Hg +”, Physical Review Letters **85**, 2462–2465 (2000).

[109] C. Tamm, D. Engelke, and V. Bühner, “Spectroscopy of the electric-quadrupole transition 2 S 1 / 2 (F = 0) – 2 D 3 / 2 (F = 2) in trapped 171 Yb +”, Physical Review A **61**, 053405 (2000).

[110] S. A. Webster, P. Taylor, M. Roberts, G. P. Barwood, and P. Gill, “Kilohertz-resolution spectroscopy of the 2 S 1 / 2 - 2 F 7 / 2 electric octupole transition in a single 171 Yb + ion”, Physical Review A **65**, 052501 (2002).

[111] J. E. Bernard, A. A. Madej, L. Marmet, et al., “Cs-Based Frequency Measurement of a Single, Trapped Ion Transition in the Visible Region of the Spectrum”, Physical Review Letters **82**, 3228–3231 (1999).

[112] G. Barwood, K. Gao, P. Gill, G. Huang, and H. Klein, “Development of optical frequency standards based upon the /sup 2/S/sub 1/2/-/sup 2/D/sub 5/2/ transition in /sup 88/Sr/sup +/ and /sup 87/Sr/sup +/”, IEEE Transactions on Instrumentation and Measurement **50**, 543–547 (2001).

[113] M. Chwalla, J. Benhelm, K. Kim, et al., “Absolute Frequency Measurement of the Ca + 40 4 s S 1 / 2 2 - 3 d D 5 / 2 2 Clock Transition”, Physical Review Letters **102**, 023002 (2009).

[114] K. Gao, “Optical frequency standard based on a single 40Ca+”, Chinese Science Bulletin **58**, 853–863 (2013).

[115] X. Fernandez-Gonzalvo and M. Keller, "A fully fiber-integrated ion trap for portable quantum technologies", Scientific Reports **13**, 523 (2023).

[116] A. Spampinato, J. Stacey, S. Mulholland, et al., "An ion trap design for a space-deployable strontium-ion optical clock", Proceedings of the Royal Society A: Mathematical, Physical and Engineering Sciences **480**, 20230593 (2024).

[117] S. Lee, K. Ravi, and S. A. Rangwala, "Measurement of collisions between rubidium atoms and optically dark rubidium ions in trapped mixtures", Physical Review A **87**, 052701 (2013).

[118] S. Dutta, R. Sawant, and S. A. Rangwala, "Collisional cooling of trapped ions with cold atoms: results and insights", Journal of Physics: Conference Series **1412**, 062001 (2020).

[119] F. G. Major and H. G. Dehmelt, "Exchange-Collision Technique for the rf Spectroscopy of Stored Ions", Physical Review **170**, 91–107 (1968).

[120] Paul, W and Steinwedel, H, "A NEW MASS SPECTROMETER WITHOUT A MAGNETIC FIELD", Zeitschrift fuer Naturforschung (West Germany) Divided into Z. Nautrforsch., A, and Z. Naturforsch., B: Anorg. Chem., Org. Chem., Biochem., Biophys., **Vol: a8** (1953).

[121] D. A. Church, "Storage-Ring Ion Trap Derived from the Linear Quadrupole Radio-Frequency Mass Filter", Journal of Applied Physics **40**, 3127–3134 (1969).

[122] H. Schaaf, U. Schmeling, and G. Werth, "Trapped ion density distribution in the presence of He-buffer gas", Applied Physics **25**, 249–251 (1981).

[123] L. S. Cutler, R. P. Giffard, and M. D. McGuire, "Thermalization of199Hg ion macromotion by a light background gas in an RF quadrupole trap", Applied Physics B Photophysics and Laser Chemistry **36**, 137–142 (1985).

[124] M. Lunney, F. Buchinger, and R. Moore, "The Temperature of Buffer-gas Colled Ions in a Paul Trap", Journal of Modern Optics **39**, 349–360 (1992).

[125] Y. Moriwaki, M. Tachikawa, Y. M. Yoshiharu Maeno, and T. S. Tadao Shimizu, "Collision Cooling of Ions Stored in Quadrupole Radio-Frequency Trap", Japanese Journal of Applied Physics **31**, L1640 (1992).

[126] M. Green, J. Wodin, R. DeVoe, et al., "Observation of single collisionally cooled trapped ions in a buffer gas", Physical Review A **76**, 023404 (2007).

[127] A. T. Grier, M. Cetina, F. Oručević, and V. Vuletić, "Observation of Cold Collisions between Trapped Ions and Trapped Atoms", Physical Review Letters **102**, 223201 (2009).

[128] C. Zipkes, S. Palzer, L. Ratschbacher, C. Sias, and M. Köhl, "Cold Heteronuclear Atom-Ion Collisions", Physical Review Letters **105**, 133201 (2010).

[129] S. Schmid, A. Härter, and J. H. Denschlag, "Dynamics of a Cold Trapped Ion in a Bose-Einstein Condensate", Physical Review Letters **105**, 133202 (2010).

[130] F. H. J. Hall, M. Aymar, N. Bouloufa-Maafa, O. Dulieu, and S. Willitsch, "Light-Assisted Ion-Neutral Reactive Processes in the Cold Regime: Radiative Molecule Formation versus Charge Exchange", Physical Review Letters **107**, 243202 (2011).

[131] I. Sivarajah, D. S. Goodman, J. E. Wells, F. A. Narducci, and W. W. Smith, "Evidence of sympathetic cooling of Na + ions by a Na magneto-optical trap in a hybrid trap", Physical Review A **86**, 063419 (2012).

[132] Z. Meir, M. Pinkas, T. Sikorsky, et al., "Direct Observation of Atom-Ion Nonequilibrium Sympathetic Cooling", Physical Review Letters **121**, 053402 (2018).

[133] R. Côté and A. Dalgarno, "Ultracold atom-ion collisions", Physical Review A **62**, 012709 (2000).

[134] R. G. DeVoe, "Power-Law Distributions for a Trapped Ion Interacting with a Classical Buffer Gas", Physical Review Letters **102**, 063001 (2009).

[135] B. Gao, "Universal Properties in Ultracold Ion-Atom Interactions", Physical Review Letters **104**, 213201 (2010).

[136] C. Zipkes, L. Ratschbacher, C. Sias, and M. Köhl, "Kinetics of a single trapped ion in an ultracold buffer gas", New Journal of Physics **13**, 053020 (2011).

[137] B. Höltkemeier, P. Weckesser, H. López-Carrera, and M. Weidemüller, "Dynamics of a single trapped ion immersed in a buffer gas", Physical Review A **94**, 062703 (2016).

[138] S. J. Schowalter, A. J. Dunning, K. Chen, et al., "Blue-sky bifurcation of ion energies and the limits of neutral-gas sympathetic cooling of trapped ions", Nature Communications **7**, 12448 (2016).

[139] H. Dehmelt, "Stored-Ion Spectroscopy", in *Advances in Laser Spectroscopy*, edited by F. T. Arecchi, F. Strumia, and H. Walther (Springer US, Boston, MA, 1983), pp. 153–187.

[140] S. Earnshaw, "On the nature of the molecular forces which regulate the constitution of the luminiferous ether.", Transactions of the Cambridge Philosophical Society **7**, 97–112 (1842).

[141] P. Kapitza, "Dynamic stability of a pendulum when its point of suspension vibrates", Soviet Phys. JETP, 588–597 (1951).

[142] D. Gerlich, "Inhomogeneous RF Fields: A Versatile Tool for the Study of Processes with Slow Ions", in *Advances in Chemical Physics*, Vol. 82, edited by C.-Y. Ng, M. Baer, I. Prigogine, and S. A. Rice, 1st ed. (Wiley, Jan. 1992), pp. 1–176.

[143] L. D. Landau, E. M. Lifšic, L. D. Landau, and L. D. Landau, *Mechanics*, 3. ed., repr, Course of theoretical physics / L. D. Landau and E. M. Lifshitz 1 (Elsevier, Butterworth-Heinemann, Amsterdam Heidelberg, 2011).

[144] D. Gerlich, *Electronic and Atomic Collision*, 1986.

[145] F. G. Major, V. N. Gheorghe, and G. Werth, *Charged particle traps: physics and techniques of charged particle field confinement*, Charged Particle Traps 37 (Springer, Berlin New York, 2005).

[146] N. W. McLachlan, *Theory and Applications of Mathieu Functions*, New (Dover Publications Inc., Feb. 1965).

[147] I. Kovacic, R. Rand, and S. Mohamed Sah, "Mathieu's Equation and Its Generalizations: Overview of Stability Charts and Their Features", Applied Mechanics Reviews **70**, 020802 (2018).

[148] *MathieuCharacteristicA—Wolfram Language Documentation*.

[149] F. Diedrich, E. Peik, J. M. Chen, W. Quint, and H. Walther, "Observation of a Phase Transition of Stored Laser-Cooled Ions", Physical Review Letters **59**, 2931–2934 (1987).

[150] M. Drewsen, "Ion Coulomb crystals", Physica B: Condensed Matter **460**, 105–113 (2015).

[151] C. Shannon, "Communication in the Presence of Noise", Proceedings of the IRE **37**, 10–21 (1949).

[152] *Classical mechanics*, Third edition, fourteenth impression (Pearson India Education Services, Noida, 2016).

[153] G. Barton, *Elements of Green's functions and propagation: potentials, diffusion, and waves*, Oxford Science Publications (Clarendon Press ; Oxford University Press, Oxford : New York, 1989).

[154] K. Ravi, "Trapping and Cooling of Ions and the Study of Ion Atom Interactions", PhD thesis (Jawaharlal Nehru University, 2013).

[155] S. Lee, "The study of trapped ion collisions with cold atoms and cold molecules", PhD thesis (Jawaharlal Nehru University, 2014).

[156] S. Jyothi, "Exploring molecular ion formation, trapping and detection in hybrid system", PhD thesis (Jawaharlal Nehru University, 2015).

[157] R. Sawant, "Interactions between ultracold dilute gas of atoms, ions, and cavity", PhD thesis (Jawaharlal Nehru University, 2018).

[158] M. Niranjan, "Ultracold Ion-Atom Scattering", PhD thesis (Jawaharlal Nehru University, 2021).

[159] V. I. Gokul, A. Bahuleyan, S. P. Dinesh, V. R. Thakar, and S. A. Rangwala, "Cavity-based nondestructive detection of photoassociation in a dark magneto-optical trap", Physical Review A **109**, 053713 (2024).

[160] M. Niranjan, N. Joshi, A. Pandey, et al., "Quantum exchange symmetry induces charge diffusion and trapping in ultracold gases", Journal of Physics B: Atomic, Molecular and Optical Physics **57**, 075201 (2024).

[161] D. Leibfried, R. Blatt, C. Monroe, and D. Wineland, "Quantum dynamics of single trapped ions", Reviews of Modern Physics **75**, 281–324 (2003).

[162] E. L. Raab, M. Prentiss, A. Cable, S. Chu, and D. E. Pritchard, "Trapping of Neutral Sodium Atoms with Radiation Pressure", Physical Review Letters **59**, 2631–2634 (1987).

[163] H. J. Metcalf and P. Van der Straten, *Laser cooling and trapping*, Graduate Texts in Contemporary Physics (Springer, New York, 1999).

[164] W. D. Phillips and H. Metcalf, "Laser Deceleration of an Atomic Beam", Physical Review Letters **48**, 596–599 (1982).

[165] T. G. Tiecke, S. D. Gensemer, A. Ludewig, and J. T. M. Walraven, "High-Flux Two-Dimensional Magneto-Optical-Trap Source for Cold Lithium Atoms", Physical Review A **80**, 013409 (2009).

[166] F. Schmidt-Kaler, H. Häffner, S. Gulde, et al., "How to realize a universal quantum gate with trapped ions", Applied Physics B **77**, 789–796 (2003).

[167] N. Herschbach, K. Pyka, J. Keller, and T. E. Mehlstäubler, "Linear Paul trap design for an optical clock with Coulomb crystals", Applied Physics B **107**, 891–906 (2012).

[168] K. Pyka, N. Herschbach, J. Keller, and T. E. Mehlstäubler, "A high-precision segmented Paul trap with minimized micromotion for an optical multiple-ion clock", Applied Physics B **114**, 231–241 (2014).

[169] M. Schioppo, N. Poli, M. Prevedelli, et al., "A compact and efficient strontium oven for laser-cooling experiments", Review of Scientific Instruments **83**, 103101 (2012).

[170] T. G. Ballance, J. F. Goodwin, B. Nichol, et al., "A short response time atomic source for trapped ion experiments", Review of Scientific Instruments **89**, 053102 (2018).

[171] L. Sharma, A. Roy, S. Panja, and S. De, "Atomic Flux Distribution from a Low-Divergent Dark Wall Oven", Review of Scientific Instruments **90**, 053202 (2019).

[172] A. Prakash, A. Ayyadevara, E. Krishnakumar, and S. A. Rangwala, "Low divergence cold-wall oven for loading ion traps", Review of Scientific Instruments **95**, 033202 (2024).

[173] N. Ramsey, *Molecular Beams*, Oxford Classic Texts in the Physical Sciences (Clarendon Press ; Oxford University Press, Oxford : Oxford ; New York, 2005).

[174] H. C. W. Beijerinck and N. F. Verster, "Velocity Distribution and Angular Distribution of Molecular Beams from Multichannel Arrays", Journal of Applied Physics **46**, 2083–2091 (1975).

[175] D. Lucas, A. Ramos, J. Home, et al., "Isotope-Selective Photoionization for Calcium Ion Trapping", Physical Review A **69**, 012711 (2004).

[176] J. R. Rumble, ed., *CRC Handbook of Chemistry and Physics*, 102nd edition 2021-2022 (CRC Press, Boca Raton London New York, 2021).

[177] G. Smith, "Collision Broadening and Shift in the Resonance Line of Calcium", Journal of Physics B: Atomic and Molecular Physics **5**, 2310–2319 (1972).

[178] W. Nörtershäuser, N. Trautmann, K. Wendt, and B. Bushaw, "Isotope shifts and hyperfine structure in the transitions of stable calcium isotopes and calcium-41", Spectrochimica Acta Part B: Atomic Spectroscopy **53**, 709–721 (1998).

[179] R. F. Wuerker, H. Shelton, and R. V. Langmuir, "Electrodynamic Containment of Charged Particles", Journal of Applied Physics **30**, 342–349 (1959).

[180] S. Seidelin, J. Chiaverini, R. Reichle, et al., "Microfabricated Surface-Electrode Ion Trap for Scalable Quantum Information Processing", Physical Review Letters **96**, 253003 (2006).

[181] B. Stein, "Contributions to a Yb^{+} Single-Ion Optical Frequency Standard", PhD thesis (Leibniz Universitat Hannover).

[182] G. B. Arfken, *Mathematical methods for physicists: A Comprehensive Guide*, Seventh edition (Elsevier, New Delhi, 2021).

[183] J. D. Jackson, *Classical electrodynamics*, 3rd ed (Wiley, New York, 1999).

[184] D. J. Griffiths, *Introduction to Electrodynamics*, 5th ed. (Cambridge University Press, Nov. 2023).

[185] T. Lindvall, K. J. Hanhijärvi, T. Fordell, and A. E. Wallin, "High-accuracy determination of Paul-trap stability parameters for electric-quadrupole-shift prediction", Journal of Applied Physics **132**, 124401 (2022).

[186] Q. A. Turchette, Kielpinski, B. E. King, et al., "Heating of trapped ions from the quantum ground state", Physical Review A **61**, 063418 (2000).

[187] N. Daniilidis, S. Narayanan, S. A. Möller, et al., "Fabrication and heating rate study of microscopic surface electrode ion traps", New Journal of Physics **13**, 013032 (2011).

[188] *COMSOL - Software for Multiphysics Simulation*, https://www.comsol.com/.

[189] M. Doležal, P. Balling, P. B. R. Nisbet-Jones, et al., "Analysis of thermal radiation in ion traps for optical frequency standards", Metrologia **52**, 842–856 (2015).

[190] *Mechanical Engineering Services | Raman Research Institute*, https://www.rri.res.in/facilities/mechanical-engineering-services.

[191] *Central Manufacturing Technology Institute – Govt. of India*, https://cmti.res.in/.

[192] *Home - Government Tool Room & Training Centre*, https://gttc.karnataka.gov.in/english.

[193] *Thorlabs - TS10 Vacuum Epoxy, Low Vapor Pressure - Two Part*.

[194] W. Macalpine and R. Schildknecht, "Coaxial Resonators with Helical Inner Conductor", Proceedings of the IRE **47**, 2099–2105 (1959).

[195] J. D. Siverns, L. R. Simkins, S. Weidt, and W. K. Hensinger, "On the application of radio frequency voltages to ion traps via helical resonators", Applied Physics B **107**, 921–934 (2012).

[196] S. Panja, S. De, S. Yadav, and A. Sen Gupta, "Note: Measuring capacitance and inductance of a helical resonator and improving its quality factor by mutual inductance alteration", Review of Scientific Instruments **86**, 056104 (2015).

[197] T. Guo, P. Liu, and C. Lee, "New designed helical resonator to improve measurement accuracy of magic radio frequency", Chinese Physics B **31**, 093201 (2022).

[198] Y. Park, C. Jung, M. Seong, et al., "A New Measurement Method for High Voltages Applied to an Ion Trap Generated by an RF Resonator", Sensors **21**, 1143 (2021).

[199] P. Müller, K. König, P. Imgram, J. Krämer, and W. Nörtershäuser, "Collinear Laser Spectroscopy of Ca + : Solving the Field-Shift Puzzle of the 4 s S 1 / 2 2 → 4 p P 1 / 2 , 3 / 2 2 Transitions", Physical Review Research **2**, 043351 (2020).

[200] W. Nagourney, G. Janik, and H. Dehmelt, "Linewidth of single laser-cooled ^{24} Mg $^{+}$ ion in radiofrequency trap", Proceedings of the National Academy of Sciences **80**, 643–646 (1983).

[201] R. J. Cook and H. J. Kimble, "Possibility of Direct Observation of Quantum Jumps", Physical Review Letters **54**, 1023–1026 (1985).

[202] T. Sauter, R. Blatt, W. Neuhauser, and P. E. Toschek, "Quantum Jumps in a Single Ion", Physica Scripta **T22**, 128–132 (1988).

[203] P. A. Barton, C. J. S. Donald, D. M. Lucas, et al., "Measurement of the lifetime of the 3 d 2 D 5 / 2 state in 40 Ca +", Physical Review A **62**, 032503 (2000).

[204] H. Shao, Y. Huang, H. Guan, et al., "Precise determination of the quadrupole transition matrix element of Ca + 40 via branching-fraction and lifetime measurements", Physical Review A **95**, 053415 (2017).

[205] F. Riehle, *Frequency Standards: Basics and Applications*, 1st ed. (Wiley, Sept. 2003).

[206] D. J. Berkeland, J. D. Miller, J. C. Bergquist, W. M. Itano, and D. J. Wineland, "Minimization of ion micromotion in a Paul trap", Journal of Applied Physics **83**, 5025–5033 (1998).

[207] F. Arecchi and R. Bonifacio, "Theory of optical maser amplifiers", IEEE Journal of Quantum Electronics **1**, 169–178 (1965).

[208] J. Olivero and R. Longbothum, "Empirical fits to the Voigt line width: A brief review", Journal of Quantitative Spectroscopy and Radiative Transfer **17**, 233–236 (1977).

[209] M. Knoop, M. Vedel, and F. Vedel, "Lifetime, collisional-quenching, and j -mixing measurements of the metastable 3 D levels of Ca +", Physical Review A **52**, 3763–3769 (1995).

[210] G. Ritter and U. Eichmann, "Lifetime of the level from quantum jump statistics of a single laser-cooled ion", Journal of Physics B: Atomic, Molecular and Optical Physics **30**, L141–L146 (1997).

[211] M. Block, O. Rehm, P. Seibert, and G. Werth, "3d", The European Physical Journal D **7**, 461 (1999).

[212] H. Walther, "Phase Transitions of Stored Laser-Cooled Ions", in *Advances In Atomic, Molecular, and Optical Physics*, Vol. 31 (Elsevier, 1993), pp. 137–182.

[213] J. D. Prestage, A. Williams, L. Maleki, M. J. Djomehri, and E. Harabetian, "Dynamics of charged particles in a Paul radio-frequency quadrupole trap", Physical Review Letters **66**, 2964–2967 (1991).

[214] V. L. Ryjkov, X. Zhao, and H. A. Schuessler, "Simulations of the rf heating rates in a linear quadrupole ion trap", Physical Review A **71**, 033414 (2005).

[215] M. W. Van Mourik, P. Hrmo, L. Gerster, et al., "Rf-induced heating dynamics of noncrystallized trapped ions", Physical Review A **105**, 033101 (2022).

[216] E. L. Pollock and J. P. Hansen, "Statistical Mechanics of Dense Ionized Matter. II. Equilibrium Properties and Melting Transition of the Crystallized One-Component Plasma", Physical Review A **8**, 3110–3122 (1973).

[217] W. L. Slattery, G. D. Doolen, and H. E. DeWitt, "Improved equation of state for the classical one-component plasma", Physical Review A **21**, 2087–2095 (1980).

[218] J. Hoffnagle, R. G. DeVoe, L. Reyna, and R. G. Brewer, "Order-Chaos Transition of Two Trapped Ions", Physical Review Letters **61**, 255–258 (1988).

[219] R. Blümel, C. Kappler, W. Quint, and H. Walther, "Chaos and order of laser-cooled ions in a Paul trap", Physical Review A **40**, 808–823 (1989).

[220] R. G. Brewer, J. Hoffnagle, and R. G. DeVoe, "Transient two-ion chaos", Physical Review Letters **65**, 2619–2622 (1990).

[221] J. Hoffnagle and R. G. Brewer, "Frequency-locked motion of two particles in a Paul trap", Physical Review Letters **71**, 1828–1831 (1993).

[222] L. Duca, N. Mizukami, E. Perego, M. Inguscio, and C. Sias, "Orientational Melting in a Mesoscopic System of Charged Particles", Physical Review Letters **131**, 083602 (2023).

[223] J. Liang and P. C. Haljan, "Hopping of an impurity defect in ion crystals in linear traps", Physical Review A **83**, 063401 (2011).

[224] A. Benassi, A. Vanossi, and E. Tosatti, "Nanofriction in cold ion traps", Nature Communications **2**, 236 (2011).

[225] A. Bermudez, M. Bruderer, and M. B. Plenio, "Controlling and Measuring Quantum Transport of Heat in Trapped-Ion Crystals", Physical Review Letters **111**, 040601 (2013).

[226] S. Ulm, J. Roßnagel, G. Jacob, et al., "Observation of the Kibble–Zurek scaling law for defect formation in ion crystals", Nature Communications **4**, 2290 (2013).

[227] M. Drewsen, C. Brodersen, L. Hornekær, J. S. Hangst, and J. P. Schifffer, "Large Ion Crystals in a Linear Paul Trap", Physical Review Letters **81**, 2878–2881 (1998).

[228] V. Ursekar, J. M. Silvester, Y. S. Nam, and R. Blümel, "Prediction of exotic ion-crystal structures in a Paul trap", The European Physical Journal D **72**, 165 (2018).

[229] A. Dantan, J. P. Marler, M. Albert, D. Guénot, and M. Drewsen, "Noninvasive Vibrational Mode Spectroscopy of Ion Coulomb Crystals through Resonant Collective Coupling to an Optical Cavity Field", Physical Review Letters **105**, 103001 (2010).

List of Figures

1 Ion trap assembly mounted inside the vacuum chamber ix

2 Top Panel: Image of the mounted oven on CF16 feedthrough used for the characterisation. Bottom Panel: A 2D sketch of the oven with details of the components. x

2.1 (a) Shape of the potential in x-z plane at time $t = 0$.(b) The shape of the potential in the x-z plane at time $t = \frac{\pi}{\Omega}$. 7

2.2 Electrode configuration to generate potential of quadrupolar form 9

2.3 Stability diagram for equation 2.19 in z—direction. The stability plot has been generated using the inbuilt function in Mathematica [148] 12

2.4 Stability diagram for equation 2.19 in x and y directions. The stability plot has been generated using the inbuilt function in Mathematica [148] . . . 13

2.5 Lowest stability zone of equation 2.19 in $r-z$ plane formed by intersection of individual stability curves in r and z directions. 14

2.6 Position of a trapped calcium ion in ideal Paul trap geometry for $q_x = 0.1$, $\Omega_{rf} = 2\pi \times 30$ MHz 15

2.7 Power spectrum of the ion position in time and peaks are at the fundamental frequency, first and second harmonics. 15

2.8 (a) 3D view of linear Paul trap (4 pole), RF field is applied on cylindrical rods to achieve confinement in 2 directions and static field is applied on ring electrodes to provide confinement in the remaining direction. (b) View of the trap in the x-y plane with voltage configuration of electrodes. . . . 16

2.9 2D view of electrode and voltage configuration of different multipole traps. Only RF voltage-carrying electrodes are shown for clarity. 16

2.10 Position of a trapped $^{40}Ca^{+}$ in time for 4 pole trap for the initial condition mentioned in table 2.3 18

2.11 Discrete transform of the ion's position shown in figure 2.10. The peak at 1.77×10^5 Hz corresponds to the secular frequency mentioned in equation 2.30, and other peaks are higher harmonics mentioned in equation 2.29. . 19

2.12 Position of a trapped $^{40}Ca^{+}$ in time in 6 pole trap for the initial condition mentioned in table 2.4 19

2.13 Discrete transform of the ion's position shown in figure 2.12 20

2.14 Position of a trapped ion in 8 pole trap. 21

2.15 Discrete transform of the ion's position data in time shown in figure 2.14 21

2.16 Orbit of a trapped calcium ion in different trap geometries for different initial conditions. (a) Orbit in a 4-pole trap; it is closed except for micro-motion. Angular momentum is non-zero, so the particle never samples the origin. (b) Orbit in a 6-pole trap for zero angular momentum. (c) Orbit in an 8-pole trap for non-zero angular momentum. The orbit is not closed, and the particle never samples the origin. (d) Orbit in an 8-pole trap for non-zero angular momentum. The orbit is not closed, and the particle never samples the origin. 22

2.17 Change in the trajectory of an ion due to micromotion interruption. (a) Original and modified trajectory of an ion after collision with an atom at rest. Here, a collision takes place at a point where the rf force is directed away from the trap centre. (b) Collision with an atom away from the turning point. (c) zoomed view of the instance of collision shown in (a) . 23

2.18 Trajectory for ion and atom during collision. When the first collision occurs at $\phi = \pi/2$, the energy change is maximum during a single collision, and it is sufficient to knock the atom far away from its starting point. For the first collision at $\phi = 3\pi/2$, the total energy change will be negative. So, more than one collision is required to knock the atom away. 27

2.19 Change in total secular energy as a function of the phase of trapping field ϕ. 28

2.20 (Top Panel) Position of ion and atom during collision process, (Bottom Panel) Kinetic energy of ion during the process. (a) 4-pole trap, (b) 6-pole trap, (c) 8-pole trap, (d)End-cap type trap. 29

2.21 Change in secular energy of the ion-atom system with respect to the phase of the trapping field at the time of collision. 30

4.1 (Top panel) Image of the oven mounted on the feedthrough using a Macor block. This oven is used for the characterization presented in this chapter. (Bottom panel) 2D schematic diagram of the oven assembly 37

4.2 An image of aligned groove grabber with ss plate inside the vacuum chamber. The needle shown in the images passes smoothly through the brass plate (not visible in the image), and the ss plate is mounted via groove grabbers. 38

4.3 (Left Panel)Experimental setup with mounting assembly. (Right Panel) Fluorescence at the centre of the chamber due to the interaction of the atomic beam with a laser beam (L1). 39

4.4 (Left Panel) Schematic diagram showing the alignment of the oven and laser beams with respect to the vacuum chamber. (Right Panel) Optical setup showing the arrangement for the frequency, scan range measurement and the beam division for spectroscopy of the oven's atomic beam where WSU-2 is the wavemeter used to measure the scan range, BS 70 : 30 is the beam splitter, which divides the incoming beam in the ratio of 70 and 30, Ca HCL is calcium hollow cathode lamp, PBS is a polarising beam splitter, PD is the photodiode, $\lambda/4$ is quarter waveplate, and NDF is neutral density filter. 40

4.5 (Top Panel) The averaged fluorescence image captured on the CCD camera and (Bottom Panel) the experimental data along the centre line of the above image with Gaussian fit. 41

4.6 Experimental data and fit function corresponding to the L1 and L2 beams (Voigt + MBD) for 4.5 A. Purple colour are actual data points, Violet colour is showing error bar corresponding to the data points, and black is the fitted function. 42

4.7 Fluorescence spectrum of the atoms emitted from the oven when addressed by a resonant laser in single-pass (top panel) and retro-reflected configurations (mid panel), with reference to the SAS transmittance (bottom panel). 44

4.8 Averaged fluorescence signal showing the peaks for ^{40}Ca, ^{42}Ca and ^{44}Ca. The dotted lines mark the isotope shifts of ^{42}Ca and ^{44}Ca with respect to ^{40}Ca peak [178]. 45

4.9 Fluorescence signal of the oven after switching on the heating current, and temporal evolution of the signal. Here, the red curve shows the change in oven current, and the blue curve represents the fluorescence signal. 46

5.1 2D schematic of electrode configuration in End cap type trap 50

5.2 Central plane cut view of the final ion trap assembly. 52

5.3 Screenshot of Comsol interface showing the mesh for complete and final trap model with all components to solve Poisson's equation with appropriate boundary condition. Insulators and metal parts are shown in different colours. 55

5.4 Contour plot of trap potential in the region of interest around the trap centre. 56

5.5 Effect of the fork's shape on potential generated by full trap assembly at the centre. 57

5.6 Scanning Electron Microscope (SEM) image of the first trap prototype built at RRI workshop. We have used stainless steel to make all the parts. It is evident from the image that we need better machining precision and methods to constrain the position of electrodes with respect to the frame. The strands are residue of the lens cleaning tissues. 58

5.7 Image of the modified trap assembly to align the outer electrode. The frame is made from CuCrZr, the electrodes are made from stainless steel, and Teflon is used as an insulator. 59

5.8 SEM image of the one side of the trap electrodes. We observe a positive impact of the guiding insulators on alignment. 59

5.9 SEM image of the inner electrode for the case of interference fit trail. . . . 60

5.10 The Left image shows the M2 tap and slot to align the inner electrode. The right image is showing the top view of the top arm. 61

5.11 SEM image of the inner electrodes. The diameter of the inner electrodes is 905 μm and 908 μm. 62

5.12 Left Panel: (Top) AFM image of the top surface of the inner electrode 1, (Bottom) Corresponding surface undulation along the lines marked in the top image. RMS roughness, in this case, is approximately 208 nm. Right Panel: (Top) AFM image of the top surface of the inner electrode 2, (Bottom) Corresponding surface undulation along the lines marked in the top image. RMS roughness, in this case, is approximately 26 nm 63

5.13 (a) SEM image of the top portion of the conical electrode 1. It is almost circular on the inner as well as the outer side. (b) SEM image of the top portion of the conical electrode 2. It is almost circular inside, but the outer side has a significant deviation. We will observe the effect of this distortion in the final assembly. 63

5.14 Close view of the aligned trap assembly installed inside the vacuum chamber. 64

5.15 SEM image of the aligned assembly. (a) Co-axial deviation between the inner electrodes. (b) Distance between the inner electrodes. (c) Alignment of the conical electrode 1 with respect to the pin electrode shown in (a). (d) Alignment of the conical electrode 2 with respect to the pin electrode shown in (b). (e) Alignment of the conical electrode 1 with respect to the pin electrode shown in (a) in the orthogonal direction shown in (c). (f) Alignment of the conical electrode 2 with respect to the pin electrode shown in (b) in the orthogonal direction shown in (d). The length scale of individual images is shown at the bottom of the image. 65

6.1 (Top) Rendered image of the full assembly setup with all critical components and mounting frame made using aluminium profile channels and plate to hold the vacuum chamber in place. (Bottom) Detailed view of the trap mounting structure and feedthroughs for connection. 71

6.2 Mounting assembly for the trap, to mount the whole setup inside the chamber, showing SS plate, insulator and Copper bolts. Copper Bolt 1 is used to provide the electrical connection to the outer electrode. The middle bolt in copper bolt 2 is used to provide the RF connection to the trap; counter sink screws replace the other two bolts in copper bolt 2 to avoid any contact of the mounting assembly to the chamber. Macor® plate and spacers isolate the copper bolts and the trap from the SS plate, respectively. Machining design details of the plate and other parts are given in **??**. The trap shown in the image is not the aligned trap. 72
6.3 (a) Image of the complete assembly mounted on an optical table in the lab. (b) Zoomed view of the components inside the chamber. 74
6.4 Image of the setup ready for the baking process. Yellow wires are k-type thermocouples attached to the surface of the vacuum assembly at different points. 75
6.5 Change in temperature of the thermocouples with time during the baking process. Temperature variation of 4 thermocouples are shown in the figure, out of which three are installed on the chamber body near viewports, and the 4th is installed on the TSP cartridge arm. At t_0, we stopped increasing the current in the heater coil on day 1. At t_1, on the next day, we stopped increasing the current in the heater coil and left the system unperturbed till time t_2. After t_2, we started decreasing current in the heater coil. . . . 76
6.6 Change in Pressure on the ion gauge and temperature of the Front viewport trap side with time during the baking process. The current in the heating tape is constant between the time t_1 and t_2 77
6.7 Schematic diagram of a helical resonator showing the position of coils and other parts. 79
6.8 Lump circuit model of RF source, helical resonator, trap and other connecting parts. L_a is the inductance of the antenna coil, L_h is the inductance of the main coil, R_h is the resistance of the main coil, C_h is the capacitance of the main coil, R_j is the resistance of the main coil to the shield joint,R_s is the resistance of shield, C_s is the capacitance between the shield and the main coil, C_w is the capacitance of wire used to connect the resonator to the trap, C_t is the capacitance of the trap and R_t is the resistance of the trap. 79
6.9 Schematic of experimental setup for measurement of Q factor 82
6.10 (a) Normalized reflection spectrum for the unloaded case. (b) Normalized reflection spectrum for the loaded case 82
6.11 (a) Normalized reflection spectrum for the unloaded case. (b) Normalized reflection spectrum for the loaded case 82
6.12 Schematic of probe circuit and details of components 83
6.13 Calibration curve for the source and the probe. The set voltage on the source is 2000 mV. 84

6.14 Transmission spectrum of the resonator integrated with the trap mounted inside the chamber before baking. Resonance frequency is ≈ 18.4 MHZ and Q is ≈ 115 84
6.15 Transmission spectrum of the resonator integrated with the trap mounted inside the chamber before baking. Resonance frequency is ≈ 19.67 MHZ and Q is ≈ 114 85
6.16 (a) Schematic showing RC and Pi filters used to filter the noise of DC output and their position in the setup. (b) Transmission spectrum of the filter. . 86
6.17 Schematic diagram showing the grounding arrangement of the system . . 86
6.18 Relevant energy levels and corresponding transition wavelengths of Ca and Ca^+ 87
6.19 Schematic diagram of the optics assembly used to collect fluorescence from the trapped ions. The focal length of the lenses from left to right is 60 mm, 75 mm, -50 mm, 100 mm and 1000 mm. 88
6.20 Signal observed on PMT from trapped ion cloud. The Change in signal with the trap voltage and repump laser status confirms that the signal is real. 90
6.21 Functioning experimental setup. 91

7.1 False colour image of the ion clouded loaded in the trap. The cloud shape is elliptical because the trap is stiffer in $z-$ direction compared to the x and y directions, $\omega_z \approx 2\omega_x$. 94
7.2 Ion loading signal observed on PMT. This data is taken at 4.1 A oven current. Initially the fluorescence signal is at the background level. The fluorescence signal increases after loading of every ion in the trap. Wait time to load the first ion is not shown in the image. 95
7.3 Energy levels of $^{40}Ca^+$ showing cooling transition, 397 nm, repump transition, 866 nm, and 850 nm transition used to observe quantum jumps. 96
7.4 (a) Quantum jumps signal for single ion. When the electron is shelved into $3D_{5/2}$ metastable stable, PMT fluorescence goes to the background level. (b) When one ion goes to metastable $3D_{5/2}$, the fluorescence signal decreases to half, and when both go to $3D_{5/2}$, the fluorescence signal drops to the background level. The number of steps in the fluorescence signal equals the number of trapped ions. 96
7.5 (a) Image of a single loaded and cooled ion in the trap (b) Image of two loaded and cooled ions in the trap. These ions are loaded at 4.1 A oven current. 97
7.6 Dip observed in the fluorescence signal of ion cloud during forced oscillation. Trap drive voltage is 300 V and dc offset is −5 V. 98

7.7 Secular frequency of the trap for different trap parameters measured by forced oscillation method. Discrete data points are experimentally obtained value and line are best fit for a given q_z value and various dc offsets. x and y directions are degenerate, so we get two very close points on the graph for secular frequencies along these directions. 100

7.8 Photon correlation signal of an uncompensated ion. 102

7.9 Photon correlation signal of a compensated ion. $\Delta S/S_0$ for resonator, oven and ionization beams are -.06,-0.06 and 0.03 respectively. 103

7.10 Photon correlation signal of a compensated ion. $\Delta S/S_0$ for resonator, oven and ionization beams are .015,0.014 and 0.01 respectively. 104

7.11 Ion hold time without cooling laser. 104

7.12 Normalized fluorescence rate versus laser detuning for a single trapped ion. Laser power for data_1 is 0.22μW and for the data_2 is 65.3 μW. 106

7.13 Weighted fit and data points for different laser powers. x-axis is scaled laser power because we measure the power outside the vacuum chamber. The value of intercept on the γ'^2 is ≈ 801. 106

7.14 Fitted function and experimental data for lifetime determination of metastable state $D_{5/2}$. 107

7.15 Cloud to crystal transition of 4 ions for different trapping voltages. 109

7.16 Image of 2 ion crystal, RF voltage applied to the trap is ≈ 310 V and the RF drive frequency is $2\pi \times 18.63$ MHz. (a) Rod configuration, ions are aligned along a line in the radial plane, dc offset is 0 V (b) pop out phase, dc offset is -9 V. (c) pop out configuration, dc offset is -10 V. (d) Rod phase, aligned along $z-$axis, dc offset is -13 V. 111

7.17 Image of 3 ion crystal, RF voltage applied to the trap is ≈ 250 V and the RF drive frequency is $2\pi \times 18.63$ MHz. (a) Rod configuration, ions are aligned along a line in the radial plane, dc offset is 0 V (b) planar configuration, dc offset is -6 V. (c) pop out phase, dc offset is -7 V. (d) Rod configuration, aligned along $z-$axis, dc voltage in this case is -12 V. 112

7.18 Image of 3 ion crystal, RF voltage applied to the trap is ≈ 250 V and the RF drive frequency is $2\pi \times 18.63$ MHz. (a) Rod configuration, ions are aligned along a line in the radial plane, dc offset is 0 V (b) planar configuration, dc offset is -6 V. (c) pop out phase, dc offset is -7 V. (d) Rod configuration, aligned along $z-$axis, dc voltage in this case is -12 V. 113

7.19 Image of 4 ion crystal, RF voltage applied to the trap is ≈ 225 V and the RF drive frequency is $2\pi \times 18.63$ MHz. (a) Rod phase, ions are aligned along a line in the radial plane, dc offset is 0 V (b) pop out configuration, dc offset is -7 V. (c) Zig-zag configuration, dc offset is -8.4 V. (d) Rod configuration, aligned along $z-$axis, dc voltage in this case is -9 V. 114

7.20 Image of 4 ion crystal, RF voltage applied to the trap is ≈ 225 V and the RF drive frequency is $2\pi \times 18.63$ MHz. (a) A possible tilt phase configuration, ions are aligned along a line in the radial plane, dc offset is −4.4 V (b) A possible configuration, dc offset is −6 V. Due to imaging limitations, these phases can not be identified to a particular tilt phase. 115

B.1 Macor spacer present behind the ss plate. It is used to isolate the screws for electrical connection from the ss plate. 129
B.2 SS plate for mounting trap with respect to the groove grabbers. 130
B.3 Macor spacer used to isolate the trap from the ss plate. 131
B.4 Screw used to provide electrical connection to the trap. Feedthrough fits into the circular hole at the head of the screw and hold in place using M2 screws. 132

List of Tables

2.1 Form of the potential for different linear Paul trap configuration. 15

2.2 Parameters for trajectory simulation of a charged particle in 2n pole traps 17

2.3 Initial parameters used for trajectory simulation in 4 pole trap. $x(0), y(0)$ are position of ion in x and y directions, respectively. $x^{'}(0), y^{'}(0)$ initial velocity in x and y directions, respectively. 18

2.4 Initial parameters used for trajectory simulation in 6 pole trap. $x(0), y(0)$ are position of ion in x and y directions, respectively. $x^{'}(0), y^{'}(0)$ initial velocity in x and y directions, respectively. 20

2.5 Initial parameters used for trajectory simulation in 8 pole trap. $x(0), y(0)$ are position of ion in x and y directions, respectively. $x^{'}(0), y^{'}(0)$ initial velocity in x and y directions, respectively. 20

2.6 Parameters for simulation of rf heating 22

2.7 Parameters for ion-atom collision trajectory simulation in 2n pole traps. Here, r_{i-a} is the initial separation between atom and ion, r_{max} is the maximum separation between atom and ion, r_{min} is the distance of minimum approach between atom and ion, ϕ_1 is the angle atom makes with the x-axis at the start of the simulation. 30

5.1 Relation between multipole coefficients and fitted coefficients 51

5.2 Comparison of multipole coefficients for different trap geometries. We have simulated already published trap geometries similar to our design and compared the values of multipole coefficients with their literature values. 54

5.3 This table presents the alignment analysis of the SEM images shown in figure 5.15. From the 5th row onwards, all the rows represent the outer diameter of the conical electrode and the gap between the inner electrode and conical electrodes on both sides. All the dimensions mentioned in the table are in mm. 66

7.1 Parameters for secular frequency experimental data. According to our simulation, difference between secular frequency in x and y direction will be very small, so the parameters for forced oscillation are same in x and y directions are same. 99

7.2 Fitted parameters for forced oscillation case. 99

7.3 Laser and trap parameters for correlation signal acquisition in uncompensated case. 103
7.4 Compensation voltage on the different electrodes for the case shown in figure 7.10 103
7.5 Lifetime of $D_{5/2}$ state reported in previous experiments 107